

Development of Ion Irradiation Experimental Capabilities and the Irradiation Response of ZrC

A Thesis Written by Jacob Lewis-Fell

University of Huddersfield

March 2022

Copyright Statement

The author of this thesis (including any appendices and/ or schedules to this thesis) owns any copyright in it (the “Copyright”) and he has given The University of Huddersfield the right to use such Copyright for any administrative, promotional, educational and/or teaching.

Copies of this thesis, either in full or in extracts, may be made only in accordance with the regulations of the University Library. Details of these regulations may be obtained from the Librarian. This page must form part of any such copies made.

The ownership of any patents, designs, trademarks and any and all other intellectual property rights except for the Copyright (the “Intellectual Property Rights”) and any reproductions of copyright works, for example graphs and tables (“Reproductions”), which may be described in this thesis, may not be owned by the author and may be owned by third parties. Such Intellectual Property Rights and Reproductions cannot and must not be made available for use without permission of the owner(s) of the relevant Intellectual Property Rights and/or Reproductions.

Abstract

The work presented in this thesis describes how an *in-situ* ion beam with Transmission Electron Microscope (TEM) system was upgraded to allow for the undertaking of experiments that will further the understandings of material science. In order to achieve more accurate experimental results, the MIAMI-1 (Microscopes and Ion Accelerators for Materials Investigations) in situ TEM ion beam line at Huddersfield University was upgraded. The beamline now has direct line of sight with the TEM reducing maintenance and improving alignment. The ion beam line can produce ions of various species. The energies of the ions run from 2-100 keV. This produces fluxes in the range of 10^{10} - 10^{14} ions/cm²/s. A new system for measuring dosimetry has been introduced ensuring that experimental results are accurate and can be compared with the wider literature.

Accompanying this was the development of pre-experimental calculation techniques to allow for more accurate experimental parameter setup for use in spherical and cylindrical nanoparticle experiments. These calculations have already been used in the publications of papers and it is hoped that they will continue to be useful for future experiments.

The characteristics of ZrC once it had undergone helium ion implantation was also reported on. The formation and density of bubbles in the material were explored. Amorphisation analysis was performed with it being discovered that ZrC amorphises at 600°C under helium ion irradiation at 1 DPA a new discovery for the scientific community.

List of Publications Arising and Declarations of Contributions

The following work was published alongside the work submitted in this thesis; in each work the authors contribution is stated below:

Low-temperature investigations of ion-induced amorphisation in silicon carbide nanowhiskers under helium irradiation, 10.1016/j.apsusc.2019.143969

Assisted with sample preparation and during the experimental work.

Radiation damage suppression in AISI-316 steel nanoparticles: Implications for the design of future nuclear materials, 10.1021/acsanm.0c01611

SICMod Code used for pre-experiment calculations.

In Situ TEM Investigations of the Microstructural Changes and Radiation Tolerance in SiC Nanowhiskers Irradiated with He Ions at High Temperatures, 10.2139/ssrn.3674678

Assisted with sample preparation and during the experimental work. SICMod Code used for pre-experiment calculations.

Enhanced Radiation Tolerance of Tungsten Nanoparticles to He Ion Irradiation, 10.3390/nano8121052

Assisted with sample preparation and during the experimental work. SICMod Code used for pre-experiment calculations.

Direct Comparison of Tungsten Nanoparticles and Foils under Helium Irradiation at High Temperatures Studied via In-Situ Transmission Electron Microscopy, 10.1017/s1431927619008614

Assisted with sample preparation and during the experimental work. SICMod Code used for pre-experiment calculations.

Acknowledgements

The author would like to acknowledge the following people and institutions, without whom this work would not have been possible:

The EPSRC who funded the research.

The members of the MIAMI facilities all of whom were willing to give time and expert knowledge.

The main supervisors Jonathan Hinks, Stephen Donnelly, and Emily Aradi whose time and training were an immense help.

The author's parents Robert Fell and Vyvian Lewis for their financial and emotional support.

The authors cat Sweep who was a constant companion in the writing of this report.

Contents

1 Introduction	19
2 Literature Review	21
2.1 Transmission Electron Microscopy Basic Principles.....	21
2.1.1 A Brief History of the Initial TEMs	21
2.1.2 Advantages of TEM	22
2.1.3 Electron Scattering	23
2.1.4 Electron Diffraction	30
2.2 TEM Construction.....	31
2.2.1 Gun system	32
2.2.2 Lenses	33
2.2.3 Apertures	34
2.2.4 Deflectors.....	37
2.2.5 Stigmators.....	37
2.2.6 Goniometer and Sample Holders	38
2.2.7 TEM Image Capturing	38
2.2.8 Additional Features	39
2.3 Nuclear Reactors	40
2.3.1 Introduction	40
2.3.2 Introduction to Nuclear Power.....	40
2.3.3 Reactor Basics	40
2.3.4 Current Reactors.....	41
2.3.5 Future Reactors	43
2.3.6 Current Reactor Materials	52
2.3.7 Fusion Reactors	53
2.3.8 Nuclear Reactors Conclusions	55
2.4 Atomic and Microscopic Effects of Irradiation on a Material	56
2.4.1 Introduction	56
2.4.2 Atomic Collisions in Solids	56

2.5 Types of Defects	59
2.5.1 Introduction	59
2.5.2 1D Defects.....	59
2.5.3 2D Defects.....	63
2.5.4 3D Defects.....	69
2.5.5 Volume Defects	69
2.6 Physical Effects of Irradiation.....	71
2.6.1 Introduction	71
2.6.2 Radiation induced segregation	71
2.6.3 Voids and Bubbles	73
2.6.4 Irradiation hardening.....	74
2.6.5 Embrittlement of irradiated materials	75
2.6.6 Reducing Irradiation hardening and embrittlement	76
2.6.7 Fatigue	77
2.6.8 Irradiation Creep and Growth	77
2.6.9 Stress Induced Preferential Nucleation (SIPN)	78
2.6.10 Stress Induced Preferential Absorption (SIPA)	79
2.6.11 Preferred Absorption Glide (PAG)	79
2.6.12 Dislocation bias contribution to climb and glide	80
2.6.13 Transient creep.....	81
2.6.14 Loop un-faulting	83
2.6.15 Recovery creep	83
2.6.16 Amorphization	85
2.6.17 Chemical Effects	85
2.7 Ion irradiation.....	86
2.7.1 Introduction	86
2.7.2 Sputtering	86
2.7.3 Gibbsian Absorption	89
2.7.4 Recoil Implantation.....	89
2.7.5 Cascade Mixing	91
2.7.6 Ballistic Mixing	91

2.7.7 Chemical Effects on Ion Beam mixing	92
2.8 TEM with in-situ Ion Beam	93
2.8.1 Introduction	93
2.8.2 Accelerating and Transporting Ions	93
2.8.3 TEM Selection	94
2.8.4 Interfacing an ion beam with a TEM	95
2.8.5 Ion Beam Dosimetry	96
2.8.6 Vibrational isolation	98
2.8.7 Computational Control	98
2.9 SiC-Based Materials and Their Properties	99
2.9.1 Introduction	99
2.9.2 Basic Properties and Structure	99
2.9.3 Bonding	101
2.9.4 Thermal Properties	101
2.9.5 Mechanical Properties	102
2.9.6 Oxidation	103
2.9.7 Chemical Properties	104
2.9.8 Neutron Irradiation	104
2.9.9 Ion Irradiation	106
2.9.10 Current Uses	107
2.9.11 SiC Fabrication	107
2.9.12 SiC as an ATF (Accident Tolerant Fuel)	108
2.9.13 Ceramic Matrix Composite SiC	108
2.9.14 SiC future recommendations	109
2.10 Zirconium Carbide	110
2.10.1 Introduction	110
2.10.2 Basic Properties and Structure	110
2.10.3 Bonding	112
2.10.4 Thermal properties	112
2.10.5 Mechanical Properties	113
2.10.6 Oxidation	113

2.10.7 Chemical Properties.....	114
2.10.8 Neutron Irradiation.....	115
2.10.9 Ion Irradiation	115
2.10.10 ZrC Fabrication.....	117
2.10.11 ZrC as an ATF	118
2.10.12 ZrC future recommendations	118
2.11 The use of nanomaterials.....	119
2.11.1 Introduction.....	119
2.11.2 Sample Preparation	119
2.11.3 Defect Accumulation	119
2.11.4 Amorphization Resistance	120
2.11.5 Mechanical Properties.....	121
2.11.6 Conclusions	121
3 Experimental Procedure	122
3.1 Introduction.....	122
3.2 Sample Preparation.....	122
3.2.1 Ultrasonic Disc Cutting	122
3.2.2 Surface grinding.....	123
3.2.3 Dimpling.....	124
3.2.4 Precision Ion Polishing.....	125
3.2.5 Nanoparticle dispersion.....	127
3.2.6 Microparticle dispersion.....	128
3.3 Pre-experiment calculations	129
3.3.1 Stopping and Range of Ions in Matter/Transport of Ions in Matter (SRIM/TRIM).....	129
3.3.2 SICMod (Spherical Ion Calculations Modifier).....	131
3.3.3 DPA Calculations	133
3.4 Amorphization Analysis.....	134
4 MIAMI-1 Upgrade	136
4.1 Introduction.....	136
4.2 Final Deflection Problems	137

4.3 Support Structure	139
4.4 Electrostatic Deflector	140
4.5 New Einzel lens.....	142
4.6 New HV Shield	146
4.7 Condenser Mini Lens Column Section.....	147
4.8 Skimmer.....	148
4.9 Insertable Dosimetry Device	151
4.10 Bellows	152
4.11 Ceramic Standoffs	152
4.12 Earthed Cage and Support Structure Modifications	153
4.13 Cold Finger.....	154
4.14 Complete Design	155
4.15 Quantification of System Performance.....	156
4.16 Future Recommendations.....	156
5 ZrC irradiation	157
5.1 9keV He ⁺ Ion irradiation effects on ZrC	157
5.2 Experiments on Nanoparticles	159
5.2.1 SICMod Calculations for Nanoparticles	159
5.2.2 Irradiation of ZrC Nanoparticles	161
5.2.3 Helium Bubble Formation and Evolution in Nanoparticles	163
5.2.4 Sputtering	163
5.2.5 Amorphization	164
5.3 Experiments on Microparticles	170
5.3.1 SRIM Calculations for Microparticles	170
5.3.2 He Bubble formation and Evolution in Microparticles.....	172
5.3.3 Sputtering	178
5.3.4 Amorphization	178
5.3.5 ZrC 9keV He⁺ Ion Irradiation Bubble Density Comparison	183
5.4 Discussion.....	186
5.4.1 Nanoparticles vs Microparticles	186

5.4.2 ZrC compared to SiC	187
5.5 Future Recommendations.....	189
6 Conclusions	190
7 References	191
8 Appendix	225
8.1 SICMod Code (Python 2.7)	225
8.2 SICMod Guide.....	266
8.3 Figures	269

List of Figures

<i>Figure 1. A Picture of The First Electron Microscope [10]</i>	21
<i>Figure 2 Electron Elastic Scatter with Backscatter, Large Angle Scatter, and Low Angle Scatter Respectively</i>	28
Figure 3 Overview of TEM Optics Ray Diagram	31
Figure 4 TEM Gun Alignment Using Undersaturated Filament to Produce Cross-section of Kiwi [14]	32
Figure 5 Objective Aperture Situated in Bright Field Mode Ray Diagram	35
Figure 6 Dark Field Mode Ray Diagram	35
Figure 7 Selected Area Aperture Ray Diagram	36
Figure 8 TEM Deflection System Showing Shifted and Tilted Beam	37
Figure 9 Cross-sectional View of Basic Sample Holder Inserted into TEM with Vacuum Highlighted	38
Figure 10 Main Reactor Types as of 2015 reproduced from World Nuclear Association [20]	42
Figure 11 Schematic diagram of a pressurised-water reactor reproduced from World Nuclear Association [20]	43
Figure 12 Schematic diagram of an advanced gas-cooled reactor reproduced from World Nuclear Association [20]	43
Figure 13 GFR reproduced from Gen IV international forum 2002 [4]	45
Figure 14 LFR reproduced from Gen IV international forum 2002 [4]	46
Figure 15 MSR reproduced from Gen IV international forum 2002 [4]	47
Figure 16 SFR reproduced from Gen IV international forum 2002 [4]	48
Figure 17 SCWR reproduced from Gen IV international forum 2002 [4]	49
Figure 18 VHTR reproduced from Gen IV international forum 2002 [4]	50
Figure 19 Reproduced from D. M. Duffy[35] Cross Sectional Schematic Representation of a Fusion Power Plant Design. The Superconducting Magnets are the Outer Layer. The Vacuum Vessel, the First Wall and the Blanket are Inside the Vacuum Vessel and the Dark Region Round the Base of the Tokamak Represents the Divertor	54
Figure 20 Overview of Atomic Collision	57
Figure 21 Overview of Atomic Placement in Various 1D Defects	60
Figure 22 BCC Dumbbell Interstitial Lattice Position Where the Blue Circles are the Original Lattice Points and the Black Circles are the Interstitials	62

Figure 23 Lattice View of Edge Dislocation Migration Showing how Atomic Bonds are Broken and Reformed on the Slip Plane	64
Figure 24 Outline of Screw Dislocation reproduced from [53].....	65
Figure 25 The edge of a Stacking Fault with the Right of The Image Being in Stacking Fault Formation and the Left Being in Correct Formation for an FCC Material	66
Figure 26 Overview of a Twin Boundary Fault Showing how the Crystal Lattice is Mirrored Either Side oof the Boundary	68
Figure 27 Stress vs Strain as a Function of Irradiation for FCC and BCC Metals Reproduced from [32]	74
Figure 28 PAG Pinning Point Evolution Point 1 Shows Initial Locations Evolving Through to Point 3 Where the Dislocation is Overcome Before the Tension is Balanced at Point 4	80
Figure 29 Typical Point Defect Accumulation Under Irradiation as a Function of Time	81
Figure 30 Dislocation Glide of 2 Dislocation Sources Pinning[88]	84
Figure 31 Dynamic Recovery Creep Showing How 2 Dislocations Mutual Attraction Overcomes the Flow Stress[88]	84
Figure 32 Schematic Diagram of the Ion Beam Sputtering Process Reproduced From N. Yao[116]	87
Figure 33 Recoil Impurity Formation	90
Figure 34 Correlation between mixing rate and average cohesive energy reproduced from [134]	92
Figure 35 MIAMI 1 initial internal deflection device reproduced from J. Hinks et al [148]	96
Figure 36 MIAMI 1 Ion Beam Skimming Dosimetry Device Reproduced From J. Hinks [15] ..	97
Figure 37 Different SiC Polytypes Showing the Configuration of 2H, 4H, 6H, 15R, and 3C reproduced from T.Ayalew [165]	100
Figure 38 The Phase Diagram for SiC. reproduced from Olesinski, R. W. et al. [151]	101
Figure 39 Density Changes in CVD SiC due to Neutron Irradiation at Various Temperatures, Highlightiing how a Greater Density Change is Observed at Lower Temperatures,. Reproduced From Report by Snead at al. [155]	105
Figure 40 TRISO geometry reproduced from Nairi, B et al. [209]	107
Figure 41 ZrC Phase Diagram reproduced from E.K. Storms [226]	111
Figure 42 ZrC FCC Crystal Structure	111
Figure 43 Ultra Sonic Disc Cutter	123
Figure 44 Gatan Disc Grinder	124
Figure 45 Cross Sectional Side View of Dimple	124

Figure 46 Testbourne Dimpler	125
Figure 47 PIPS II.....	126
Figure 48 Thin Disc Preparation.....	126
Figure 49 TRIM GUI Overview.....	131
Figure 50 Cross-sectional view of SICMod Sphere with examples of an unmodified entry point and a modified entry point.....	132
Figure 51 Example of Amorphization Grey Value Graph.....	135
Figure 52 MIAMI 1 Prior to upgrade	136
Figure 53 a Frame Lower b Frame Upper c Frame Complete.....	139
Figure 54 Electrostatic Deflector Internal.....	141
Figure 55 Electrostatic Deflector Internal Actual	141
Figure 56 Electrostatic Deflector Housing	142
Figure 57 Einzel Diagram	143
Figure 58 Einzel Magnetic Field Diagram Field Diagram	143
Figure 59 Einzel Internal	145
Figure 60 Einzel Assembly and Bill of Materials	145
Figure 61 High Voltage Connector	146
Figure 62 Dosimetry Whole cross-section	150
Figure 63 Dosimetry Cross-section	150
Figure 64 Insertable Dosimetry Cross-section Highlighting the Key Components.....	151
Figure 65 Bellows and Ceramic Standoff Position	152
Figure 66 Cold Finger Modified with Slot to Allow Ions to Pass Through	154
Figure 67 MIAMI 1 SolidWorks Design Complete.....	155
Figure 68 SICMod Results 9keV He into ZrC Nanoparticle of Ø50nm Showing Collisions	159
Figure 69 SICMod Results 9keV He into ZrC Nanoparticle of Ø50nm Showing Implantations	160
Figure 70 Graph of SICMod Results 9keV He into ZrC Nanoparticle of Ø50nm Showing Implantations Distance to Surface.....	160
Figure 71 ZrC NP Prior to Irradiation BF and DF Red Ring Highlighting SAA Position. Dark Field Beam Highlighted in Figure 81.....	162
Figure 72 ZrC NP Diffraction Pattern Prior to Irradiation Red Ring Highlights DF in Figure 80	162

Figure 73 ZrC NP 400°C 1DPA under and over focus with example of bubbles highlighted .	163
Figure 74 Diffraction Patterns ZrC 400°C 0DPA, 1DPA, 2DPA, 3DPA Left to Right	164
Figure 75 Left Image Shows ZrC 800°C Prior to Irradiation, No Sputtered Material Can be Seen on the Thin Film. Right Image Shows ZrC 800°C 3DPA With Sputtered Material on the Thin Film.....	164
Figure 76 Diffraction Pattern of ZrC Nanoparticles at 0DPA 600°C Red ring highlights SAA	165
Figure 77 Diffraction Pattern of ZrC Nanoparticles at 1DPA 600°C Red ring highlights SAA	166
Figure 78 Diffraction Pattern of ZrC Nanoparticles at 2DPA 600°C Red ring highlights SAA	167
Figure 79 Diffraction Pattern of ZrC Nanoparticles at 3DPA 600°C Red ring highlights SAA	168
Figure 80 Changes in Nanoparticle Diffraction as a Function of DPA and Temperature	169
Figure 81 Microparticle prior to irradiation.....	170
Figure 82 Graph of Number of Collisions in 20 Angstrom Steps for 9keV Helium Ions into ZrC	171
Figure 83 Graph of Number of Zirconium and Carbon Vacancies, and Helium Knock-Ons in 20 Angstrom Steps for 9keV Helium Ions into ZrC	172
Figure 84 ZrC Microparticle 600°C 2DPA Showing Example of 50x50nm Selection Area Highlighted in the Yellow Box Expanded Image in Figure 85	173
Figure 85 50x50nm Area Used to Analyse Bubble Density with UnSharp Mask Filter Applied Underfocus with the White Circles Being the Observed Bubbles	174
Figure 86 Helium Bubble Density Changes Between 0.3 and 3 DPA 400°C ZrC Microparticles	174
Figure 87 Data on number of bubbles observed in 9keV He irradiated ZrC Microparticles. Different colours represent different particles. Room Temperature was conducted on both MIAMI 1 and 2, MIAMI 1 is noted as M1.....	175
Figure 88 He Bubble Density in 50x50nm Square Section of ZrC Microparticles as a Function of DPA and Temperature	176
Figure 89 Overview of Microparticle Evolution Under 9keV He Ion Irradiation	177
Figure 90 Image of ZrC at 400°C 3DPA Left part of image is Carbon Grid, Right is Microparticle.....	178
Figure 91 Crystallinity as a function of temperature at 3DPA.....	179
Figure 92 Scatterplot of ZrC Amorphisation Percentage to DPA Under 9keV He irradiation at 600°C	179
Figure 93 Smoothed line of ZrC Amorphisation Percentage to DPA Under 9keV He irradiation at 600°C.....	180

Figure 94 Scatterplot of ZrC Amorphisation Percentage to DPA Under 9keV He irradiation at 600°C Second Experiment Data	181
Figure 95 Scatterplot of ZrC Amorphisation Percentage to DPA Under 9keV He irradiation at 600°C Compiled Experiment Data	181
Figure 96 Smoothed line of ZrC Amorphisation Percentage to DPA Under 9keV He irradiation at 600°C Compiled Experiment Data	182
Figure 97 Schematic Showing Examples of The Theoretical Evolution of The Amorphous Fraction Depending on The Proposed Models For Amorphization And Where Complete Amorphization Occurs At The Same Fluence. Reproduced From O. Camara Et Al[288]	183
<i>Figure 98 ZrC MP Irradiated on MIAMI-1 Using 9keV He+ at 2.5 DPA, screened on MIAMI-2 Showing Under Over and at Focus BF Images.</i>	<i>184</i>
<i>Figure 99 50x50nm Area Used to Analyse Bubble Density with UnSharp Mask Filter Applied Sample Irradiated on MIAMI-1</i>	<i>184</i>
<i>Figure 100 Comparison of Bubble Density with Identical 9keV experiments on M1 and M2</i>	<i>185</i>
Figure 101 TRIM Setup GUI.....	266
Figure 102 TRIM Confirmation.....	267
Figure 103 SICMod GUI.....	267
Figure 104 Minimum Distance Surface Diagram for Implanted Ions	268
Figure 105 Examples of SICMod Heatmaps	268
Figure 106 Electrostatic Plate	269
Figure 107 Support Strip	270
Figure 108 End Piece Electrostatic Deflector.....	271
Figure 109 Electrostatic Deflector Housing	272
Figure 110 Einzel Enclosure	273
Figure 111 Einzel Ground Tube.....	274
Figure 112 High Voltage Tube.....	275
Figure 113 High Voltage Isolator.....	276
Figure 114 Deflector Plate	277
Figure 115 End Piece.....	278
Figure 116 Einzel assembly	279
Figure 117 High Voltage Tube.....	280
Figure 118 End Piece.....	281
Figure 119 High Voltage Tube V2.....	282

Figure 120 End Piece V2.....	283
Figure 121 CML key locations	284
Figure 122 CML with flanges.....	285
Figure 123 Skimmer Enclosure 1.....	286
Figure 124 Skimmer Enclosure 2.....	287
Figure 125 1st Suppression Cup.....	288
Figure 126 Suppression Cup 2.....	289
Figure 127 Skimmer Cup	290
Figure 128 Skimmer Cap	291
Figure 129 Skimmer Case.....	292
Figure 130 Skimmer Assembly without Cap	293
Figure 131 Skimmer assembly cross-section	294
Figure 132 Dosimetry Insert Case	295
Figure 133 Dosimetry Arm	296
Figure 134 Modified Cold Finger.....	297

List of Equations

<i>Equation 1 Rayleigh Criterion</i>	22
<i>Equation 2 Total Scattering</i>	24
<i>Equation 3 Cross Sectional Area</i>	24
<i>Equation 4 Elastic Scattering Radius</i>	24
<i>Equation 5 Total Cross Section for Scattering</i>	24
<i>Equation 6 Probability of Scattering for a Given Thickness</i>	25
<i>Equation 7 Mean Free Path</i>	25
<i>Equation 8 Probability of Scattering</i>	25
<i>Equation 9 Scattering Angle Relationship</i>	26
<i>Equation 10 Scattering Angle Relationship 2</i>	26
<i>Equation 11 Differential Scattering Cross Section</i>	26
<i>Equation 12 Cross Sectional Area for all Scattering Angles Greater Than θ</i>	26
<i>Equation 13 Electron-Electron Scattering</i>	27
<i>Equation 14 Electron-Nucleus Scattering</i>	27
<i>Equation 15 Differential Cross-Section for Backscatter</i>	28
<i>Equation 16 Electron-Nucleus Scattering EQ2</i>	28
<i>Equation 17 Probability of a Scattering Event at a Single Atom in a Specimen of Thickness t</i> 29	
<i>Equation 18 Electron Cloud Screening</i>	29
<i>Equation 19 von Laue diffraction 3D</i>	30
<i>Equation 20 Bragg Equation</i>	30
<i>Equation 21 Vacancy Concentration</i>	59
<i>Equation 22 Fick Law Formula</i>	61
<i>Equation 23 Sputtering Yield</i>	87
<i>Equation 24 Sputtering Yield EQ2</i>	88
<i>Equation 25 DPA for Thin Films</i>	133
<i>Equation 26 DPA for Nanoparticles</i>	133

1 Introduction

The UK is facing a shortage in electricity production in the 2020s [1]. This is partially due to the closure of all coal power plants by 2025 [2] and in part to the retirement of much of the nuclear fleet in the UK [3]. This will create a gap in power generation for the country which will require filling with new power plant capacity [3]. Advancements to nuclear reactor designs are continually being sought after. Two of the improvements which are of great importance are increasing the life span of current nuclear plants and being able to operate them at higher temperatures, thus creating an increase in power output [4]. One of the main obstacles to these developments is the damage caused to the materials in the plants due to neutron irradiation [5]. Another area of interest in radiation damage of materials where materials are constantly bombarded by radiation is space exploration and the colonization of other planets [6]. It is important that there is an understanding of how much radiation damage a material can withstand before the properties change to a point that the material is no longer fit to perform.

Several methods exist to gain an insight into how a material will react to irradiation. One method is to place a material within an experimental or test nuclear reactor and, once it has been sufficiently irradiated, examine the material for any defects. However, this process can take many years to accomplish and with the vast selection of candidate materials can lead to delays in gaining understanding. A much quicker method is to simulate neutron damage with ions. This allows a material to receive a radiation flux in a matter of minutes that would otherwise take years. If an ion beamline is placed *in-situ* with a Transmission Electron Microscope (TEM) then damage processes can be observed in real time. It is also possible to simulate damage using computational techniques.

The aim of the following work was to develop an understanding of materials properties and to allow future researchers to be able to gain an understanding of how material characteristics evolve under radiation. It is hoped that in doing so the work will contribute to advancements in material design and selection, allowing for improvements in nuclear reactor design amongst other things. To this end, gaps in material research capability in both physical and computational areas were discovered and addressed. The bulk of the

work contained herein was the upgrade of an *in-situ* ion beam TEM allowing for a greater confidence in experimental results and less down time of the system. Accompanying this computational code was developed to gain more accurate results in calculating how ions are transmitted and interact throughout a nanoscale material. A gap in the literature regarding ZrC response to ion irradiation was discovered and experiments conducted to address this.

2 Literature Review

2.1 Transmission Electron Microscopy Basic Principles

In the current work, when conducting experiments, materials were observed in real time using a TEM. Various techniques were used which will be outlined in this chapter. As part of the work undertaken involved the modification of a TEM it is important to gain an understanding of their functions, construction, and operation.

2.1.1 A Brief History of the Initial TEMs

In 1925 Louis de Broglie proposed what became the de Broglie hypothesis [7]. He theorised that electrons had wave-like characteristics with a wavelength much shorter than visible light. Davisson and Germer conducted an experiment in 1927 to confirm the de Broglie hypothesis [8]. In this experiment electron diffraction was observed in nickel. This was achieved by cutting a single crystal of nickel parallel to its {111} plane and firing a 370-volt electron beam at the crystals with normal incidence. In 1931 Max Knoll and Ernst Ruska at the Berlin Technosche Hochschule invented the electron microscope [9]. Figure 1 shows this microscope.



Figure 1. A Picture of The First Electron Microscope [10]

The first commercial TEM was produced in the UK in 1936, called the Metropolitan Vickers EM1 [11]. The purpose of this TEM was to demonstrate that optical microscopes and electron microscopes image production was comparable. The EM1 did not surpass the resolving power of light. After World War II TEMs became widely available from sources all over the world. The TEM was shown to be an instrument that material scientists could use in 1949 when Heidenreich successfully thinned metal foils to electron transparency. This work was built upon by a team in Cambridge, consisting of J. Dyson, T. Mulvey, J. Wakefield, and M. E. Haine, who developed the theory of electron diffraction contrast, which allows for the identification of line and planar defects in TEM imaging.

2.1.2 Advantages of TEM

The TEM offers high-resolution imaging far greater than that of the optical microscope. This is due to the shorter wavelength of the electron compared to photons. This is given by the Rayleigh Criterion δ which is the minimum separation between two light sources that may be resolved into distinct objects. By having a shorter wavelength the Rayleigh criterion can be increased as shown below:

$$\delta = \frac{0.61\lambda}{\mu \sin\beta}$$

Equation 1 Rayleigh Criterion

Where λ is the wavelength, μ is the refractive index, and β is the semi-angle of collection of the magnifying lens.

This higher resolution allows for microscopists to be able to view nanoscale defects in materials.

2.1.3 Electron Scattering

When a free electron passes by or through an atom it interacts with the electron cloud of the atom. This interaction results in electron scattering. Electron scattering is the fundamental underlying principle that allows for transmission electron microscopy. Just like with photons, unless an electron scatters or diffracts no image will be produced. In the TEM we are primarily concerned with electrons that do not deviate far from the incident electron beam. It is therefore important to understand how electrons scatter and diffract. Electron scattering can be grouped into different terms. These are: elastic; inelastic; coherent; and incoherent.

Coherent scattering is where the scattered particle/wave has a fixed phase relation to the initial particle/wave, such that the interference between the scattered particle/wave and the initial particle/wave can be observed. Incoherent scattering does not have this relation. In incoherent scattering the incident particle/wave encounters randomly moving scattering elements, such as a free electron, which causes the scattered particle/wave to exhibit random variations in its phase and amplitude.

Elastic scattering is a scattering event where the kinetic energy of a particle is conserved but its direction of propagation is modified. Elastic scattering usually occurs at relatively low angles ($1-10^\circ$). When elastic scattering occurs at angles higher than 10° it becomes increasingly incoherent. Due to the fact that the scattering strength generally decreases as the angle of scattering increases, TEMs are mainly used in the observations of forward scattered electrons.

Inelastic scattering is a scattering event where the kinetic energy of a particle is modified along with its direction of propagation. The kinetic energy can either be increased or decreased and is transferred to/from the electrons of the target. Inelastic scattering is almost always incoherent. It generally occurs at angles less than 1° .

The probability of an electron undergoing interaction with an atom is determined by the interaction cross section. This is fundamental to understanding scattering events. The cross section is defined in barns. One barn is equal to 10^{-24}cm^2 . The cross section is not a physical

area, however when divided by the area of an atom it represents the probability of a scattering event occurring within a physical area. Scattering can be viewed in two different ways. The first way to view scattering is at the level of an isolated atom. The total scattering occurring at an isolated atom can be described in terms of the cross section σ_T which can be seen as the sum of all elastic ($\sigma_{elastic}$) and inelastic ($\sigma_{inelastic}$) scattering cross sections [12]:

$$\sigma_T = \sigma_{elastic} + \sigma_{inelastic}$$

Equation 2 Total Scattering

The cross-sectional area can be defined as the effective area under the radius r of the scattering centre [12]:

$$\sigma = \pi r^2$$

Equation 3 Cross Sectional Area

The value of r differs for each scattering process. In the case of elastic scattering the radius is given by [12]:

$$r_{elastic} = \frac{Ze}{V\theta}$$

Equation 4 Elastic Scattering Radius

V is the potential across which the electron has been accelerated, and the electron charge is given as e . Z is the atomic number and θ is the scattering angle. This equation shows many general behaviours of electron scattering. The higher the V the less the scatter. The greater the angle the less scatter. The heavier the atom the more scatter.

The second way to view scattering is to consider a specimen that contains N atoms/unit volume. This allows for the total cross section for scattering Q_T to be observed as [12]:

$$Q_T = N\sigma_T = \frac{N_0\sigma_T\rho}{A}$$

Equation 5 Total Cross Section for Scattering

N_0 is the Avogadro number, A is the atomic weight of the atoms in the specimen, and ρ is the density. Therefore, Q shows the number of scattering events per unit area. For a given thickness t the probability of scattering is given by [12]:

$$Q_T t = \frac{N_0 \sigma_T (\rho t)}{A}$$

Equation 6 Probability of Scattering for a Given Thickness

Rather than using an area to describe the probability of an electron interaction we can use a length. This is known as the mean free path λ . The mean free path is the average distance an electron travels between scattering events. This factor becomes important when determining the required thickness of our sample to avoid multiple scattering events, allowing for easier interpretations of acquired images. The mean-free path is the inverse of the total cross-section for scattering [12]:

$$\lambda = \frac{1}{Q} = \frac{A}{N_0 \sigma_T \rho}$$

Equation 7 Mean Free Path

Typically, λ values for scattering at TEM working voltages are in the order of tens of nm. This indicates that sample thickness should be in this magnitude. We can also use the mean free path equation to work out the probability of scattering p as [12]:

$$p = \frac{t}{\lambda} = \frac{N_0 \sigma_T (\rho t)}{A}$$

Equation 8 Probability of Scattering

Which is the same as seen earlier in equation 6.

Due to the importance of the scattering angle on the radius of elastic scatter, it becomes necessary to calculate the differential cross section to gain a deeper understanding of electron trajectory. Electrons are scattered through a semi-angle θ into a solid angle Ω . There is a simple geometrical relationship between the two [12]:

$$\Omega = 2\pi(1 - \cos \theta)$$

Equation 9 Scattering Angle Relationship

Therefore [12]:

$$d\Omega = 2\pi \sin\theta d\theta$$

Equation 10 Scattering Angle Relationship 2

The differential scattering cross section can be calculated by [12]:

$$\frac{d\sigma}{d\Omega} = \frac{1}{2\pi \sin\theta} \frac{d\sigma}{d\theta}$$

Equation 11 Differential Scattering Cross Section

By integrating the equation, σ can be calculated for all scattering angles greater than θ [12]:

$$\sigma_{\theta} = \int_{\theta}^{\pi} d\sigma = 2\pi \int_{\theta}^{\pi} \frac{d\sigma}{d\Omega} \sin\theta d\theta$$

Equation 12 Cross Sectional Area for all Scattering Angles Greater Than θ

The integral shows that as the scattering cross section σ increases so does angle of scattering θ . The integration is limited by the fact that θ values vary from 0 to π dependant on the type of scattering.

Combining all of the scattering equations we can predict the likely range of an electron trajectory in a thin foil.

Scattering can result in different angular distributions. This is due to the fact that electrons can be scattered more than once. If an electron is scattered at an angle of less than 90° then it is classified as forward scattering. If the angle is greater than 90° then it is known as backscattering. As a material becomes thicker the number of scattering events increases and the angle of scattering generally increases. This leads to more backscattering. The

angle of scattering is also affected by the electron coulombic interaction with an atom. As shown in Figure 2 an electron may interact with the electron cloud and be attracted by the positive potential of a nucleus. This will deflect the electron towards the core. If the incoming electron penetrates the electron cloud and approaches the nucleus it will undergo a strong repulsion force from the electron cloud upon exit and may be scattered through a large angle that can in rare cases approach 180° , known as complete backscattering. The electron-electron and electron-nucleus scattering cross sections can be easily expressed by[12]:

$$\sigma_{electron} = \pi r_e^2 = \pi \left(\frac{e}{V\theta} \right)^2$$

Equation 13 Electron-Electron Scattering

$$\sigma_{nucleus} = \pi r_n^2 = \pi \left(\frac{Ze}{V\theta} \right)^2$$

Equation 14 Electron-Nucleus Scattering

Where θ is the scattering angle, e is the electron charge, Z is the atomic number, V is the electron velocity, and r is the cross-sectional radius.

This shows that the atomic number Z affects the elastic interaction with the nucleus whereas the electron-electron scattering is only a function of the incident electron energy eV .

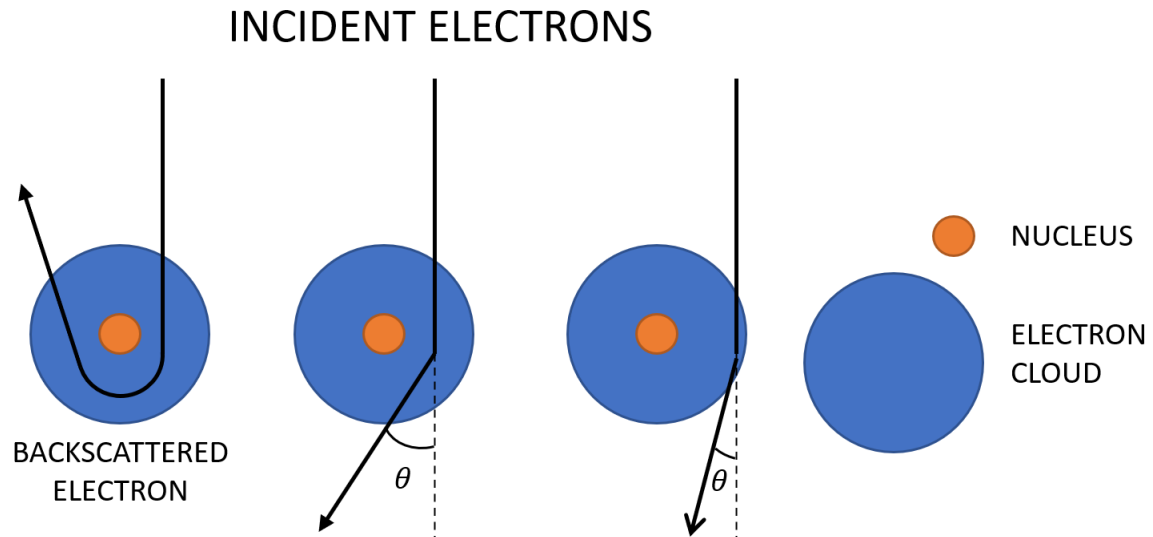


Figure 2 Electron Elastic Scatter with Backscatter, Large Angle Scatter, and Low Angle Scatter Respectively

Rutherford derived an equation for the differential cross section for backscattered electrons [13]:

$$\frac{d\sigma(\theta)}{d\Omega} = \frac{e^4 Z^2}{16(E_o)^2 \sin^4 \frac{\theta}{2}}$$

Equation 15 Differential Cross-Section for Backscatter

The expression assumes that the electron is scattered elastically, keeping its energy equal to the initial energy. As such E_o , the initial energy, is of fixed value. By substituting values for the various constants and integrating the differential cross section from 0 to π the elastic nuclear cross section can be found in a more accurate form than previously discussed [12]:

$$\sigma_{nucleus} = 1.62 \times 10^{-24} \left(\frac{Z}{E_o}\right)^2 \cot^2 \frac{\theta}{2}$$

Equation 16 Electron-Nucleus Scattering EQ2

As before the main factors affecting the probability of a scattering event occurring are the beam energy, angle of scatter, and the atomic number. The expression can be modified to

show the probability of a scattering event occurring on a single atom in a specimen of thickness t [12]:

$$Q_{nucleus}t = \left(N_0 \frac{\rho}{A} t\right) \sigma$$

$$= 1.62 \times 10^{-24} \left(N_0 \frac{\rho}{A} t\right) \left(\frac{Z}{E_0}\right)^2 \cot^2\left(\frac{\theta}{2}\right)$$

Equation 17 Probability of a Scattering Event at a Single Atom in a Specimen of Thickness t

The mass thickness dependency remains. However, the strong dependence on atomic number is clearly demonstrated.

The Rutherford differential cross section shown thus far ignores the electrostatic screening effect of the electron cloud. This cloud reduces the differential cross section, resulting in less scattering. In order to account for the electron cloud screening, it is necessary to modify the $\sin^2(\theta/2)$ expression with $[\sin^2(\theta/2) + (\theta_0/2)]$ where θ_0 represents the screening parameter [12]:

$$\theta_0 = \frac{0.117Z^{0.33}}{E_0^{0.5}}$$

Equation 18 Electron Cloud Screening

This shows that when the scattering angle is greater than θ_0 the electron-electron interactions become less relevant, and the nucleus interactions become dominant.

2.1.4 Electron Diffraction

In 1913 von Laue theorised that diffraction could be used as a method of probing atomic structure and in 1914 he received the Nobel prize in Physics for deriving three equations which once simultaneously satisfied would result in diffraction [12]. The three equations are:

$$a(\cos\theta_1 - \cos\theta_2) = h\lambda$$

$$b(\cos\theta_3 - \cos\theta_4) = k\lambda$$

$$c(\cos\theta_5 - \cos\theta_6) = l\lambda$$

Equation 19 von Laue diffraction 3D

Where abc are the distances between the scattering centres, θ is the angle of scatter of the incident beam with wavelength λ , and hkl are the indices of the diffracted beam equivalent to the miller indices (hkl) of the diffracting crystal plane.

Another way to describe diffraction is with Bragg's law. In 1913 Sir William Henry Bragg and Sir William Laurence Bragg argued that waves which are diverted from scattering centres must have equal path differences to an integral number of wavelengths [12]. Bragg's Law is given by:

$$n\lambda = 2d \sin \theta$$

Equation 20 Bragg Equation

Where n is the integer, λ is the wavelength, θ is the angle of incidence, and d is the distance between atomic layers.

2.2 TEM Construction

To appreciate how a TEM works it is important to have a basic understanding of its construction. Typically, a TEM consists of a filament which is part of the electron “gun”, several lenses and apertures, a specimen holder, a viewing screen and/or camera, several deflector coils, and a vacuum system. Figure 3 is a ray diagram which shows the basic overview of a TEM.

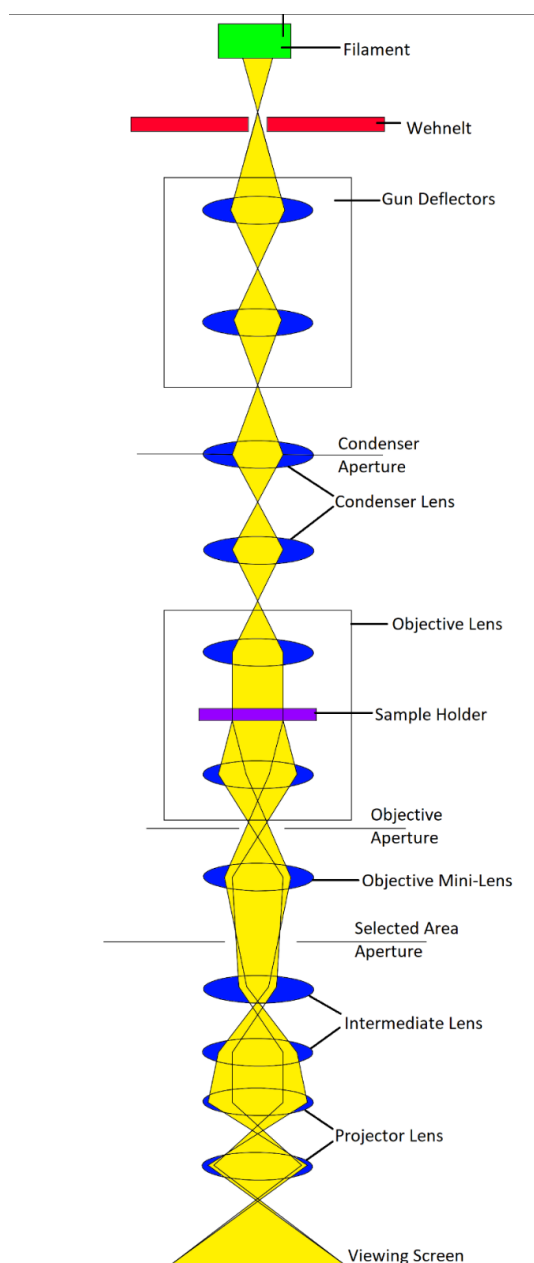


Figure 3 Overview of TEM Optics Ray Diagram

2.2.1 Gun system

The electron gun consists of a source (which produces the electrons), wehnelt cap (which focuses the produced electrons), and an anode (which provides initial acceleration). There are two main types of electron guns. These are field emission guns (FEG) and thermionic emission guns (TEG). The main difference between the two systems is that FEGs use a high potential gradient to create field electron emission and TEGs use high temperatures to overcome the work function of the material. As the TEMs used in this thesis used thermionic emission systems those are what shall be detailed here.

The source is usually LaB_6 (Lanthanum hexaboride) or W (Tungsten). In order to produce electrons, the source is heated to a temperature great enough to overcome the work function. The work function is the minimum amount of energy required to free an electron from a solid. This heating is done via Joule heating. As the gun may not always be perfectly mechanically on axis the gun system also consists of a set of deflectors which can be adjusted to bring the beam on axis. The beam can be verified to be on axis by undersaturation of the gun emission and observing the produced beam. When aligned correctly the image will appear to resemble the cross section of a kiwi. Figure 4 reproduced from the JEOL TEM 2000FX manual[14] shows an aligned and misaligned gun.



Figure 4 TEM Gun Alignment Using Undersaturated Filament to Produce Cross-section of Kiwi [14]

2.2.2 Lenses

A TEM consists of various electron lenses. These lenses can be split into different groups which all have their own purpose. The groups are; condenser, objective, intermediate, and projector.

The condenser lens defines the illumination of the sample. It consists of two lenses. The lens closest to the gun forms an image of the gun crossover whilst the second lens focuses the image.

The objective lens is what defines the position of the eucentric plane, the plane where the electron crossovers at the objective lens will align with the crossovers at the first image plane. This plane is what defines the focus of the sample. The centre of the objective lens is also what defines the TEMs optical axis.

The intermediate lenses are used to magnify the image by the desired amount. When in diffraction mode these lenses also are used to create the crossover points which are used to form the diffraction image produced by the objective lens.

The projector lens acts to spread the beam to fill the phosphor screen or camera CCD. Phosphor is used as electrons hitting it results in the emittance of photons which allows the human eye to view an image.

2.2.3 Apertures

Throughout the TEM there are three adjustable apertures which are used to exclude certain electrons for various reasons. Working from the gun down to the screen the apertures are condenser, objective, and selected area, respectively.

The condenser aperture in the TEM has the same purpose as that of an optical microscope. It is used to exclude electrons outside the area being examined. This reduces spherical aberration. Caution needs to be employed when changing or moving the condenser aperture as significant x-ray flux may result due to the large number of electrons hitting it. The user is usually protected from these rays by lead shielding built into the TEM, but some machines will allow the operator to remove the aperture leading to x rays being generated from the large number of electrons traveling down the TEM column.

The objective aperture is used as a means to prevent electrons of different scattering angles than that which is desired for generating an image. This acts to sharpen contrast, although simultaneously reduce brightness, in bright field imaging (see Figure 5 Objective Aperture Situated in Bright Field Mode Ray Diagram). Adjusting the aperture to only collect more heavily scattered electrons will result in darkfield images being formed (see Figure 6). The aperture is situated at the first crossover plane after the objective lens, hence its name.

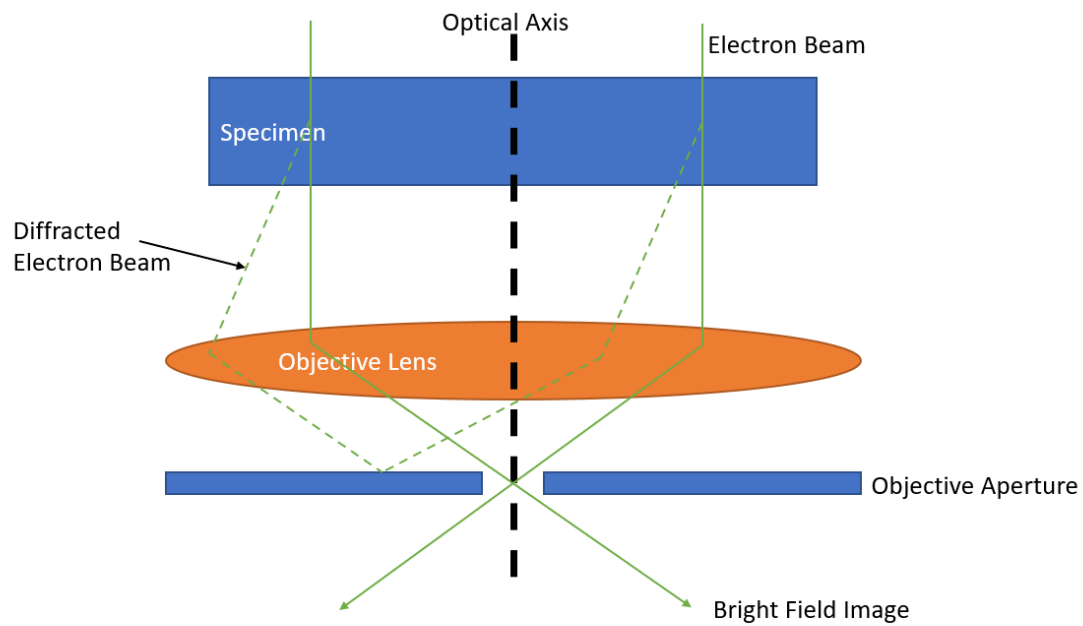


Figure 5 Objective Aperture Situated in Bright Field Mode Ray Diagram

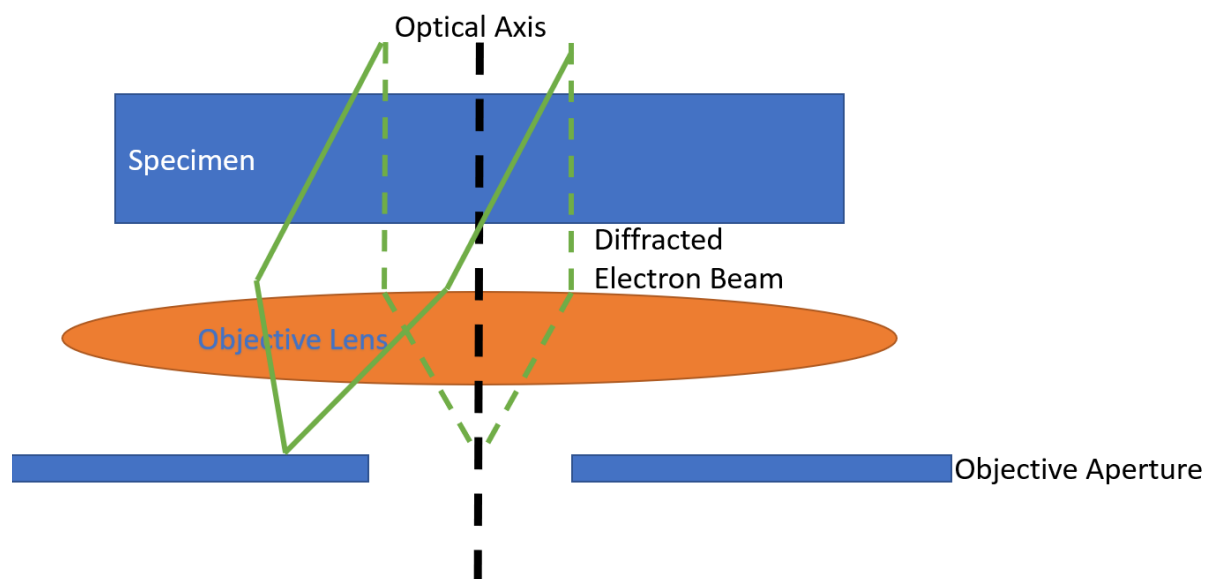


Figure 6 Dark Field Mode Ray Diagram

The selected area aperture is used when generating diffraction patterns. It is situated in the image plane before the intermediate lens. Its primary purpose is to ensure that the

diffraction pattern being generated is only coming from the desired area of the specimen, see Figure 7.

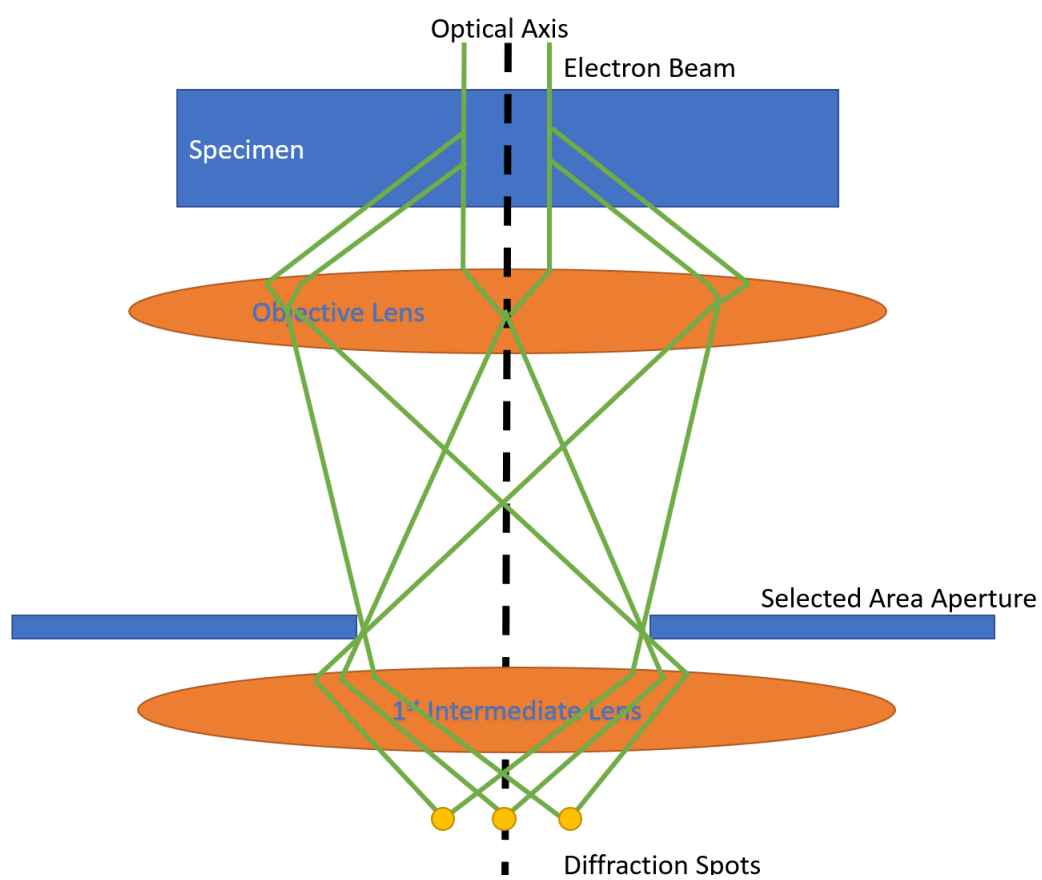


Figure 7 Selected Area Aperture Ray Diagram

2.2.4 Deflectors

The TEM has three main deflections systems. These are the image, beam, and the aforementioned gun deflectors. The purpose of these systems is to ensure that the electron beam has the tilt and deflection required for the desired imaging. This is achieved by either shifting and/or tilting the beam. The deflectors operate in pairs to allow for shifting without tilting which can be useful in aligning the beam, Figure 8 shows this principle.

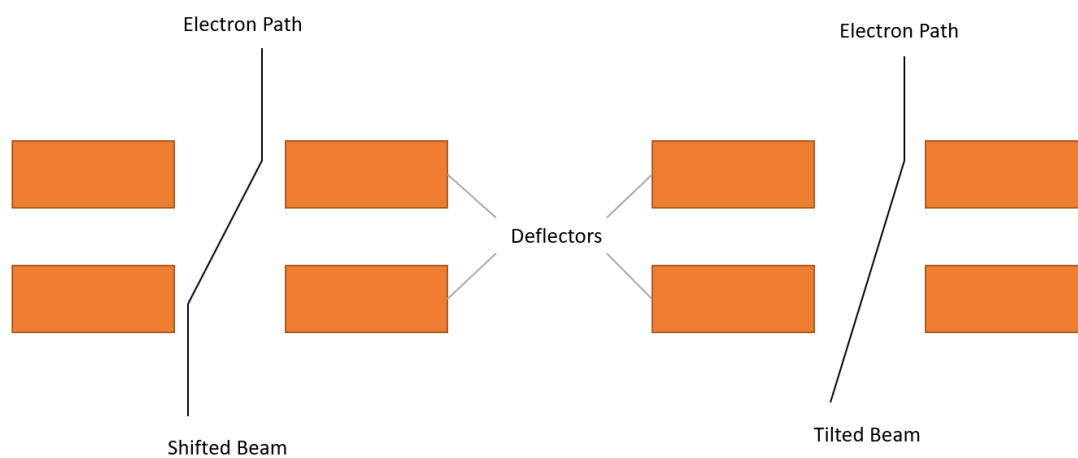


Figure 8 TEM Deflection System Showing Shifted and Tilted Beam

2.2.5 Stigmators

A TEM lens consists of a cylinder of copper windings placed in an Fe shroud with a central spherical aperture to focus the beam. It is impossible to machine a perfectly round cylindrical bore and all materials have a certain amount of surface roughness that cannot be completely eliminated. On top of this small amounts of contamination will be present within a TEM column. These facts lead to variations in the magnetic field strength of the TEM lenses which affect the electron beam. This phenomenon is known as astigmatism. To overcome astigmatism TEMs contain several octupoles throughout the column which introduce a balancing magnetic field. These octupoles are known as stigmators.

2.2.6 Goniometer and Sample Holders

In order to view a specimen in a TEM it is necessary to introduce it into the vacuum system and place it at the correct height in the centre of the objective lens system. This is achieved with the use of sample holders and a goniometer. A sample holder in its most simple form consists of a way of fixing a specimen in place and providing a vacuum seal, as seen in Figure 9. The goniometer allows the user to move the holder within the microscope in the x, y, and z directions as well as tilt the sample in one dimension. There also exist more complex sample holders which allow for double tilting, in-situ heating/cooling, and rotation of the sample once it is in the TEM.

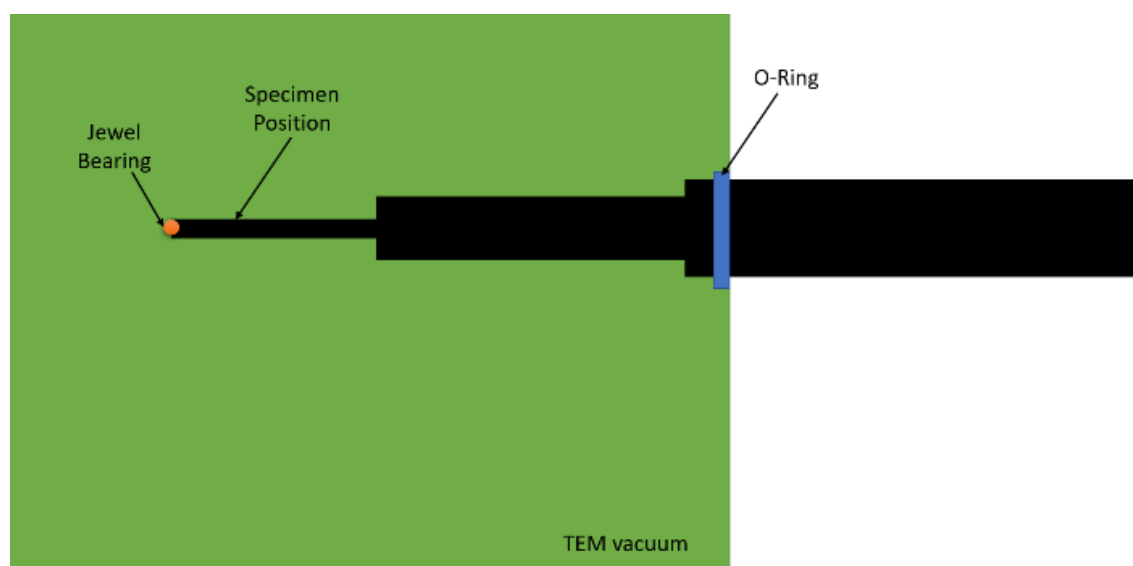


Figure 9 Cross-sectional View of Basic Sample Holder Inserted into TEM with Vacuum Highlighted

2.2.7 TEM Image Capturing

When the electron beam has reached the viewing screen it becomes possible to store an image. This is achieved by removing the phosphor viewing screen from the electron path and having a CCD sensor beneath the screen. When the electrons interact with the sensor a digital image is produced. Depending upon the distance of the CCD from the phosphor screen additional magnification of the image is created. It is therefore important to calibrate a CCD to ensure that the extra magnification is accounted for. Over time CCDs become damaged by the electrons interacting with them. In the case of diffraction mode, the center

spot can also cause damage to the CCD if not correctly blocked. For these reasons using a CCD all the time, as a replacement for the phosphor screen, is not recommended.

2.2.8 Additional Features

There are many devices that can be attached to a TEM that assist the user in obtaining valuable experimental results. One of the most common attachments to a TEM is a Charge-Coupled Device (CCD) camera. Depending upon the particular specifications of the camera they allow the user to record live video during experiments and acquire detailed images of the specimen. In 1986 the first in-situ TEM system with an Electron Energy Loss Spectroscopy (EELS) system attachment was built in Japan [15][16]. The use of an EELS system allows the user valuable insights into a specimens atomic composition, chemical bonding, and surface properties [17]. An Energy-Dispersive X-ray Spectroscopy (EDS) system can also be added to a TEM. EDS allows the chemical composition of a specimen to be measured [18]. Other devices employed in materials research with in-situ irradiation, not necessarily directly attached to the TEM, include the Scanning TEM (STEM) and the Scanning Electron Microscope (SEM). These systems allow the user to see a larger area of a sample than a conventional TEM with some loss to resolution.

2.3 Nuclear Reactors

2.3.1 Introduction

This chapter will discuss nuclear reactors focusing on the materials used in their construction historically, currently, and prospective future materials. The qualities of the materials will be outlined along with the problems facing the materials in a radiation environment.

2.3.2 Introduction to Nuclear Power

At 15:25 on December 2nd 1942, the first self-sustained man-made nuclear reaction was performed by a team of scientists at the University of Chicago. Although the following years were initially focused on the development of nuclear weapons for use in World War 2, this initial reaction would lay the foundation for nuclear reactor systems. The push for safer, cheaper, and more efficient power has placed a challenge for engineers to improve power system design. This has been a constant demand placed upon engineers in all forms of power production. It was this pursuit of advancement that led to the initial Generation I early prototype nuclear reactors in the 1950s and 1960s. Throughout the following decades nuclear reactors improved first with the implementation of Generation II reactors during the 1970s, and then Generation III reactors in the 1990s [4].

2.3.3 Reactor Basics

Electricity generation from a nuclear reactor is similar to that from fossil fuel plants in which water is heated to steam which spins a turbine and generates an electrical current. The obvious difference is the source of the heat, whereas a fossil fuel plant burns a material a nuclear reactor relies upon the principal of nuclear fission or fusion. Fission occurs when a neutron collides with sufficient energy and is absorbed by an atom which causes it to split into two smaller atoms and in turn releases additional neutrons which continue the chain reaction. Usually, a fission reactor uses either U or Pu as the atoms to be split. U^{235} are more commonly used. The chance of fission occurring is also dependent on the energy of the neutron and the neutron absorption cross section of the target. In U^{235} a slow neutron or thermal neutron, of approximately 1 MeV, has approximately 1000x more chance of

initiating fission than a fast neutron, of approximately 10 MeV, one. The neutrons produced from fission are of a spectrum of high energy and low energy. As such reactors employ moderator materials to slow the high energy neutrons down and increase their chance of interaction. These are usually C in the form of graphite, used in gas cooled reactors and light water reactors, or H_1/H_2 in the form of water or heavy water, used in pressurized water reactors, boiling water reactors, and pressurized heavy water reactors. These materials slow the neutrons as they undergo collisions with them absorbing some of the neutron energy without absorbing the neutron itself. Reactors are controlled by either sustaining, increasing, or decreasing the number of neutrons allowed to collide with the fissile material. This is achieved via the use of control rods. Control rods consist of a material which readily absorbs neutrons, usually a material such as B^{10} or Cd^{113} although others are also viable. By configuring the rods, the number of neutrons free to induce fission can be controlled.

2.3.4 Current Reactors

Initially, reactors were used as either testing facilities, to gain an insight into radiation damage and power generation, or as a means of producing fissile materials for the use in nuclear weapons. Some initial reactors were not used for energy production, such as the UK Windscale reactor. Nuclear reactors are now used throughout the world as both research tools and power generators. Nuclear reactors often have high upfront costs and yet the profits over the lifespan of the reactor are generally greater than that of other power production methods. In recent times nuclear reactors have been gaining support for use as power generating facilities largely due to their lower greenhouse gas impact when compared to traditional coal plants [19][2]. Whilst other green power generation techniques exist, they often need a suitable location, such as hydroelectric or geothermal plants, or the power generated is intermittent, such as wind and solar. For these reasons nuclear is seen as a good alternative to provide a base load of power to a national grid. As of 2015 there were 6 different types of nuclear reactors in commercial use across the globe. Figure 10 shows the main variations used by each country. This does not include outliers such as the UKs Sizewell B, which is the UKs only Pressurised Water Reactor (PWR).

Reactor type	Main countries	Number	GWe	Fuel	Coolant	Moderator
Pressurised water reactor (PWR)	US, France, Japan, Russia, China	282	264	enriched UO ₂	water	water
Boiling water reactor (BWR)	US, Japan, Sweden	78	75	enriched UO ₂	water	water
Pressurised heavy water reactor (PHWR)	Canada, India	49	25	natural UO ₂	heavy water	heavy water
Gas-cooled reactor (AGR & Magnox)	UK	14	8	natural U (metal), enriched UO ₂	CO ₂	graphite
Light water graphite reactor (RBMK & EGP)	Russia	11 + 4	10.2	enriched UO ₂	water	graphite
Fast neutron reactor (FBR)	Russia	3	1.4	PuO ₂ and UO ₂	liquid sodium	none
TOTAL		441	384			

Figure 10 Main Reactor Types as of 2015 reproduced from World Nuclear Association [20]

Currently the most common commercial nuclear power plant is the PWR [20]. Figure 11 is a schematic diagram of this type of reactor. PWRs use light water as both the coolant and moderator. The water is pressurised to increase the boiling point and allow operations at high temperatures. This pressure is maintained by the pressuriser. The PWR is considered a Gen II reactor [21] although Gen III variants do exist. In the UK however, the most common type of reactor is the Advanced Gas-cooled Reactor (AGR) which span Gen II and Gen III reactors. AGRs use graphite as a moderator and carbon dioxide as the coolant which transports the heat to a steam generator on a secondary loop. Figure 12 shows this type of reactor.

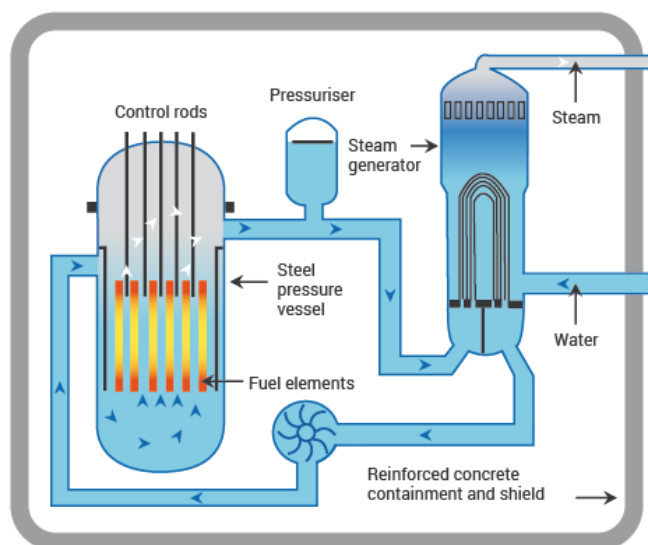
A Pressurized Water Reactor (PWR)

Figure 11 Schematic diagram of a pressurised-water reactor reproduced from World Nuclear Association [20]

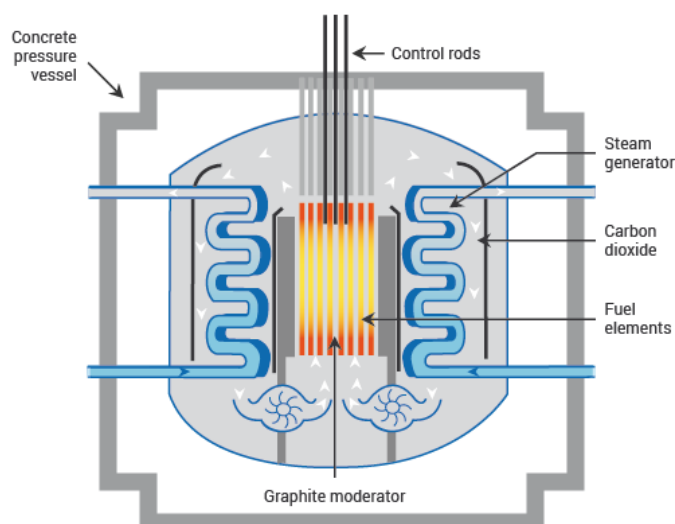
An Advanced Gas-cooled Reactor (AGR)

Figure 12 Schematic diagram of an advanced gas-cooled reactor reproduced from World Nuclear Association [20]

2.3.5 Future Reactors

In the short-term future countries are attempting to develop Gen III+ and Small Modular Reactors (SMR). In order to increase production past the current Gen III capacity, ten countries – Argentina, Brazil, Canada, France, Japan, the Republic of Korea, the Republic of South Africa, Switzerland, the United Kingdom, and the United States – have agreed to work together to develop Generation IV reactors [22]. The initial intended goal was to have new

nuclear power plants built from 2030 to be fourth generation systems, however this has since been pushed back.

In 2014 the Gen IV International Forum (GIF) highlighted 6 system designs as being the most promising for use as Gen IV reactors [21]. These systems were:

Gas-cooled fast reactor (GFR)

Lead-cooled fast reactor (LFR)

Molten salt reactor (MSR)

Sodium-cooled fast reactor (SFR)

Supercritical-water-cooled reactor (SCWR)

Very-high-temperature reactor (VHT)

All the above systems require various research and development in order to make them viable as a commercial power production facility. Part of this is the selection and development of materials able to withstand the neutron radiation and high temperatures that are produced by these reactors.

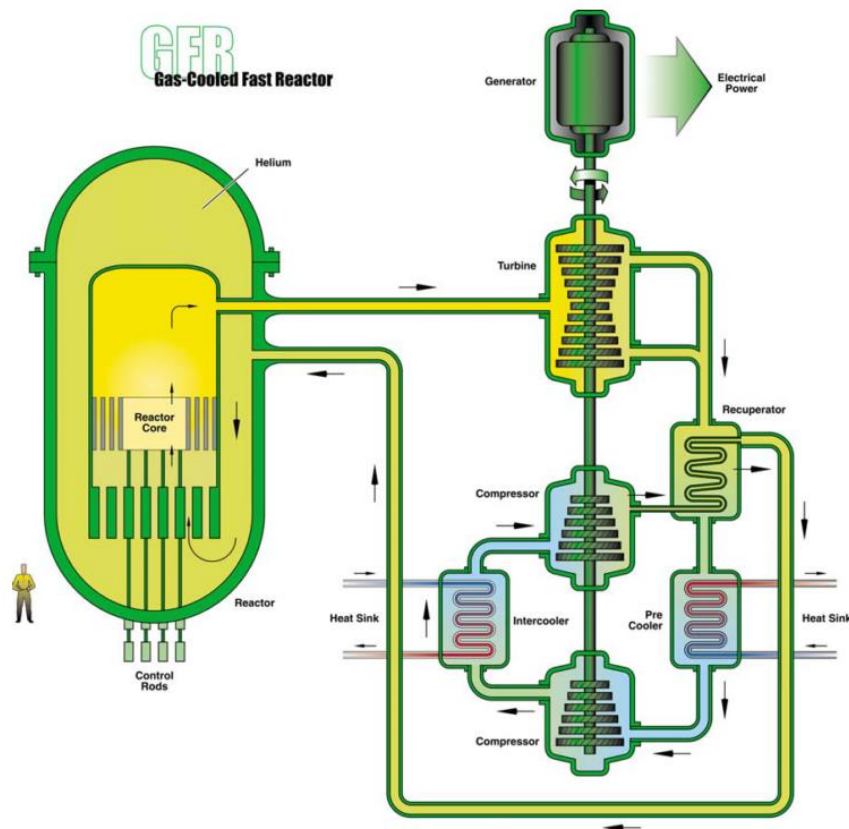


Figure 13 GFR reproduced from Gen IV international forum 2002 [4]

GFR systems are high-temperature helium-cooled fast-spectrum reactors with closed fuel cycles. Closed fuel cycle is a term used to describe the reprocessing of spent fuel to become reusable in a reactor environment as opposed to open fuel cycle where the fuel is not reprocessed. The GFR system is designed to combine both the advantages of fast-spectrum systems, where the fission chain reaction is sustained by fast neutrons which creates long term sustainability and minimal waste, and high-temperature systems, allowing for efficient industrial use of generated heat. GFR systems do not require moderation because the neutron absorption cross section of fast neutron for the type of fuel used is high. Carbon and nitride fuels, where the uranium is bonded to either carbon or nitrogen respectively, are the most promising for GFR systems, both of which are proposed to use SiC as a cladding material[23]. Several obstacles need to be overcome in the development of GFR systems. An acceptable fuel system still needs to be developed. Part of this is the development of a cladding material that conforms to both the mechanical properties required and is compatible with helium coolant and the irradiation conditions. The main systems also

require experimental data to ensure that they perform in line with the theory. Work is also required on decay heat removal technologies [21].

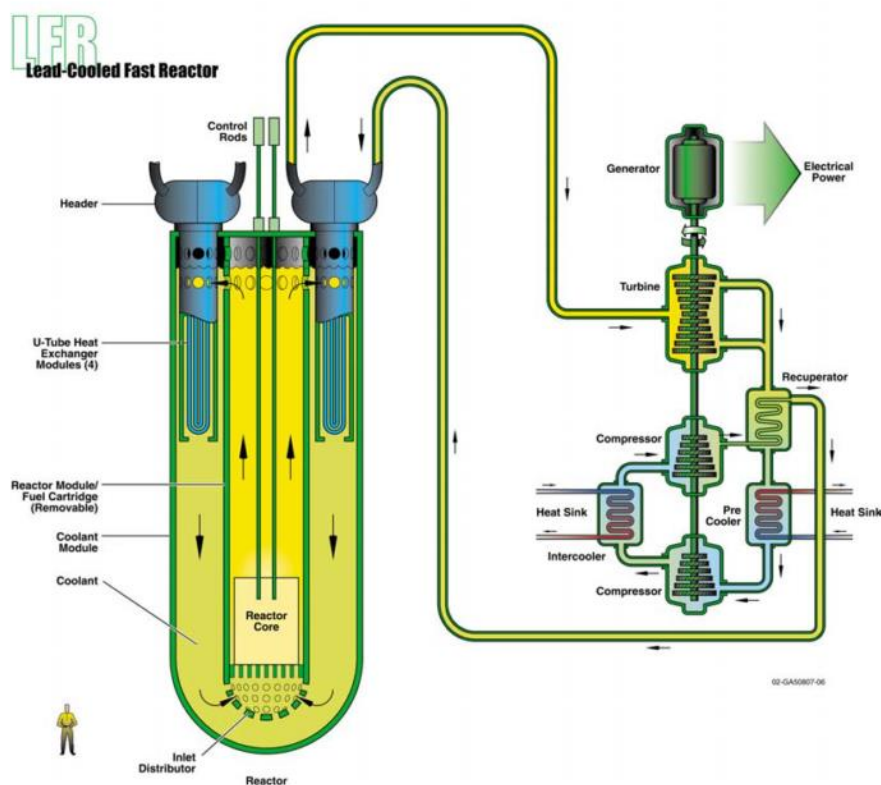


Figure 14 LFR reproduced from Gen IV international forum 2002 [4]

LFR systems, as the name suggests, are fast spectrum reactors cooled by lead or lead-bismuth eutectic (LBE). The use of lead as a coolant has several advantages as outlined in *Generation IV nuclear reactors, Current status and future prospects* [22]. LFRs have excellent neutron and thermo-fluid-dynamic properties. This facilitates the establishment of a natural convection which simplifies heat transfer, increasing intrinsic safety. LFRs do not react with air or water. The Lead used as coolant has a high boiling point that does not limit the maximum temperature of the thermodynamic cycle.

There remain several issues to overcome with LFRs. There is a need for coolant chemical control to prevent the oxidation and subsequent erosion of structural steels in the coolant system. The heavy weight of the coolant also creates structural issues. Also, the opacity of lead makes inspection of the in-core components difficult. The high melting point of 327°C

of pure lead requires that the coolant be kept at high temperatures to avoid solidification which could create bursts in the systems pipes [21]. This can be overcome with the use of LBE, however this produces polonium that needs to be extracted through complex treatments [24].

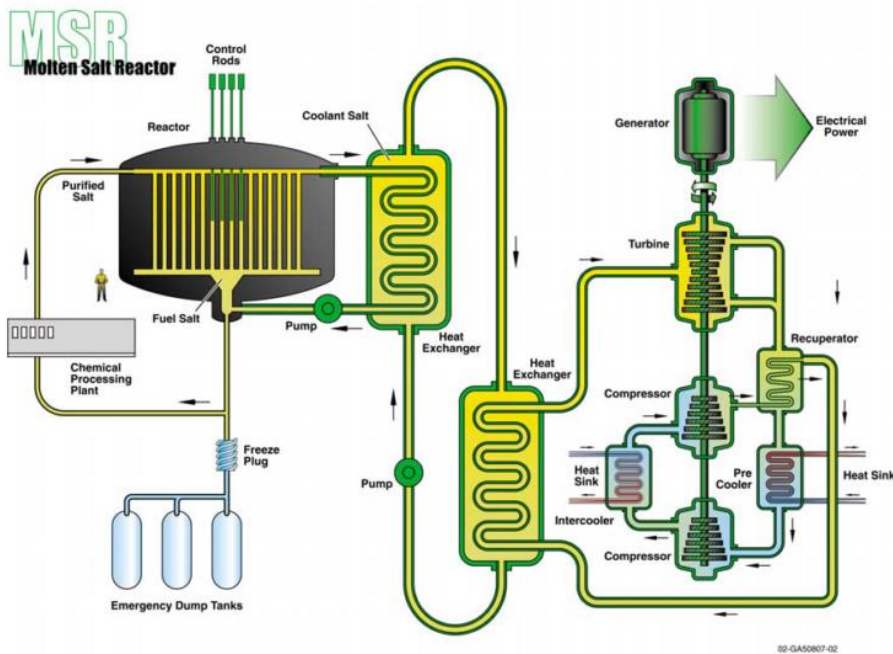


Figure 15 MSR reproduced from Gen IV international forum 2002 [4]

MSRs were originally proposed by Ed Bettis and Ray Briant during a post-World War 2 attempt to design a nuclear-powered aircraft in the USA. Interest in the aircraft dwindled in the 1950s and MSR development was transferred to civilian reactors. Throughout the following decades MSRs were developed and proven to work [25]. However, in 1976 the MSR project in the USA was shutdown. Due to budget restraints the USA chose to pursue liquid-metal-cooled fast breeder reactors (LMFBR) in place of MSRs. Interest has remained in MSRs despite this and they remain a candidate for Gen IV reactors [4]. This is largely due to the assumed safety of the reactors when compared to LWRs [26]. MSRs use molten liquid salts as their coolant system. The nuclear fuel is liquid and dispersed in the coolant. As a result, MSRs do not require fuel fabrication. The fuel has a homogenous composition which allows fissile materials to be added without hot spots forming creating great flexibility in the fuel cycle. They have a high working temperature. Safety is increased due to the reactivity

condition and the option to remove the fuel from the core in accidental situations [22]. This is achieved via the use of a freeze plug which requires constant power to freeze a section of the molten salts. In the case of an emergency the freeze plug ceases operation leading to the salts melting and draining into emergency dump tanks.

As with all the Gen IV reactors there remains obstacle to be overcome in MSRs. The physical-chemical behaviour of fuel salts needs to be examined in greater detail, along with the development of simulation tools to study both normal operating and accident conditions. The compatibility of salts with structural materials needs to be examined. In-situ measurements need to be developed to control the redox potential and limit the corrosion of the salts, as well as measure the composition of the fissile and fertile, a material that can be converted into fissile by neutron absorption, elements of the salts. On site fuel processing also need to be developed [21].

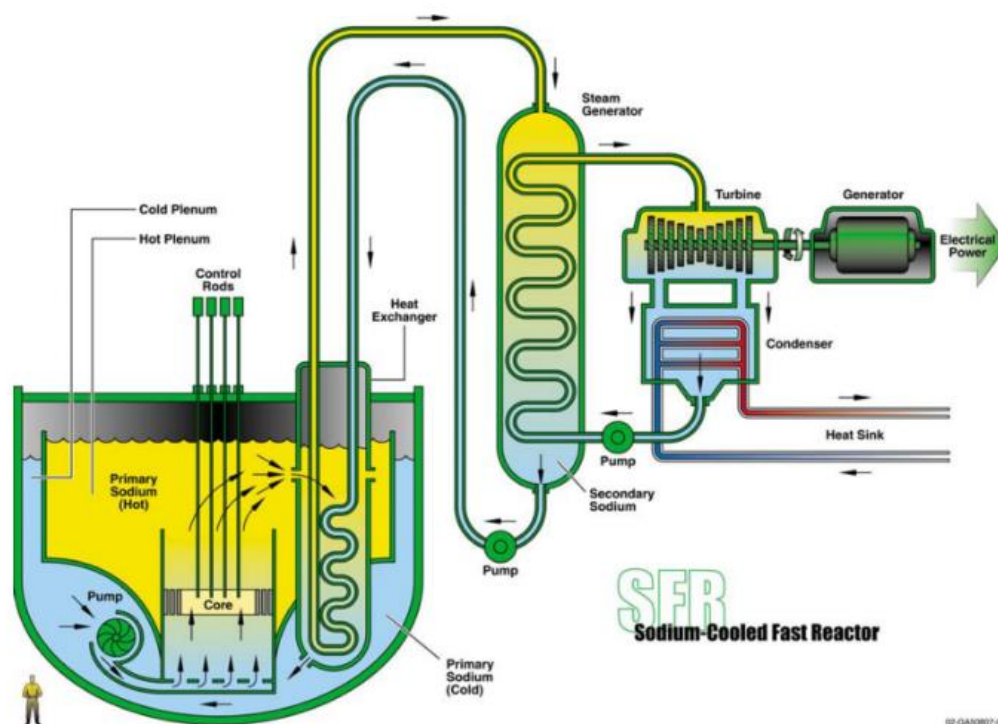


Figure 16 SFR reproduced from Gen IV international forum 2002 [4]

SFRs are fast reactors cooled by liquid sodium. They are the most extensively researched type of fast reactor. One of their advantages are their ability to efficiently convert fertile material into fissile. This increases the efficiency of the fuel by approximately 50 times. SFRs require a closed fuel cycle to reduce the required amount of radioactive fuel. Two options for this are currently under investigation, advanced aqueous process and pyro-metallurgical process. Sodium has a melting point of 98°C which is lower than that of lead used in LFRs. This means that SFRs do not have the problem of LFRs where solidification can damage the system. Sodium is also less corrosive than lead. Sodium boils at 883°C which constrains the maximum operating temperature. Since sodium reacts with air and water SFRs require an airtight system [22].

SFR research and development objectives can be separated into different categories. These are; Safety and operation project, Advanced fuel and Global Actinide Cycle International Demonstration projects, Component design and balance-of-plant project, and System integration and assessment project [21].

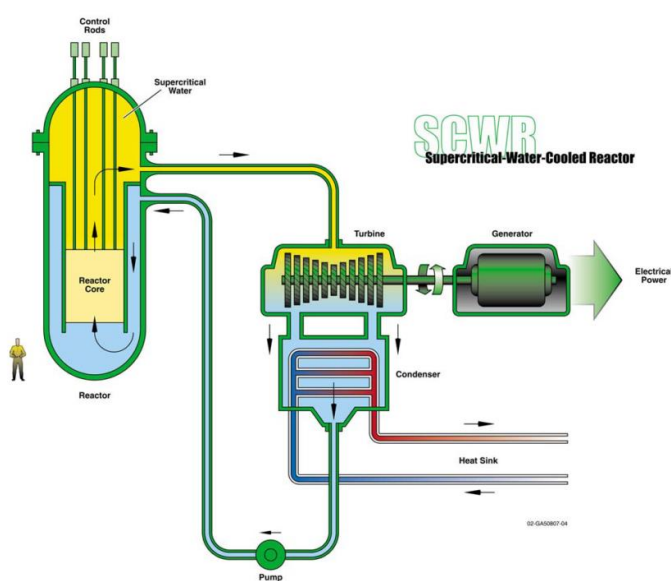


Figure 17 SCWR reproduced from Gen IV international forum 2002 [4]

SCWR systems have two fuel cycle options. The first is an open cycle that uses a thermal neutron spectrum reactor. The second is a closed cycle that uses a fast-neutron spectrum reactor and full actinide recycle, where by all the actinoid materials can be recycled

reducing waste [4]. The systems are cooled by supercritical water. Supercritical water is water that is at a temperature and pressure that is above its critical point. At this stage distinct liquid and gas phases cease to exist. SCWRs are considered evolutions of the current BWRs. The main differences between SCWRs and BWRs are; expected 10% higher net electrical efficiency, reduced flow rate of water allowing for smaller pipelines and pumps, and simplification of the plant layout due to the use of single phase coolant, a coolant that does not undergo a phase change in this case steam to water, eliminating the need for steam dryers, steam to water converters, and recirculation systems [22].

As with all Gen IV systems, there remain several areas of research needing completion for SCWR systems. These include developing computational tools for SCWR applications, selection and qualification of alloys for key components (including cladding), testing of fuel assembly, and decisions about a prototype size and location [21].

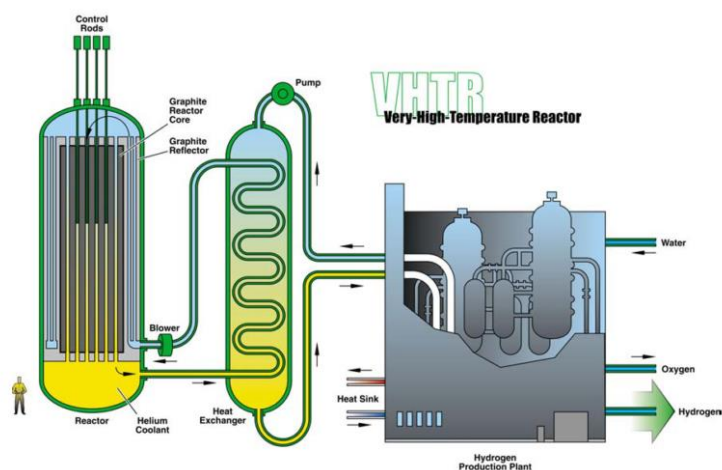


Figure 18 VHTR reproduced from Gen IV international forum 2002 [4]

VHTRs are thermal reactors cooled by helium gas moderated by graphite. The main advantages of VHTRs are the high maximum operating temperature (which gives a high net electrical efficiency), and the availability of high temperature coolants that can be used to produce hydrogen [22]. The reactor core of VHTRs can be either pebble-bed type, such as the Chinese HTR-10, or prismatic-block type, such as the Japanese HTTR. Pebble bed reactors are named such due to the fuel elements being spherical and resembling pebbles. The pebble-bed has a lower power density than the prismatic-block, the more conventional

rods inserted into a prism shaped block system, which gives the core greater neutron stability and improves its lifespan but increases the construction cost. The operating temperature is lower on the pebble-bed design. This allows conventional steel to be used for the reactor pressure vessel [22].

The following research and development objectives, highlighted in Technology Roadmap Update for Generation IV Nuclear Energy Systems [21], are required to implement VHTRs. There remains a need to develop and demonstrate Tri-structural ISOtropic (TRISO) fuel at high temperatures proposed in VHTRs. TRISO fuel is explained in more detail in the SIC-based materials chapter. New coating material needs to be developed for TRISO fuel to replace Zr, ZrC has been proposed. C/C and or SiC/SiC composites require developing for use in control rods. Extra data is required to qualify LWR pressure vessel steels to be used in VHTRs as well as other internal core structures such as heat exchangers. The performance of high-quality graphite needs to be examined for use as core internals material.

In conclusion, all generation IV reactors have material challenges which need to be overcome. The research in this thesis aims to help overcome some these challenges by observing how materials properties evolve under radiation and providing a platform to allow future users to do the same.

2.3.6 Current Reactor Materials

Various materials are used in current reactors dependent upon the application or area of the reactor. A modern reactor uses three layers of physical boundaries between the radioactive fuel rods and the exterior of the reactor plant. These are the fuel cladding, the reactors pressure vessel, and the reinforced concrete containment shield.

2.3.6.1 Fuel Cladding

The fuel cladding is the outer layer of the fuel rods[27], [28]. It sits between the coolant and the nuclear fuel. The main tasks of the fuel cladding are to physically hold the fuel in place and prevent fission fragments escaping from the fuel into the coolant. When designing a fuel cladding especial consideration must be given to the properties of a material [27], [29], [30]. The chemical compatibility of the fuel and the cladding as well as the coolant and other core components of the reactor should be ensured. The phase change and melting temperature of the material is important and should be designed with a safety factor in case an accident occurs. The material also needs to be as stable as possible under irradiation. A low absorption cross section for thermal neutrons is required to ensure that the cladding does not act as a moderator, allowing fast neutrons to pass through the material. **Error! Reference source not found.** shows the thermal neutron capture cross sections of various materials showing why some materials are not suitable as cladding.

THERMAL NEUTRON CROSS SECTIONS (BARNs)	
Magnesium	0.059
Lead	0.17
Zirconium	0.18
Zircaloy-4	0.22
Aluminum	0.23
Iron	2.56
Austenitic Stainless Steel	3.1
Nickel	4.5
Titanium	6.1
Hafnium	104
Boron	750
Cadmium	2,520
Gadolinium	48,890

Table 1 Thermal Capture Cross Sections reproduced from N. Ramasubramanian, "ZIRCONIUM ALLOYS Composition data sheet," [145]

2.3.6.2 Challenges Facing Materials in Fission Reactor Environments

There remain many challenges in the field of nuclear materials research. With new reactor designs potentially pushing materials to higher temperatures and more corrosive environments, as expanded upon in future reactors chapter, and the lifecycle of existing reactors being extended it is important to gain an insight into these challenges.

It is worth remembering the Fukushima disaster of March 2011. Whilst discussing all of the events of the disaster is beyond the scope of this work a brief outline will be discussed here, if a more complete picture is desired the author recommends reading “The 2011 Fukushima nuclear power plant accident : how and why it happened” [31]. The disaster began with a magnitude 9.0 earthquake of the east coast of Japan which led to several tsunami waves hitting the coast. The Fukushima “Daiichi” (literally translated to Big One) plant, a BWR was subsequently submerged which led to a failure of all AC power as well as the complete failure of DC power in core 1 and partial failure of core 2, 3, and 4. This resulted in the failure of emergency coolant systems. This type of accident is termed LOCA (Loss of Coolant Accident). Despite the fact that the plant was placed into shutdown mode immediately upon detection of the earthquake and all control rods were inserted, the decay heat produced was no longer being exchanged and the temperature in the reactors core began to rise and the remaining coolant in the system became steam. As a result the zirconium cladding rapidly oxidised forming ZrO_2 [32]. This chemical process can be described as $\text{Zr} + \text{H}_2\text{O} = \text{ZrO}_2 + \text{H}$. The hydrogen formed eventually led to three hydrogen explosions at the plant. Since the accident there has been a large drive in the nuclear industry community to find a fuel cladding that would be able to withstand a LOCA.

2.3.7 Fusion Reactors

Nuclear fusion is currently not used commercially but is of great interest to the scientific community due to its potential to offer an almost inexhaustible source of energy for future generations[33]–[35]. The fundamental challenge facing fusion is to be able to emit more energy than is injected into the system. The main research is centered on Tokamak reactors which confine a plasma of deuterium and tritium in a magnetic field created by superconducting magnets. A cross sectional schematic overview of a Tokamak reproduced from D. M. Duffy is shown in Figure 19 Reproduced from D. M. Duffy[35] Cross Sectional Schematic Representation of a Fusion Power Plant Design. The Superconducting Magnets

are the Outer Layer. The Vacuum Vessel, the First Wall and the Blanket are Inside the Vacuum Vessel and the Dark Region Round the Base of the Tokamak Represents the Divertor. In the schematic the superconducting magnets are the outer layer. The interior is a vacuum vessel with the first wall, blanket, and divertor inside. The first wall acts as a barrier layer to protect other materials from the neutron flux and transfer heat effectively. Within the first wall the blankets act to breed neutrons and harness power. The divertor acts to remove waste from the plasma whilst the tokamak is running.

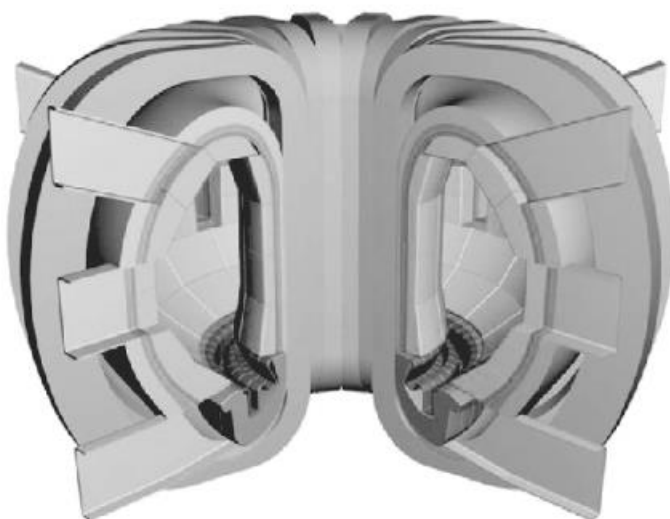


Figure 19 Reproduced from D. M. Duffy[35] Cross Sectional Schematic Representation of a Fusion Power Plant Design. The Superconducting Magnets are the Outer Layer. The Vacuum Vessel, the First Wall and the Blanket are Inside the Vacuum Vessel and the Dark Region Round the Base of the Tokamak Represents the Divertor

The materials within the vacuum vessel experience the most extreme environment in a fusion reactor. The first wall materials will be subject to typical neutron fluxes of approximately 8×10^{14} neutrons/cm²/s⁻¹ and a DPA of up to 120[35]. This is combined with temperatures of 900–1500K. Currently reduced activation ferritic/martensitic (RAFM) steel, vanadium alloys, and SiC fibre/SiC composite materials are being considered as likely first wall materials.

There are additional challenges for plasma facing materials in the reactor. Consideration needs to be taken on not only how the plasma affects the material but also on how the material affects the plasma. This is due to the potential for sputtered material escaping from the surface of the wall, entering the plasma and subsequently cooling it. Currently beryllium is widely used in research reactors for this task. This is due to its low atomic weight which allows for low energy ionization. However, beryllium is highly toxic and has high erosion rates leading people to look for an alternative. Tungsten has been proposed due to its high melting temperature and good thermal conductivity[36], [37]. However, tungsten is prone to form a layer of nanofuzz which degrades the materials performance[38].

2.3.8 Nuclear Reactors Conclusions

When a material is in a reactor it is often subjected to extreme temperatures and radiation fluxes. These can alter the properties of the material with radiation inducing changes in the material ductility and stress resistance. Thermal properties such as conduction, expansion, diffusivity, and specific heat capacity of a material must be considered. The oxidation of a given material as well as its general chemical resistance are also of importance dependent upon how the material is intended to be used. In the following chapters these properties will be explored in more detail.

2.4 Atomic and Microscopic Effects of Irradiation on a Material

2.4.1 Introduction

This chapter will discuss the effects of displacing radiation in solids. This is of particular importance to materials in nuclear environments which are exposed to the combined effects of neutron environments and high temperatures [4]. It is important to develop a fundamental understanding of radiation damage in order to help predict how materials currently in service will behave under such conditions and assist the design of the next generation of advanced materials. This is essential to increase both the safety and lifetimes of current and future nuclear reactors [39].

2.4.2 Atomic Collisions in Solids

When an energetic particle collides with a lattice atom it transfers some of its energy to the atom [40]. If the energy transferred is sufficient then the atom may be displaced from its lattice site, if this energy was transferred from an initial ion the atom becomes known as the Primary Knock-on Atom (PKA). The production rate and energy spectrum of PKAs can be estimated from the irradiation flux and differential cross section through statistical analysis [41]. The displaced PKA may collide with another atom within the crystal lattice leading to further displacements [42]. If these collisions and displacements continue, a collision cascade is created. A collision cascade leads to a cluster of vacancies and interstitials within a localised area of the crystal lattice. This primary damage occurs across a timescale of the order of 0.1 – 1 ps [41], [43].

The calculations to discover whether an atomic collision will result in a displacement are very simple [44]. Take the incident atom to have an atomic number of Z_1 and an energy E prior to collision. After the collision the incident ion energy becomes E_1 . The target atom has an atomic number of Z_2 and once struck an energy of E_2 . This can be seen in Figure 20. The displacement energy is E_d , and the lattice binding energy is E_b . Displacement energy is defined as the minimum kinetic energy required to permanently displace an atom in a solid from its lattice site. The lattice binding energy is the energy required to convert one mole of an ionic compound into the gaseous ions the compound consists of.

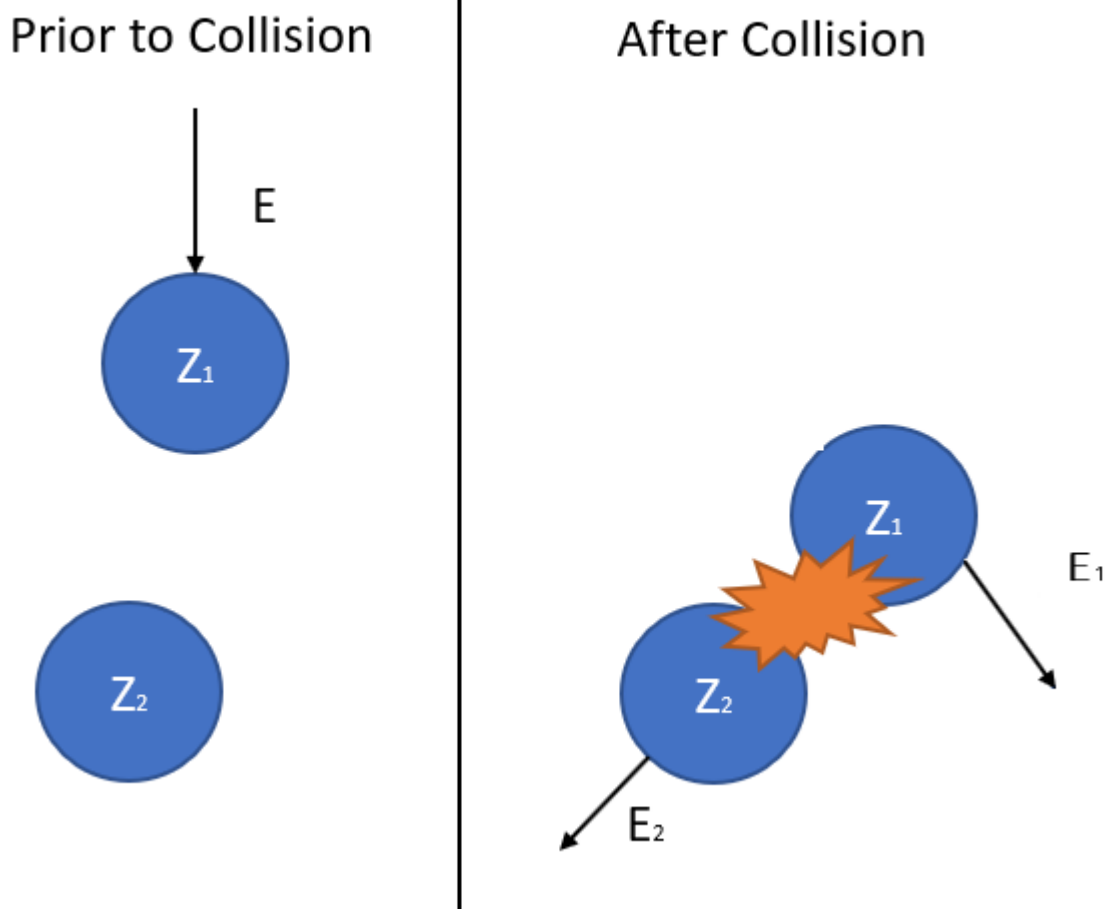


Figure 20 Overview of Atomic Collision

A displacement will occur if $E_2 > E_d$ as previously discussed [44]. A vacancy will be produced if both $E_1 > E_d$ and $E_2 > E_d$, so both the incoming ion and the target atom have greater energy than the displacement energy. This results in both atoms leaving the lattice site and contributing to the collision cascade. The energy of Z_2 will be reduced by the binding energy E_b when it leaves its lattice site. This is due to the energy state of the crystal being lower than that of a free atom.

In the case of $E_2 < E_d$ the struck atom does not have enough energy to leave its lattice site and will vibrate back into position releasing the E_2 energy as phonons. If after collision $E_1 < E_d$, $E_2 > E_d$, i.e. the energy transferred to the target atom is greater than the displacement energy but the incident ion has lost more energy than the displacement energy, and $Z_1 = Z_2$ then the incident atom will replace the struck atom on its lattice site leading to a replacement collision with E_1 released as phonons. In the same case as above yet with $Z_1 \neq Z_2$, Z_1 will stop on the lattice site and become either an

interstitial impurity or a substitutional atom. If after a collision both $E_1 < E_d$ and $E_2 < E_d$, then Z_1 will become an interstitial with E_1 and E_2 releasing as phonons.

2.5 Types of Defects

2.5.1 Introduction

The result of atomic collisions is the formation of defects. By gaining an insight into the type of defects that form allows for a fundamental understanding of how the properties of a material evolve due to radiation. The following chapter discusses many of these defects.

2.5.2 1D Defects

The crystal lattice describes the structure of a crystal and a lattice point within a crystal lattice represents the position of an atom. A point defect is classified as an atom missing or sitting in an irregular position in the crystal lattice of a material creating a 1D “point” in the crystal structure [45]. There are various types of point defects which will be explained in more detail in this section. These include vacancies, self-interstitial atoms, substitutional atoms, interstitial impurity atoms, anti-site defects, and topological defects. **Error! Reference source not found.** shows some of the different types of point defects.

2.5.2.1 Vacancy

A vacancy point defect is where there is a missing atom in the crystal lattice. Vacancies occur naturally within a material. Their number has been observed to increase with temperature and the concentration of vacancies can be calculated by:

$$N_v = N \exp\left(\frac{-Q_v}{k_B T}\right)$$

Equation 21 Vacancy Concentration

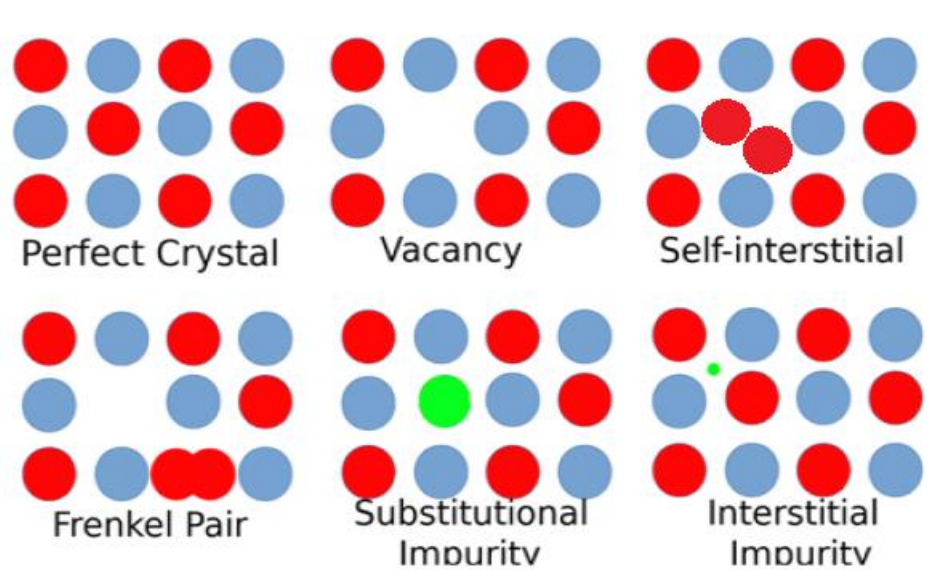


Figure 21 Overview of Atomic Placement in Various 1D Defects

Where N_v is the vacancy concentration, Q_v is the energy required for vacancy formation, k_B is the Boltzmann constant, T is the absolute temperature, and N is the concentration of atomic sites.

It has been observed that under ion and neutron irradiation the number of vacancies in a material increases [46] and that these vacancies cluster, especially in BCC materials [47]. The increased clustering in BCC materials takes place during the thermal spike phase of a collision. A thermal spike occurs when the incident ion is heavy and energetic enough that the collisions between ions cannot be considered independent of one another. This creates a under dense region of atoms in the centre of the cluster area, and an over dense region surrounding it. Under neutron irradiation, vacancy concentrations in Ni have been observed at lower temperatures 20–200K [48]. This temperature range is below 350K, the temperature below that which vacancies become mobile in Ni. These vacancy concentrations have been postulated to be formed by collision cascades as single impacts would not account for the number of vacancies observed.

Vacancies can migrate through the crystal structure of a material. This occurs when an atom moves from its original lattice position to the position of the vacancy, which leaves a vacancy in its previous location. In order for this to happen chemical bonds in a material need to be broken and new bonds formed. This requires an activation energy. The most stable state of vacancies in a material is when they are evenly spread throughout the crystal [49] which can be seen in the Fick law formula (Equation 22). However, vacancies often become trapped in a sink, such as a void or grain boundary, leading to uneven concentrations and clustering.

$$J_x = -D_x \frac{\Delta C}{\Delta x}$$

Equation 22 Fick Law Formula

Where J_x is the flux of vacancies in direction x , D_x is the material constant, and $\frac{\Delta C}{\Delta x}$ is the difference in the concentration of vacancies.

2.5.2.2 Self-Interstitial atoms

Self-interstitial atoms (SIA) consist of an atom of the element already existing within a compound, as opposed to one introduced from an incident ion or a knock on from a different alloying element. A self-interstitial can occupy an area outside of the crystal lattice points. However, most self-interstitials have what is known as a split structure where two atoms share the same lattice site [50]. When shown schematically, as shown in **Error! Reference source not found.**, the two atoms resemble a dumbbell, for this reason they are often referred to as dumbbell interstitials. In the dumbbell structure the centre of mass of the two atoms is at the lattice site and they are displaced symmetrically along the dumbbell axis. Two atoms in the dumbbell configuration on a normal lattice site generate strong repulsive forces due to atoms strongly repelling at close range. When these forces relax, a displacement field is created which spreads out into the crystal. This creates a

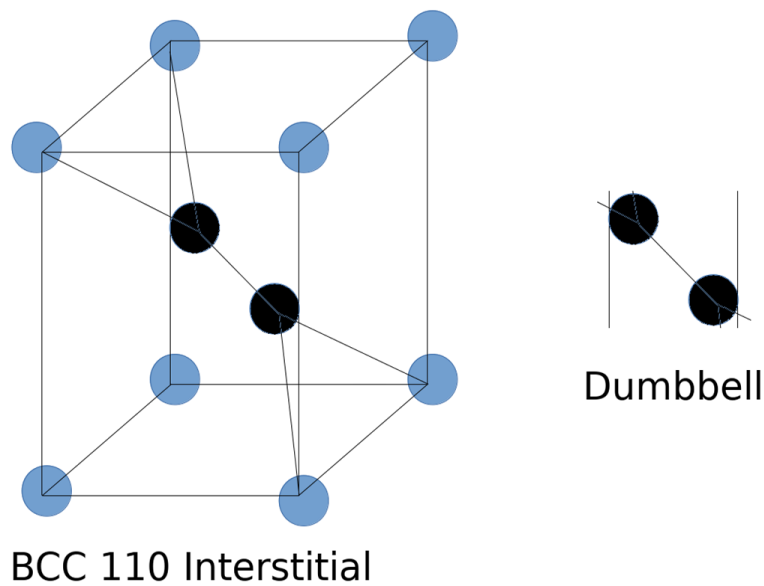


Figure 22 BCC Dumbbell Interstitial Lattice Position Where the Blue Circles are the Original Lattice Points and the Black Circles are the Interstitials

distortion and applies stress upon the lattice structure. When self-interstitial atoms are stable the axis of the dumbbell is along $\langle 100 \rangle$ in the FCC structure and $\langle 110 \rangle$ in the BCC structure [50].

2.5.3.3 Frenkel Pair defects

When an atom is displaced, creating a vacancy, it may be displaced to an interstitial site, creating an interstitial defect. This is known as a Frenkel pair defect or simply a Frenkel defect [51]. These defects do not affect the chemical properties of a single element material as no foreign atoms have been implanted. However, in the case of an alloy material the properties can be altered by an element moving site into another elements structure.

2.5.2.4 Impurity atoms

Impurity atoms are atoms of a different element to those present in the solute. There are two main types of impurity defects that occur in a material. They are substitutional and interstitial impurities. Substitutional impurities are usually close in size to the solute atoms as it is energetically favourable for them to occupy a single lattice site. If the substitutional atom is far larger than the bulk atom, they will generally cause a distortion of the lattice in their immediate vicinity. Substitutional atoms occupy a position on the lattice that would otherwise be occupied by an atom of the solute compound, as seen in **Error! Reference source not found.** These substitutional atoms act as effective traps for SIAs due to the lattice distortion [52]. Interstitial impurity atoms can, like SIAs,

cluster into an interstitial vacancy in the lattice of a material if they are smaller than the solute atoms. SIAs on a large scale throughout the material will change the materials properties creating alloys.

2.5.2.5 Interstitial impurities

Interstitial impurity atoms situate themselves in the spaces between the solute atoms. Unlike self-interstitial atoms are usually located on true off-lattice sites between lattice atoms. These impurities have a crucial role in the properties and processing of material, notably in carbon steels. The configuration of interstitial impurities may also be a mixed dumbbell. This is similar to the dumbbell interstitial shown in **Error! Reference source not found.**, however the atoms making the dumbbell are of different types.

2.5.2.6 Antisite

Antisite defects occur in ordered compound materials. They occur when an atom of a specific element exchanges places with a different element. No foreign elements have entered the material and the crystal lattice positions are maintained however the bonds may be different.

2.5.3 2D Defects

Line defects also known as linear defects are a dislocation type of defect. They are areas where the atoms in a crystal structure are out of position in a 2D configuration. The magnitude and direction of these defects is described via the Burgers vector. Dislocations occur when a stress is applied to a material. This stress could be mechanical, thermal, or radiation. They migrate under the same conditions. Migrating dislocations create plastic deformation in materials thus increasing a materials ductility until a critical threshold is reached where the material undergoes embrittlement. There are two primary types of dislocations. These are edge and screw dislocation. In real applications dislocations often exist as a hybrid between the two types.

Edge dislocations occur when an extra plane of atoms extends partially through a crystal lattice. They can also be described as part of a plane of atoms missing from the crystal structure. The plane of atoms missing in the lattice lie along a 2D line. This line lies alongside the extra partial plane. Around the immediate vicinity of the line, interatomic bonds are significantly distorted.

Edge dislocations migrate throughout the crystal structure by breaking and reforming bonds as they traverse parallel to an applied stress. However only a small fraction of the bonds are broken at one

time, this allows them to migrate at a much smaller force than breaking all bonds. Edge dislocations accommodate shear stress by migrating. This is shown in Figure 23.

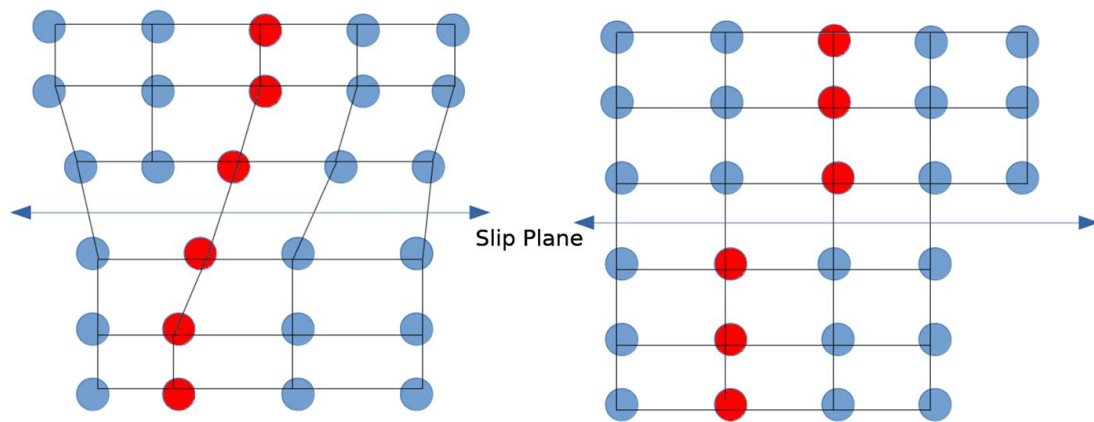


Figure 23 Lattice View of Edge Dislocation Migration Showing how Atomic Bonds are Broken and Reformed on the Slip Plane

Screw dislocations are similar to edge dislocations. They also migrate due to shear stress in the crystal structure. However, the defect line is perpendicular to the direction of the stress. The displacement occurs over one lattice distance which results in a twisting effect. The dislocations

move along the densest planes of atoms in a material due to the stress required to move the dislocation increasing with the spacing of the planes.

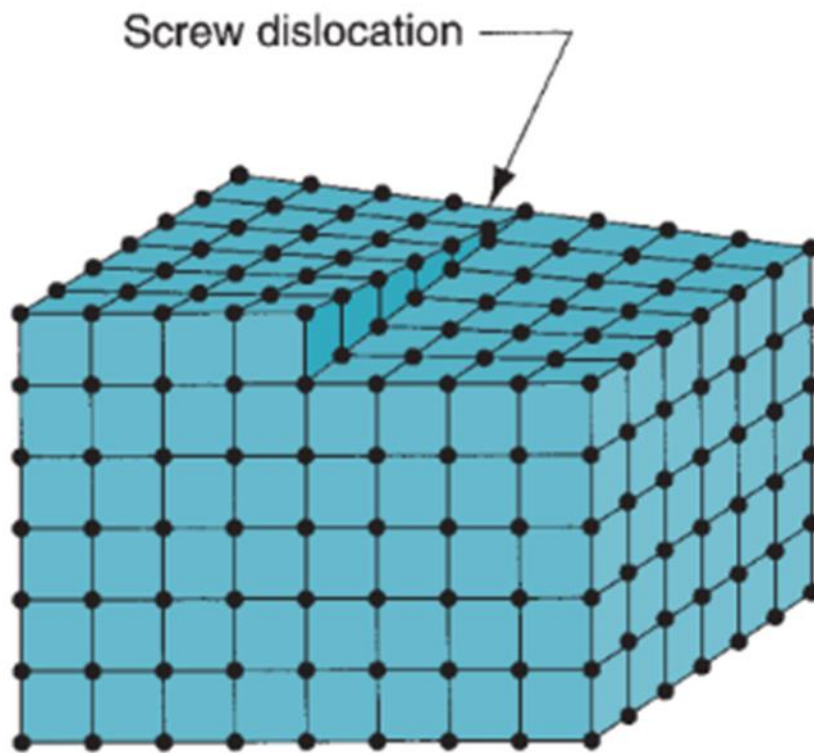


Figure 24 Outline of Screw Dislocation reproduced from [53]

2.5.3.1 Planar Defects

There are four primary types of planar defects in crystal structures. These are stacking faults, dislocation loops, twin boundaries and grain boundaries.

Stacking faults occur in a number of crystal structures. The easiest way to visualise a stacking fault is to picture a hexagonal close packed crystal structure. In such a structure the atomic planes arrange themselves ABABABAB. However, it is possible for a layer to be missing in this configuration. Under these conditions the layer would be arranged ABABAABAB. Another configuration would be Face Centred Cubic (FCC) materials with a sequence of ABCABCABC. A fault may occur leading to ABCABABC. Figure 25 shows this.

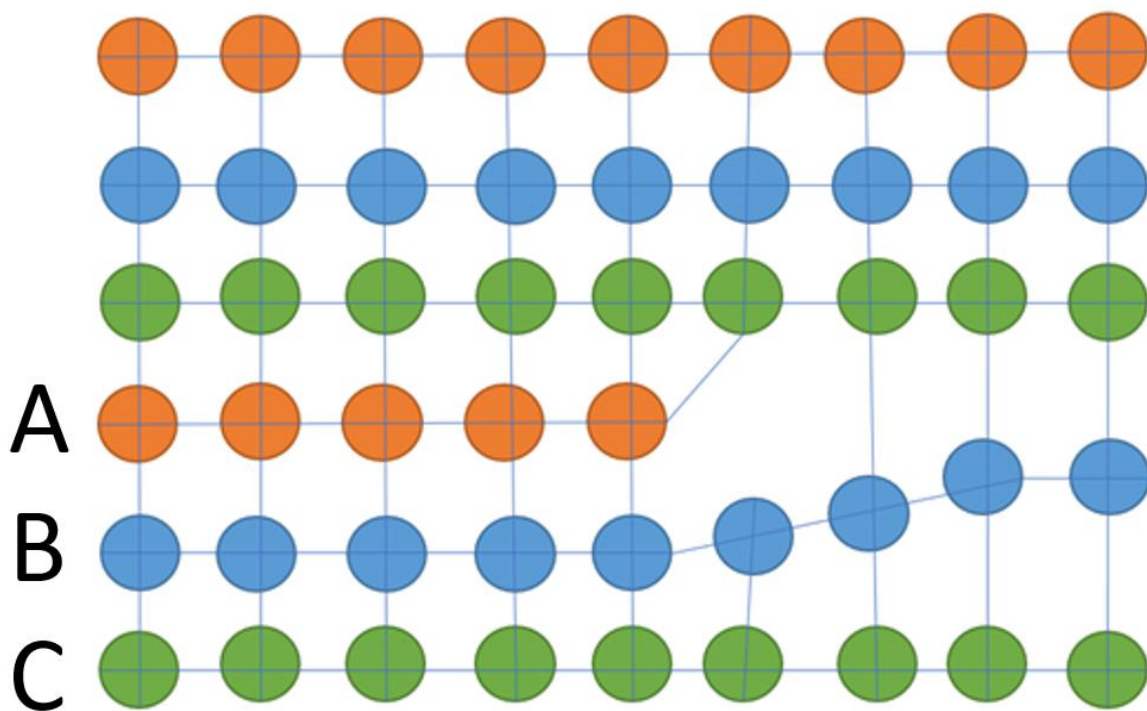


Figure 25 The edge of a Stacking Fault with the Right of The Image Being in Stacking Fault Formation and the Left Being in Correct Formation for an FCC Material

A stacking fault carries a certain amount of energy. This is referred to as stacking fault energy (SFE). The SFE can be determined by the width of the stacking fault. This is due to the repulsive forces of two partial dislocations, a type of dislocation that is not fully formed due to lattice constraints, and the attractive forces occurring due to surface tension of the stacking fault. When the stacking fault

width is low, the SFE is high, the repulsive forces due to the partial dislocations are energetically unfavourable and as such the fault requires less energy to migrate through the material.

Dislocation loops form as a result of interstitial and vacancy defects diffusing through the crystal lattice. Whilst interstitials and vacancies which are mobile are eventually removed from the lattice, by reaching sinks such as dislocations or grain boundaries, under radiation they are continually being generated. As such steady-state populations of the defects can form. These populations can attract together into discs. When enough defects accumulate, they supersaturate, which causes the disc to grow and the planes on either side to collapse due to repulsing forces. This forms a continuous lattice with a dislocation loop. Dislocation loops can be classified by the relative position of the Burgers vector to the loop plane. The Burgers vector represents the magnitude and direction of lattice distortion. If the Burgers vector lies within the loop plane the loop is classified as a slip loop. If the Burgers vector lies outside the plane the loop is classified as a prismatic loop [54]. Slip loops are generally formed by external shear pressure and appear in slip planes. A slip plane is the plane containing the greatest number of atoms per area and in close packed directions. The loops can grow by gliding and reach dimensions of over 100 μm . Dislocation motion along a crystallographic direction is called glide and the motion referred to as gliding, the plane which the glide occurs on is referred to as the glide plane.

Another type of planar defect, grain boundaries are generally very large in comparison to the faults discussed thus far, although in nanograin materials they exist in a much smaller form. They are where one grain, an area with a defined lattice configuration and orientation exists, in a material stops and another begins. Grains range in size from a few nanometres to centimetres across. Their orientation is generally rotated with respect to their neighbours. Grain boundaries limit the length and motions of dislocations. Therefore, smaller grains, with increased grain boundaries, harden a material.

Twin Boundaries are a form of grain boundary where the crystals at either side of the boundary are mirrored. Figure 26 shows this.

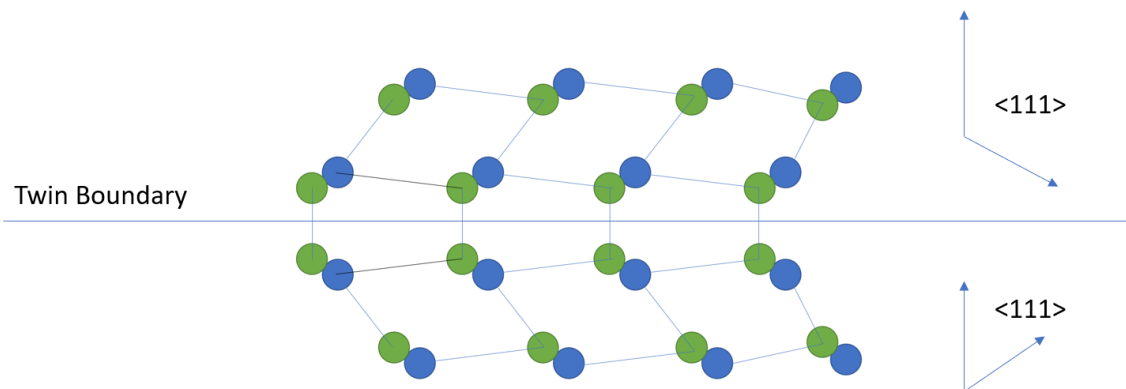


Figure 26 Overview of a Twin Boundary Fault Showing how the Crystal Lattice is Mirrored Either Side of the Boundary

2.5.4 3D Defects

In 1959 a new type of defect was discovered in quenched gold [55]. Since then they have been observed in a wide variety of cases [56]–[61]. This defect was described as a stacking fault tetrahedra (SFT). In other literature it is also referred to as a Thompson defect [62].

An SFT can be formed by vacancy defects migrating to an area surrounded by four $\{111\}$ planes which form a regular tetrahedron with a hole in its centre. Then a plane of triangular shape is removed, and the remaining atoms collapse into the original hole, placed so that it has the same openings on all four faces. Collapse all the four openings along the direction perpendicular to each plane, this will produce an SFT [56].

SFT defects are easily formed in FCC materials. This is due to the relatively small stacking fault energy. SFTs require faulted dislocation loops of type Frank and Shockley[17]. Frank loops are a stacking fault consisting of either a layer of lost atoms from vacancies, or a layer of extra atoms formed through interstitials. Shockley dislocation refers to a pair of dislocations which cause a localised stacking fault. Metals with a high stacking fault energy, such as aluminium, which have a preference for perfect dislocation loops, as opposed to faulted ones, are less likely to form SFTs [56].

SFT defects can be formed in numerous ways. Quenching is one way and this is what led to the initial discovery [55]. Plastic deformation is another way they can form. Other methods, more in line with the scope of this thesis, are electron irradiation [63] and collision cascades [56].

SFTs like other stacking faults lead to lattice hardening in a material [60]. This is due to them creating an obstacle in the glide planes of materials [57].

2.5.5 Volume Defects

Volume defects take the form of extended defects such as voids, cracks or areas of impurities in a material. They occur across three-dimensional macroscopic areas. A void is a large area of missing atoms in a material. They typically occur as a result of an imperfection in the processing of materials. They can also be formed where many vacancies or interstitials can be created. The vacancies can join together to form a void. Because voids are anomalies in a material structure, they affect the mechanical properties of a material. When stress is applied voids in a material can accelerate the formation of cracks. Voids are covered in greater depth in the next chapter. In the case of interstitials these can join together to create bubbles in a material.

Another volume defect is the amorphization of crystalline solids. This is expanded upon in the amorphization chapter.

2.6 Physical Effects of Irradiation

2.6.1 Introduction

As stated previously, due to the formation and migration of defects in a material its properties evolve. When considering a material for use in a radiation environment it is important to know how its mechanical and physical properties may change and what steps can be taken to minimize those changes. The following chapter explains how defects migrate and affect a material on the macroscopic scale and above.

2.6.2 Radiation induced segregation

In 1973 it was discovered that, during irradiation, defect-flux driven segregation processes can alter the phase stability of alloys [64]. At elevated temperatures during irradiation with neutrons or charged particles alloying elements segregate towards or away from external surfaces, grain boundaries, dislocations, voids, and other defect sinks [65]. The local compositional changes can frequently become so great that second phase precipitates are induced in previously stable under-saturated solids. This can alter precipitate morphology and distributions to produce multi-phase alloys. The point defects and defect clusters produced under irradiation have an approximately random distribution throughout a material [52]. Defects that are mobile and do not undergo recombination become re-incorporated into the crystal at defect sinks. The motion of atoms allows for the motion of defects to defect sinks creating a defect flux. Under defect fluxes any preferential association of a defect with an alloy element or precipitation will create a net flux of the elements or precipitations to the defect fluxes. It is this process that will lead to the buildup or depletion of certain alloy elements in the vicinity of defect sinks as certain elements preferentially cluster around the sink leaving a depleted zone in their path. This process is called Radiation Induced Segregation (RIS).

The irradiation dose rate and temperature of the target material affects how much RIS occurs [52]. At high temperatures large vacancy concentrations lead to a high diffusion rate of alloying elements as well as a high defect recombination rate. The increased recombination rate reduces the number of defect fluxes to sinks. Meanwhile the high diffusion rate leads to back diffusion, a phenomenon where elements diffuse in the opposite direction of the main diffusion path, of segregated alloying elements. At low temperatures vacancy mobility is low and the radiation-induced vacancy combination becomes high. This leads to the defect recombination becoming dominant and

therefore the defect fluxes to sinks decreasing and segregation becoming reduced. At intermediate temperatures $\sim 250^{\circ}\text{C}$ the thermal vacancy concentration becomes so low that it can be ignored. The radiation induced excess vacancy concentration also becomes relatively low. This leads to a low defect recombination rate, and therefore more defect fluxes to sinks, leading to significant segregation.

The lower the dose rate the lower the temperature under which RIS will occur [52]. This is due to the lower dose rates generating point defects slower than higher dose rates. However, this does not affect the thermal mobility of defects. The lower number of defects within the material lattice at a given point in time increases the probability that they will find a sink rather than recombining if there is a sink present. At higher temperatures irradiation produced defects have less of an impact on segregation due to a lower displacement rate. This means that their effect on segregation will be less than at a higher dose rate.

Impurities within a material can influence the behavior of RIS at grain boundaries [52]. This is due to the impurities acting as traps for vacancies and interstitials [66]. The trapping of point defects leads to an increase in recombination which reduces the number traveling to sinks, and therefore, the amount of segregation.

2.6.3 Voids and Bubbles

Voids were first observed to form in irradiated metals in 1967 by Cawthorne and Fulton [30]. Since that time scientists have been working to understand their formation and growth. The formation of voids can lead to volumetric swelling of a material [52]. Voids can lead to tens of percent increases in the volume of a material. It is important to understand the swelling magnitude so that it may be accommodated for in reactor designs.

During bombardment with energetic neutrons, ions, or electrons voids can form [67]. Voids form initially due to a supersaturation of vacancies and more than one type of defect sink being present. At least one defect sink within the material must preferentially absorb vacancies so that an excess of them gather and form a void.

It is known that under irradiation inert gasses can group together in a material to form bubbles. This effect has been observed in many materials and under both ion and neutron irradiation [68]–[75]. In the case of ion irradiation, the inert gas is implanted from the ion beam. Under neutron irradiation the gas is formed via transmutation effects, the changing of one element into another by radioactive decay or nuclear bombardment. Bubble growth usually occurs by the inert gas collecting in a defect sink and with increasing irradiation. This process relies upon the inert gas being mobile within a material and finding a defect to pin the gas.

2.6.4 Irradiation hardening

A material that is subject to irradiation can harden. This is known as irradiation hardening. Whilst such hardening increases the yield strength the ductility is decreased. This modifies the stress/strain of a material. Figure 27 reproduced from Fundamentals of Radiation Materials Science [52] shows this for both a FCC and a BCC metal.

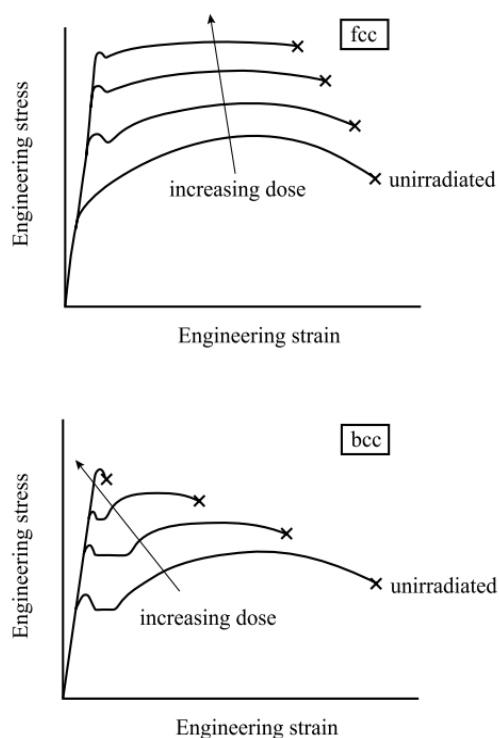


Figure 27 Stress vs Strain as a Function of Irradiation for FCC and BCC Metals Reproduced from [32]

The reasons a material hardens under irradiation is twofold. Firstly, a material hardens due to source hardening [76]. Source hardening has been observed in unirradiated materials such as BCC metals and is believed to be caused by impurity atoms [52]. These impurity atoms cause dislocation lines to become pinned or locked. The same effect happens with crystal defects caused by irradiation. In order for a defect to slide along its plane it must first be unpinned by a stress force, increasing the overall stress required to slide the dislocation.

The second way that a material hardens is via friction hardening. This term refers to the stress required to maintain the plastic deformation of a material [52]. The force required to plastically deform a material rises due to the dislocations traveling through a crystal lattice being resisted by defects acting as obstacles. The source of the hardening is characterised as either short- or long-range stresses. Long range stresses are created by the stress fields generated from dislocation-

dislocation interaction. Short range stresses are caused by the moving dislocation encountering discrete defects. In both cases the stresses resist defect mobility similar to how friction resists mobility of an object sliding across another, hence the term friction hardening.

2.6.5 Embrittlement of irradiated materials

Irradiated materials also experience a loss of ductility and work hardening [52]. This is due to the same cause as the hardening, the interaction of dislocations and the materials microstructure. The loss of ductility in a material creates embrittlement. This embrittlement can lead to the development of cracks in a material. These cracks can grow under stress and develop into a fracture causing early failure of the material. Within alloys, solutes segregate creating brittle phases, the grain boundaries also become embrittled [77], more details of this phenomenon are described in the radiation induced segregation chapter.

Within nickel-based alloys two effects are postulated to be causing a loss of ductility. At temperatures below 500°C embrittlement is attributed to irradiation induced point defect clusters [77]. At temperatures greater than 500°C it was found that inert gas atoms form into bubbles which accumulate and grow mostly on dislocation lines and grain boundaries [78]. The formation of bubbles of inert gas affects many materials under both ion and neutron irradiation at various temperatures [79]–[82]. These bubbles have been shown to initiate crack formation and intergranular brittle failure, known as high temperature helium embrittlement when the bubble is formed of helium [83].

2.6.6 Reducing Irradiation hardening and embrittlement

The main factors affecting the degree of material hardening and embrittlement are the microstructure of the material, the temperature of the material, and the radiation flux [52]. With regards to the microstructure, the embrittlement can be reduced by decreasing the dislocation migration path. This can be achieved by reducing the grain size or interparticle spacing [84]. The grain boundaries in a material act as a sink for defects which trap embrittling elements. However as previously discussed bubbles will also form on the grain boundaries which can lead to an increase in embrittlement. As such simply increasing the number of grain boundaries may not lead to a reduction of embrittlement and their presence can act to pin dislocations increasing a materials hardness.

Adding substitutional elements to alloys can also affect the level of irradiation hardening and subsequent embrittlement. These substitutional elements can form precipitates under irradiation. The precipitates increase the hardness of the material and cause embrittlement [85]. This is common in alloys, for example duralumin where copper precipitates harden the otherwise relatively malleable aluminum.

The exposure temperature of a material under irradiation affects the level of embrittlement due to the fact that annealing processes are accelerated at higher temperatures [52]. Therefore, a material that undergoes irradiation at high temperature will embrittle less than the same material at a lower temperature. The annealing can prevent some of the precipitates and dislocations being introduced by the irradiation from growing extensively by increasing their mobility leading them to travel to defect sinks and recombine with other dislocations.

The level of embrittlement a material experiences is linked to the neutron fluence, and subsequent Displacement Per Atoms (DPAs), that the material is exposed to [52]. However, at a certain DPA materials harden, and subsequently embrittle, at a much slower rate. This is known as the saturation point or effect[57]. The required fluence and resulting dose to achieve this saturation varies for different materials due to their different properties.

Saturation occurs due to the number of obstacles being created reducing as recombination of defects becomes dominant [57][83].

2.6.7 Fatigue

During the lifespan of a material various structural changes occur due to thermal and load induced cyclical stress. These changes can be used to split the fatigue process into four phases. The first phase is the crack initiation. The second phase is slip band crack growth. This is where the initial crack deepens on planes with high shear stress. The third phase is crack growth on planes of high tensile stress. This is where a crack grows and is well defined in the direction normal to the maximum tensile stress. The fourth and final stage is ultimate ductile failure. This occurs when the crack becomes long enough that the cross section remaining cannot support the applied load [52]. Neutron irradiation affects the fracture toughness of a material by introducing defects which can pin slip bands allowing for greater growth. This leads to the formation of cracks and fatigue failure at lower cycles of stress than unirradiated material [86]. This happens particularly at phase four fatigue crack growth, which is dependent on the fracture toughness of a material.

2.6.8 Irradiation Creep and Growth

Creep is defined as the time-dependent deformation of a metal under constant load and at an elevated temperature [52]. There are three components of strain: elastic, anelastic, and plastic. Elastic is instantaneous independent of time and reversible when the stress is released. Anelastic strain is reversible dependent upon the strain rate, it is easily thought of as a state between elastic and plastic strain. Plastic strain is irreversible and dependent upon time. Plastic strain is characterized by a change in shape or distortion of the sample where the volume is conserved. Creep is the time dependency of plastic strain [52].

Creep is generally a temperature dependent process. It requires the thermal formation and motion of vacancies, grain boundary diffusion, or dislocations to climb over obstacles and glide along slip planes [52]. The increase in temperature gives the material enough thermal energy for the dislocations to overcome obstacles and be in motion. However, irradiation creep is not very temperature dependent. Irradiation creep is defined as the difference in

dimensional changes between a stressed and an unstressed sample irradiated under identical conditions. It is due to the production of defects provided by energetic atomic displacements as opposed to thermal energy. Irradiation creep is an important factor in lifespan and stress limit determination as well as understanding design limits in functional applications such as flow channel inserts within the blanket region of a fusion reactor [87]. Irradiation creep, unlike thermal creep, is not a result of accelerated diffusion rates. It instead occurs due to an enhanced defect production and changes in the microstructure of the material due to radiation damage. The exact underlying mechanism of irradiation creep remains debated [88]–[90]. This chapter will discuss the most commonly reported and discussed mechanisms.

2.6.9 Stress Induced Preferential Nucleation (SIPN)

When an external stress is placed upon a material the probability of interstitial loops nucleating on planes with a preferred orientation increase. These interstitial loops are most likely to nucleate upon planes perpendicular to a tensile stress. However, vacancy loops have a preferential tendency to form on planes parallel to a tensile stress. In both cases the preferential loop formation causes the material to elongate in the direction of the applied stress [52]. This process is called Stress Induced Preferential Nucleation (SIPN) [91][92]. It is worth noting that SIPN cannot fully account for the total amount of creep strain in a material. Whilst it has been observed that preferred loop orientation increases with tensile stress the amount of creep strain is higher than can be accounted for with preferential loops on a magnitude of 2-4 [88]. This does not mean that SIPN should be totally discounted however. Whilst it may not be an accurate model for describing the total creep, it may be a viable mechanism for a portion of the observed creep.

2.6.10 Stress Induced Preferential Absorption (SIPA)

Stress Induced Preferential Absorption (SIPA) is defined as the transfer of atoms from planes parallel to an applied stress to planes perpendicular to the stress. It is a process that occurs at steady state. This process leads to the climb of dislocations. SIPA occurs due to the stress induced interaction energy between an inhomogeneity and a dislocation [93]. For an elastic inhomogeneity, the interaction is dependent on the dislocation orientation relative to the external stress via the change of crystal elastic constants introduced by the defect [94]. SIPA also occurs due to anisotropic diffusion and elastic-diffusion. Whilst the origins may differ all of the mechanisms result in preferential absorption of interstitials by dislocations [52].

2.6.11 Preferred Absorption Glide (PAG)

Preferred Absorption Glide (PAG) results from SIPA. However, it is an additional component of creep strain. PAG describes the glide contribution to the strain, as opposed to SIPA which describes the only the climb contribution [95]. When a stress is applied, pinned dislocations will glide to try and reach a configuration where the restoring force due to line tension is balanced by the applied stress [52]. Due to dislocations being pinned, the creep process becomes limited to approximately the length of one elastic deformation [96]. Climb allows the dislocation to overcome the initial pinning points [97]. The process that enables this is the released segments bowing out between pinning points until the line tension is balanced where they are pinned again [52]. Figure 28 shows this process.

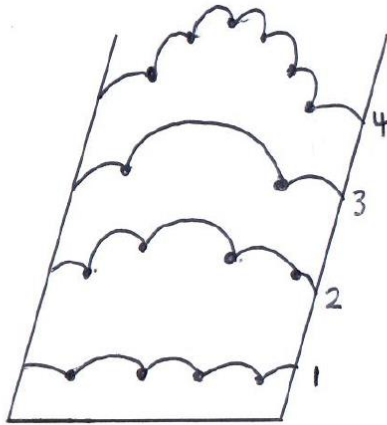


Figure 28 PAG Pinning Point Evolution Point 1 Shows Initial Locations Evolving Through to Point 3 Where the Dislocation is Overcome Before the Tension is Balanced at Point 4

Each cycle of glide and climb to pinning points results in strain being produced as well as an elastic deflection. Together the strain and elastic deflection account for the total creep strain in the solid.

2.6.12 Dislocation bias contribution to climb and glide

SIPN and PAG are both processes which describe creep that is driven by stress induced preferential absorption [52]. However, creep can also be governed by dislocation bias. If a material has net absorption of vacancies by sinks other than dislocations, such as voids, then dislocations will net absorb interstitials. This creates creep much in the same way that thermal creep mechanisms do. However, the vacancies that create these mechanisms are replaced by interstitials. The interstitials collected at dislocations create an energy bias which allows the dislocations to climb.

2.6.13 Transient creep

Figure 29 shows the concentration of point defects with time under irradiation.

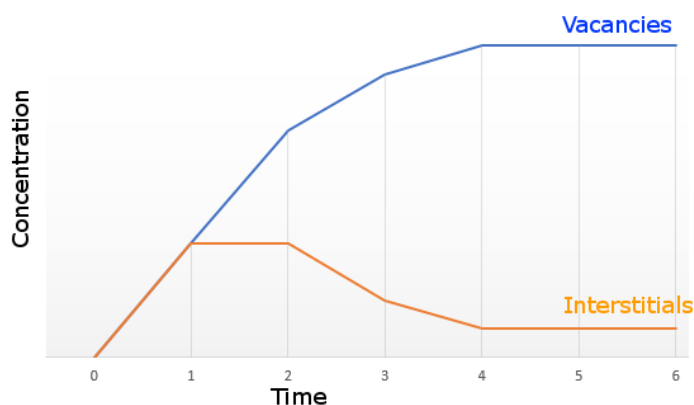


Figure 29 Typical Point Defect Accumulation Under Irradiation as a Function of Time

After irradiation flux is initiated point defects build up equally for a time [98], point 1 on Figure 29. Typically, this time of equal build up is in the range of microseconds to milliseconds. After this time elapses the interstitials begin to be lost at sinks which stabilizes the concentration due to their migration throughout the target material. After some more time the vacancies reach a level where recombination with interstitials is no longer negligible, point 2 on Figure 29. The vacancy concentration continues to increase but at a decreasing rate. At the same time the interstitial concentration begins to decrease. At point 3 on Figure 29 mutual recombination begins to dominate interstitial loss. After point 4, vacancies begin to be lost at sinks and both concentrations reach their steady state values. The time of this steady state can range from a few milliseconds or less to infinity, dependent upon the material and temperature.

Creep can occur prior to a steady state being achieved by vacancy and interstitial concentrations [52]. This creep is referred to as transient creep. There are three primary processes that this occurs by. They are: glide induced transient absorption, start-up induced transient absorption, and cascade creep.

After a dislocation has climbed over one obstacle it glides to another one [98]. This glide is normally so fast that steady state concentration cannot be maintained near the dislocation. As a result, the dislocation absorbs an unbalanced number of excess vacancies and interstitial fluxes whilst trying to regain a steady state at a new location. The unbalanced vacancy concentration far exceeds the numbers of interstitials to an extent that the interstitials will have a negligible effect. The increased vacancy accumulation causes the dislocation to climb which can lead to it being released from an obstacle enabling further glide and producing creep. This process is known as glide induced transient absorption.

Due to the high mobility of SIAs compared to vacancies, under irradiation and prior to the point defect population achieving a steady-state, dislocations may receive large excess interstitial fluxes [98]. This leads to start-up induced transient absorption. Prior to point 4 on Figure 29 the interstitial concentration is greater than it is after, at steady state. This is due to interstitials being absorbed by dislocations at point 1 while vacancies only begin to be absorbed after point 4. This leads to creep. This process is most active at lower temperatures where it takes longer for a concentration to reach stage 4 [99].

Cascade diffusion theory is used to calculate the superpositions of point defects that have occurred earlier in time at any point in the material from local concentrations of defects [100], [101]. As a result of cascade diffusion large fluctuations of point defects occur as a result of each cascade [98]. Due to the different diffusion characteristics of vacancies and interstitials, dislocations receive fluxes of defects even though the sum of fluxes over time may be equal. As a result of these different fluxes, a dislocation will climb. Because of the climb the dislocation may become unpinned and subsequently lead to creep. This process is known as cascade induced transient absorption.

2.6.14 Loop un-faulting

The faulted loop is either the insertion or removal of a layer of atoms which creates a corresponding stacking fault which is associated with the condensation of a planar monolayer of vacancies and SIAs, respectively[102]. A mechanism that can produce creep strain is loop un-faulting [52]. Dislocation loops can form and grow under irradiation. They can grow until they become unstable and eventually un-fault at which point they become part of the dislocation network. The interaction between dislocations and loops can also lead to the loops un-faulting. The extra dislocations produced become mobile and may then participate in the creep process by SIPA, PAG or climb and glide driven by interstitial biases thereby increasing the amount of creep. When loops interact, they coalesce which leads to them either annihilating, creating a larger loop, or contributing to the network dislocation density. As the network dislocation density increases the number of loop interactions with dislocations increases. Loop un-faulting also contributes to irradiation creep strain as the presence of a stress will assist nucleation of the un-faulting dislocations with favourable orientations, thereby resulting in an increase in the probability of un-faulting. An application of shear stress in the plane of the loops will cause more loops to shear in the direction of the stress. This will result in a net shear of the crystal and appear as creep.

2.6.15 Recovery creep

During creep, dislocations are removed from the material [52]. This phenomenon leads to recovery creep. For example, J. Holmes et al. found that strain recovery was observed during cyclic creep loading of SiC-Fiber Si₃N₄ composites[103]. The amount of strain recovery was influenced by the cycle duration with greater recovery creep ratios at shorter creep recovery cycles. Recovery creep rate can be expressed in terms of dislocation density [88]. Dislocation glide will occur when the force on individual dislocations is balanced by internal stresses created by other dislocations. This means that the glide distance, the distance a defect will glide before becoming pinned, can be determined directly by the dislocation density. As such, when dislocations are removed the glide distance may increase, which in turn increases the creep rate. Figure 30 reproduced from Matthews, J.R. et al [88] shows this process.

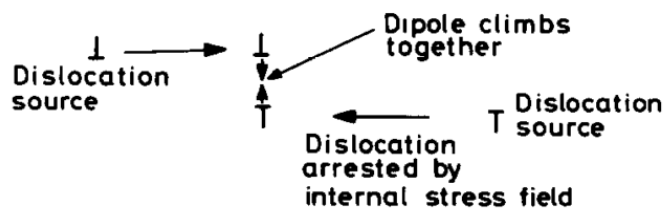


Figure 30 Dislocation Glide of 2 Dislocation Sources Pinning[88]

Another mechanism that contributes to recovery creep is known as dynamic recovery creep[104]. This process occurs when climbing dislocations pass close enough to one and other that their mutual attraction overcomes the flow stress. This leads to some segments to glide together and annihilate. Figure 31 reproduced from Matthews, J.R. et al [88] shows this process.

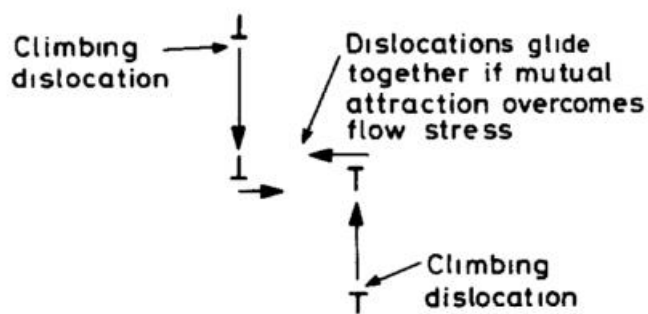


Figure 31 Dynamic Recovery Creep Showing How 2 Dislocations Mutual Attraction Overcomes the Flow Stress[88]

In conclusion by understanding and observing defects and their evolution in a material it is possible to gain insight in how a material's properties will change. This information is especially useful in determining the life span of a material in a hostile environment such as a reactor core.

2.6.16 Amorphization

A material undergoing irradiation may amorphized. This phenomenon is known as irradiation-induced amorphization. An amorphous solid is one that lacks the long-range order that a crystal has. The first report of amorphization dates back to the 1800s [105]. The process of a material becoming amorphous is complex and relies upon numerous factors including temperature, dose and flux, and the materials microstructure [106].

Amorphization can occur across an entire material or in small pockets known as amorphous zones [107]. When a crystal becomes amorphous its properties change [107]–[112]. These changes are numerous. To list a few of key interest in reactor materials, density, elastic modulus, and hardness have been observed to all be affected [107]. For example, L.L. Snead et al. found that amorphous 6H-SiC had a density decrease of 10.8%, a hardness decrease from 38.7 to 21.0 GPa, and a decrease in elastic modulus from 528 to 292 GPa when compared to crystalline 6H-SiC[107].

The point at which a material becomes amorphous under irradiation is known as the critical amorphisation dose. It has been observed that electron irradiation has a higher amorphisation critical dose compared to neutron and ions [113][111]. This is thought to be due to the collision density being greater in heavier particles, leading to a greater defect density.

A material may recover from amorphization and become crystalline again. This is typically achieved by annealing the material at high temperature, approximately half the melting temperature of a given material [107], [110].

2.6.17 Chemical Effects

In a reactor environment transmutation of elements occurs. These elements have a chemical effect on materials and can alter the reaction properties of the fuel. Transmutations are also often radioactive and require containing within the reactor. Some of the long-lived transmutations are ^{79}Se , ^{93}Zr , ^{99}Tc , ^{107}Pd , ^{129}I , and ^{135}Cs [114]. These isotopes require containment in the reactor, and as such the diffusion properties of the cladding material is important to understand.

2.7 Ion irradiation

2.7.1 Introduction

The physical effects of radiation discussed in the last chapter can be formed via neutron irradiation, for example in a reactor environment, or via ion irradiation. Ion irradiation is used in place of neutron irradiation due to several advantages that it holds. Ion irradiation allows for easy changes in parameters such as, dose, dose rate, and temperature. By changing these parameters various simulated conditions can be achieved. Neutron irradiation experiments in test reactors typically require 1-3 years of core exposure to reach fluence levels for post-irradiation examination. These experiments involve the design and production of capsules, along with disassembly and cooling. By comparison, ion beam experiments can be conducted in a day. It is worth noting that ion irradiation can produce different effects to neutron irradiation [115]. Therefore, it is important that studies be verified with a neutron irradiation experiments. However, the time saving of ion experiments makes them a good choice for scoping trials. Ion irradiation is also important in understanding ion bombardment that occurs in fusion reactor system where deuterium and tritium ions, which are hydrogen isotopes and fuse to create helium, impact the components of the reactor, especially the first wall. In the case of fission, transmutation of elements will also lead to the implantation of ions. The purpose of this chapter is to discuss processes that occur in ion-solid interactions.

2.7.2 Sputtering

Under ion-bombardment, atoms sputter and are ejected from the surface of a material. This occurs due to the bombarding ion transferring energy in collisions to the target materials atoms that recoil with enough energy to generate further recoils. Some of the recoils that are directed towards the surface will recoil with enough energy to escape the solid. Figure 32 reproduced from the homepage of N. Yao[116] shows this. This can induce compositional changes in the near-surface of the material if non-self-ions are used. Different elements will sputter with different rates. The surface composition changes as a function of these probabilities.

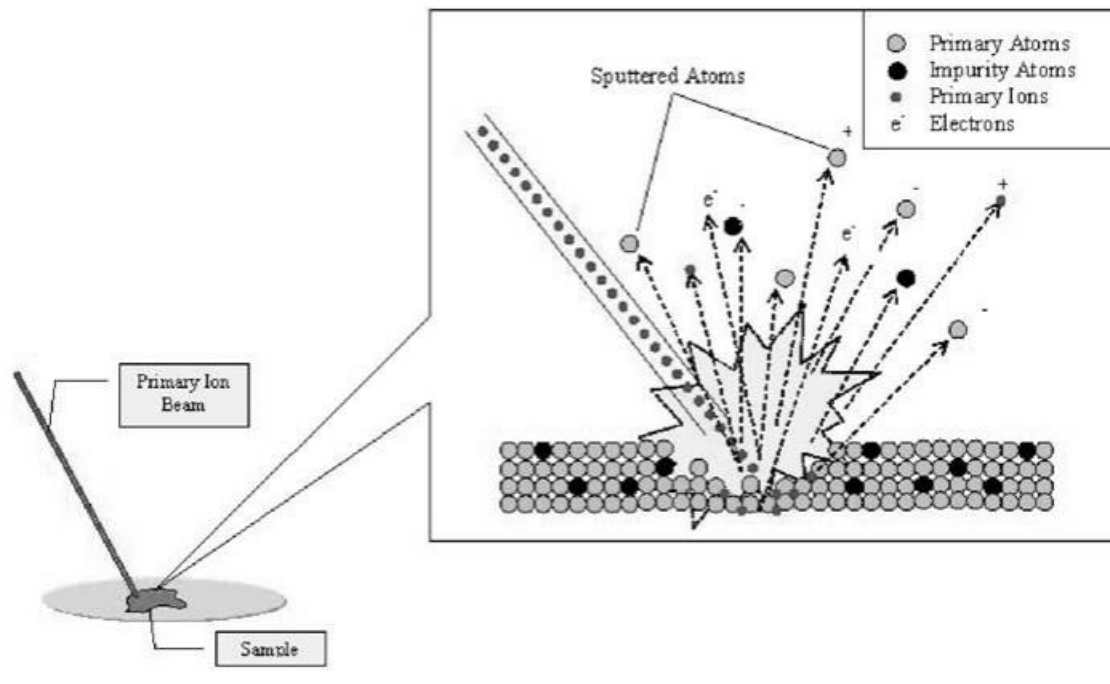


Figure 32 Schematic Diagram of the Ion Beam Sputtering Process Reproduced From N. Yao[116]

The amount of sputtering that occurs can be characterised by the sputtering yield, Y , which is the mean number of emitted atoms per incident atom. The yield value is affected by various factors including the atomic number density and the surface binding energy of the target material, as well as the incident beam energy and angle of incidence.

The sputtering yield Y can be expressed as [52]:

$$Y = \Lambda F_D(E_0)$$

Equation 23 Sputtering Yield

Y is the number of atoms emitted per incident particle, E_0 is the incident particle energy, Λ is the binding properties of the material, and F_D is the density of deposited energy per unit depth.

Sputtering increases with a higher angle of incidence, the angle between the incident ion beam striking the surface and the plane perpendicular to the surface. This is due to more ion energy being deposited close to the surface. At low energy sputter yield decreases, this

is again due to less energy being deposited upon the materials surface. Due to the elastic scattering cross section decreasing with energy the energy deposited on the surface region drops at higher energies. This causes the scatter yield to decrease. This relation on the incident energy results in a peak in sputtering yield at intermediate energies.

In the case of an energetic ion hitting a compound of more than one element it becomes necessary to understand preferential sputtering. This is because not all elements of the compound will sputter with the same yield. The probability of sputtering of an individual atom is dependent upon the type and energy of the incoming ion, the type of sputtered atom, its surface binding energy etc. Since the probability differs for different atomic species preferential sputtering occurs. The atomic concentration will also affect the sputtering yield, as a greater number of a particular atom will affect its probability of occupying a site. The greater the probability the more likely an atom will undergo interaction with the incoming ion and subsequently be sputtered. As seen in Figure 32 sputtered atoms in practice come from a shallow layer at the surface of a material. This layer is referred to as the surface layer and is poorly defined but is usually considered as the first two atomic layers. The sputter yield further from the surface falls off exponentially with depth. Therefore, it is possible to calculate the yield as: [117]

$$Y_A = \bar{p}_A C_A^S$$

Equation 24 Sputtering Yield EQ2

Where \bar{p}_A is the average probability of an A atom in the surface layer to be sputtered, C_A^S is the average atomic concentration of A atoms in the surface layer.

As stated previously the differences in sputtering probability is dependent upon differences in the amount of energy and momentum transferred to atoms, the atomic mass, and surface binding energies [118].

2.7.3 Gibbsian Absorption

Under ion irradiation incoming ions implant themselves in the surface layer of a material. As a result, the surface tension of a material differs from the bulk tension. This along with sputtering changes the composition of the surface of a material. This change in composition is known as Gibbsian absorption [118]. The composition change occurs spontaneously so long as the temperature of the bulk remains high enough for diffusion to occur once irradiation has ceased or due to implantation during radiation. The temperature must be greater than 0K for the jump from surface to bulk and as the temperature increases so does the migration of bulk to surface atoms, however at lower temperatures this process is so slow as to be negligible. The difference in concentration of the surface and bulk is caused by the reduced probability of thermally activated jumps. This leads to an increased concentration in the surface. This increase of a particular atom to be at the surface leads to preferential sputtering of that atom. This in turn depletes the surface of that atom due to an effort to re-establish thermodynamic equilibrium. Gibbsian absorption will then cause more of the atoms to jump to the surface. These will in turn be preferentially sputtered. This leads to a zone where a particular atom will be depleted. This zone will continue to grow in depth and surface area until steady state is reached where the composition of the sputtered atom flux is equal to the bulk composition leaving a material completely depleted of a particular atom.

2.7.4 Recoil Implantation

The term recoil implantation is used to describe the net transport parallel to the ion beam direction of some types of atoms relative to others [42]. Recoil implantation occurs when the lighter atoms in a compound are preferentially transported in the direction of the ion beam, or when an atom from a contamination layer is transported [118]. This is due to the incoming ion beam imparting its momentum to the atoms of the solid. However, the net atom transport in the beam direction will not be significantly changed due to the solid material relaxing to approximately its normal density [42]. Recoil implantation will lead to atomic mixing in the solid [119]–[122] as well as the introduction of impurities from thin

contaminant surface layers [123]. Figure 33 shows how a contamination layer can be mixed into a substrate.

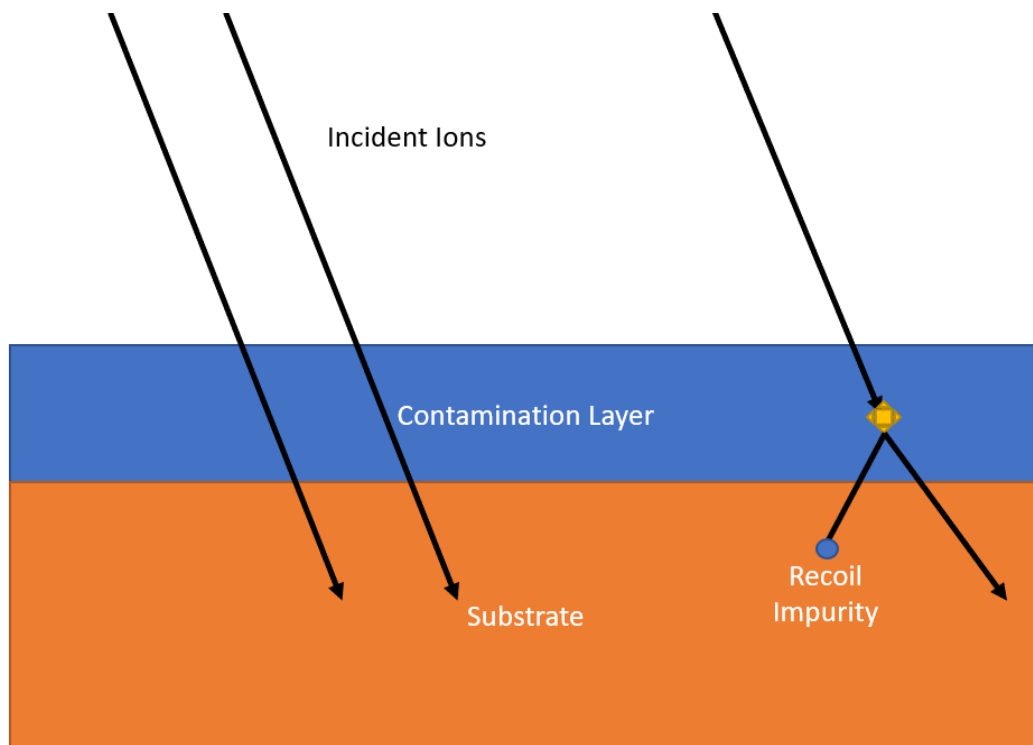


Figure 33 Recoil Impurity Formation

2.7.5 Cascade Mixing

During a collision cascade, incoming ions with a high kinetic energy transfer their energy to target atoms. The energy in a cascade is sufficient to break molecular bonds and initiate relocations in the material lattice. As a result of rapid transfers of energies from recoiling atoms of the solid to other atoms randomization of recoil directions occurs. This results in relocations of atoms in energetic cascades leading to partial isotropic mixing at interfaces, as opposed to recoil implantation previously discussed. Elastic collisions in the layers of a material create defects which assist the diffusion across the interface. Molecular dynamic calculations show that the number of replacements within a displacement event result in a mean square diffusion distance of atoms, $\langle x^2 \rangle \sim 30 a^2$ per defect pair, where a is the closest neighbour distance. Therefore, an atomically sharp interface is broadened by $\langle x^2 \rangle^{1/2}$, approximately 5 atomic planes per 1 dpa [52]. Since the atomic sharp interface broadening increases proportionally with the square root of dose, ion beam mixing of multilayer targets is an effective way of homogenizing a solid.

2.7.6 Ballistic Mixing

Ballistic mixing is similar to diffusion processes. It occurs as a result of the momentum of displaced atoms in energetic collision cascades. The distribution of the displaced atoms is nearly isotropic [43]. The mixing is called ballistic mixing due to the fact that alloy components are observed to travel down gradients, not ones in their chemical potential which they would otherwise follow, in their concentrations during irradiation [43]. There are several ballistic mixing models, known as such due to them only considering the ballistic aspects of collision cascades. Haff [124] and Matteson [125] developed diffusion models to describe the effects of mixing in a collision cascade. Kelly et al. [126], Sigmund and Gras-Marti [127], [128], Sanders et al. [129], [130], and Hofer and Littmark [121] developed ion mixing models based on the Lindhard, Scharff, and Schiott (LSS) transport theory of atomic collisions. All of these models work on the Binary Collision Approximation (BCA) and approximate the inter-atomic potential with an inverse power potential [131].

2.7.7 Chemical Effects on Ion Beam mixing

Systems with similar ballistic characteristics have been shown to have large variations in the mixing rates [132]. This shows that the ballistic models discussed previously do not paint the whole picture in atomic mixing. Johnson found that fundamentally diffusion is driven by a chemical potential gradient and not a concentration gradient [133]. This shows that only in ideal circumstances does Fick's law apply. Johnson found that the random walk will be biased when the potential energy is dependent on the configuration of the chemical potential gradient. The degree of biasing depends upon δ . δ is a natural energy scale for diffusion intermixing [133].

Another thing that effects the mixing of layers is the cohesive energy, which is the binding energy per atom of an alloy. Rossum et al. studied the mixing in 5 metallic bilayers and found a correlation between the mixing rate and the average cohesive energy [134]. Figure 34 shows the mixing rate (y axis) vs the cohesive energy (x axis) reproduced from their report shows this [134].

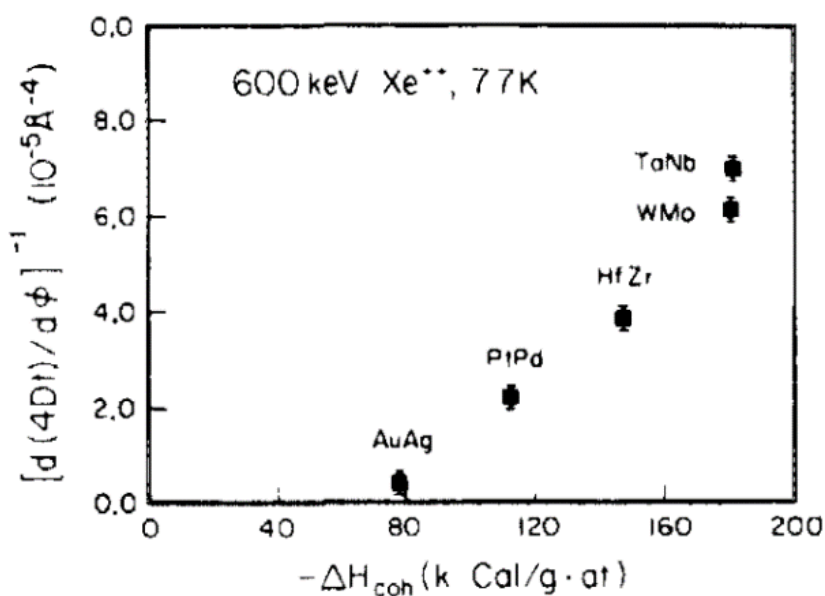


Figure 34 Correlation between mixing rate and average cohesive energy reproduced from [134]

2.8 TEM with in-situ Ion Beam

2.8.1 Introduction

Transmission Electron Microscopy (TEM) offers microscopists opportunities to observe and characterise microstructures at a high resolution[135]. Additional experimental parameters such as temperature, and atmosphere may be controlled in a TEM allowing the operator to investigate the formation and evolution of microstructures under such conditions. This provides insight into the atomistic processes at work.

There remain challenges in understanding the consequences of particle bombardment in materials research. As discussed in the ion-irradiation section of this chapter, materials that are exposed to ion irradiation undergo changes. Understanding these changes is of critical importance to many industrial and scientific areas including: the nuclear, semiconductor, space, and other irradiating environments. Whilst a TEM offers the ability to observe the end state of a materials exposure to radiation, as a sole tool they cannot monitor the processes as they occur. As such in-situ ion irradiation systems have been developed [15]. These systems are capable of irradiating TEM sized samples, such as thin films, but lack the ability to irradiate larger samples which cannot fit in a TEM holder.

2.8.2 Accelerating and Transporting Ions

Depending upon the area of research one intends to pursue, various choices of ion sources and accelerators exist which will be explored in the coming chapters. Ion sources and accelerators are generally used in vacuum systems to prevent the chances of air becoming ionised or blocking the beam path. Low energy light ions such as H or He scatter more readily when travelling. This results in a loss of ion beam flux the further they travel. As such having a compact system with a short flight tube is desirable when transporting low energy ions. Alternatively, an ion may be decelerated before encountering the specimen [136]. This allows the transportation with minimal scattering whilst allowing low energy impacts. Heavy ions are typically used at higher energy values to create many atomic displacements unless the study is focusing upon sputtering or surface implantation. They do not scatter as greatly

as low energy ions and can therefore be transported greater distances with minimal loss of flux.

Two or more ion sources are sometimes interfaced with the TEM. This allows for a greater variety of ion beams by allowing the possibility of multiple ion types and/or energies. The ion beam is usually selected via use of a magnet. A magnet can be set to bend the ion beam of appropriate energy and mass down the beam line, whether it be a single ion or a multiple ion system. Systems have been constructed which are able to switch between ion sources during experimentation [137]. To explore synergistic effects of multiple ions of differing mass interacting with materials it is necessary to attach two or more beamlines, that can be operated simultaneously, to a TEM. Ion sources can also be incorporated into large facilities external of TEM use. This allows ex-situ irradiation to take place on the beamlines. The University of Tokyo [138], Hokkaido University [139], National Institute for Materials Science [140], Argonne National Laboratory [141], Centre de Spectrometrie Nucleaire et de Spectrometrie de Masse [142], and Wuhan University [143] all incorporate multi beam facilities.

2.8.3 TEM Selection

The TEM selection for use with an in-situ ion beam must permit the normal conditions of the desired sample to be examined. Beyond this there are other issues that should be considered. Any TEM used must be able to be modified to allow extra components that transport the ions to the specimen position. There must also be adequate space to allow for ion beam current measurement devices, such as Faraday cups, as well as any required electrical feedthroughs. Ideally a TEM will include at least one vacuum port at or above the sample position to allow for easy interfacing of the ion beam. It is theoretically possible to have an ion beam come from underneath the sample, yet no facility currently implements this. A pole gap in the objective lens that is sufficiently wide to allow the ion beam to pass to the sample without degrading the microscope performance which may occur if the ion beam sputters the pole piece when struck and will also help interface a beamline in the case of a beam entering near sample level.

Some users may desire to create displacements using the electron beam of the microscope. If so, then a microscope that has a sufficient accelerating voltage to exceed the incident electron threshold energy of a given material should be selected. If it is desired that the electron beam does not create displacements, then having an accelerating voltage that is below the threshold should be selected. Most TEMs allow the accelerating voltage to be set to the needs of the user within a specified range.

2.8.4 Interfacing an ion beam with a TEM

There are three main ways in which an ion beam can be interfaced with a TEM [15]. The one employed in the first instruments built in the USA [144], [145] and France [146], is to bring the ion beam through the gap between the upper and lower pole pieces of the TEM objective lens. There are often ports present at this height in modern TEM columns, which are used for additional features such as X-ray diffraction. However, if the angle of the beam is not sufficient to have line of sight with the sample, which using these ports it may not be, there are several disadvantages. The sample will be required to tilt to a high angle to avoid a glancing incidence between the ion beam and the sample. This results in a reduced range of useable crystallographic orientation and increases the amount of material that the electron beam must pass through thus reducing the area thin enough to be electron transparent. The high angle of the specimen holder can also result in shadowing, shielding the specimen from the electron beam and potentially the ion beam. These disadvantages may be overcome by modifying the sample holder, to reduce the thickness and angle of the holders and clamps, and by appropriate sample preparation techniques.

The second technique is to use a deflection system within the TEM column. This technique uses electrostatic deflectors, rather than bending magnets, due to the space constraints within the TEM column. The MIAMI-1 facility originally used this system [147]. This technique can provide a high angle of incidence with the specimen. However, the construction and operation of the instrument becomes more difficult, these difficulties are expanded upon in the MIAMI upgrade results chapter. It also brings difficulty when servicing the system. Figure 35, reproduced from J. Hinks et al [147], shows the original MIAMI-1 deflection system.

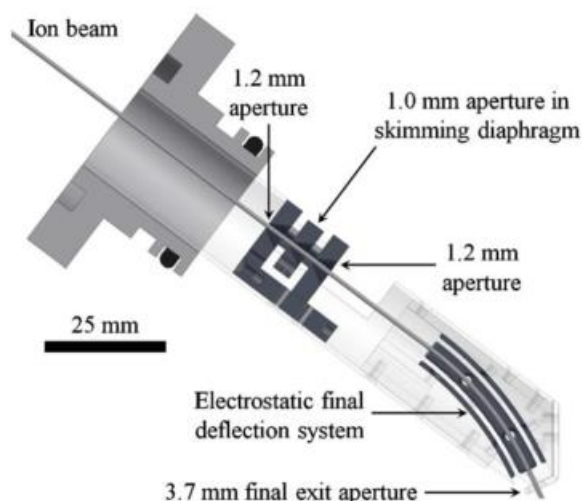


Figure 35 MIAMI 1 initial internal deflection device reproduced from J. Hinks et al [148]

The third approach is to bring the ion beam into the TEM at a high angle. To allow for direct line of sight with the sample it is sometimes necessary to modify the upper objective pole piece. This is dependent upon the internal geometry of the TEM being interfaced. When modifying the pole piece it is important to remember that it is easy to degrade the spatial resolution of the TEM [149]. These modifications often involve narrow bores or apertures which can limit the effectiveness of the deflection system on the ion beam line. On top of this the magnetic field of the microscope lenses and deflectors can interfere and deflect the incoming ion beam. This is particularly apparent when low energy light ions are used due to their tendency to be easily deflected which causes them to easily miss small apertures [15].

2.8.5 Ion Beam Dosimetry

To measure the flux of an ion beam a dosimetry device is required. Usually, a Faraday cup is employed. A Faraday cup is a conductive cup designed to capture electrons or ions in a vacuum. This results in a current which can be measured to derive a flux. These cups are sometimes designed to swing into position or may be attached to a sample holder.

However, using such methods requires the ion beam to no longer be striking the sample. Therefore, measurements cannot be made whilst experiments are ongoing. To resolve this, Faraday cups with exit apertures can be employed close to the sample [147]. These are known as Faraday skimmers. In order to avoid loss of secondary electrons the Faraday

skimmers are fitted with apertures with a negative electrical bias relative to the Faraday cup. Figure 36 reproduced from J. Hinks[147] shows a skimming aperture, labelled Ion beam skimming aperture. A more detailed skimming aperture overview can be found in the MIAMI-1 upgrade skimmer section.

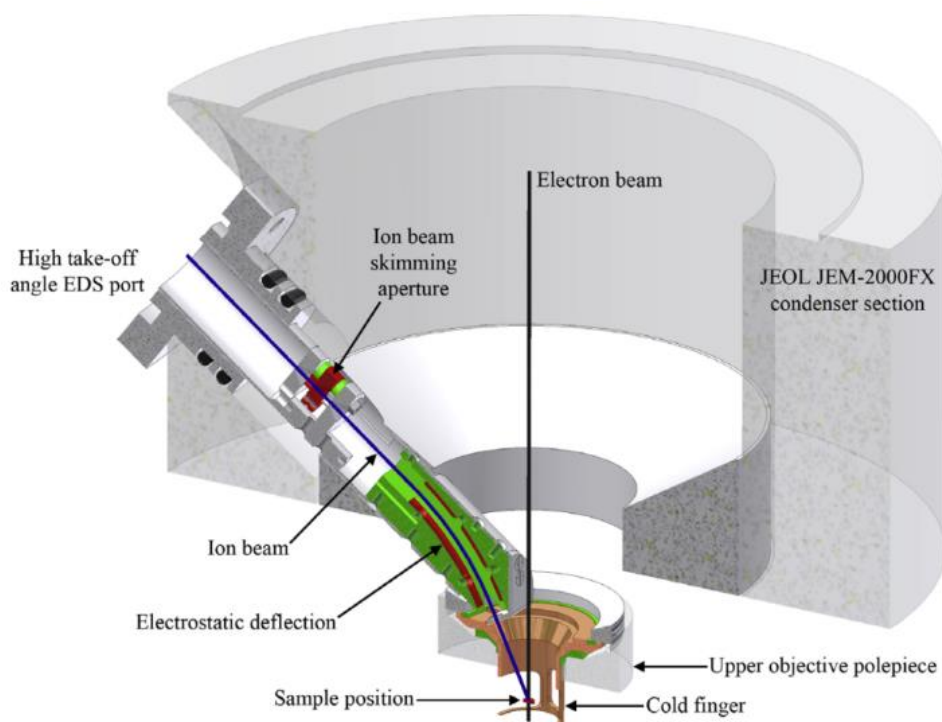


Figure 36 MIAMI 1 Ion Beam Skimming Dosimetry Device Reproduced From J. Hinks [15]

It is also possible to measure an ion beam flux via the use of aperture strips, which contain a variety of sized apertures [150], or insertable slits, which reshape the beam into a rectangular or oblong shape [139], placed along the beam line close to the sample. Another method is to use collection plates placed at the sample position which measure the current generated from the beam striking them[70]. By splitting the dosimetry devices into isolated quadrants it is also possible to use the devices to align the beam, each quadrants current can be measured to gain knowledge of where the beam is [70]. This is achieved by measuring the flux on each quadrant and deflecting the beam so that the flux is greatest where the operator wants the beam to travel.

2.8.6 Vibrational isolation

When connecting an ion beam line to a TEM mechanical vibrations can be induced from local sources of the beam line such as the vacuum systems[15]. These vibrations can impact the spatial resolution of the TEM. Efforts must therefore be made to isolate the vibrations from the TEM. The most widespread techniques used in the installation of TEMs is to place the instrument on cushioned feet and sand floors [143]. Other techniques also exist. Positioning the mechanical roughing pumps away from the microscope by approximately 10m has been shown to dramatically reduce vibrations [149] by increasing the distance that the vibrations must travel and allowing additional damping measures to be implemented in the space, thus increasing the damping effects. Placing the ion accelerator on a different floor is another method to achieve this [138][142][151][143]. The material choice and machining method of the connecting piece of the ion beam to the TEM also has an impact on the levels of mechanical vibrations that the TEM will endure[146]. Using bellows along the beam line can absorb some of the vibrations [151][152][153]. Increasing the mass of certain components so that they act as a damper for mechanical vibrations is another technique employed [143]. Changing the vacuum pumps also influences the level of vibrations by replacing larger pumps with smaller ones [143], using magnetically levitated turbo molecular pumps [140], or by using non-mechanical pumps [153].

2.8.7 Computational Control

To form, tune, and control an ion beam entering a TEM, computer systems are sometimes employed. For example, Hitachi developed a system in the 1980s which used an ion source that was capable of producing two species simultaneously which could be switched between using computer controls. The system used feedback from a skimming aperture to control relevant parameters of the beam line, via the use of a connected computer, and then switch between ion species [70]. Adding a computer control to a beam line allows the user to be isolated from the line when setting up and performing experiments which can be useful when dealing with hazardous materials.

2.9 SiC-Based Materials and Their Properties

2.9.1 Introduction

Silicon carbide is a potential material being explored as a cladding candidate and is used currently in TRISO fuel [154]–[156]. It is also being considered as a structural material for fusion applications [157]. This is due to many favourable properties of the material. These include a low neutron cross section, high thermal conductivity, and radiation resistance. Neutron-induced effects in high purity SiC, such as single crystal or produced using CVD (chemical vapour deposition) or CVI (chemical vapour infiltration), is different to that of lower purity forms. Significant impurity levels in the material has been shown to lead to unstable behaviour under neutron irradiation [158], [159]. Stoichiometric materials however, exhibit high radiation tolerance. The work undertaken in this report was conducted on ZrC and some have suggested replacing SiC with ZrC [160]–[164]. It is therefore important to summarise SiC and compare its properties to ZrC. Unless otherwise stated the materials discussed in this chapter will be stoichiometric.

2.9.2 Basic Properties and Structure

SiC exists in many different polytypes. There are 3 major polytypes relevant to the nuclear industry. They are β 3C, α 4H, and α 6H. Figure 37 reproduced from T.Ayalew [165] shows the different SiC polytypes, the 3C structure is the primary focus of this work. 3C SiC has a cubic zinc-blende structure and a space group of F43m.

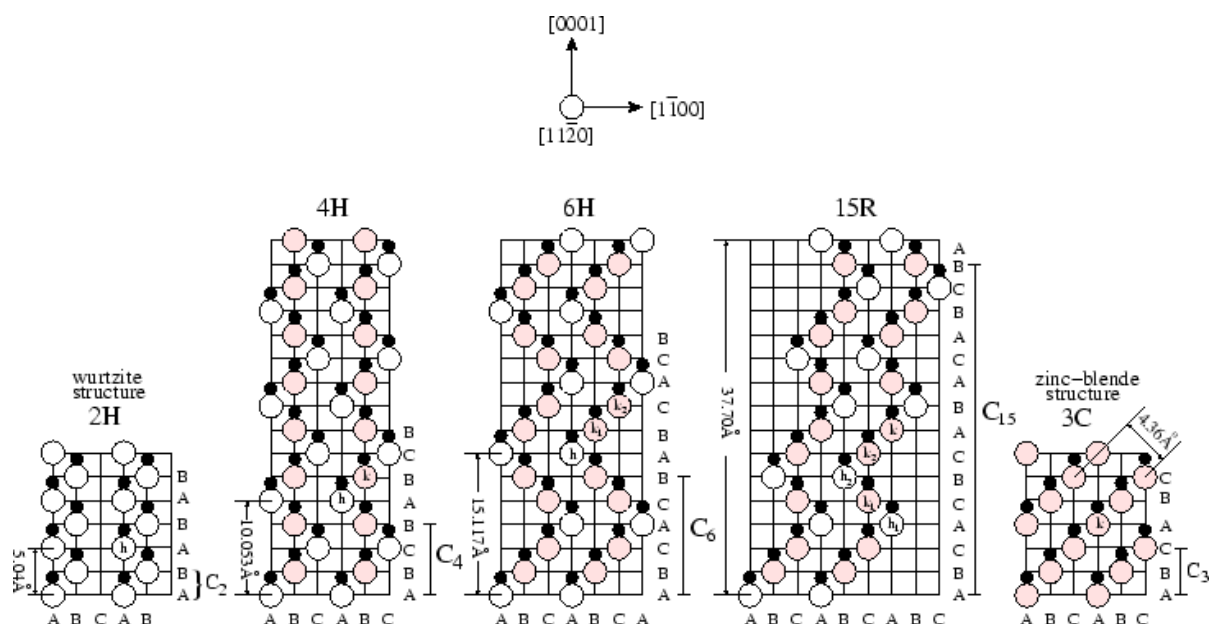


Figure 37 Different SiC Polytypes Showing the Configuration of 2H, 4H, 6H, 15R, and 3C reproduced from T.Ayalew [165]

The different polytypes of SiC have differing density and lattice spacing [166]. Table 2 SiC Density and Lattice Spacing for Three Common Polytypes shows some of these values.

Polytype	Density (g/cm ³)	Lattice spacing (nm)
β3C	3.214	0.43596
α4H	3.235	0.3076
α6H	3.211	0.308

Table 2 SiC Density and Lattice Spacing for Three Common Polytypes

SiC has a very high melting point and begins to decompose at 2700°C [167]. Figure 38 reproduced from Olesinski, R. W. et al.[168] shows the phase diagram for SiC showing how stoichiometric SiC is stable up to ~2545°C.

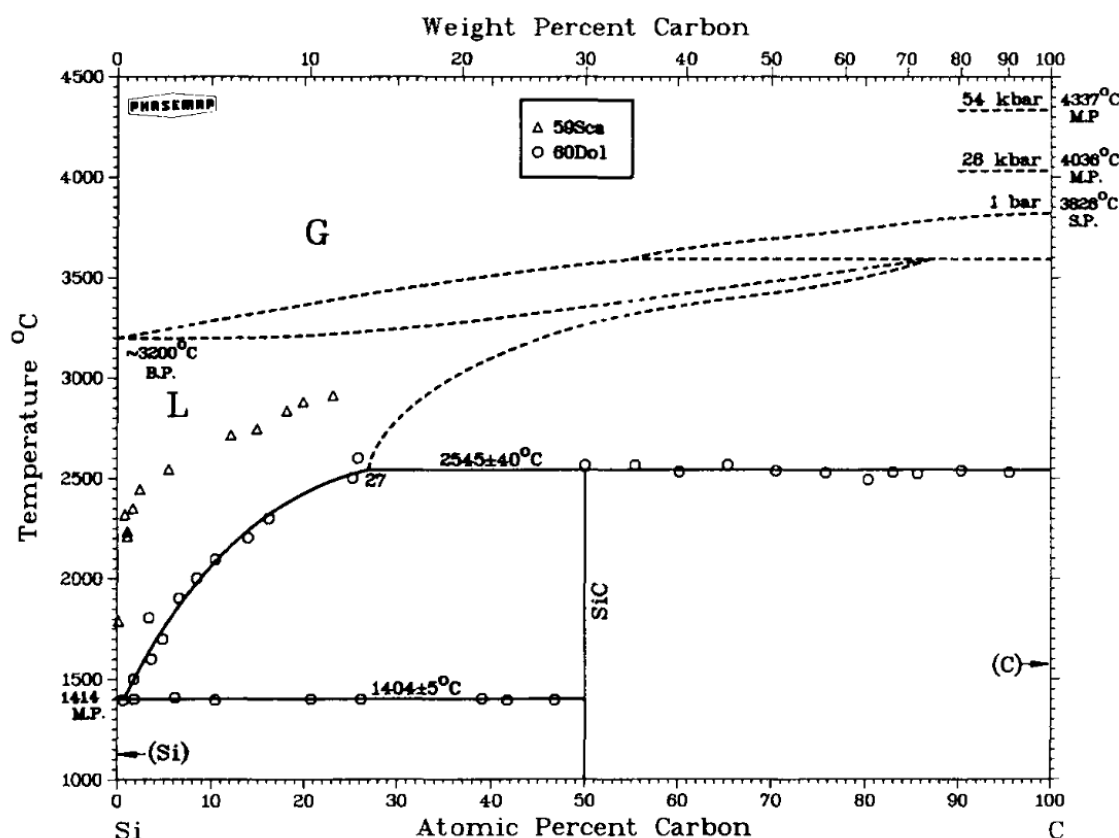


Figure 38 The Phase Diagram for SiC. reproduced from Olesinski, R. W. et al. [151]

2.9.3 Bonding

SiC bonding is largely covalent with a bonding energy of 12.58eV [169][166]. The covalent bonding is strong due to both atoms being relatively small and having a short bond length. The other type of bonding in SiC is ionic bonding. However these bonds are much weaker than the covalent ones[170].

2.9.4 Thermal Properties

SiC is considered to have favourable thermal properties relevant to the nuclear industry. Dependent upon the polytype of SiC its thermal properties differ. The thermal conductivity of α SiC is greater than that of β with a value of 41W/m $^\circ\text{C}$ compared to 25.5W/m $^\circ\text{C}$ at 20 $^\circ\text{C}$ [166]. This suggests in applications where heat transfer is desired α would be preferential to β . However, α SiC has a thermal expansion rate greater than β at $5.12 \times 10^{-6}/^\circ\text{C}$ vs $3.8 \times 10^{-6}/^\circ\text{C}$. at 20 $^\circ\text{C}$. This greater thermal expansion will likely cause stress upon any components in contact with the SiC. It should be noted that as temperature increases the thermal

expansion rate of SiC has been shown to decrease [171]. The thermal diffusivity of SiC decreases as the temperature increases, this means that at higher temperatures less thermal energy is diffused [172]–[174]. This is typical of non-metallic ceramics [175]. The specific heat capacity of SiC is greater than that of other refractory carbides and nitrides [155], [172]–[174], [176]–[178]. At temperatures below 200K the specific heat capacity of SiC rises greatly as temperature increases. At greater temperatures the increase is much slower. This has been demonstrated in both α [172], [174] and β [171], [176]. The relative stability of the specific heat capacity at higher temperatures is a useful trait in high temperature reactors as the energy transferred to the material will not cause high thermal fluctuations.

2.9.5 Mechanical Properties

The mechanical properties of silicon carbide vary depending upon the polytype, manufacturing method, purity, and porosity [179]. Amorphous SiC has been found to have an elastic modulus of ~ 200 GPa [179] whilst Chemical Vapour Infiltration (CVI) pure SiC has been found to have a value of 400 GPa [180] highlighting how great the mechanical changes can be. High purity dense SiC has been observed to have the greatest elastic modulus [155]. However, the polytype and grain size has not been shown to influence the modulus. A rise in temperature will lead to a decrease in the modulus value [107]. This indicates that if SiC amorphized under use in a reactor environment that the reduction in elastic modulus could lead to the material cracking and failing. Indeed Singh, G et al. found that SiC tubular specimens did crack when tested in a reactor environment [181].

SiC has a Poisson ratio, the deformation of a material in directions perpendicular to the loading, which varies wildly with the polytype, purity, porosity, and stoichiometry. A value of 0.13 was observed in β SiC with 6.35% free Si [182]. Values of 0.14 [155] - 0.2 are observed in sintered SiC [183] and 0.21 in reaction bonded SiC [184]. Whilst CVD SiC has a Poisson ratio of 0.22 [155]. The CVD SiC is representative of what is currently used in TRISO fuel. The 0.22 ratio is comparable to glass which has a ratio of 0.2-0.27 or cast iron 0.22-0.3 and indicates that the material should not greatly contract or expand when placed under lateral or longitudinal strain.

A study into the hoop strength of SiC/SiC tubular composites found that the hoop strength was reduced 10-60% under varying durations of coolant and neutron exposure [185]. The test was designed to simulate a PWR environment. Another study was conducted to simulate SiC triplex tubes under LWR conditions. It was found that the inner SiC layer failed a tensile test which led to extensive microcracks throughout the composite [186].

The changes of hoop stress and elastic modulus of SiC in reactor environments pose a challenge for the material in a structural capacity. Any SiC used within a reactor may need to be incorporated as a layer with another material, as is the case in TRISO, to minimise the stress and strain placed upon the material. Alternatives would be to use the material only in a capacity of low stress/strain or to reduce the workload by changing a reactor design, however both of these options seem limited.

2.9.6 Oxidation

Materials in a reactor may be exposed to oxygen either through contact with coolant or air. SiC has been shown to oxidise at high temperatures under various conditions [187]–[190]. SiC oxidation can be split into two regions. The active and passive regions. The passive region is a surface scale of SiO_2 that forms at high partial oxygen pressures and temperatures. This scale acts as a barrier layer and prevents further oxidation of the compound. Any impurities within the SiC will accelerate the oxidation process. Active regions appear when SiC is subjected to very high temperatures and a low partial pressure of oxygen. These regions are SiO and will form without the presence of the SiO_2 layer. It has been found that SiO_2 becomes soluble in water especially LWR conditions. This leads to mass loss of the SiC and in time could lead to the material dissolving as the oxide layer is removed, allowing further oxidation of the SiC which is then removed again, and so forth [191]. This effect could be countered by placing a barrier material between the SiC and coolant.

2.9.7 Chemical Properties

When in a reactor environment a material will be subject to various fission by-products and other elements which have the potential to chemically react with and alter the material. SiC is highly inert, and as such does not undergo chemical changes without a great amount of force. Additionally, SiC has low activation characteristics [179]. This property will allow for easy disposal when its core residence time has come to an end [160]. SiC has been shown to trap tritium on its surface [180][181]. It has also been shown that the tritium has low permeation, unlike metals [182]. Tritium permeation is a significant challenge in nuclear fusion applications. To meet regulation requirements, the amount of tritium permeation must be minimised [183].

SiC has been shown to be susceptible to Pd attack [192]. When used in TRISO fuels Pd has been observed penetrating the pyrolytic carbon (PyC) layer and reacting with the SiC causing significant corrosion. The level of corrosion is such that it is expected that Cs release would occur. Both Pd and Cs are by products of fission and need to be contained to prevent radiation leaks. It has also been seen that the amount of corrosion increases with temperature. With regards to Sr retention the breakthrough time in SiC has been observed as >70days at a temperature of 1400°C [192]. This is greater than PyC where Sr is much more readily released. This shows one of the reasons why a SiC layer is useful in TRISO. With Xe and Kr SiC has been demonstrated to be an effective barrier to release [193]. Overall, SiC fission product retention is favourable, with the notable exception of its Pd corrosion behaviour.

2.9.8 Neutron Irradiation

SiC has been shown to be stable under high irradiation doses, with the notable exception of swelling of the material [112], [194]–[196]. It has been indicated in previous work that the swelling of SiC occurs due to the formation of point defects [155] and the material becoming amorphous [107]. The amount of swelling that occurs in amorphized SiC has been reported to be 4.42% volumetric swelling at 2×10^{22} neutrons/cm² [197]. There is evidence that the density of the amorphized SiC is dependent on the irradiation conditions such as dose and temperature [110].

At temperatures less than several hundred Kelvin the microstructure of neutron irradiated SiC appears to contain “black spots” when viewed in a TEM. It has been speculated that these spots are small clusters of self-interstitial atoms in various indeterminate conditions [155]. At temperatures less than 423K irradiation-produced defects can cause the crystal to become amorphous [110], [198], [199]. For temperatures greater than the critical amorphization 423K the swelling of SiC increases logarithmically with dose until saturation is achieved [155]. The swelling in SiC is highly temperature dependant. Figure 39 reproduced from report by Snead et al. [155] shows how saturation values of swelling are approximately five times higher at 473K, in comparison to 1073K. This work was for HFIR (High Flux Isotope Reactor) neutron irradiated CVD SiC manufactured by Rohm and Hass.

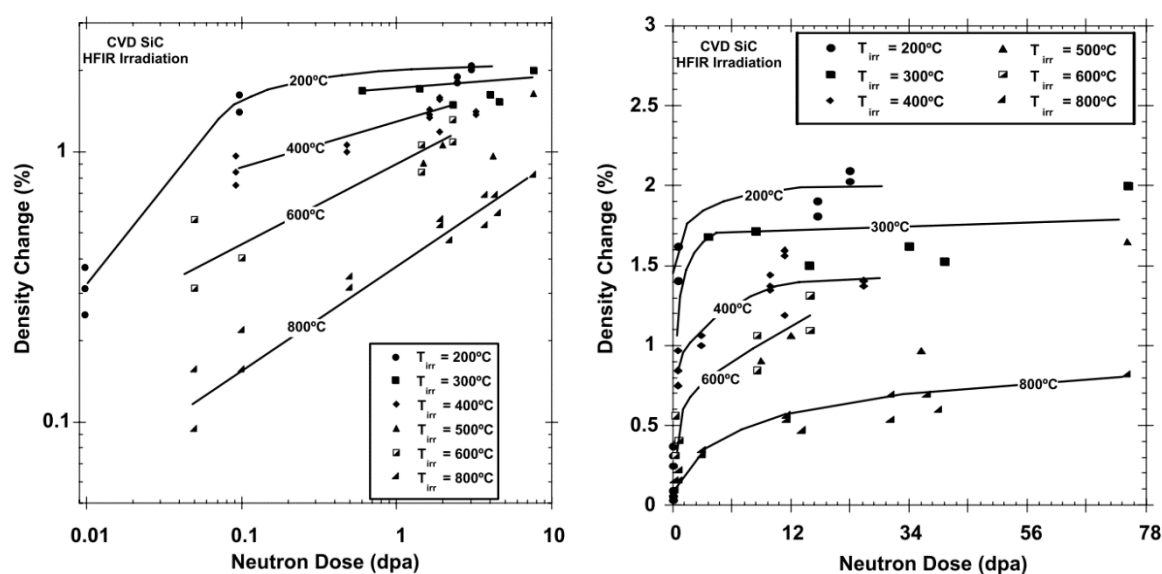


Figure 39 Density Changes in CVD SiC due to Neutron Irradiation at Various Temperatures, Highlighting how a Greater Density Change is Observed at Lower Temperatures,. Reproduced From Report by Snead et al. [155]

Fully crystallized SiC ceramics and composites have been shown to undergo radiation induced swelling [56][140]. This swelling occurs soon after irradiation has begun. The swelling saturates typically before a few dpa is achieved [56]. At higher temperatures the swelling is slower ~1% at 600°C and >2% at 300°C [56]. The reduced swelling with increased temperature is attributed to the recombination of C and Si Frenkel pair defects as well as

the migration of C and Si interstitials [200]. It should also be noted that swelling saturates at a relatively low value. At a few DPA the swelling has found its saturation value [155].

Because of the swelling an accumulation of matrix defects occurs. This leads to the lower conductivity previously discussed. It has also been predicted that the swelling will lead to substantial tensile stress on the inner surface of the cladding wall [187].

The swelling is not considered in itself to create a limit in the operating temperature of a nuclear reactor [201]. However the swelling has been shown to lead to an increased elastic strain within a material [202]. This increase whilst relatively small could lead to early life failure of the material. The strain reduces the Young's Modulus at low temperatures. As the temperature increases the Young's Modulus increases until at a temperature of 1273K or higher is achieved. At this point the initial reduction is negligible [155].

At high temperatures, interstitial Frank fault loops become the dominant defect in SiC [196], [203]. Frank fault loops have also been observed at lower temperature neutron irradiation at very high doses.

2.9.9 Ion Irradiation

A large amount of work has been, and continues to be, conducted on SiC response to ion irradiation. When exposed to 70keV He ions, SiC has been shown to amorphise at 1DPA at room temperature [204]. Using a combination of near edge X-ray absorption fine structure spectroscopy, Raman spectroscopy, and TEM techniques Liu et al discovered that during 70keV He ion irradiation the crystalline bonds of the Si-C decompose and Si-Si as well as C-C bonds form in their place. Along with this a large number of Si vacancies were discovered. No bubble formation was discovered at room temperature irradiations. However, at elevated temperatures bubble formation has been observed in pure SiC and its composites.

S. Kondo et al. irradiated 3C-SiC with 5.1 MeV of Si₂ ions to gain an understanding of its microstructural changes [201]. They found that at lower temperatures (280°C) linear swelling was approximately 5 times greater than higher temperatures (1000°C). This was proposed to be due to 2D defect clusters, which at elevated temperatures are more mobile

and able to reach defect sinks. This demonstrates that at low temperatures where He bubble formation will not occur SiC is still prone to swelling from defect production.

2.9.10 Current Uses

Currently SiC is used as part of TRISO (Tristructural-isotropic) fuel particles. TRISO fuel was developed initially for use in HTGR (High Temperature Gas Reactors) [205]. It has since been used in prototype reactors in China and Japan [206]–[208]. TRISO fuel consists of five regions, as depicted in Figure 40 reproduced from Nairi, B et al [209]. The inner most region is a fuel pellet consisting of a radioactive element, typically uranium or plutonium. Surrounding the fuel is a porous carbon layer which acts to dampen recoiling fission particles and store any excess gas pressure that may build up [156]. Around this there are three layers which consist of an inner pyrolytic carbon layer a layer of SiC and an outer pyrolytic carbon layer. The SiC layer provides both mechanical strength and acts as a barrier for diffusing fission products [210]. The pyrolytic layers act to protect the SiC layer from chemical reactions. There remain many challenges facing TRISO fuels which exist outside of the scope of this work, if the reader is interested the author recommends the review by J. Powers et al [205].

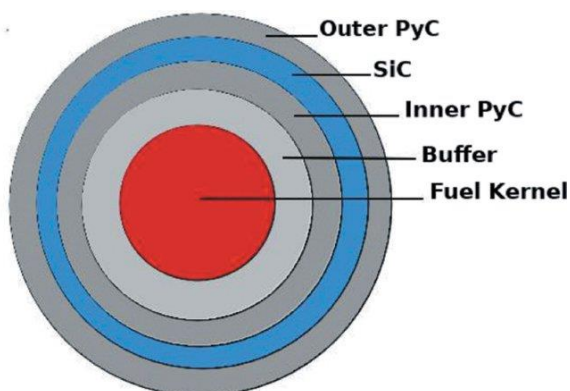


Figure 40 TRISO geometry reproduced from Nairi, B et al. [209]

2.9.11 SiC Fabrication

One of the drawbacks of SiC as a material for use in industry has been the poor ability to manufacture pure SiC. As discussed earlier, impurities in SiC vastly change the properties of the material. Traditional manufacturing techniques have introduced these impurities. SiC was first fabricated by Acheson in 1892 [211]. This was achieved by coking SiO₂. SiC formed

via this production is known under the trade name Carborundum. Since this time various other methods have been developed for fabricating SiC. These include sintering, gas phase reaction, polymer pyrolysis, and direct conversion [155]. CVD is a gas phase reaction technique which is most commonly used to fabricate high purity stoichiometric SiC [155], [212]. The CVD process works by depositing material, in a vapour phase, upon a substrate via chemical decomposition [213]. SiC whiskers are fabricated using polymer pyrolysis techniques [214]. This technique involves converting an organometallic polymer to an inorganic substance via chemical processing. SiC can also be reaction bonded, a direct conversion technique, which can result in a material with various crystal structures separated into different grains [215]. Due to the non-uniform nature of the crystal structure this approach is not favoured for reactor materials as the properties of the SiC varies with different polytypes.

2.9.12 SiC as an ATF (Accident Tolerant Fuel)

SiC has been suggested for use as an ATF [27], [202], [216], [217]. In accident situations such as LOCA or a LOFA (Loss of Flow Accident) the temperature of a reactor can rise to levels above the intended design limits as seen in the Fukushima incident 2011. This can cause a material to be damaged beyond repair. Irradiation creep was studied in CVD SiC. The SiC exhibited weak temperature dependence at <0.7 dpa at temperatures between 400 to 1030°C [87]. This would indicate that SiC would resist burst failure which occurred in Fukushima. The oxidation resistance of SiC also allows for the material to withstand high temperature steam environments that can arise as a result of a LOFA. β SiC-based cladding has been shown to keep its strength and not creep up to 1300°C [218][219]. SiC has also been observed to have a low decay heat [220][221]. These properties ensure that in the case of an accident where the temperature rises above the normal operating temperature the material will not deform or move.

2.9.13 Ceramic Matrix Composite SiC

CMCs (Ceramic Matrix Composites) are a group of materials which consist of ceramic fibres embedded in a ceramic matrix. One of the materials considered as a cladding candidate is SiC CMC. SiC CMC properties make it an attractive choice for cladding. The material has

minimal chemical activity, reasonable thermal conductivity, high strength at high temperatures, and decomposes at 2700°C [167]. When compared to zirconium SiC CMC show little chemical reaction at elevated temperatures. Before irradiation SiC CMC has a greater conductivity than zirconium. However, extended irradiation leads to lower conductivity, approximately a half to a third of that of zirconium. This can be mitigated somewhat by optimising the material design and thickness of the material. SiC CMC is made up of SiC fibres which have a very high modulus which leads to the materials strength. The soft bonding interface layer between the matrix and the fibres allows for cracking in the matrix and stress distribution to the included fibres [167]. This property increases the ductility of the material compared to a pure ceramic. The weak interface is not compatible with creep and fatigue resistance at high temperature, where strong interfaces are required to resist the nucleation and growth of cavities [222].

2.9.14 SiC future recommendations

One of the problems facing SiC as a fuel cladding is its swelling. The swelling of SiC will inevitably lead to extra stress being placed on surrounding materials. If SiC and its composites could be developed to have lots of areas of defect sinks some of the defects may be arrested leading to less swelling. Another area of interest would be to observe how well amorphous SiC retains its mechanical strength, as well as its fission product retention. As SiC amorphises at ~1DPA a lack of understanding these properties could limit the life cycle of a cladding material. Corrosion from Pd attacks is also an area of concern and an interesting study could be conducted using an alternative barrier layer than PyC to better contain the Pd fission products.

2.10 Zirconium Carbide

2.10.1 Introduction

Zirconium Carbide is of interest to the nuclear industry due to the material possessing both metallic and ceramic like properties [164], [223]. ZrC was first proposed as a nuclear fuel coating in the 1960s as part of the Rover Nuclear Engine for Rocket Vehicle Applications (NERVA) project [224]. One noticeable advantage of ZrC discovered during the NERVA project was that the material does not readily react with H_2 , a feature which may be advantageous in reactors. It was ultimately selected as the coating material of the nuclear rocket reactor, although ultimately the rockets were never flown as the project was scrapped. During the project ZrC was found to have poor thermal stress resistance when rapid fluxes of heat were applied [225]. In more recent times ZrC is once again being considered as a material for nuclear reactors such as the HTGR [207]. Outlined in this chapter are the properties of ZrC.

2.10.2 Basic Properties and Structure

ZrC has a high melting temperature of $3420^{\circ}C$ [226], high thermal conductivity [227], and a low neutron absorption cross section [228]. It should be noted that ZrC eutectically melts with C at $2850^{\circ}C$, a value that should be considered when combining with a C layer such as in TRISO fuel [226]. Figure 41 reproduced from Storm [226] shows the phase diagram for ZrC.

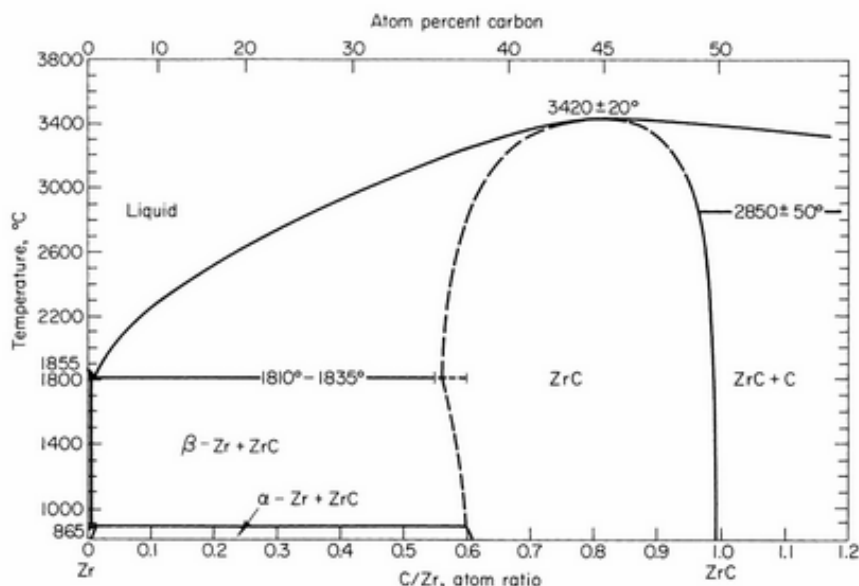


Figure 41 ZrC Phase Diagram reproduced from E.K. Storms [226]

The properties of ZrC are dependent upon the degree of stoichiometry. ZrC can exist in a range of sub-stoichiometric compositions which can lead to the presence of graphitic carbon phases within a material, ultimately affecting the materials properties [164], [226], [227]. The density of stoichiometric ZrC is 6.61 g/cm³ [226]. There is only one stable structure of ZrC which is mono-carbide with the carbon atoms located at octahedral sites stoichiometrically as seen in Figure 42[164]. The crystal structure is the same as NaCl which is close packed FCC B1 with Fm3m space group.

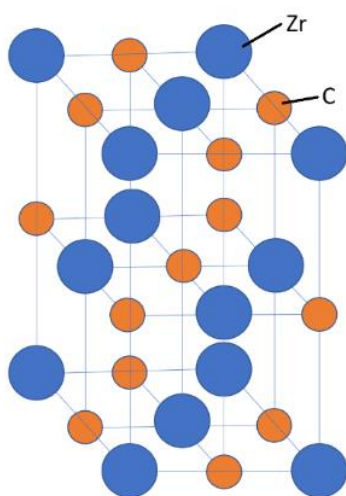


Figure 42 ZrC FCC Crystal Structure

The lattice parameter is significantly dependent upon composition [226]. As the C/Zr ratio increases so does the lattice parameter [164]. This peaks at $\text{ZrC}^{0.83}$ with a lattice parameter of $\sim 0.4702\text{nm}$ [229] beyond which the parameter begins to decrease. When C is greater than Zr, i.e. $\text{ZrC}^{>1.0}$, the lattice parameter remains at the stoichiometric value [230]. That value is $\sim 0.4698\text{nm}$ [164]. As would be expected a change within the lattice parameter will result in a change of the materials density. The smaller lattice parameter results in a higher density [164]. It is likely that the change in lattice parameter can be correlated to other changes observed in the properties of a material with regards to stoichiometry discussed later in this chapter.

2.10.3 Bonding

There are three types of bonds holding the ZrC atoms in the lattice [226]. These bonds are ionic, covalent, and metallic [164]. The bonds in the ZrC (100) and (110) planes are predominantly polar covalent bonded, a type of bond where a pair of electrons is unequally shared between 2 atoms, whilst ZrC (111) is a mixture of metallic and polar covalent bonding [231]. It is reported that the ZrC properties are dominated by strong covalent bonds with the metallic bonds assisting [232]. ZrC bonding energy has been approximated to be 5.812eV [226] which is higher than that of SiC (4.677eV [164]). ZrC favourable thermal and mechanical properties are often attributed to this bonding characteristic.

2.10.4 Thermal properties

As stated previously ZrC has favourable thermal conductivity. However the thermal conductivity of ZrC differs from many other metals and ceramics [164]. As the temperature of the material increases so too does the thermal conductivity [233], [234]. In non-metallic ceramics the thermal conductivity typically decreases greatly as temperature increases and in simple metals the conductivity decreases much more gradually. The electrical resistance of ZrC has also been shown to increase with temperature, due to an increased scattering of electrons, although it does so at a slower rate than a simple metal. The thermal expansion of ZrC happens linearly with increasing temperatures [235]–[237] with $\sim 1.5\%$ expansion at $\sim 2250\text{K}$. The thermal conductivity and electrical resistance are also affected by the stoichiometry of the material. A greater conductivity and lower electrical resistance is

observed for stoichiometric ZrC compared to sub-stoichiometric ZrC [164]. Decreasing the C content has been attributed to an increase in the scattering of conducting photons and electrons by vacancies which is believed to cause the reduction in thermal conduction [233]. Having ZrC as close to stoichiometric as possible is clearly the most desirable state. Due to the thermal conduction properties being favourable at high temperatures, as well as the high melting temperature, ZrC would appear to be a favourable choice for high temperature reactor environments. However, as the properties of ZrC become less favourable in a non-stoichiometric state RIS will need to be minimised. Of course, there remain other characteristics to discuss which will be outlined in the remainder of this chapter.

2.10.5 Mechanical Properties

Like most metal carbides ZrC is a hard material [164], [226]. ZrC at room temperature has a Young's modulus of 406 GPa and a Poisson's ratio of 0.25 [238]. The favourable hardness values are due to the covalent bonds of ZrC. These bonds reduce plastic deformation and under enough load the material will instead brittle fail [239].

2.10.6 Oxidation

ZrC begins to oxidize at relatively low temperatures relevant to the nuclear industry. Oxidisation initiates in air at 500-900 K [227]. The oxidisation process results in the formation of a ZrO_2 layer. This oxide layer will act to impair the further oxidisation of ZrC. However when this scaling reaches a thickness of 2-4 μm it begins to crack as a result of the different thermal expansion coefficients of the layers [240]. This results in oxygen once again reaching the ZrC layer creating a further ZrO_2 layer. This process repeats itself resulting in a linear oxidisation rate over time. Zr will oxidise at temperatures <973 K which is insufficient to oxidise C. This leads to the C being liberated from the compound. The C may then precipitate at the ZrC ZrO_2 interface [240]–[242]. Alternatively the C may join the ZrO_2 lattice [227]. At higher temperatures C is more readily oxidised. This results in the formation of CO and CO_2 gases. At 1473-1773K the ZrO_2 layer will be completely C free [227]. The readiness of ZrC to oxidise presents a serious challenge for its use in a reactor environment, although this may be overcome with the use of other materials as a barrier preventing O contact.

2.10.7 Chemical Properties

It is important to understand how ZrC reacts with fission by-products. To prevent fission-by-product interaction a barrier layer can be placed over the ZrC like in TRISO fuel.

ZrC has a high resistance to Pd attack [243]. This is especially important as Pd forms during the fission process. It has been shown that ZrC is comparable to SiC, which is currently used in TRISO fuels, in regards to Cs diffusion barriers [244]. Cs is another fission by-product along with Sr that needs to be retained as it is a source of gamma radiation. ZrC has good retention of Sr but it is not as good as other fission by-products [245].

Xe is also a fission by-product. Xe acts as a poison in the reactor process, with large quantities slowing and even possibly stalling a fission reactor. Xe can migrate and form bubbles which will affect a materials performance. It can also then decay to Cs. Xe diffusion into ZrC varies with the carbon content of the material [246]. With stoichiometric ZrC Xe diffusion is consistent with a covalent bonding model.

Data on other fission by-products is minimal. Whilst efforts have been made to discover ZrC Ag retention [247] there is not enough information in the literature to state its retention values. Little data exists on Eu and Ce retention of ZrC although Minato et al. found fractional releases when annealing at 1800°C for 3000 hours [210]. Ogawa et al. found that Ru Ba and Nb have limited diffusion within ZrC [248]. However, Ru was found to have penetrated to ~30µm.

Overall ZrC has been found to be an effective barrier against fission by-products, yet some questions remain about its effectiveness with regards to certain elements highlighted above.

2.10.8 Neutron Irradiation

Limited data exists in the literature regarding the effect of irradiation on ZrC when compared to materials such as Zircalloy, SiC, or W [164]. In 2010 Snead et al. [160] reviewed the available literature and in 2013 Katoh et al. [164] also reviewed the available literature. Their findings along with some more recent reports are reviewed here.

Three main studies have been conducted on neutron irradiated ZrC [160], [249], [250]. During neutron irradiation ZrC was found to initially swell, peaking at a 3% volume increase at $\sim 2 \times 10^{21}$ neutrons/cm², before beginning to reduce in volume with extended doses. Keilholtz et al. [250] found that less than 50% of the volumetric swelling was due to lattice parameter increases. Therefore, the bulk of the swelling was to be accounted for by either the formation of precipitates or by He bubbles within the materials grains. However, Keilholtz et al. noted that He bubble formation would only account for $\sim 15\%$ of the observed swelling. It is probable that non-bubble defect accumulation accounts for the rest of the observed swelling. Snead et al. [160] found that under fast neutron irradiation the dominant defects formed were loops. At 660°C these loops were of an unidentified type and existed alongside black dot damage. At 1023-1260°C the loops were Frank loops and at 1496°C prismatic loops. This would suggest that defects are thermally mobile and agglomerate into larger loops as temperature increases.

2.10.9 Ion Irradiation

ZrC irradiation response has also been studied using protons [161], [251]–[253], krypton ions [163], [254], and gold ions [223], [255]–[257].

In the case of protons Gan et al. irradiated ZrC at 800°C up to 1.8 DPA [161]. They observed under TEM analysis that as a result of irradiation small faulted loops had emerged with an average size of 7.2nm and a density of $4.2 \times 10^{16} \text{cm}^{-3}$. They did not detect any voids or amorphization. Yang et al. (2008) irradiated ZrC at 800°C up to 0.7 DPA and then furthered it to 1.5 DPA [252]. They analysed the material post irradiation using SEM (Scanning Electron Microscopy) and discovered that an oxide layer had formed that was $\sim 350\text{nm}$ thick. Further analysis via TEM discovered faulted loops at both 0.7 and 1.5 DPA. It was noted that at the

higher DPA value the loops had grown in size and density. This matches the observations of Gan et al. and of Snead et al. Yang et al. (2014) irradiated ZrC with various C/Zr ratios from 0.8-1.2 at 1125°C to 2 DPA [253]. Once again, the predominant defects were loops. It was observed that these loops were larger in size at higher C/Zr ratios. The higher ratios also formed graphite precipitates. At these precipitates the dislocation density was greater. This may be due to the precipitates acting as a C knock-on source for interstitial defects. As with the neutron case under proton irradiation the ZrC lattice parameter increases [252], which in turn contributes to material swelling.

Ulmer et al. conducted a series of experiments using Kr ions at various temperatures with 2 C/Zr ratios of 0.8 and 0.9 [163]. At 50 K they observed using a TEM no damage until 0.6 DPA when black dot damage began to manifest. These increased swiftly up to ~3 DPA when the rate slowed. At 6 DPA the defect density appeared to stabilize. All of the defects were stable. This would support the theory from the work of Snead et al. [160] that the defects are thermally mobile with RIS playing little to no part. The further experiments conducted by Ulmer et al. strengthen this argument. With higher temperatures (673 K) the threshold of damage was lowered to 0.4 DPA and dislocation loops begin to form at higher DPAs, 3.9DPA at 673 K and 1.3 DPA at 1073 K. The later of these values matches well with the proton and neutron values discussed earlier, which suggests that the use of Kr ions to simulate neutron damage production is valid. Another important observation from Ulmer et al. was that no amorphization was observed even at 12.6 DPA 50 K. Indicating ZrC high resistance to amorphization.

Several experiments involving Au ions have been conducted at the CSNSM facility [223], [255]–[257]. Unfortunately, the DPA value has not been recorded in these experiments. The samples were also porous and partially oxidized. However, they also observed the defect production observed in the other experiments.

Taubin et al. neutron irradiated ZrC, to a flux of $4 \times 10^{16} \text{ cm}^{-2}$ and temperature up to 700K, to discover any thermal properties change and discovered none [258] whereas Snead et al. found minor degradation when irradiating with fast neutrons in the dose and temperature

range of $1\text{--}10 \times 10^{25} \text{ N/m}^2$ ($E > 0.1 \text{ MeV}$) and $635\text{--}1480 \text{ }^\circ\text{C}$ [160]. This is important as one of the main attractions of ZrC is its favourable thermal properties.

Irradiation has also been shown to increase ZrC hardness value increasing by $\sim 9\%$ at 2 DPA and $\sim 68\%$ at 6 DPA [164].

Overall ZrC appears to be a good candidate material to withstand radiation in a fission reactor. However, it suffers from swelling and there is a lack of understanding of the exact defects that form. Further study is needed and it is was to gain a fundamental understanding of radiation damage in ZrC that the work reported later in this thesis was undertaken.

2.10.10 ZrC Fabrication

There are various methods by which ZrC may be fabricated [164]. The method employed will affect the characteristics of the material. This is due to differing methods producing differing chemical compositions, microstructures, and impurities. One method of fabrication is by carbothermic reactions [259]. This method relies upon the reduction of O in ZrO_2 via the use of C as the reducing agent. The ZrO_2 and C are heated to high temperatures at which point a chemical reaction occurs resulting in the creation of ZrC, CO, and CO_2 . The literature contains conflicting reports on the temperature of the reaction, 1600°C [259], 1800°C [164], [226], and $1900\text{--}2100^\circ\text{C}$ [260]. In order to fabricate purer ZrC via this method repeated cycles are required resulting in a long process time of 16-24 hours. The process must also be conducted in either an inert gas or vacuum environment in order to prevent oxidation occurring. The resulting ZrC from this process is in powder form. The powder form is used as an abrasive. In order to create a bulk material, the powder is then sintered.

Another way in which ZrC can be fabricated is via the use of solution based processing [261]. This process involves a metal oxide being refluxed with acetylacetone. This creates a metal-organic-precursor which is then hydrolysed via the introduction of water. The solvent is then evaporated leading to a powder. This powder is then heat treated at temperatures close to 1500°C . It is then possible to sinter into bulk form. However, the compounds produced via

this method have been shown to include C and O impurities in the crystal lattice. These could be removed with further heat treatment in temperatures in excess of 1600°C.

ZrC can also be fabricated as a coating via CVD [262]. This method involves a Zr metal sponge being heated and having a halide gas passed over it. This causes a chemical reaction resulting in the creation of zirconium halide. The zirconium halide is then reacted with a high-carbon-content hydro-carbon source, commonly CH₄. This creates a gaseous ZrC which is then deposited upon a substrate. This method has been shown to produce high purity ZrC and is most often used for nuclear fuel applications.

2.10.11 ZrC as an ATF

As mentioned previously ZrC has been shown to oxidise readily and convert to ZrO₂, which caused the accident at Fukushima. Therefore, an additional layer should be considered to prevent ZrC from reaching oxidising compounds, such as the case of TRISO fuel. In the case of an accident such as a LOCA, a barrier material may thermally expand at a different rate than the ZrC layer potentially causing cracks and exposure to O. It is therefore very important that any material choice is well considered and understood.

2.10.12 ZrC future recommendations

There remain questions on how damage evolution will occur in ZrC with heavy ions other than Kr. It would be of interest to compare an ion such as Xe to the neutron case. Despite Keilholtz et al. [250] postulating upon the impact of He bubbles on volumetric swelling there is a gap in the literature regarding them. It would therefore be an interesting study to implant He ions into ZrC and observe the bubble formation process. There also exists a lack of data on ZrC nano particles. All irradiation experiments on ZrC conducted prior to this work have been on thin films or bulk materials. As nano-particles have been shown to react differently to thin films and bulk in other materials, this remains a gap in understanding[73].

2.11 The use of nanomaterials

2.11.1 Introduction

One of the best ways to improve the radiation resistance of a material is to improve its recovery rate. This can be achieved by increasing defect mobility or increasing the number of defect sinks. As defect mobility is largely dependent upon variables that are set by the environment a material is set in i.e., temperature and dose rate, improving the number of defect sinks is the main way to improve recovery rate. This can be done by introducing a larger number of grain boundaries[263]–[265] or by increasing the surface area to volume ratio [73][266], [267]. Nanoporous materials are ones that have been designed to have large networks of nanopores throughout the material leaving the actual solid to be a series of connected ligaments similar to a sponge. These materials have a very large surface to volume ratio and are therefore seen to have potential in the nuclear industry[40], [73], [268], [269]. The free surfaces facing the open pores of a nanoporous material acts as an unsaturable defect sink. The pores can also act as areas to accommodate gas which can be produced during the fission process in fuels.

2.11.2 Sample Preparation

One of the struggles for in-situ TEM work is that nanoporous materials remain difficult to fabricate into a sample thin enough to observe whilst remaining nanoporous. Therefore, in order to study these materials nanoparticles and nanowires are used as a substitute[270], [271]. These particles have a large surface area to volume ratio whilst also being small enough for easy viewing in a TEM.

2.11.3 Defect Accumulation

It has been observed that nanoparticles are more resistant to black spot defects than thin films in W [272] and American Iron and Steel Institute (AISI) 316 [270]. As black spot damage has been shown to contribute to the swelling of bulk materials [273] these findings support the narrative that nanomaterials will be resistant to swelling. In the case of 4H SiC, a material prone to irradiation swelling, Nono-Wires (NW) were seen to swell less when compared to thin films. The NWs were irradiated simultaneously alongside SiC thin foils using 6 keV He ions at temperatures between 100 and 400 K and doses up to 50 dpa.

Relatively-low swelling ($\sim 8\%$) due to amorphisation was detected in the NWs compared to the foils ($\sim 14\%$) irradiated at room temperature[274].

Nanoparticles have also been shown to have a high tolerance to He bubble swelling. Due to the increase in diffusivity to the material interfaces He bubbles form less and are limited in their size[275]. For example, when comparing W Nanoparticles to thin films it was found that at 750°C bubbles were found in both the thin films and the nanoparticles but in the latter they were larger with a lower areal density compared to areas of the foil with thickness corresponding to an equivalent volume of material[272]. This is also true in the case of voids which is another contributing factor towards swelling.

One of the critical features of the radiation tolerance of a nanomaterial is its size[276], [277]. At smaller sizes, $\sim <5\text{nm}$, materials are prone to break apart under ion bombardment with energies great enough to penetrate the particle. At larger sizes, $\sim >1,000\text{ nm}$, defect accumulation can match that of bulk materials. It is therefore important that the synthesized material size be taken into account.

The large free surface area of nanomaterials is also thought to lower the thermal conductivity[278]. This may give rise to higher local temperatures from thermal spikes which in turn will enhance defect mobility. Cascade development is also thought to play a role in this enhancement. In a bulk material a cascade is free to expand as it travels. In the case of nanomaterials, the cascade would quickly reach the end of the material preventing or decreasing further damage.

2.11.4 Amorphization Resistance

Nanomaterials have also been observed to have a higher amorphization resistance than their thin film and bulk counterparts [279], [280]. For example, in 4H SiC a relatively-high critical dose for amorphisation (5 dpa) was observed in NWs for irradiations below room temperature compared to thin foils (0.7 dpa). Amorphisation was also completely avoided for NWs irradiated above 200 K – lower than the critical temperature in the foils which was $\sim 300\text{ K}$ [274]. Due to the reduced dimensions in a nanomaterial, energy dispersion from ion impacts is reduced. This leads to reduced defect production compared to bulk materials.

This difference in defect production is believed to play a part in the amorphization resistance. Further to this the proximity of defects to sinks will lead to increased recombination and reduced accumulation slowing the rate of amorphization.

2.11.5 Mechanical Properties

Whilst nanomaterials have increased resistance to radiation damage the materials mechanical properties should also be considered. In the case of nanoporous materials, the mechanical properties are often weakened. As a result, using the material in a structural capacity, i.e., in the use of a pressure vessel, is not feasible. However, if the material is incorporated as a barrier layer, where little to no mechanical stress is placed upon it, the material remains a useful resistance layer.

2.11.6 Conclusions

As a whole nanoparticles have been observed to have greater resistance to black spot damage, bubble formation, extended defects, and amorphization. The biggest challenge facing their use is their mechanical properties. There also remains questions regarding the change in defect production and mobilisation in specific materials. This work hopes to gain an insight into answering some of these questions regarding ZrC.

3 Experimental Procedure

3.1 Introduction

When conducting experiments on ZrC microparticles and nanoparticles, laid out in the results chapters of this thesis, various techniques and calculations were performed which are outlined in the following chapter.

3.2 Sample Preparation

For a sample to be electron transparent it is generally necessary to reduce the thickness to less than 100nm, although this thickness depends upon the Z value of the sample and the electron energies being used in the TEM. Unprocessed samples are typically greater than 100nm thick or in a form that cannot easily be mounted to the specimen rod for viewing in the TEM, therefore it is necessary to thin the samples and fabricate them for use in experimentation. The initial samples used within this work were in bulk and nanoparticle form. The methods of fabrication of these samples are outlined below.

3.2.1 Ultrasonic Disc Cutting

The sample holders used in this work for the TEMs have a 3mm countersunk step where the samples sit and then a 2mm aperture. Therefore, it was necessary to cut samples into a 3mm disc so that they could seat correctly in the TEM holder. The cuts were made using a Gatan model 6061 USDC (UltraSonic Disc Cutter). USDCs work by oscillating a slurry of SiC or Boron Carbide microparticles at a frequency of 20-40 kHz. This frequency resonates with the slurry and the large oscillations cause the microparticles to grind through the target material.

To use the USDC the bulk sample was initially glued, via the use of low melting temperature wax, onto a phosphor bronze stub. This was achieved by heating the stub to a temperature of ~200-250°C using a hot plate. Low temperature wax was then applied to the stub and the sample placed on the wax. The stub was then allowed to cool to room temperature to allow the wax to harden. The stub was then placed upon the USDC. A slurry of BC was then fed through the cutter to the sample and cutting would commence. The depth of the cut was

monitored via the DTI (Dial Test Indicator) on the USDC. Once the sample had been cut to depth it would be placed in acetone to dissolve the wax. At this stage a 3mm disc would be prepared and ready for further thinning.

Figure 43 shows the USDC.

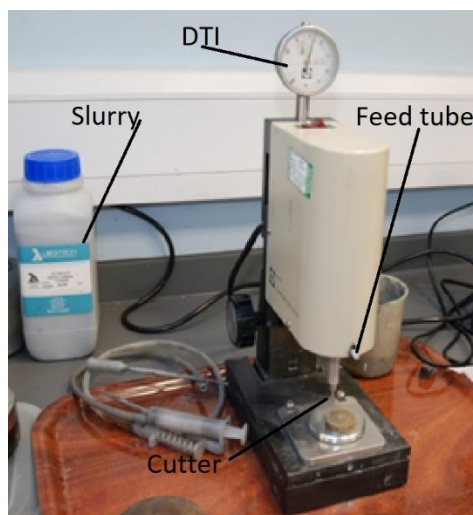


Figure 43 Ultra Sonic Disc Cutter

3.2.2 Surface grinding

Once the 3mm disc(s) were obtained it became necessary to thin them to a size where they became electron transparent on the TEM. The first step in this process was to surface grind them to $\sim 100\mu\text{m}$. The disc(s) were again glued, using the same method as outlined in the USDC section, onto a stub for use on a Gatan disc grinder 623 tool. The samples were then ground down to $\sim 100\mu\text{m}$ using emery cloth of various grit values from 180 to 1200 on an ESC 300 GTL rotary table as seen in Figure 44. The disc(s) were then removed from the holder via the use of acetone as before.



Figure 44 Gatan Disc Grinder

3.2.3 Dimpling

Once a thickness of $100\mu\text{m}$ was achieved the samples were further thinned via a Testbourne 515 dimpler shown in Figure 46. This process grinds a spherical dimple into a sample as seen in cross section in Figure 45. The dimpling process involves rotating the sample at approximately 60 RPM. An arm spinning at approximately 120RPM is then lowered onto the sample. This arm is coated in a diamond paste of either $5\mu\text{m}$, for initial rough grinding, or $1\mu\text{m}$, for final finish. An attached digital micrometer is used to monitor the depth of the dimple. The disc(s) were dimpled to $20\mu\text{m}$ thick, approximately an $80\mu\text{m}$ deep dimple.



Figure 45 Cross Sectional Side View of Dimple



Figure 46 Testbourne Dimpler

3.2.4 Precision Ion Polishing

Reducing the sample further was then achieved via the use of PIPS (Precision Ion Polishing System) [Gatan PIPS II System] milling. This process works by bombarding the sample with Ar ions at an energy selectable from 0.5-8 keV. This bombardment sputters the sample to a thickness that is thin enough to observe in a TEM. As the sample is being hit with ions it is rotating to ensure that both the top and bottom of the disc is thinned. The samples were milled from both the top and bottom at an angle of 8°, using argon ions at 8keV until a hole of 50 μ m was created. Further milling was then conducted at 4° using 4keV for 30 minutes. Then finally 2° at 2keV. This creates a large thin area for TEM viewing. Figure 47 shows the PIPS II machine used for this process.



Figure 47 PIPS II

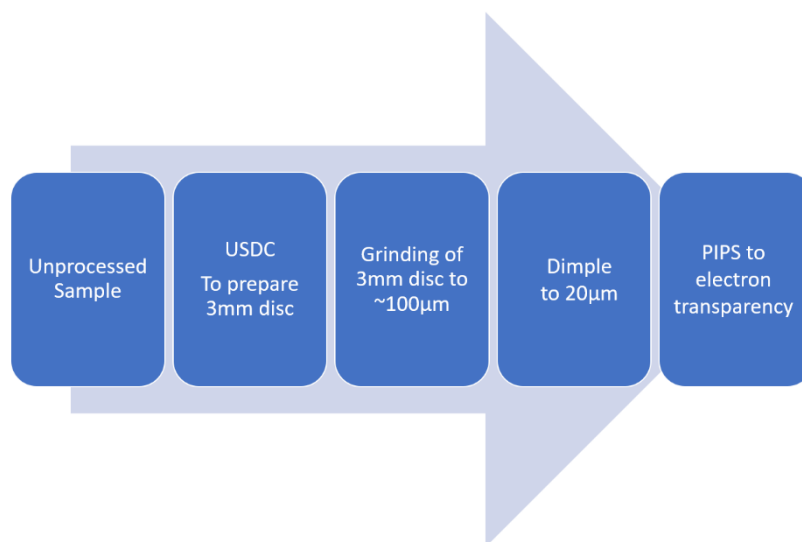


Figure 48 Thin Disc Preparation

3.2.5 Nanoparticle dispersion

In order to view ZrC nanoparticles (Sourced from US Research Nano Materials Inc stock US2068) on the TEM they needed to be dispersed onto a 3mm disc. These discs were either a carbon coated copper grid sourced from Agar Scientific (product code AGS160), a carbon coated molybdenum grid sourced from Quantifoil (N1-C73nMH20-01), or a thin film sample dependent upon the experiment taking place. The discs consisted of mesh grids of a 20-30nm film of the relevant material. If only nanoparticles were to be experimented upon at room temperature, then copper grids were used. At higher temperatures molybdenum grids were used to avoid any possibilities of the copper contaminating the TEM heating holder. If nanoparticles were to be compared to thin films, then they could be dispersed on a thin film of the same material.

In all cases particles were first dispersed in an ethanol solution. The solution was then stirred and placed in an ultrasonic bath for 30 minutes. This mixed the samples and reduced the number of clumped particles. A drop of the solution was then placed on a 3mm disc in an extractor cabinet and the solution evaporated leaving only the particles on the grid with an even distribution.

3.2.6 Microparticle dispersion

The microparticles experimented upon in this work were prepared almost the same way as the nanoparticles. There was however one additional step. In order to ensure that the particles would be thin enough to be electron transparent they were initially crushed via the use of a mortar and pestle. This resulted in particles having thin edges suitable for experiments. The microparticles ranged in size from $\sim 1\mu\text{m}$ – $10\mu\text{m}$.

3.3 Pre-experiment calculations

Prior to conducting an experiment, calculations on how the ions are likely to be transmitted and interact with a sample need to be made. This is to ensure that experimental time is being used efficiently and that experiments can be designed to either compare with a prior work in the literature or industrial applications. This section will focus on how these calculations were conducted.

3.3.1 Stopping and Range of Ions in Matter/Transport of Ions in Matter (SRIM/TRIM)

SRIM is an assortment of software which is used to calculate many features of the transport of ions in matter[44]. The programs use the Monte Carlo calculation approach. It is an important tool that can be used to simulate experiments and gain valuable insights into the types of damage production one can expect. It is important to understand the basic principles to ensure that the work of adapting the code, which follows, remains valid. These basics will be outlined in this chapter.

TRIM, a part of the SRIM software suite, calculates ion-solid interactions based on several parameters[44]. The displacement energy, atomic number, incident energy, and lattice binding energy all play a role. Initially TRIM calculates the free flight path. The free flight path is the distance that an energetic ion will travel between collisions. TRIM lowers the amount of CPU resources by omitting calculating collisions with “negligible” amounts of energy transfer and deflection angles. It is important to understand the collisions that TRIM considers negligible. TRIM calculates the free flight path by calculating a path of length L with a small deflection angle of approximately 5° . It then calculates the smallest impact parameter, the distance between the projectile and target, over the length L . This newly calculated length is then reduced by a random number between (0–1). This is done to disperse the collision to occur randomly amongst the length. TRIM then checks that electronic energy loss does not exceed 5%, if the energy loss is greater than 5% the length is reduced and recalculated. This is due to the probability of an ion receiving >5% electronic energy loss without undergoing a collision being very small. If the amount is less than 5%, then a collision is calculated to have taken place at that length, this is where TRIM will

determine where an atom is located, prior to this the atoms have no placement in the material. The length then becomes known as the free flight path.

TRIM then calculates the type of collision that occurs. If the incident ion transfers a greater energy than the atom it is colliding with has binding energy a displacement occurs. If the ion maintains a higher energy than the binding energy a vacancy is created. If not, and the ion atomic number is the same as the target then a replacement occurs. If the atomic number is different an interstitial is created. The excess energy in all cases where an atom is not displaced is transmitted as phonons. When an atom is displaced, it loses kinetic energy as phonons equal to the lattice binding energy before continuing. In order to get accurate results in TRIM it is necessary to run a large quantity of ions to build up statistical accuracy with the Monte Carlo code being used.

These calculations are initially applied to the incident ion projectile. Then they are applied to the Primary Knock-on Atom (PKA), then secondary knock-ons and tertiary knock-ons and so on. All the data that is calculated is placed in a text file in the SRIM directory which can be viewed later. In addition to this data, backscattered ions, transmitted ions, vacancies/ion, ion distribution, ionization, energy to recoils, sputtered ions, and number of phonons can be viewed in the TRIM program as seen in Figure 49.

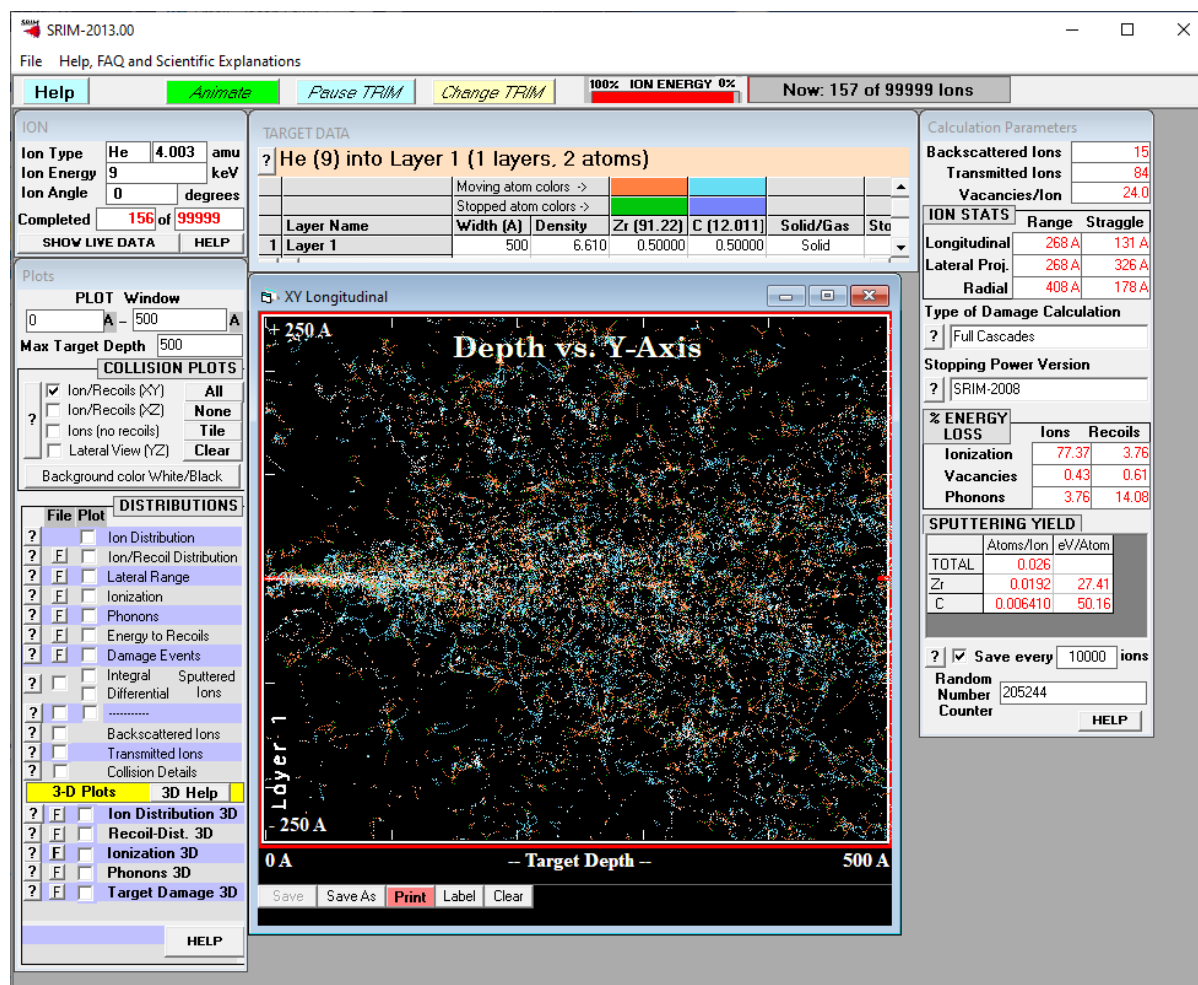


Figure 49 TRIM GUI Overview

3.3.2 SICMod (Spherical Ion Calculations Modifier)

TRIM assumes that the Y and Z lengths of a material that it is calculating for are of infinite lengths with X being the user defined thickness. For a thin film sample this approach is intuitive as the Y and Z lengths are very large in comparison to the width so any lateral travelling of the ions is almost guaranteed to occur within the film. For example, on an electron transparent thin film 3mm disc the ratio of X to Z is approximately 1:30000 or greater. However, for a nanoparticle this is not the case. The Z value varies and can no longer be considered infinite. As a result of this discrepancy TRIM will calculate damage events that in reality would be outside of the diameter of the nanoparticle. This would

result in more damage being calculated than actually occurred. To address this, a Python 2 program was created by the author called Spherical Ion Calculations Modifier (SICMod).

SICMod models a sphere at a diameter specified by the user. It then ensures that the TRIM collision calculations that take place outside of the calculated sphere are not taken into consideration when calculating the total damage. SICMod modifies the TRIM config files so that the TRIM program runs with no user input and runs multiple times generating a new random seed number on each run. It does this in order to calculate multiple individual collision cascades; ions are assumed to impact uniformly over the circular area presented to the ion beam by the sphere and a different cascade for each ion is mapped onto the sphere. The reason for this is that an ion is highly unlikely to enter a particle at the same point multiple times and dependent upon where the particle enters the X value will differ resulting in a different number of collisions. The program then takes the output file generated by TRIM and creates graphical outputs showing the collision densities, implantation densities and the minimum distance to the surface. If an ion exits the volume of the sphere irrespective of whether it re-enters subsequent collisions are discarded, this applies to all energetic ions and knock-ons.

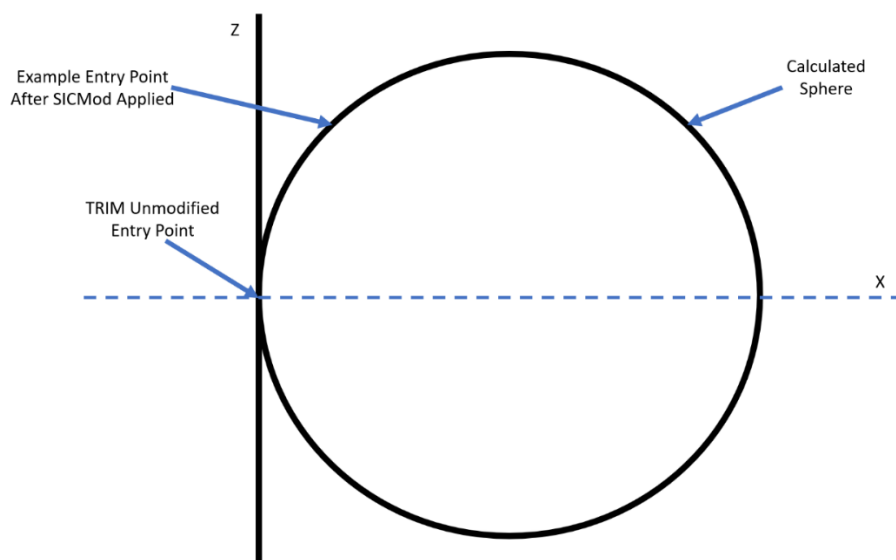


Figure 50 Cross-sectional view of SICMod Sphere with examples of an unmodified entry point and a modified entry point

The SICMod code can be found in the appendix along with a user guide.

3.3.3 DPA Calculations

DPA (Displacements Per Atom) is a measure used to quantifying ion and neutron damage within the scientific community that has been used since 1949 [281]. However, there exists some debate as to how to quantify DPA that has persisted throughout the years [282]–[287]. Until a standard is adopted by the community it is the view of this author that the method for calculating DPA quoted in scientific literature should be explicitly stated in each scientific paper. To this end the DPA calculation method used in this work is outlined below.

For the use of thin films DPA is calculated by:

$$DPA = \frac{v * f}{d}$$

Equation 25 DPA for Thin Films

Where v is the vacancies per angstrom per ion, obtained from SRIM running in detailed calculations mode. f is the fluence in ions/cm² and d is the atomic density in atoms/cm³.

For the use of nanoparticles, the DPA is calculated by:

$$DPA = \frac{t_d/t_i * f}{x * d}$$

Equation 26 DPA for Nanoparticles

Where t_d is the total number of displacements, t_i is the total number of ions, and x is the volume of the particle. This is essentially the same calculation as for thin films (equation 25) but with v modified to allow for the calculation of a non-uniform depth.

A DPA calculator was also coded in python 2 to allow for quick calculations. This code can be found in the appendix.

3.4 Amorphization Analysis

The amorphization process of a material can be described as either homogenous, heterogenous, or a combination of the two [288], [289]. Under the homogenous model amorphization occurs abruptly when the defects in a material reach a certain threshold where it becomes energetically favourable to be amorphous. By comparison, under the heterogenous model amorphization occurs gradually over time as small pockets of a material become amorphous, which accumulate until the entire material is amorphous. It is possible to observe which model is at work in amorphization of a material by analysing diffraction patterns. As a material becomes amorphous, amorphous rings appear in diffraction patterns and the model can be determined by analysing the difference in grey value, i.e. the photon intensity. In order to achieve this, it is important to conduct an experiment where the TEM condenser lens and selected area aperture settings are unchanged. This ensures that the light intensity changes are not being modified by the operator.

Once diffraction images have been taken at various fluences/DPA the light intensity of the images can be checked by using ImageJ. This is done by selecting an area of the image free from diffraction spots and plotting the data of light values. This data can then be exported to excel and plotted into a line graph. Using the graph as a visual aide it is possible to subtract the background intensity data leaving only the peaks from the amorphous rings. An example of these graphs can be seen in Figure 51.

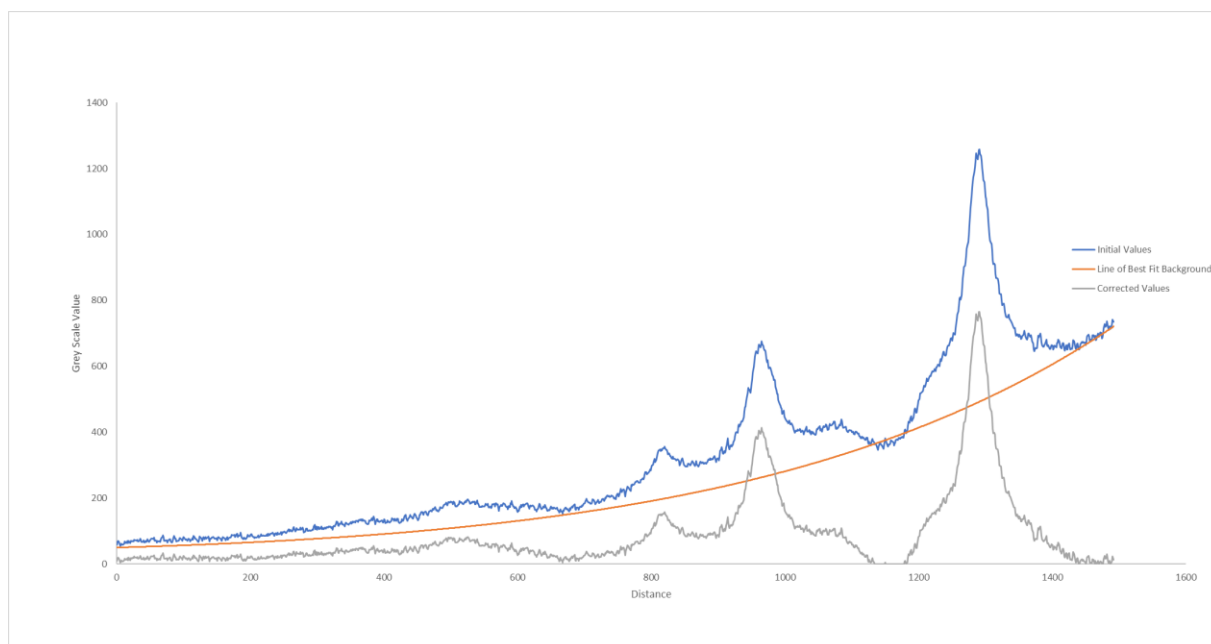


Figure 51 Example of Amorphization Grey Value Graph.

It is then possible to collate all the data from the diffraction patterns and plot the grey value change as a function of fluence/DPA. By observing the produced graph, the model of amorphization can be determined. A graph with a sharp rise would indicate a homogenous model and a gentler rise would indicate heterogenous. It is often the case that the amorphization can be attributed to a combination of the models and the produced graph will highlight this.

4 MIAMI-1 Upgrade

4.1 Introduction

In order to achieve more accurate experimental results, the MIAMI-1 (Microscopes and Ion Accelerators for Materials Investigations) in situ TEM ion beam line at Huddersfield University was upgraded. This chapter will explain the reasons for the upgrade, how it was done, and show the designed parts.

The MIAMI-1 system was first installed at the University of Huddersfield in 2011. It consists of a JEOL JEM-2000FX TEM connected to an ion accelerator. The system was designed and constructed by Dr Jonathan Hinks, Professor Stephen Donnelly, and Professor Jaap van den Berg. Figure 52 shows the system prior to upgrade.

The JEOL JEM-2000FX TEM has a magnification in the order of 100-800,000 times. The accelerating voltage is from 80 kV to 200 kV. The system is fitted with a Gatan Orius 4 megapixels digital camera which adds an additional 20 times magnification. This allows for easy image acquisition.

The ion beam line is capable of producing ions of various species. The energies of the ions run from 2-100 keV. This produces fluxes in the range of 10^{10} - 10^{14} ions/cm²/s.

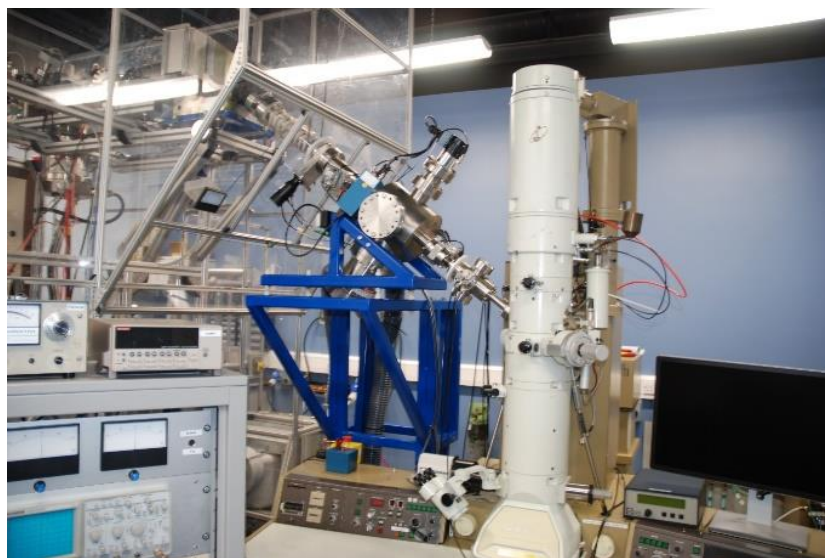


Figure 52 MIAMI 1 Prior to upgrade

4.2 Final Deflection Problems

The initial design of the MIAMI 1 facility lacked line of sight for the ion beam to the sample position. This meant that the beam was bent via electrostatic deflectors in the microscope before encountering the specimen. When setting up an experiment the ion beam current would be measured at the sample position via use of a custom-made sample holder to ensure that the correct parameters were set. However, whilst the experiment was being conducted there was no way to measure the beam after the final in-column deflection. The beam was measured after the experiment and if it had not changed it was assumed that it had remained constant. This assumption left some degree of potential error in the results. As a result, the final deflection system was modified to have a skimmer system installed to measure the beam dosimetry after the final deflection. Regardless, the system would frequently break down and required a lot of maintenance. The maintenance involved removing the beam line from the TEM which led to significant machine down time. It is estimated that the machine was down for maintenance for 2 weeks every 2 months or ~25% of the time. The final deflection system also made it difficult to align the beam to the sample position. This led to an increased time being spent setting up experiments. It would normally take ~4 hours to set up the ion beam line for an experiment.

In order to solve the problem, it was decided that the final deflection system would need to be removed. As a result, the beamline would need direct line of sight with the sample. However, to achieve this the angle of incidence would need to be increased. The original beam line was interfaced with the TEM using an existing port (designed for interfacing an X-ray diffraction device) which was at the wrong angle, hence the final deflection system. To achieve the higher angle the condenser mini lens (CML) column section of the microscope was redesigned by a previous student Ewan Vanderboon. Ewan Vanderboon also did the initial designs for the electrostatic deflection system, the skimmer, the support structure, and the beam profile monitor T piece. Those designs were modified and implemented by the author of this work. The modified CML column also included seating for the skimmer to allow the beam to be monitored before the sample at close range. Changing the final deflection system also required a change of several other key pieces of the MIAMI 1 system

such as the height of the beamline. As this was the case other upgrades such as better electrical isolation was implemented alongside this work. The work involved the design and manufacture of many bespoke components. Special consideration had to be given not only to the mechanical strength of components but also their ability to perform under various conditions such as high vacuum, high tensile electricity, as well as withstanding impacts from stray ions. The following outlines the major components of this upgrade.

4.3 Support Structure

To support the new ion beamline at its increased angle and height a new structure had to be designed. This support structure needed to be sturdy enough to support the weight of the beamline components and be able to fit within the available space of the MIAMI 1 lab and be able to be moved into and out of position for maintenance work to be carried out. It was split into 2 components to allow for electrical isolation. The bottom piece was designed to have wheels at the bottom. This allows for easy manoeuvrability of the frame. Two rubber feet were added to provide extra stability when the frame is in position. To keep costs and weight down the frame was made from 55mm mild box steel. The steel was coated in blue paint to prevent rust and keep to the existing aesthetic of the room. Due to the interference of a cabinet on the TEM, the bottom of the frame needed to be angled. This let the frame sit in a space under the cabinet. The top of the frame extends over the top of the cabinet.

Figure 53 shows the bottom frame.

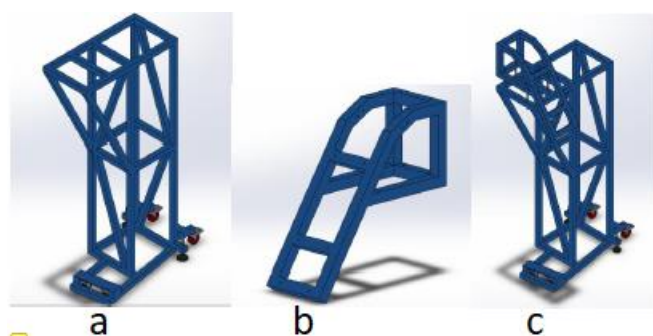


Figure 53 a Frame Lower b Frame Upper c Frame Complete

The upper frame was designed to secure the bending magnet, einzel lens, and the beam profile monitor, all discussed later in this chapter. To achieve this the frame was designed with an angled overhang. The frame consists of 4 cross sections to allow for clamps to be fixed to secure the aforementioned pieces. Figure 53 b shows the upper frame.

The upper frame was attached to the lower frame via the use of 4 nylon studding which ensured electrical isolation in the event of a HT breakdown. The height of the upper frame could be adjusted by changing the standoff between the 2 frames. Figure 53 c shows the complete frame.

4.4 Electrostatic Deflector

To achieve direct line of sight with the specimen the angle of the incoming ion beam as it enters the TEM needed to be increased from the previous 28° to 56° relative to the horizontal floor. To do this within the limited one-story space of the MIAMI 1 facility it was necessary to bend the beam from its horizontal position to the incident angle. This was made possible by introducing a new electrostatic deflection system. The electrostatic system needed to incorporate materials which were vacuum safe. It was also necessary to ensure that the static plates would be electrically isolated from the external of the beam line and that the correct angle of deflection could be achieved without blocking the beam path in anyway. The design was also made easy to assemble and fit/remove from the system in the case of any maintenance being conducted in the future. The electrostatic deflector consists of 2 aluminium electrostatic plates bent to achieve the desired angle of 56° , see Figure 106 in appendix. The plates are fastened to 6 PTFE blocks, 3 for each plate, via counter sunk screws to avoid them protruding into the ion beams path. The blocks are then secured to the 2 ground plates, see Figure 107 in appendix. The ground plates have straight ends which slot into 2 end pieces, see Figure 108 in appendix. which have 4 machined holes each to allow for aperture strips to be added. To secure the standoff plates they are bolted down to the end piece. The end pieces were designed to be round to allow them to be slid into and out of the deflector housing with ease.

The electrostatic deflector when assembled appeared as in Figure 54 and Figure 55.

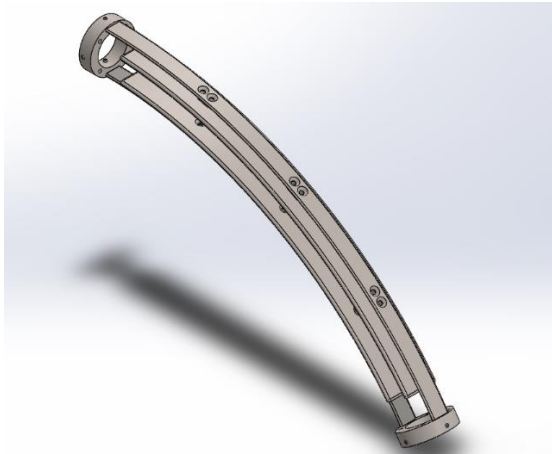


Figure 54 Electrostatic Deflector Internal

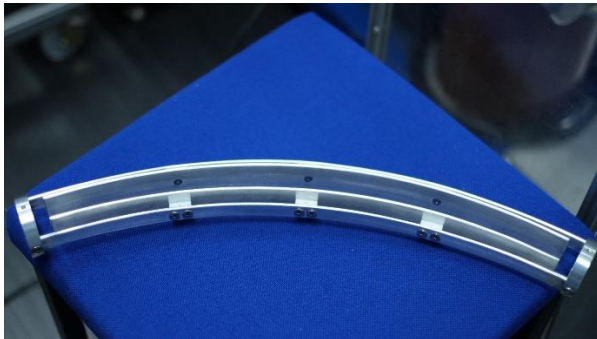


Figure 55 Electrostatic Deflector Internal Actual

The deflector was then secured into a large housing. The housing was designed to also incorporate the turbo pump of the ion beam vacuum system. The pump was an existing part of the original line. Due to the weight of the pump the housing was designed to not only secure to the support structure via clamps, but also fasten to the sides of the structure. Two ports were added to the top of the housing to allow for optical alignment when fitting the piece. Additional ports were added to allow for the electrical feed through of the deflector lens. Figure 56 shows the electrostatic deflector housing.

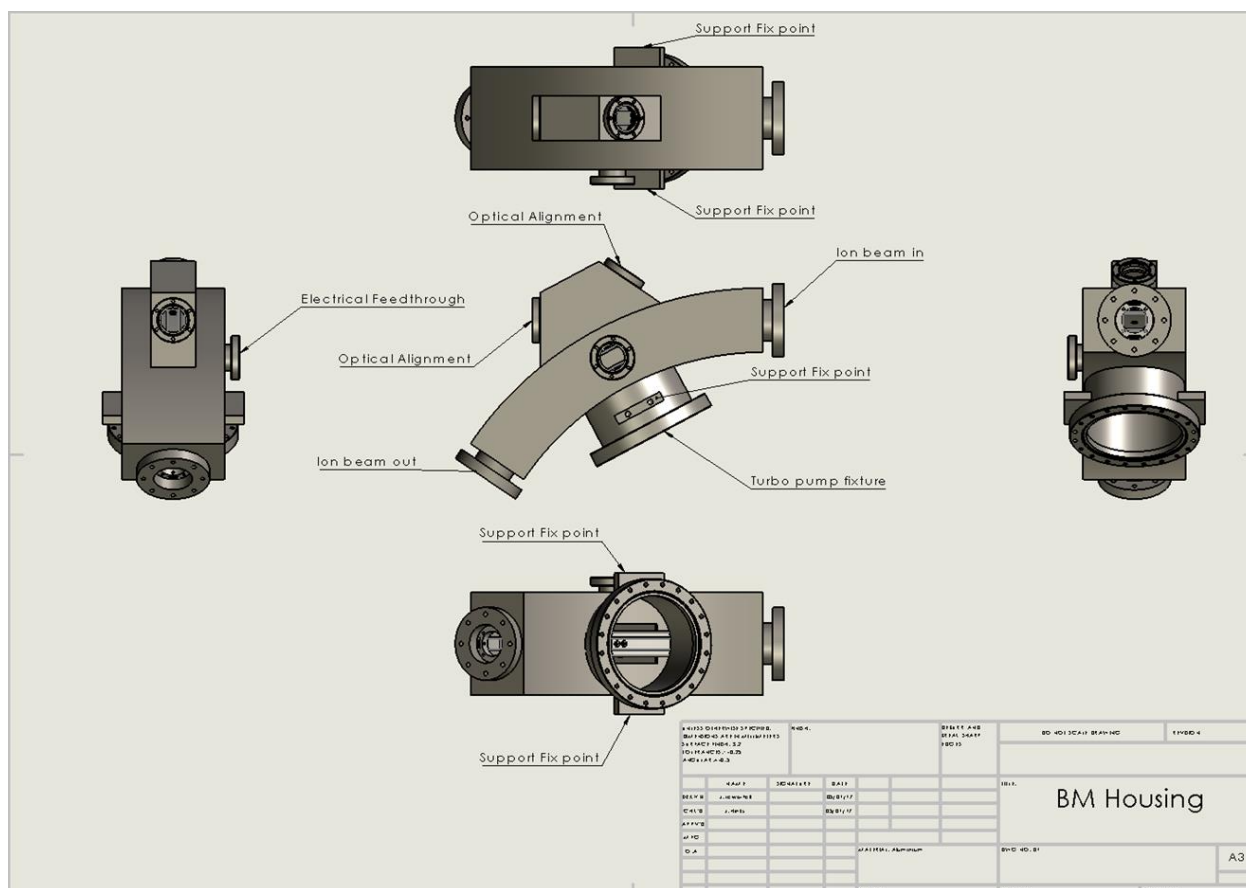


Figure 56 Electrostatic Deflector Housing

4.5 New Einzel lens

An Einzel lens is a lens that is used to focus charged particles without changing their energies. Its design consists of 2 ground tubes with 1 tube at high tension located between the 2 ground tubes. The charge of the high-tension tube, negative or positive, depends upon the charge of the particle which is desired to be converged. If the particle is positive, then the tube will be negative and vice versa for negative. The incident beam initially diverges towards the high-tension tube, and then converges away from it, as seen in Figure 57. This is due to the electrical field generated between the tubes. This field may be mapped out using equipotential surfaces, as seen in Figure 58. These surfaces are analogous to the contours on a height map [290].

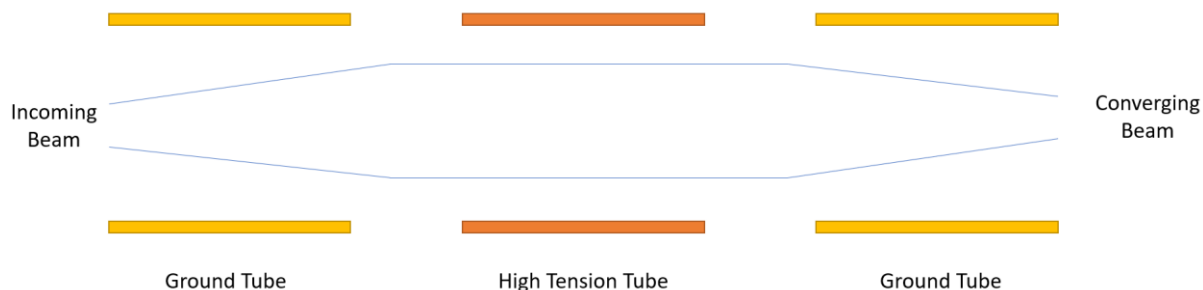


Figure 57 Einzel Diagram

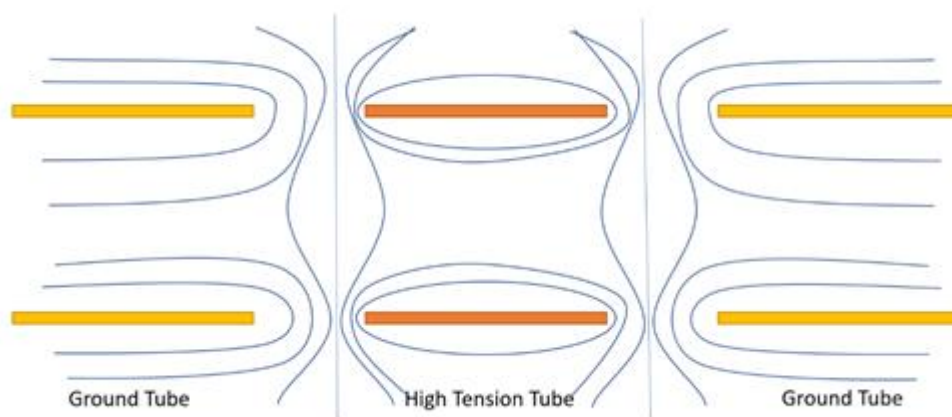


Figure 58 Einzel Magnetic Field Diagram Field Diagram

Part of the upgrade process was to design a new einzel lens to focus the ion beam and direct it via the use of deflectors. A housing for the lens had already been designed so it was important that the new lens design was able to fit within the existing housing. Figure 110 in appendix shows the existing housing dimensions.

The constraining dimensions on the housing were the ID of 64.2mm and the overall length of 396.6mm. Ideally a lens would be able to slide into the enclosure and then be fixed in place, with ease of removal in case of a machine break down.

To achieve these conditions, it was decided that the lens should be assembled into a solid piece outside of the enclosure. This limited the assembled lens OD to a maximum of 64mm. the lens assembly was designed to be cylindrical to achieve this.

A design was created with 2 grounded tubes made from aluminium, see Figure 111 in appendix, and 1 aluminium pipe for the high voltage to be applied, see Figure 112 in appendix. To attach a wire to the high voltage tube an m6 hole was added to allow for a screw to clamp the wire. They were assembled with 4 m4 studding bars cut to length. The m4 studding would have PTFE pipe of 1mm thickness covering it to isolate it from the high voltage and to set the pieces at the correct distance from each other. To further isolate the high voltage tube from the studding a PTFE tube was press fitted to the OD, see Figure 60 Einzel Assembly and Bill of Materials. This tube would have the m4 studding passing through the PTFE pipe that was used to surround the studding was designed to fit in counter sunk holes.

To deflect the beam 4 plates were designed at the end of the einzel lens. Two of the plates have a low voltage applied to them whilst the other two opposite plates would be grounded. This creates a differential across the system and deflects the beam in the y and z axis, whilst the relatively low voltage avoids focusing effects. In order to fit to the studding whilst remaining isolated the deflectors were designed to have a 90° angle bend piece with a hole for a ceramic split bushing to seat in at each side. Initially this caused the piece to extend beyond the 64mm OD. This was remedied by bringing the m4 studding closer together. Figure 114 in appendix shows the deflector plate design. The deflector plates were originally designed to be made from aluminium. However, the spot welding machine was unable to provide a good enough weld, resulting in the wires pulling free, when they were added. Therefore, the plates were changed to AISI 316.

In order to complete the assembly and be able to secure it to the enclosure 2 end pieces were designed. These would attach to either end of the m4 studding. If at a later date an aperture was required, it could be fit to the studding. 4 tapped holes were added running laterally to allow for grub screws to clamp the pieces into the enclosure. Figure 115 in appendix shows the end pieces.

Once assembled the einzel lens was shown to meet the requirements placed upon it. Figure 60 shows the assembled drawing for the lens.

4.6 New HV Shield

The high voltage cable to the new einzel lens required a way to be shielded to avoid the operators, or any other persons, coming in contact with it. Figure 61 shows this.



Figure 61 High Voltage Connector

To do this a design was created. This design uses a polycarbonate tube of 5mm wall thickness to fit over the high voltage connector and clamp via 4 screws onto the einzel housing. An end piece would then be fastened to the tube via 8 nylon screws. This would ensure that the piece was insulated. A Hole was tapped to m20 x 1.5mm in the centre of the end piece to allow for a cable clamp to be assembled into the piece and secure the cable.

However, a problem occurred when the design went to manufacturing. Due to the stress created by drilling holes in polycarbonate, cracks in the material appeared. In order to overcome this the design was modified. The polycarbonate tube was changed to a simple length of tube with no holes machined into it, Figure 119 in appendix shows this. The end piece was changed from polycarbonate to PVC with a stepped OD and was fastened in place with glue. In order to fit the tube in place 6 holes were drilled in the end piece equally spaced. This would allow the assembly to fasten on to studding extending from the CF70 flange on the einzel housing. Figure 120 in appendix shows the new end piece.

4.7 Condenser Mini Lens Column Section

Prior to the authors work on the MIAMI 1 upgrade, a new Condenser Mini Lens (CML) column section piece had been designed and manufactured. The piece seats beneath the condenser lens aperture and houses the condenser mini lens. An outline of this piece has been included in this thesis as it is an important part of the upgrade. The author claims no part in the CML design and development. The CML piece was designed to replace the current piece within the JEOL JEM-2000FX TEM. This became necessary to allow for the implementation of a skimmer and dosimetry device, discussed later in this chapter. The CML has some complex geometry that will be outlined here.

Figure 121 in appendix shows the key locations of the CML piece. The vacuum port, cold finger port, and existing port were all on the original microscope. The ion beam port has replaced what was originally a port to attach an X-ray diffraction device but was used for the original ion beam. The port has a higher angle of incidence in relation to the horizontal plane than the original to allow the ion beam direct line of sight with the sample chamber. The dosimetry port was added to allow the insertable dosimetry system, discussed later in this chapter, to enter below the skimmer. The electrical feedthrough port was added to allow for the wires to be fed at vacuum to the skimmer and dosimetry device. The location of the skimmer has been highlighted to show where it will sit. A slot and 2 tapped holes were in place to allow the skimmer to be fixed and the ion beam to pass through. The fixtures for the condenser mini lens and the other parts in the microscope were mirrored from the initial design. However, the overall height of the piece was increased to allow a skimmer to be fitted. This height could not be extended too much as it would result in a large, potentially un-correctable, change in the optics of the microscope. Flanges were added to allow the dosimetry port and electric feedthrough to be fitted to vacuum parts. Figure 122 in appendix shows this.

4.8 Skimmer

A skimmer was designed and fitted to allow the beam current to be measured in-situ during experiments. The skimmer was fitted in the CLA piece after the ion beam had undergone its final bending. This ensured that the beam current density being measured was accurate, and not fluctuating during experiments. The skimmer system consists of many parts.

The enclosure for the system needed to fit within the space provided in the CLA, securely house the skimming pieces, allow for the wiring to be fed to the CLA ports, and incorporate the dosimetry device discussed later in this chapter.

The enclosure was designed to allow for the ion beam angle of incidence. It was made from AISI 316. A tall base was designed to keep the footprint small enough so that the piece could fit into the CLA piece yet have enough clearance to allow a bolt head to rotate at the top of the base. Increasing the height of the base achieved this due to the stem being angled. The enclosure had a square cut out on its base to allow the insertable dosimetry device to slide in and out of the piece. The hole through the centre of the enclosure was tapered to minimize any sputtering created by the ion beam traveling through the device. The $\varnothing 6\text{mm}$ countersunk hole provides a seating point for the first suppression cup. The three off 1.1mm holes seat ceramic rods that run the length of the skimmer and secure the parts in place. The two off 1.6mm holes secure the cap onto the device. Figure 123 and Figure 124 in appendix show the enclosure design.

The first suppression cup was designed to slot into the skimmer enclosure whilst maintaining a gap to the surface of the cap. It is a grounded component and is made from AISI 316. The 5mm extension allows the cup to be fastened to the second suppression cup. The three 1mm holes locate onto the ceramic rods that run through the whole device. Figure 125 in appendix shows the first suppression cup.

The second suppression cup has the same geometry as the first cup except for the 8.5mm leg added to the 5mm extension. As the second cup sits above the skimmer the extension closes the gap between the two suppression cups. The 8.5mm extension has a tapped hole

running through its centre so that a countersunk bolt can secure the two cups together. The 1mm hole within the 5mm extension allows for a wire to be secured that can be passed to ground. Figure 126 shows the second suppression cup.

Seated between the two suppression cups is a skimmer cup. This piece comes into direct contact with the ion beam and as such was made from tungsten. This is due to the low sputter yield of tungsten. As the skimmer comes into contact with the ion beam, generating an electrical current it was required to be isolated from the grounded suppression cups. To achieve this, 3 ceramic bushes, located on the ceramic rods, were fitted to either side of the skimmer. The skimmer has a 3mm hole through the centre which the ion beam travels. The hole is then stepped down to a 1mm hole creating a 1mm thick ledge that the beam lands upon. The beam that lands upon this ledge is what is measured. The remaining beam will then continue to travel down the system through the 1mm hole. The 1mm hole is tapered at the end down from the ion beam. This lowers the amount of sputtering. The 5mm extension with a m2 tapped hole and 2mm clear hole is there to allow for the wire to be fastened to the piece. Figure 127 in appendix shows the skimmer cup.

The skimmer cap was added to the design to both create a standoff for the suppression and skim cups and increase the resistance on the ceramic rods holding them in place. The dimensions on the cap mirror those of the enclosure upon which the cap seats. Figure 128 in appendix shows the cap.

The skimmer case encases the skimming device. It protects the device from the ion beam if the beam was greatly out of position. It also acts as an aperture for the beam prior to the first suppression cup. The case has a 34° angle cut out at the bottom. This is so that once assembled it does not overhang and block the slot on the enclosure for the dosimetry device. The 4mm hole in the cases outside diameter is to allow the wires from the suppression and skim cups to feed out of the device. Figure 129 in appendix shows the Skimmer case.

Figure 130 in appendix shows the skimmer once assembled. Figure 131 in appendix shows a cross-sectional view to help identify parts. Figure 62 and Figure 63 help visualize the complete dosimetry system.

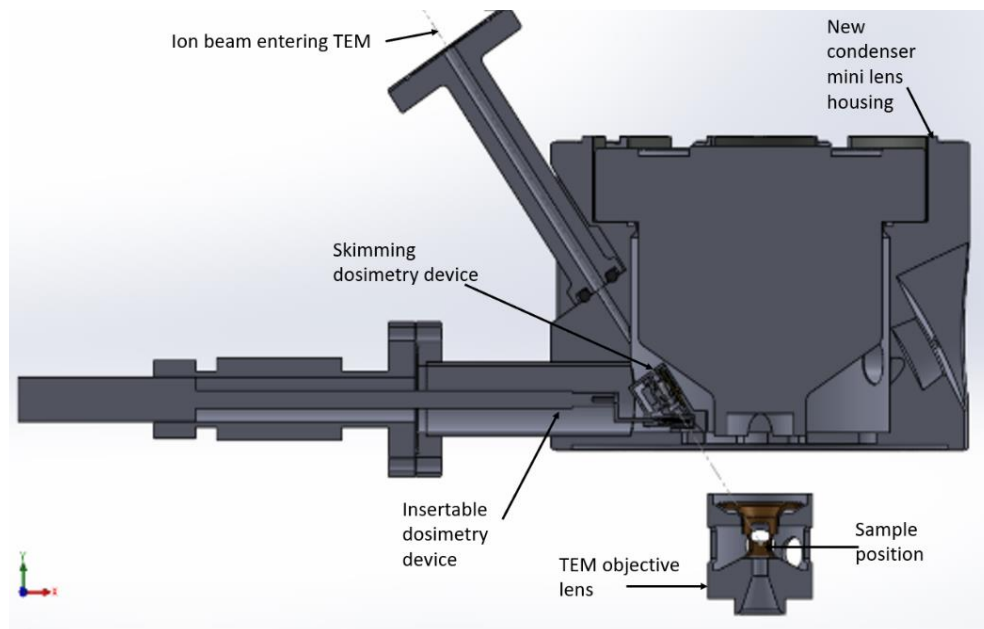


Figure 62 Dosimetry Whole cross-section

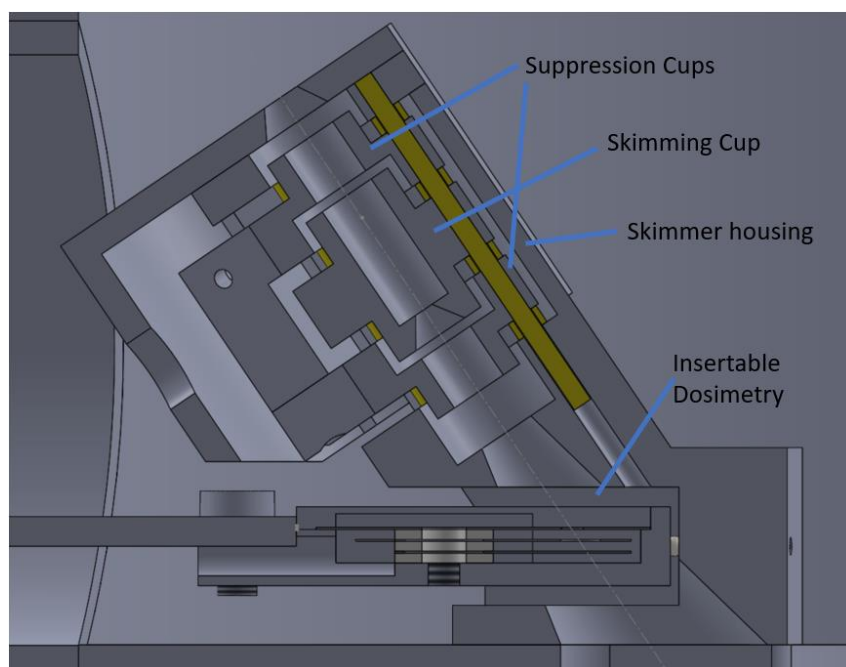


Figure 63 Dosimetry Cross-section

4.9 Insertable Dosimetry Device

The insertable dosimetry device was designed to seat beneath the skimmer. As a result, space was limited and the case that houses the dosimetry device needed to be small. The dosimetry device connected to a rod that slides into and out of position. The rod is sprung so that it naturally wants to sit in position. It can be locked out of position with a small screw clamp. The device locates its position with two sapphires which seat in two holes of the faraday skimmer case. The dosimetry is calculated via the use of three molybdenum plates. Molybdenum was selected for its good ion beam damage resistance and ease of machining. The top plate has an aperture of 1mm and was used as a suppression of the beam. The second plate had a defining aperture of 2mm. The final plate had no aperture and was used to measure the flux. The plates were isolated from one and other and ground by use of PTFE blocks. The plates located in a small square case and were clamped to the case via a screw which went through the PTFE blocks. A slot was added at the end of the case to allow electrical feedthrough to the plates. Figure 64 Shows a cross-sectional view of the assembled device.

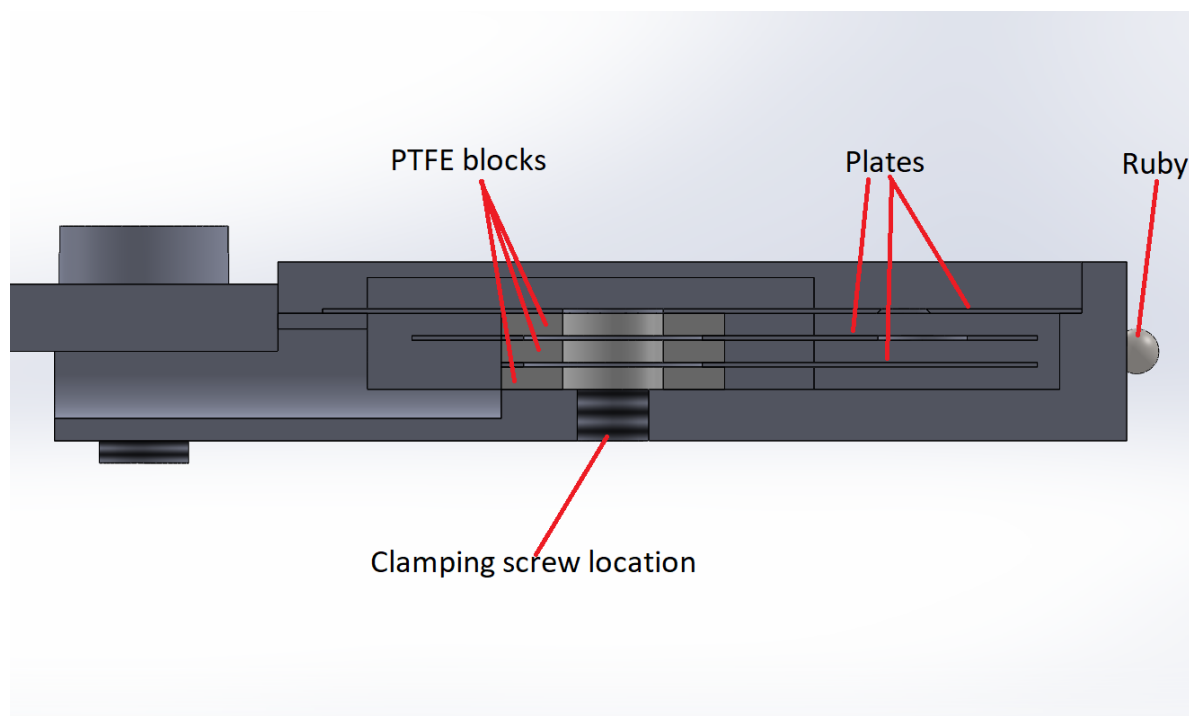


Figure 64 Insertable Dosimetry Cross-section Highlighting the Key Components

4.10 Bellows

As explained in chapter 2.8.6 Vibrational isolation, vibrations are detrimental to the operation of an ion beam system. To reduce the mechanical vibrations from the vacuum pump systems 2 sets of bellows were added to the ion beam line. By flexing these bellows act as dampers. They also allow for some margin of error to be taken up in the overall assembly. These bellows were placed at two points on the beam line. One after the accelerating lens before the support structure and one after the second ceramic standoff. These 2 positions were chosen due to the first damping the line coming from the earthed cage and the second damping just prior to the TEM. Figure 65 shows the position of the 2 bellows.

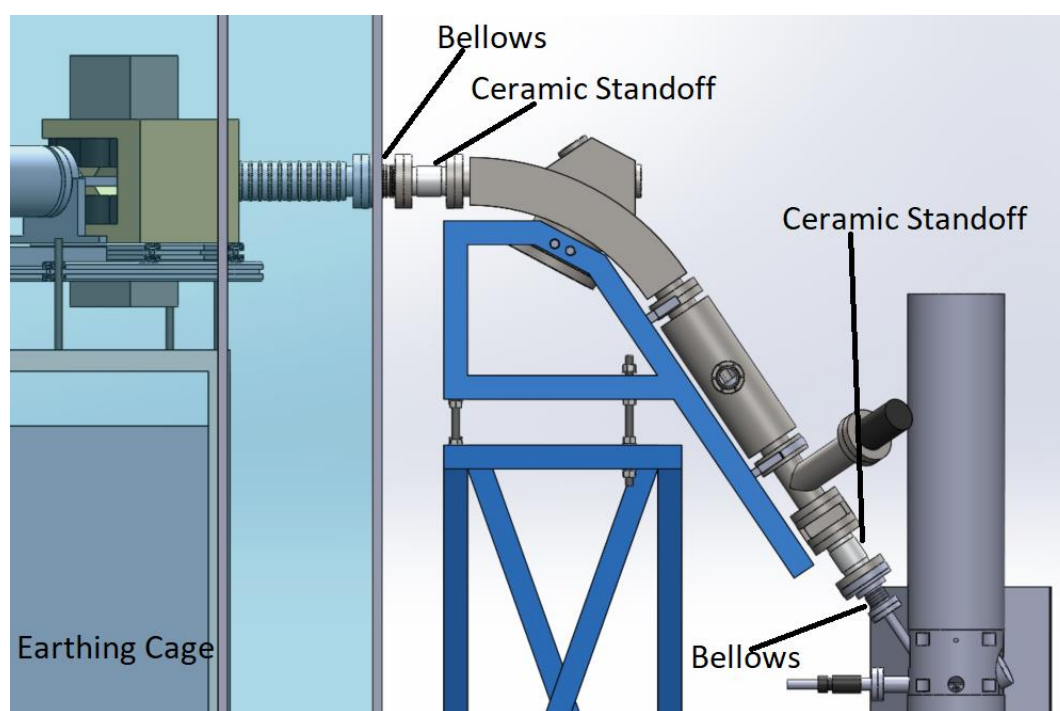


Figure 65 Bellows and Ceramic Standoff Position

4.11 Ceramic Standoffs

The original MIAMI-1 system suffered from electrical breakdowns from the HT ion source which caused damage in the TEM. Even though there were several grounded points along the original system on occasion the electricity would travel down the metallic parts of the ion beam into the TEM internals. To prevent this the original system was retrofitted with

PTFE standoffs fitted onto two flanges. This method was crude, and as the system was being upgraded an opportunity was available to design in a standoff system to avoid any electrical discharge jumping to the TEM column. As such two ceramic stand offs were installed. These standoffs consisted of two steel flanges, which were connected to an earthing cable and subsequently the main systems star point (the main grounding point), and a ceramic tube that provided the insulation. One tube was placed after the accelerating lens where the beamline had initially come to ground. A second was placed close to the TEM in case the first one failed.

4.12 Earthed Cage and Support Structure Modifications

Several modifications were made to both the earthed cage and the support structure held within. The original cage had a gap of at least 30cm between itself and the support structure. This gap was to ensure that electrical discharges did not occur when the support structure was floated to a high voltage. It was important that any modifications made to the cage and support structure maintained this gap.

The first item that was modified was the overhang on the earthing cage. This was no longer necessary as the accelerating lens, the last piece that is at high voltage, was no longer overhanging the support structure at an angle. This lowered the footprint on the earthing cage. The second item that was modified was the upper support structure. Its height was increased, and the structure now runs at an angle to accommodate the new angle introduced by the bending magnet being placed on its side, this was necessary to keep the magnet functionality as a mass selector. A new support structure for the magnet was designed and built to allow it to sit on its side. This support structure consisted of Dural extrude piece supported by M12 studding. The two control cabinets within the earthing cage switched position. This was done to allow the turbo pump on the Colutron to hang without interference. As the cabinets had been switched the electrostatic dissipative sheet, onto which the controls for the cabinets were mounted, also had to be modified to allow for the new control locations. Finally, the door to access the source was moved from the rear of the cage to the side.

4.14 Complete Design

All of the designs were placed in a Solidworks assembly mock-up of the MIAMI-1 room. This not only ensured in the design stage that all the components would assemble, but also that the system would fit within the constraints of the room. Figure 67 shows this complete design.

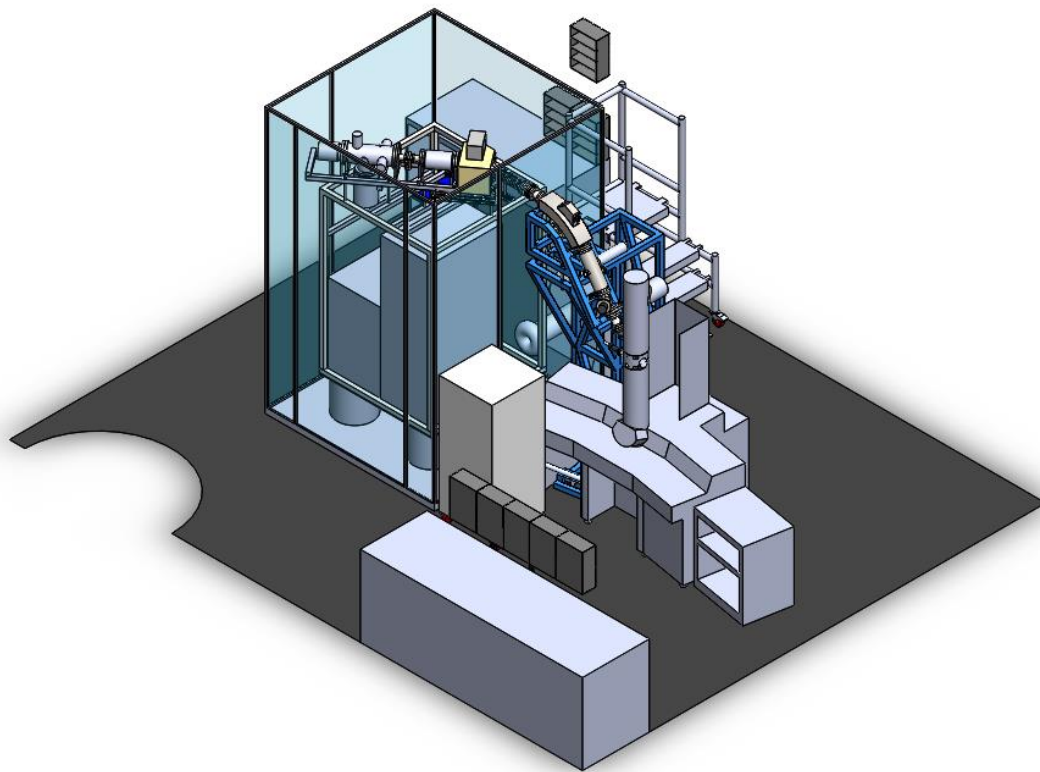


Figure 67 MIAMI 1 SolidWorks Design Complete

As can be seen, in the design of the total system a mock-up of the JEOL JEM-2000FX was included. All of these items were necessary for the system so it was crucial to ensure that they could exist alongside it.

4.15 Quantification of System Performance

In order to assess the effectiveness of the new MIAMI-1 system, quantification experiments were conducted. The initial plan was to perform a variety of experiments at different energies and using different ion species, and then conduct the same experiments on the MIAMI-2 system to compare the results. If the results tallied a high confidence that the dosimetry values of MIAMI-1 are accurate would be gained. However, the Gatan Orius Camera on MIAMI-1 broke and had to be sent to the USA for repairs. This led to the system being unable to record images for several months. Coupled with this Covid-19 led to lab closures significantly impacting time that could have been spent conducting these experiments. Experiments were conducted viewing helium bubble formation in ZrC using the phosphor screen on MIAMI-1 and using camera acquisition on MIAMI-2 the resulting bubble formation was assessed against the literature and it was discovered that both machines reported comparable results.

4.16 Future Recommendations

Whilst an experiment was conducted to try and validate the MIAMI-1 system dosimetry readings and the results showed good correlation between the systems, it would be good to perform a variety of experiments at different energies and using different ion species, and then conduct the same experiments on the MIAMI-2 system to compare the results. This could be taken further by performing identical experiments on facilities around the world to ensure that results correlate well with each other.

5 ZrC irradiation

5.1 9keV He⁺ Ion irradiation effects on ZrC

In order to gain an insight into how He implantation will affect the microstructure of ZrC nanoparticles and microparticles a series of experiments was conducted on both the MIAMI-1 and MIAMI-2 systems.

Helium irradiation was undertaken as a gap in the literature was identified and it is important to understand He accumulation effects from a nuclear industry standpoint as He is a fission and fusion by-product. It is also of interest to the scientific community the effects of He doping on materials as this can change their characteristics [33], [73], [291]. The experiments conducted saw a final He concentration far greater than the 700 appm that occurs in fission reactor environments after many years [292].

Experiments were conducted at temperatures from room temperature up to 800°C to observe any thermal effects on defect production and mobility. Both microparticles and nanoparticles were irradiated to observe how the surface area to volume ratio would affect defect production.

There are no reports in the literature of ZrC becoming amorphous under ion, neutron, or electron irradiation. By conducting experiments at various temperatures with He ions an insight on whether it is possible to amorphise ZrC will be gained. This would be a new scientific discovery and lead to a greater understanding of ZrC.

It is reported in the literature that nanoparticles have greater resistance to He bubble formation as discussed in section 2.11. By conducting experiments on both nano and microparticles a comparison of the formation in the case of ZrC can be discovered.

It is also reported in the literature that nanoparticles resist amorphization when compared to their larger counterparts. If amorphization of ZrC is found, then comparing the response of nano and microparticles will either strengthen this hypothesis or reveal new insights.

There has also been discussion in the literature of ZrC replacing SiC as a material for use in reactor environments. By gaining insight into the He ion response the results can be compared with the reports on SiC in the literature, summarized in chapter 2.9.9.

5.2 Experiments on Nanoparticles

5.2.1 SICMod Calculations for Nanoparticles

Prior to irradiation the nanoparticle samples were screened and were discovered to have an average individual diameter of approximately 50nm. TRIM was then run with various energies from 3keV to 15keV to find the optimum energy for maximum implantation. It was found that ~9keV resulted in the implantation curve peak being centered at the nanoparticles midpoint. Once this initial calculation had been conducted a more detailed calculation was performed using the SICMod code developed in the course of this project. The code ran for a total of 3,139,700 ions, a number large enough to give good data, and calculated a total number of displacements of 32,161,551. This gave a result of 10.24 displacements/ion and 0.054 displacements/A/ion.

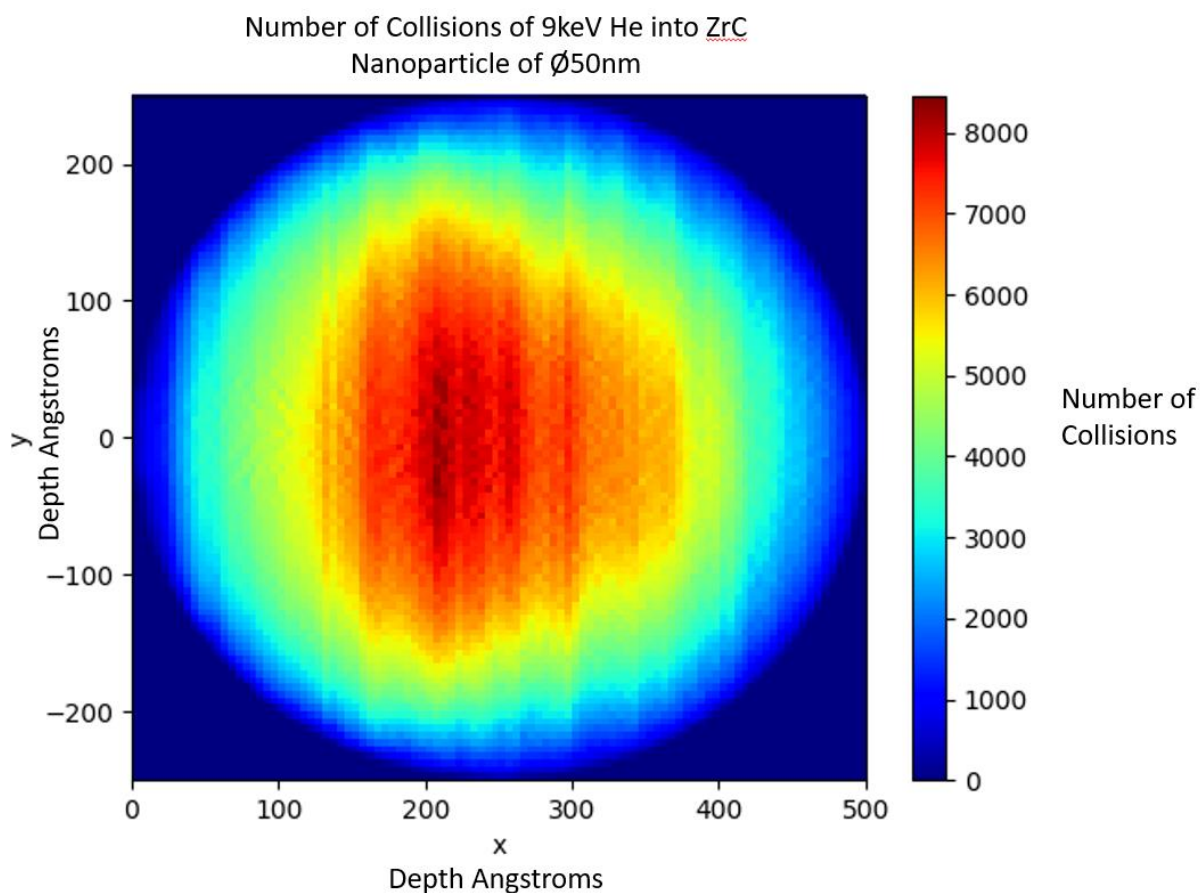


Figure 68 SICMod Results 9keV He into ZrC Nanoparticle of \varnothing 50nm Showing Collisions

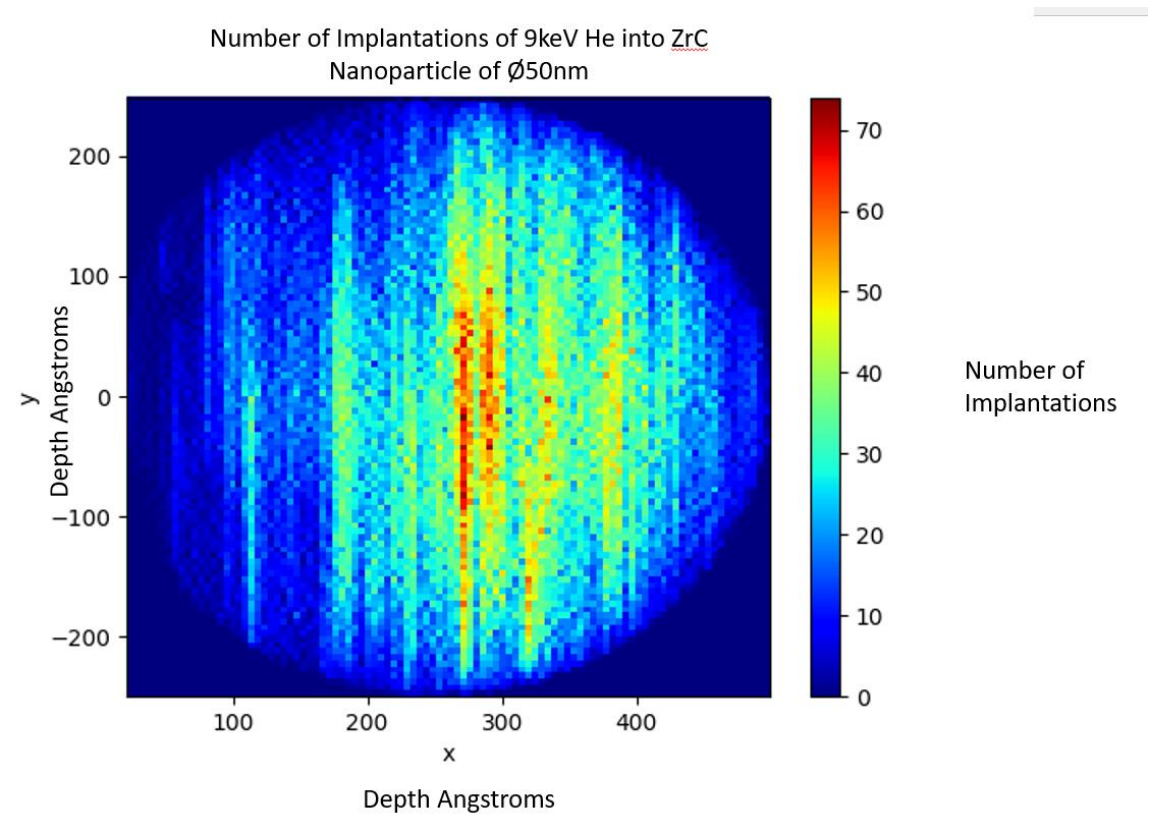


Figure 69 SICMod Results 9keV He into ZrC Nanoparticle of $\varnothing 50\text{nm}$ Showing Implantations

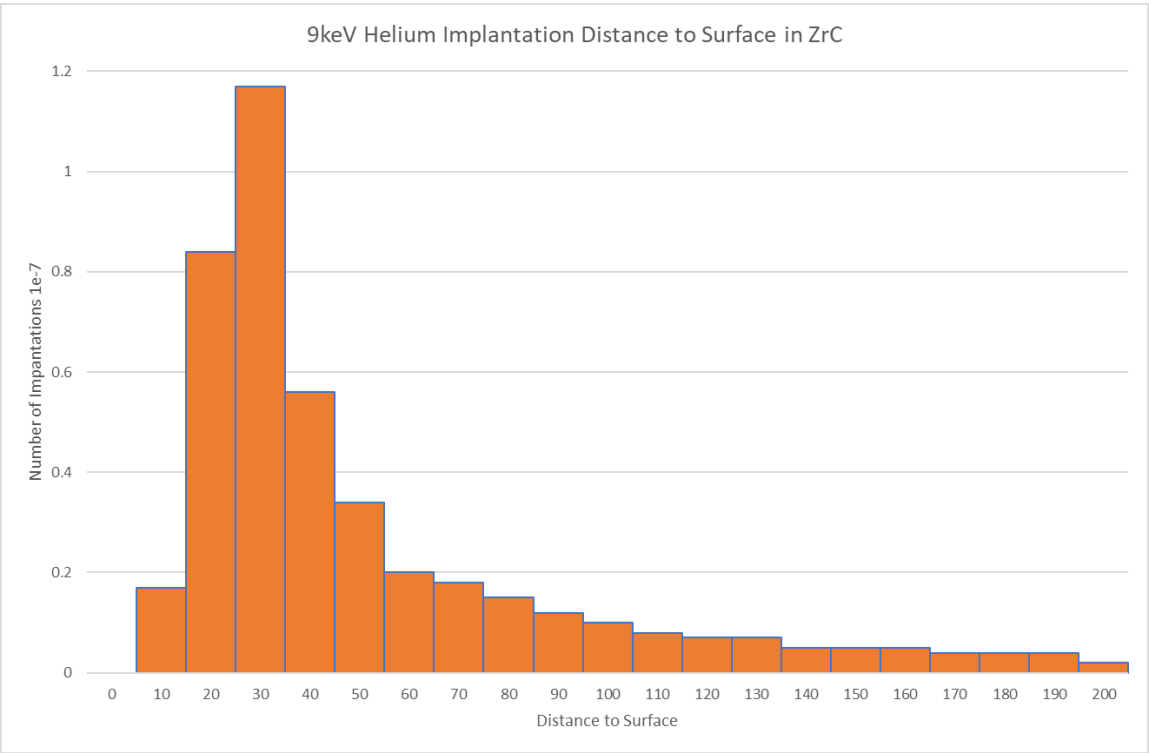


Figure 70 Graph of SICMod Results 9keV He into ZrC Nanoparticle of $\varnothing 50\text{nm}$ Showing Implantations Distance to Surface

As can be seen in Figure 68 and Figure 69 the SICMod calculations show that the collision density is peaked at ~ 200 Å and implantations are peaked at ~ 250 Å. Figure 70 shows that the majority of implantations lie at a distance of 30 Å from the surface with the amount lying deeper tailing off, which is to be expected for a specimen with a large volume to surface ratio. These calculations demonstrate that the energies used in the experiment were optimum to implant a large amount of helium ions that strike the sample whilst maintaining a uniform damage curve.

5.2.2 Irradiation of ZrC Nanoparticles

Prior to irradiation the samples were screened with bright field, dark field, and diffraction patterns being obtained see Figure 71 and Figure 72. It was endeavored to observe the same particles throughout the course of the irradiation. However, this was not always possible due to the films on the grids occasionally becoming torn during irradiation. It is safe to assume that the effects described hereafter were produced due to irradiation as they were observed in all particles across the grids, and in a control experiment, using heating and no ions no changes were observed. Due to the dispersion method of the particles, they often sat close together and even overlapped. Dark field imaging, as seen in Figure 71, showed the individual particles. During the irradiation steps the electron beam was switched off to prevent any electron beam irradiation effects which have been noted to occur in experiments [268]. It was noted that the nanoparticles were coated in a film ~ 2 nm thick. This film has also been seen in other nanoparticle materials and in those cases was observed, via the use of EELS (Electron Energy Loss Spectroscopy), to be a fine oxide layer. This layer persisted throughout the experiments at all temperatures. By using dark field imaging the nanoparticle beneath the oxide layer is highlighted as seen in Figure 71. The dark field image was obtained by tilting the electron beam so that the diffraction spot highlighted in Figure 72 was centered.

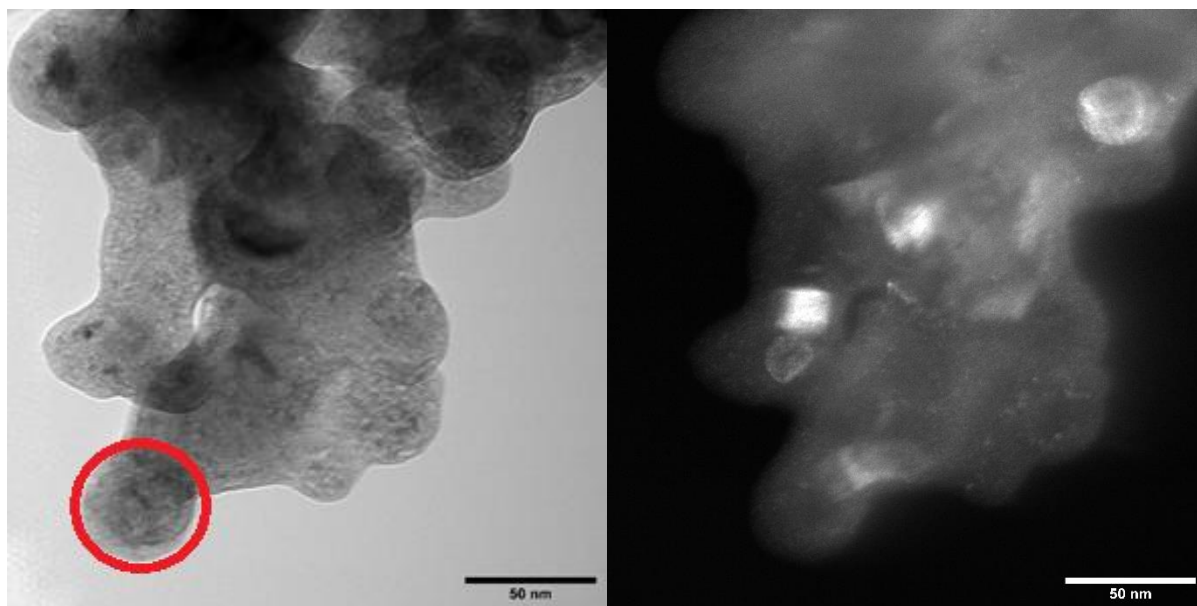


Figure 71 ZrC NP Prior to Irradiation BF and DF Red Ring Highlighting SAA Position. Dark Field Beam Highlighted in Figure 81

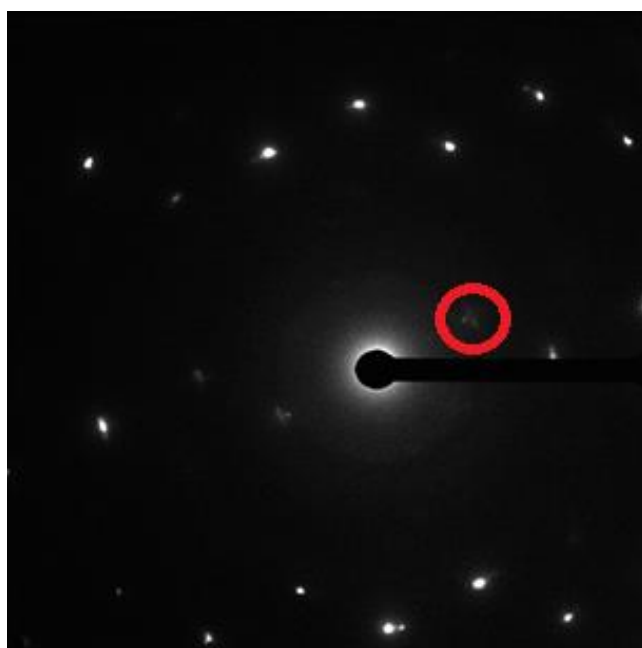


Figure 72 ZrC NP Diffraction Pattern Prior to Irradiation Red Ring Highlights DF in Figure 80

5.2.3 Helium Bubble Formation and Evolution in Nanoparticles

Across all temperatures beginning at 1 DPA small bubbles of $\sim\varnothing 1\text{nm}$ in size were observed to begin forming in the oxide layer on the nanoparticles. This was predominantly where the bubbles were observed to be forming. They likely form at the interface between the ZrC and ZrO layer as this will act as a defect sink. The bubbles were observed to form across all particle diameters. Figure 73 highlights some of these bubbles.

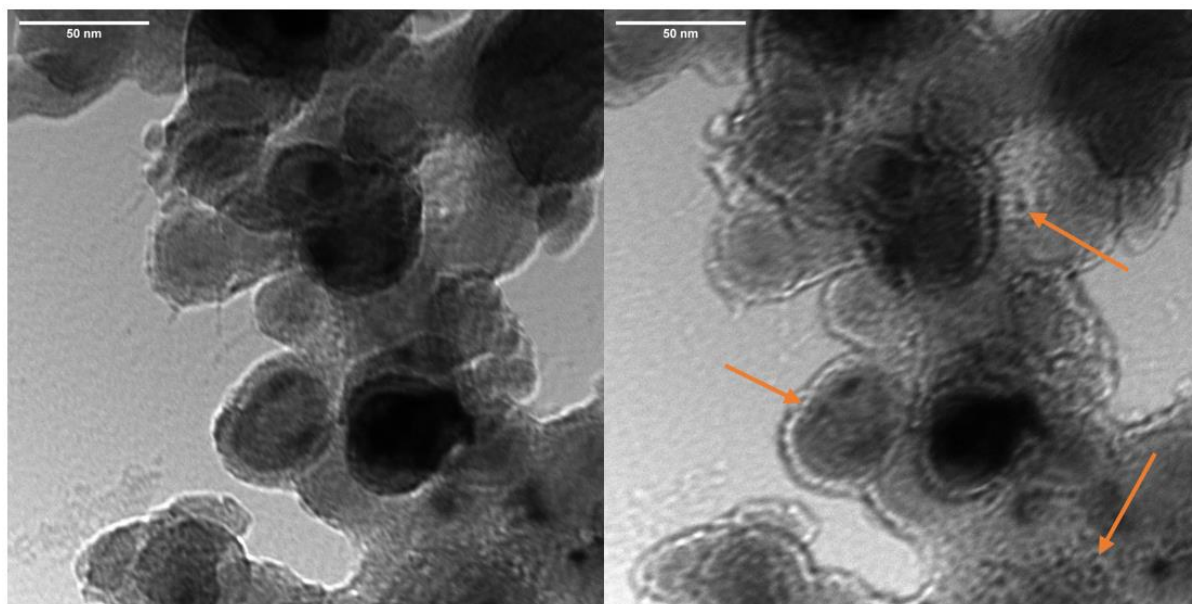


Figure 73 ZrC NP 400°C 1DPA under and over focus with example of bubbles highlighted

5.2.4 Sputtering

Throughout the experiments the main changes that were observed to occur in the nanoparticles microstructures was a sputtering of the surface. This can be seen in both the bright field images, where sputtered material can be seen accumulating on the carbon film (see Figure 75), and the diffraction patterns where extra reflections can be seen (see Figure 74). It is safe to assume that the material sputtered came from the ZrC particles as the only other material present was the amorphous carbon film and the sputtered material shows diffraction spots. In the cases where sputtering is observed to be widespread, such as Figure 75, the diffraction pattern begins to resemble a polymorphous material. This is a result of the sputtered material remaining crystalline yet being sat at different orientations on the film. It was noted that the amount of sputtering was dependent both on temperature and

fluence. At room temperature no sputtering occurred across all DPA levels. By contrast at 800°C the amount of sputtering was great even at 1DPA.

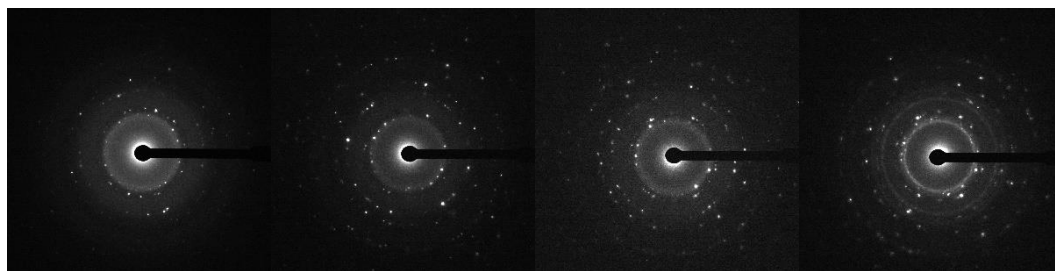


Figure 74 Diffraction Patterns ZrC 400°C 0DPA, 1DPA, 2DPA, 3DPA Left to Right

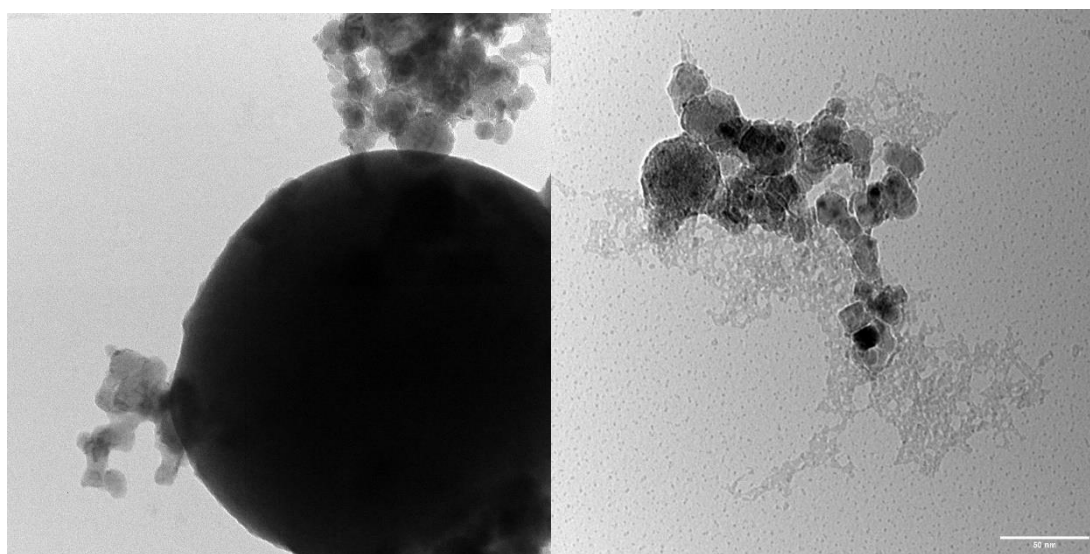


Figure 75 Left Image Shows ZrC 800°C Prior to Irradiation, No Sputtered Material Can be Seen on the Thin Film. Right Image Shows ZrC 800°C 3DPA With Sputtered Material on the Thin Film

5.2.5 Amorphization

At 600°C it was found that the particles began to become polycrystalline. This phenomenon was not observed at other temperatures. The polycrystallisation began to form at 2 DPA, see Figure 78. At 3 DPA, see Figure 79, the rings appeared more amorphous but individual diffraction spots remained visible showing that the particles had not become fully amorphous. No other defects were observed that could be attributed to this effect. An overview of the diffraction pattern changes at various temperatures can also be viewed in Figure 80.

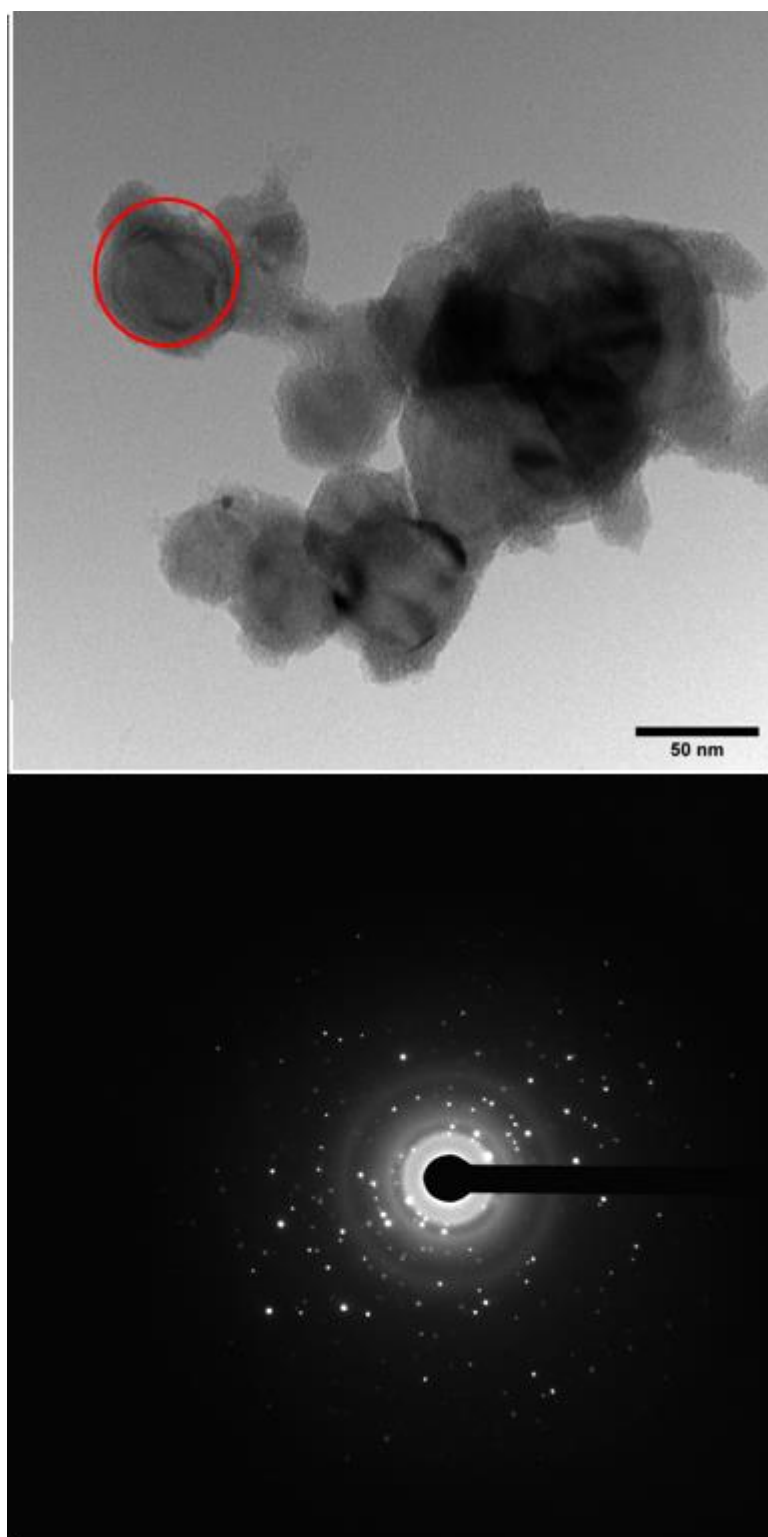


Figure 76 Diffraction Pattern of ZrC Nanoparticles at 0DPA 600°C Red ring highlights SAA

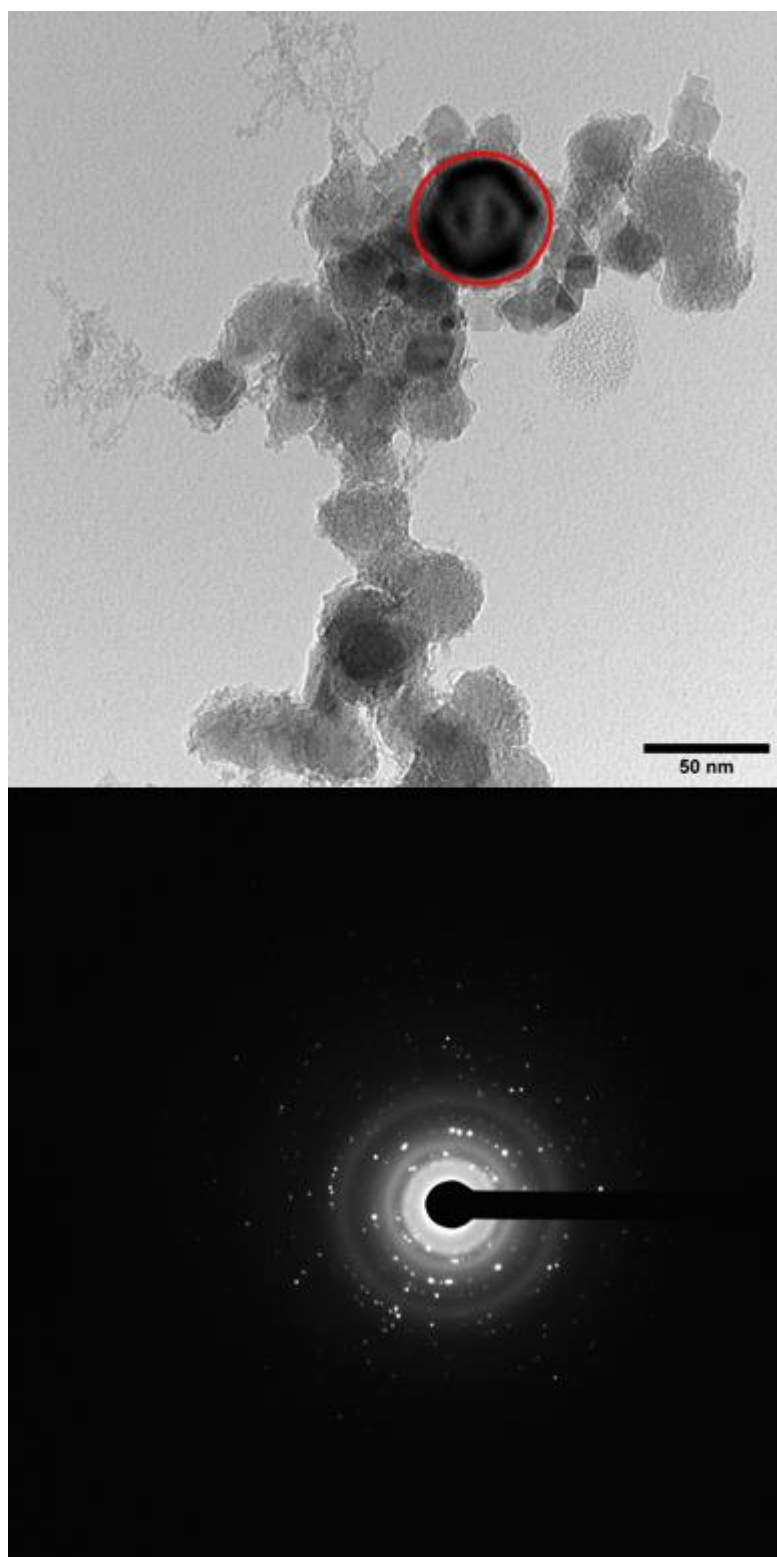


Figure 77 Diffraction Pattern of ZrC Nanoparticles at 1DPA 600°C Red ring highlights SAA

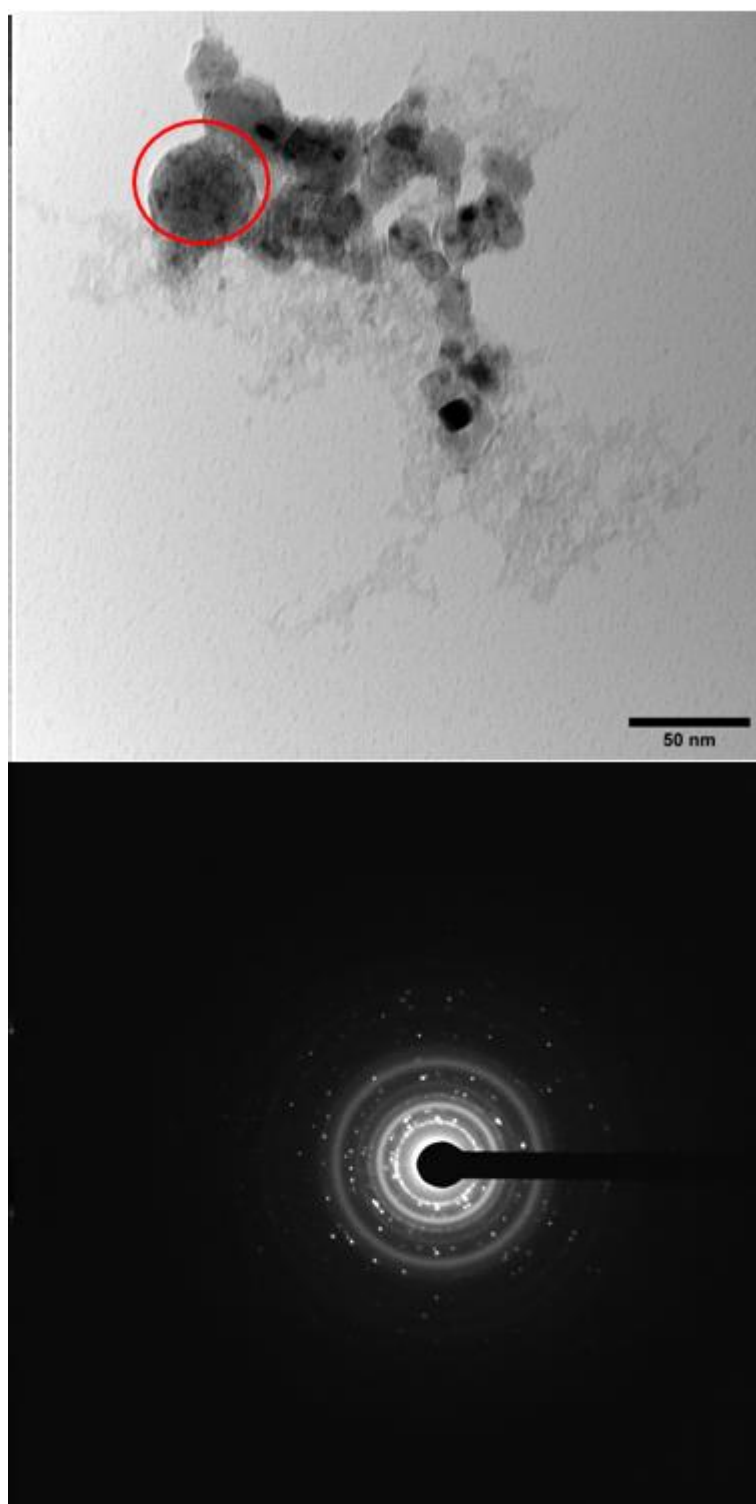


Figure 78 Diffraction Pattern of ZrC Nanoparticles at 2DPA 600°C Red ring highlights SAA

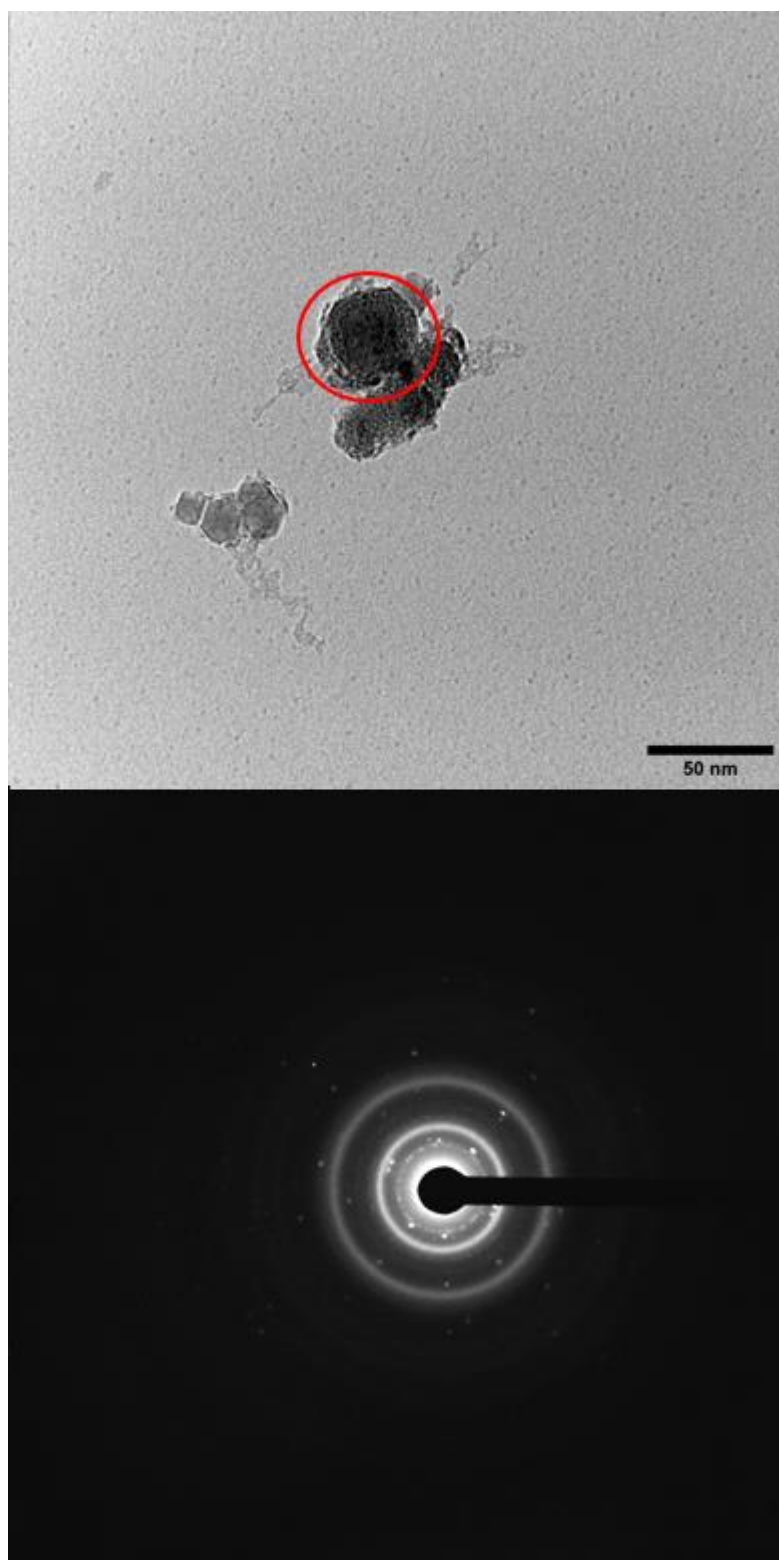


Figure 79 Diffraction Pattern of ZrC Nanoparticles at 3DPA 600°C Red ring highlights SAA

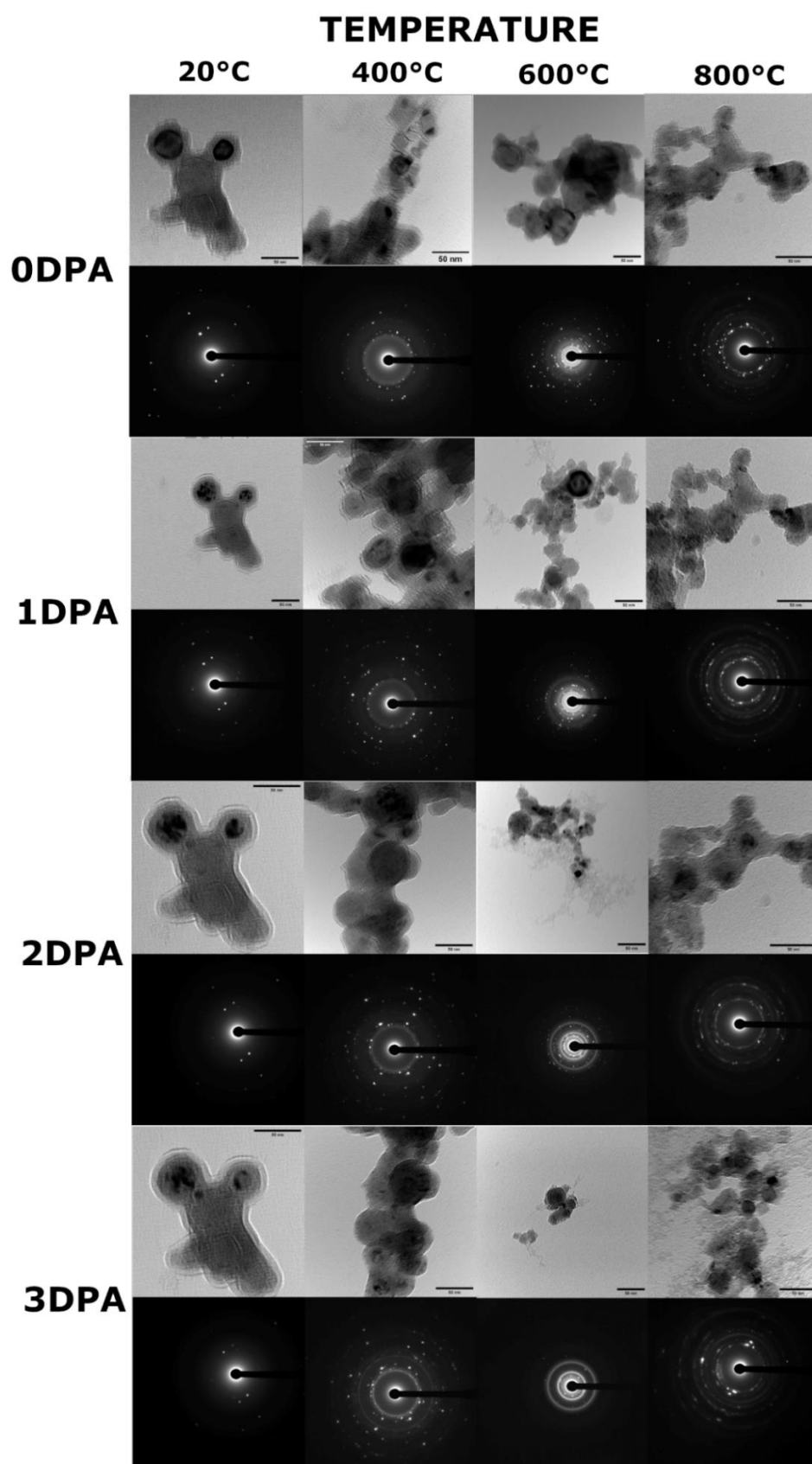


Figure 80 Changes in Nanoparticle Diffraction as a Function of DPA and Temperature

5.3 Experiments on Microparticles

Accompanying the nanoparticle experiments were a series of ion irradiations on ZrC microparticles. To best gain an insight on how the size difference will affect the radiation tolerance all ion irradiation and temperature parameters were kept the same. The ZrC microparticles were of various sizes, observed to be $\sim 0.1 - 5\mu\text{m}$ in the TEM, and thicknesses ranging from electron transparent to complete blocking of the electron beam. Only the electron transparent areas ($\sim 1000\text{ \AA}$) were used for study. This technique is similar to how thin films are experimented upon.

Prior to irradiation some strain fields were present within the microparticles. These were most likely formed during the crushing process at sample preparation and an example is provided and highlighted in Figure 81.

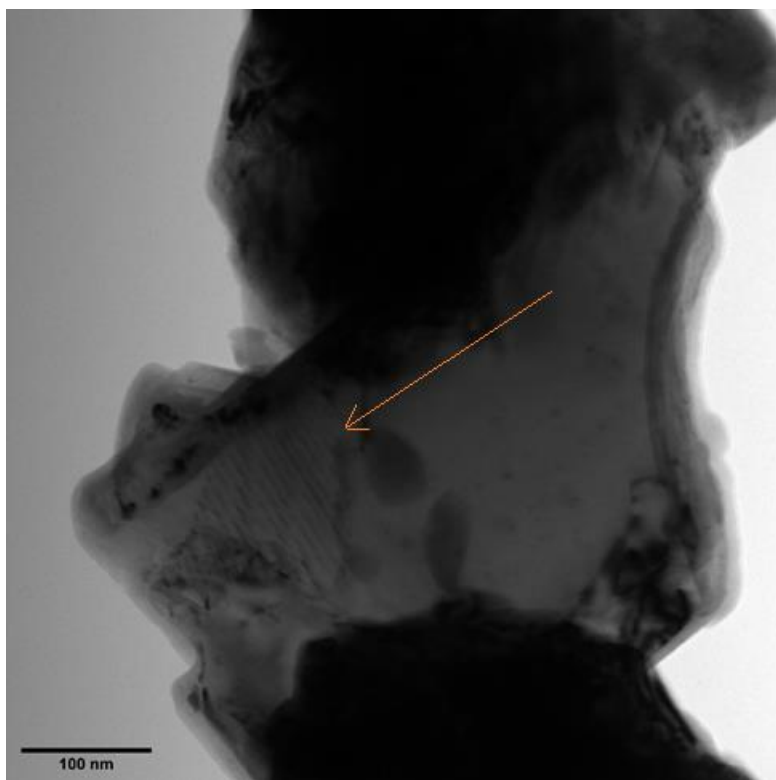


Figure 81 Microparticle prior to irradiation

5.3.1 SRIM Calculations for Microparticles

Prior to experimentation SRIM calculations were performed using 10^3 9keV helium ions incident upon a target of stoichiometric ZrC with a density of 6.73 g/cm^3 . The ion beam

angle was set to 18.7° for the calculations to match the angle of incidence on the MIAMI-2 system. Figure 82 Shows at what depth the collisions occurred. **Error! Reference source not found.** shows the number and depth of helium knock-ons, **Error! Reference source not found.** shows the number and depth of zirconium vacancies, and Figure 83 shows the number and depth of carbon vacancies.

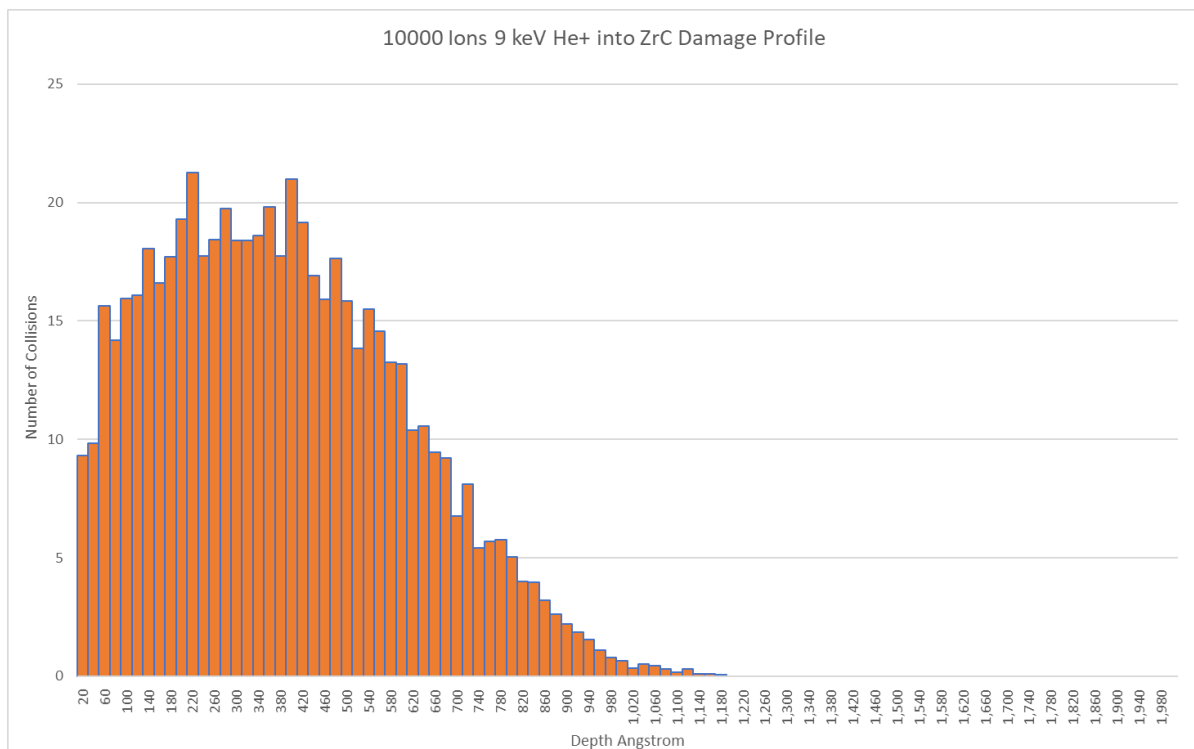


Figure 82 Graph of Number of Collisions in 20 Angstrom Steps for 9keV Helium Ions into ZrC

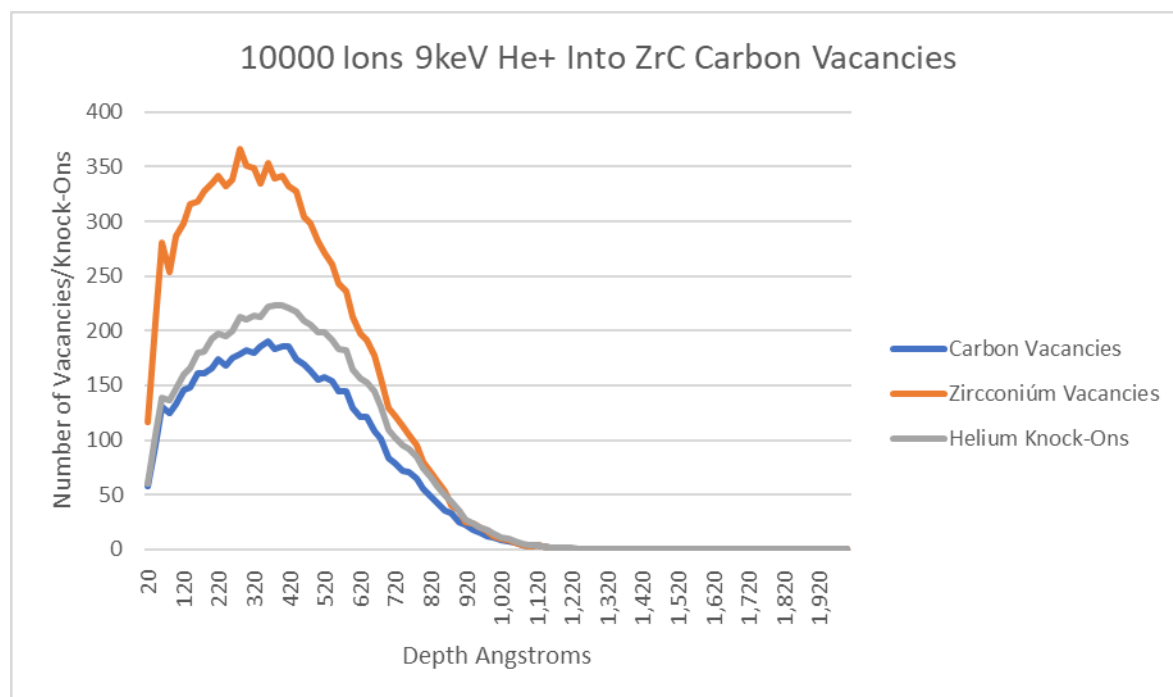


Figure 83 Graph of Number of Zirconium and Carbon Vacancies, and Helium Knock-Ons in 20 Angstrom Steps for 9keV Helium Ions into ZrC

The graphs highlight that the experiments would cause significant damage throughout the entire thickness of the electron-transparent area of the samples (~1000 Å). They also highlight that more zirconium vacancies will be produced compared to carbon and that the number of helium knock-ons is higher than the number of carbon vacancies yet less than the number of zirconium ones. These results would indicate that as more damage occurs carbon rich areas may begin to manifest in the sample as zirconium is either sputtered away or forms an interstitial. However, it is worth remembering that SRIM considers a material to be amorphous so exact details of where the displaced zirconium ends up cannot be accurately calculated with this software.

5.3.2 He Bubble formation and Evolution in Microparticles

During irradiation of the microparticles at room temperature helium bubbles ~Ø1nm began to form at the edge of the particles yet away from the oxide layer. This process began at 0.5DPA. The bubbles did not grow in size but throughout the irradiation they began forming

throughout the sample and grew in density, an example of this is shown in Figure 86. To gain an insight as to how bubble density varied as a function of temperature and DPA images from the particles were analysed using FIJI software suite. This analysis was done by selecting an area of an image measuring 50x50nm applying a UnSharp Mask filter and manually counting the number of bubbles observable. This was done at 3 different areas in the sample to account for thickness variations and an average value was calculated. Figure 84 shows an example of bubbles observed and a 50x50 window selected, and Figure 85 shows an example of processed image.

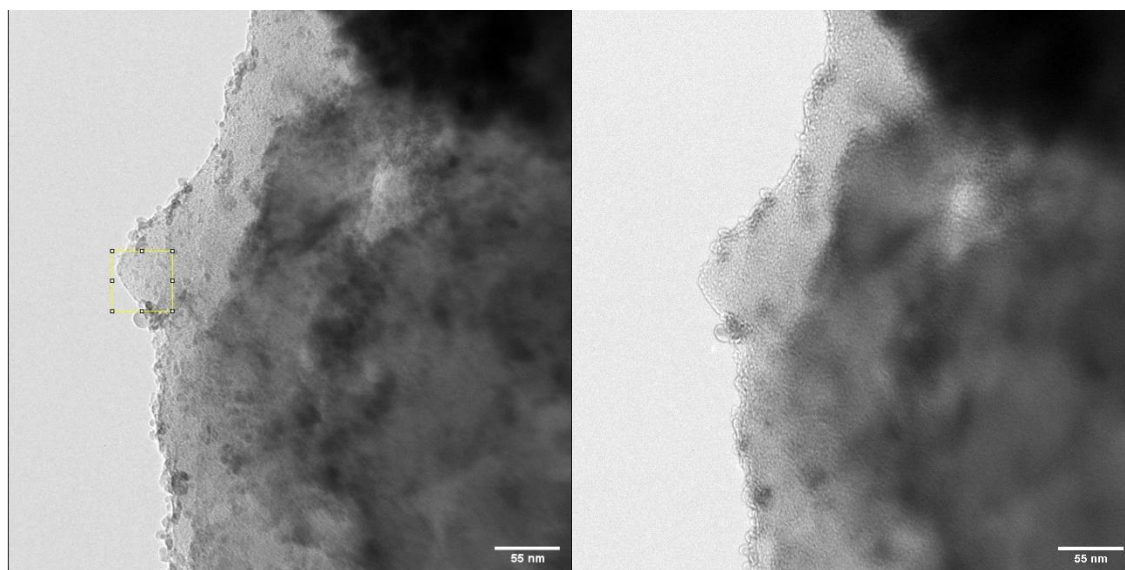


Figure 84 ZrC Microparticle 600°C 2DPA Showing Example of 50x50nm Selection Area Highlighted in the Yellow Box Expanded Image in Figure 85

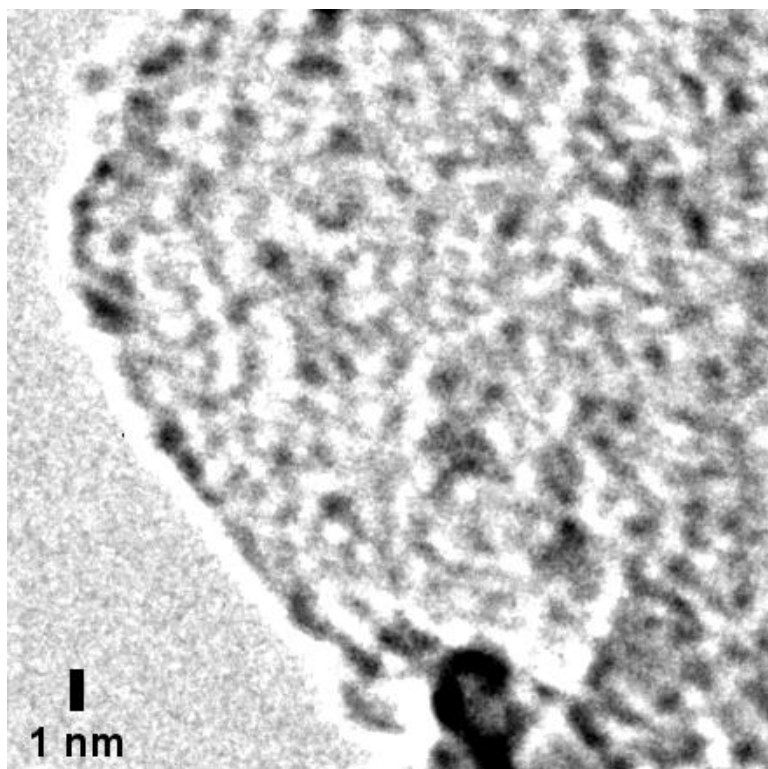


Figure 85 50x50nm Area Used to Analyse Bubble Density with UnSharp Mask Filter Applied Underfocus with the White Circles Being the Observed Bubbles

He Bubble Formation 400°C

0.3 DPA

3DPA

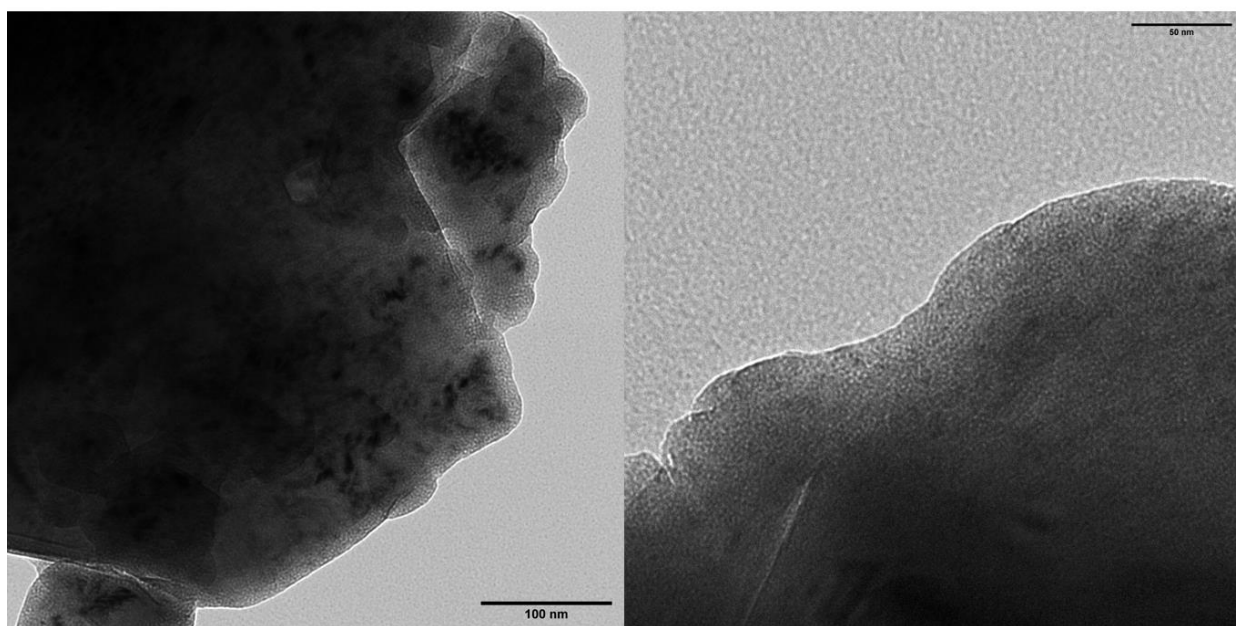


Figure 86 Helium Bubble Density Changes Between 0.3 and 3 DPA 400°C ZrC Microparticles

Whilst it was possible to observe the same area in the case of room temperature and 400°C experiments, the experiments at 600°C and 800°C contain other particles due to particles being lost during experiments. Therefore, the data on these experiments are not as accurate. They have been presented here to try to show where saturation occurs. The data can be seen in Figure 87 with different particles highlighted in different colours.

	0DPA	0.5DPA	1DPA	1.5DPA	2DPA	2.5DPA	3DPA
RT M1	0	0	15	24	36	57	57
RT M2	0	0	8	17	30	51	51
400°C	0	0	6	19	22	30	43
600°C	0	14	20	20	94	94	94
800°C	0	0	7	41	56	70	71

Figure 87 Data on number of bubbles observed in 9keV He irradiated ZrC Microparticles. Different colours represent different particles. Room Temperature was conducted on both MIAMI 1 and 2, MIAMI 1 is noted as M1.

It most cases bubbles did not manifest until 1 DPA which equates to 219,000 appm of He implantations as calculated with the pre-experiment SRIM calculations. However, bubbles were observed at 0.5 DPA in the case of 600°C. It is unlikely that bubbles were present at 0.5 DPA at the other temperatures but were not visible in the area being observed, as during the experiment various microparticles were screened between irradiation steps. Bubble saturation also differs at different temperatures. At room temperature no more bubbles formed after 2.5 DPA. At 400°C bubble density was still rising when 3 DPA was reached. Unfortunately, the data at 600°C is inconclusive. It would appear at first that the saturation occurs at 2 DPA, however the particle being observed was lost due to grid tearing leading to a different particle being observed, which may invalidate the result. Between 1 and 1.5 DPA at 600°C no extra bubbles were observed to form. This leaves a question as to whether saturation was reached at 1 or 2 DPA. At 800°C the bubbles appeared to be almost completely saturated at 2.5 DPA with only one extra seen to have formed. However, due to the different particles being observed conclusions about bubble density cannot be assumed. Figure 88 plots the results.

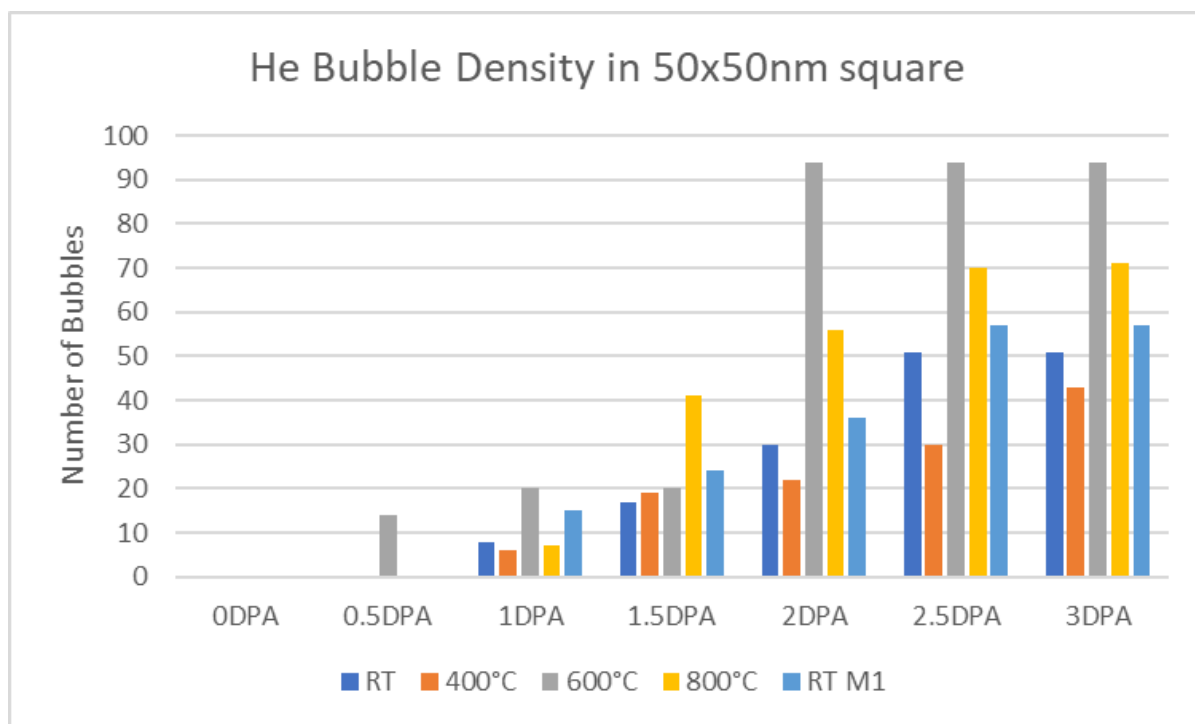


Figure 88 He Bubble Density in 50x50nm Square Section of ZrC Microparticles as a Function of DPA and Temperature

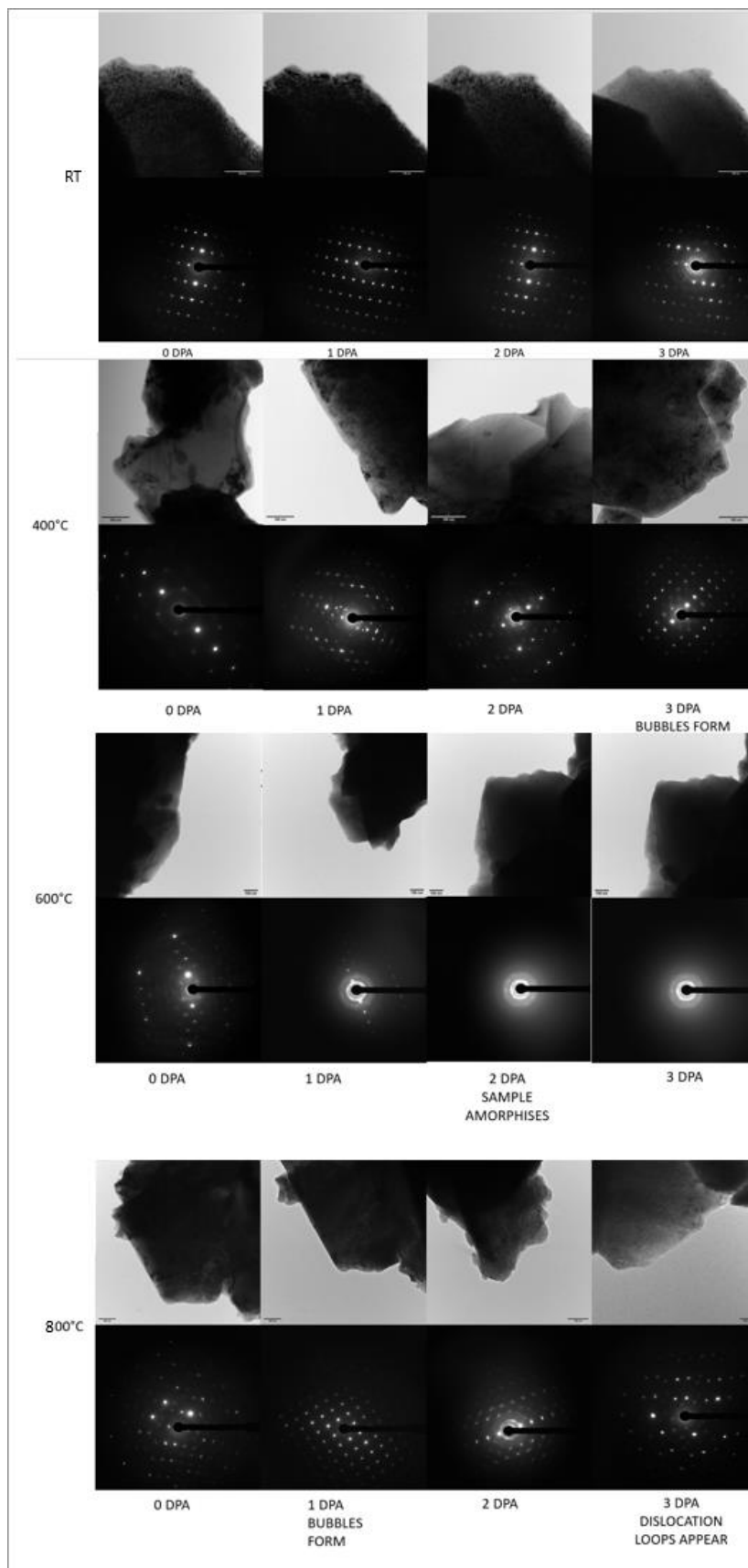


Figure 89 Overview of Microparticle Evolution Under 9keV He Ion Irradiation

5.3.3 Sputtering

Sputtering was observed in the experiment at 400°C but not at any other temperature. It is safe to assume that the material sputtered came from the ZrC particles as the only other material present was the amorphous carbon film and the sputtered material shows diffraction spots. The sputtered material could be seen in the form of small dark spots present on the carbon thin film when at focus. Figure 90 shows this. The left side of the image is the carbon film where small dark spots are visible. The right-hand side of the image is the microparticle.

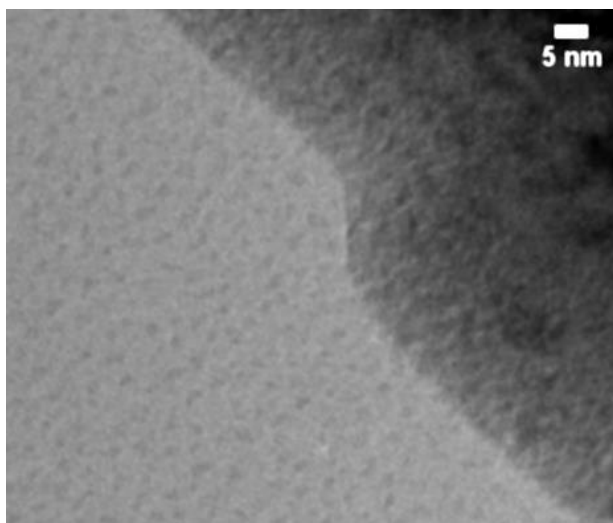


Figure 90 Image of ZrC at 400°C 3DPA Left part of image is Carbon Grid, Right is Microparticle

5.3.4 Amorphization

At 600°C in the microparticle samples amorphised. To ensure that this was not an erroneous result the experiment was repeated multiple times, with particles of various sizes ranging from ~1 - 5µm with different crystallographic orientations, with the same results. Experiments were also conducted at 550°C and 650°C to discover if the same effect occurred. At 550°C no amorphization occurred and at 650°C the particles became amorphous. However, an additional experiment at 700°C found no amorphization. To gain an understanding of the process behind this behaviour the diffraction patterns at 600°C were analysed by finding the difference in grey values of the diffraction pattern. This allows an understanding of whether the amorphization is caused by the homogenous model or

heterogenous model.

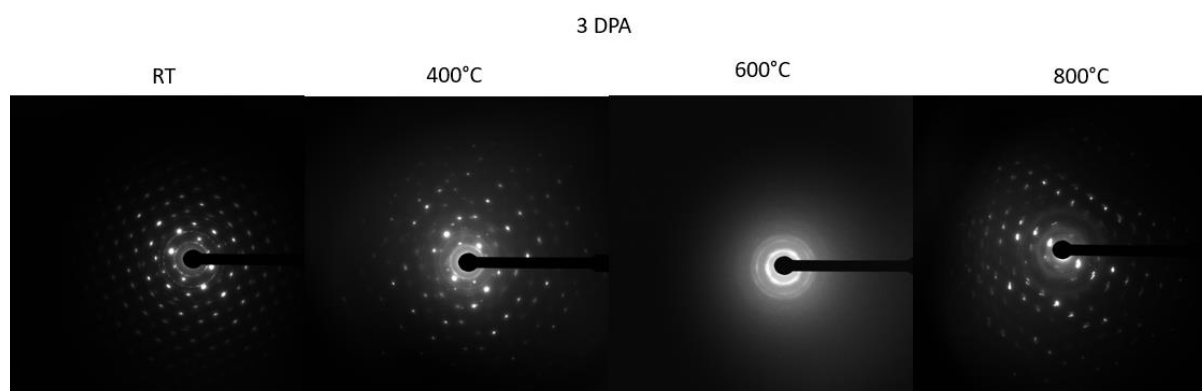


Figure 91 Crystallinity as a function of temperature at 3DPA

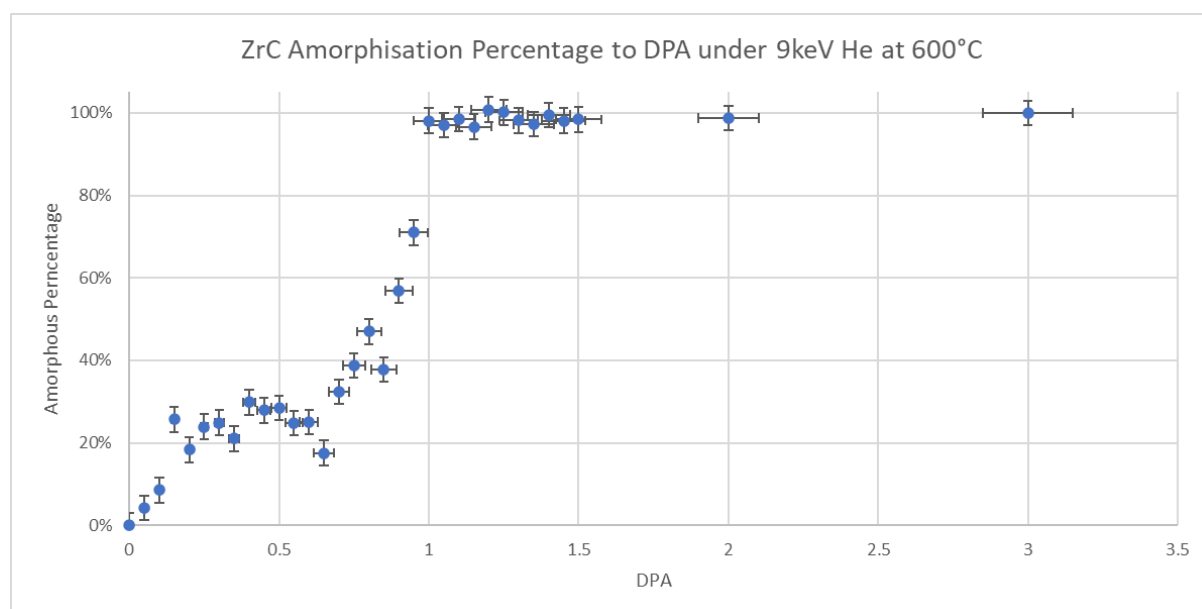


Figure 92 Scatterplot of ZrC Amorphisation Percentage to DPA Under 9keV He irradiation at 600°C

The data shown above 1.1 DPA in Figure 92 came from a different particle than the data preceding it with the sizes being approximately the same yet the crystallographic orientation being different. However, at 1.1 DPA the particles were fully amorphous allowing for the curve to be analysed. This produced a curve which can be seen in Figure 93. The curve highlights some strange behaviour in the amorphization of ZrC. Amorphisation initialises quickly but then plateaus between ~ 0.2 DPA and ~ 0.6 DPA before continuing rapidly.

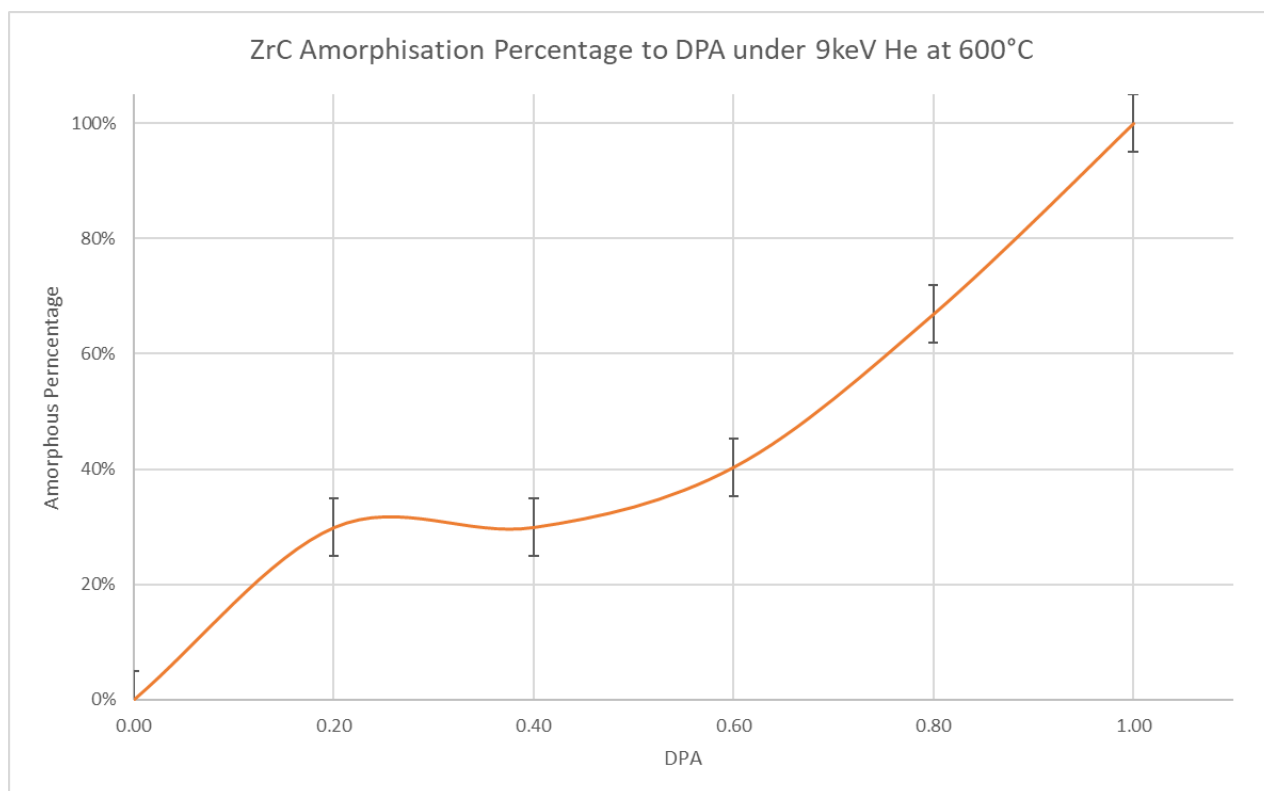


Figure 93 Smoothed line of ZrC Amorphisation Percentage to DPA Under 9keV He irradiation at 600°C

To ensure that the data collected was accurate an additional experiment was conducted under the same conditions with diffraction patterns taken every 0.2DPA up to 1DPA. The same plateau effect can be seen occurring between 0.2 and 0.6DPA. The data can be seen in Figure 94 and **Error! Reference source not found..**

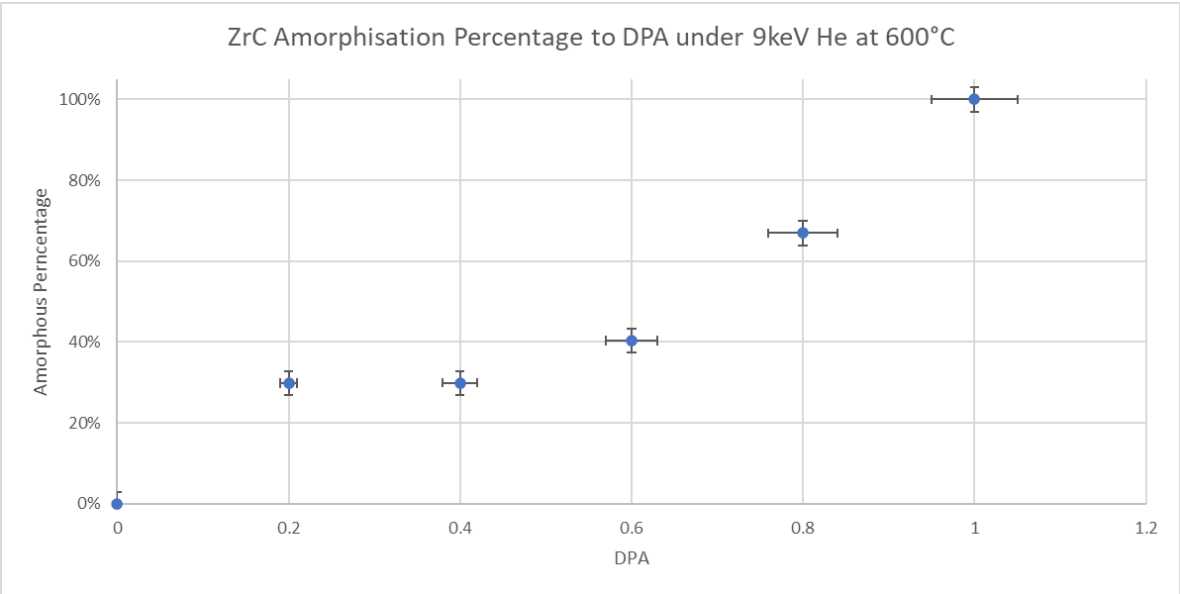


Figure 94 Scatterplot of ZrC Amorphisation Percentage to DPA Under 9keV He irradiation at 600°C Second Experiment Data

In addition to this the data was compiled onto single graphs for easier comparison. These can be seen in Figure 95 and Figure 96.

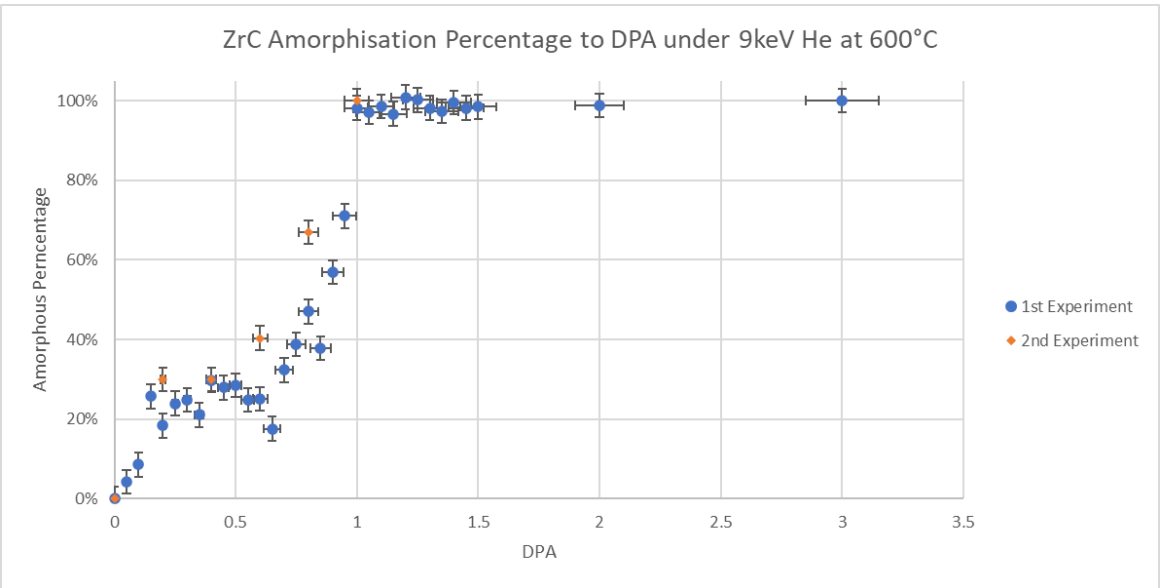


Figure 95 Scatterplot of ZrC Amorphisation Percentage to DPA Under 9keV He irradiation at 600°C Compiled Experiment Data

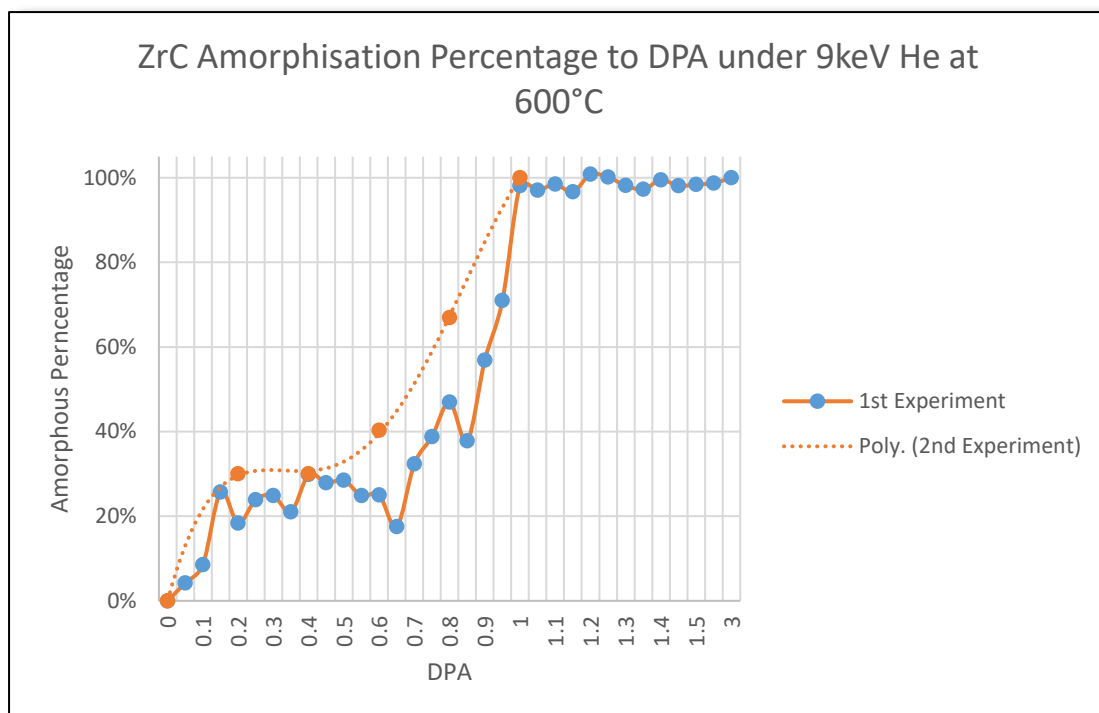


Figure 96 Smoothed line of ZrC Amorphisation Percentage to DPA Under 9keV He irradiation at 600°C Compiled Experiment Data

It can be seen that the same overall trend occurs in both experiments. Whilst the second experiment appears to have a higher amorphous percentage at 0.6 and 0.8 DPA, this may be attributed to a different particle being examined which will have had a different thickness yet remained in the electron transparent region.

When comparing the amorphisation curve to standard curves reported in the literature it becomes apparent that an unknown phenomenon appears to be at work. Under the homogenous model amorphization occurs abruptly due to defect density surpassing a threshold where it becomes more energetically favourable for the material to be in an amorphous state as opposed to a crystalline state with many defects. Under the heterogenous model a single ion impact creates an amorphous region which accumulates over multiple ion impacts to result in full amorphization. It is also possible for the two models to be at work simultaneously. Previous work by O. Camara et al[288] shows examples of the amorphization curves for different models. This can be seen in Figure 97 showing examples of the theoretical evolution of the amorphous fraction depending on the

proposed models for amorphization and where complete amorphization occurs at the same fluence.

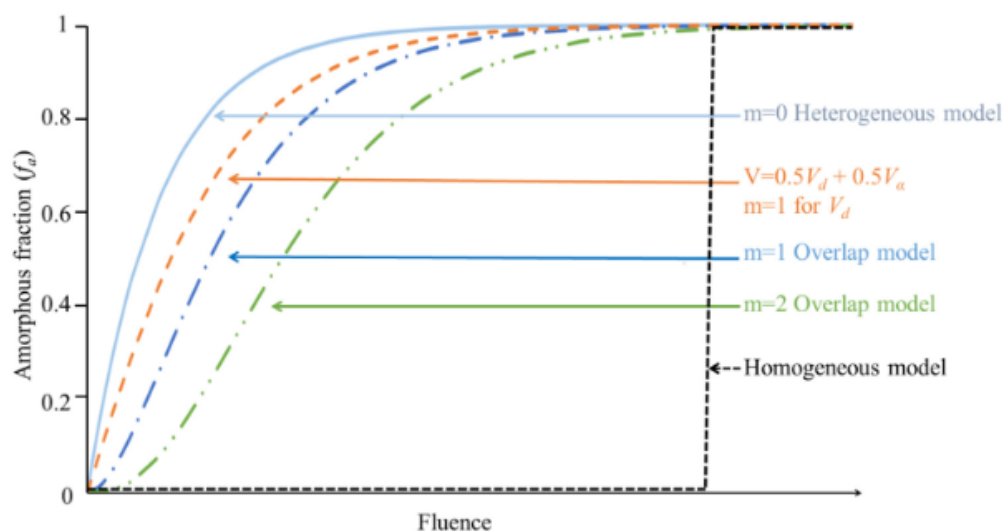


Figure 97 Schematic Showing Examples of The Theoretical Evolution of The Amorphous Fraction Depending on The Proposed Models For Amorphization And Where Complete Amorphization Occurs At The Same Fluence. Reproduced From O. Camara Et Al[288]

5.3.5 ZrC 9keV He+ Ion Irradiation Bubble Density Comparison

In order to gain quantifiable data to compare the MIAMI-2 system with the upgraded MIAMI-1 system an experiment was conducted on ZrC microparticles using the same irradiation conditions on each system. During irradiation steps the electron beam was blocked to prevent any interference effects. In the case of the MIAMI-1 experiment the sample was switched over to the MIAMI-2 system at every 0.5DPA for image acquisitions of the bubbles to be obtained. Great care was taken to ensure that the same particle was being examined each time and that the grid was not damaged or moved during switching sample holders. The bubble analysis was performed using the methods outlined in chapter 5.3.2 He Bubble formation.

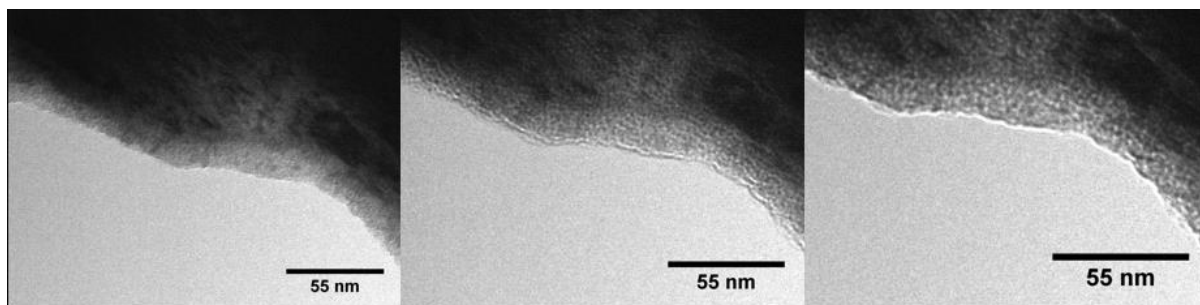


Figure 98 ZrC MP Irradiated on MIAMI-1 Using 9keV He+ at 2.5 DPA, screened on MIAMI-2 Showing Under Over and at Focus BF Images.

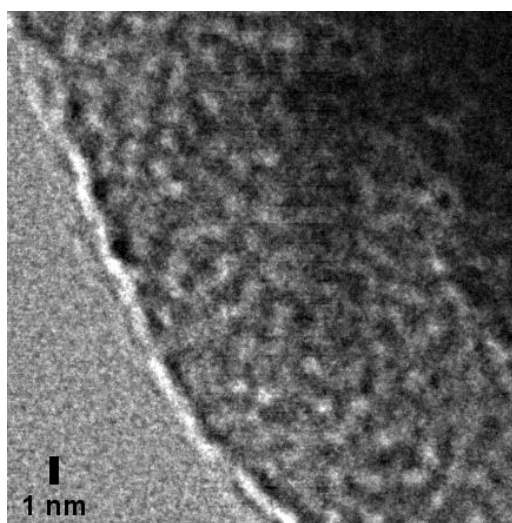


Figure 99 50x50nm Area Used to Analyse Bubble Density with UnSharp Mask Filter Applied Sample Irradiated on MIAMI-1

It was found that bubble saturation occurred at a very similar pace on both systems. Bubble formation saturated at 2.5 DPA in both cases, an example of which can be seen in Figure 98 and Figure 99. Whilst the total number of bubbles observed is not identical, this was due to different samples being screened. Potential errors in the results may come from a small counting error or a potential sample thickness difference, to reflect this error bars have been added to the analysis. An overview comparison of the results can be seen in Figure 100.

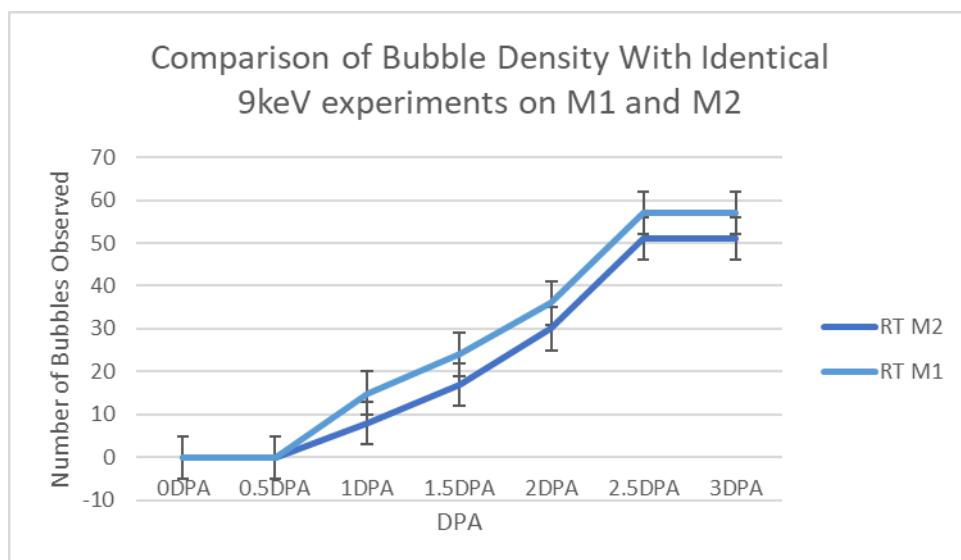


Figure 100 Comparison of Bubble Density with Identical 9keV experiments on M1 and M2

The general trendlines between the 2 systems matches very closely and should give some confidence that the MIAMI-1 system dosimetry measurements are correct.

5.4 Discussion

5.4.1 Nanoparticles vs Microparticles

Overall, the nanoparticles showed greater radiation damage resistance when compared to the microparticles with the exception of sputtering. Specific examples will be discussed in this section.

Bubbles were only observed forming in the nanoparticles at the ZrC/ZrO interface and without this interface it is safe to assume that the He would have escaped to a free surface. By comparison, the microparticles saw bubble formation across all temperatures. The bubbles formed in all cases, except 600°C, at 1 DPA. In the case of 600°C the bubbles began to form at 0.5 DPA. The bubbles in the microparticles were found to only reach a size of ~1nm. The increased bubble resistance of nanoparticles is typical when compared to their larger counterparts [2][73], [270], [274], [275]. E Aradi et al. found that when comparing He bubble formation in W nanoparticles vs their thin film counter parts that bubble formation occurred at lower fluences in the thin film and that the density in nanoparticles remained lower throughout the radiation. This result agrees with the results in this work showing the general trend that nanoparticles have a greater resistance to He bubbles vs their larger counter parts. This was also found to be the case in AISI 316 nanoparticles compared to thin films as well as SiC nanowhiskers compared to thin films. Adding to this evidence work carried out on Au nanofoams also found that the enhanced surface to volume ratio leads to a reduction in vacancy production. All of these findings support the narrative that nanomaterials display enhanced radiation endurance.

The microparticles were found to amorphise at 1 DPA at 600°C. At other temperatures the samples remained crystalline. By comparison the nanoparticles did not amorphise, but at 600°C they did become polycrystalline at 2 DPA. It has been reported in the literature that nanoparticles generally resist amorphization in comparison to larger particles. For example, in 4H SiC a relatively-high critical dose for amorphisation (5 dpa) was observed in NWs for irradiations below room temperature compared to thin foils (0.7 dpa). It may be possible to amorphise ZrC nanoparticles if the fluence was taken to a much higher dpa level.

Amorphisation was also completely avoided for NWs irradiated above 200 K – lower than

the critical temperature in the foils which was ~ 300 K[274]. However, the results in this work only show partial amorphisation at 600°C and the results obtained appear to show that this is a critical temperature. Therefore, lowering the temperature in the case of ZrC would not appear to have a greater impact on the amorphisation.

The one area where the microparticles performed better than the nanoparticles is in their resistance to sputtering. Sputtered material was only observed on the thin film at 400°C in the case of microparticles. By comparison the nanoparticles sputtered at 400°C , 600°C , and 800°C . The amount of sputtering was observed to increase as a function of both temperature and DPA. It would be expected that nanoparticles would sputter more than the microparticles due to their large surface to volume ratio. This is backed up by previous experiments conducted on nanomaterials where the amount of sputtering was observed to increase with the increase in surface area to volume ration. For example in Au nanoporous material a large amount of sputtering was observed and was linked directly to the ligament size[266].

5.4.2 ZrC compared to SiC

As some have suggested replacing SiC with ZrC in materials such as TRISO[154]–[156] the results obtained are herein compared with literature reports of SiC.

It was found in the nanoparticles that a small oxide layer formed on the surface. This suggests that oxide layers will form readily on ZrC, which agrees with literature reports. This is similar to what has been reported on SiC where two levels of oxidation occur. These are the active and passive regions. The passive region is a surface scale of SiO_2 that forms at high partial oxygen pressures and temperatures. This scale acts as a barrier layer and prevents further oxidation of the compound. Any impurities within the SiC will accelerate

the oxidation process. Active regions appear when SiC is subjected to very high temperatures and a low partial pressure of oxygen. These regions are SiO and will form without the presence of the SiO₂ layer. It has been found that SiO₂ becomes soluble in water especially LWR conditions. This leads to mass loss of the SiC and in time could lead to the material dissolving as the oxide layer is removed, allowing further oxidation of the SiC which is then removed again, and so forth [191]. This effect could be countered by placing a barrier material between the SiC and coolant. In this case there will be no real advantage in using ZrC in place of SiC.

SiC has been reported to amorphise at 1 DPA at room temperature, see 2.9.8 Neutron Irradiation. By comparison with ZrC it was found in this work that amorphisation only occurs around 600°C at the same 1 DPA. This suggests that in low temperature reactor environments ZrC will perform better than SiC.

SiC has been shown to form bubbles under helium irradiation which grow in size with increasing temperatures. It has also been reported that these bubbles will eventually form platelets at ~800°C, see 2.9.9 Ion Irradiation. This work found that helium bubbles formed in ZrC microparticles and increased in density with DPA. However, the bubbles did not grow in size beyond ~1 DPA and at no point were platelets seen to form. The reduced size of the bubbles should lead to a reduction in the amount of swelling that the material undergoes during radiation. However, as the density increases the amount of swelling will increase also.

5.5 Future Recommendations

The amount of sputtering observed in the nanoparticles is not insignificant and if the material was developed into a nano porous variety may lead to some of the ligaments weakening and potentially breaking away from the material. Therefore, the materials lifespan may be reliant upon the amount of sputtering that it undergoes as other defects do not seem to readily form. To gain a true insight as to how much sputtering the material can withstand nano porous form would require fabricating and testing ex-situ to allow a thickness greater than that of a TEM sample. The sample would then require thinning down and analysing.

Whilst the reason for the amorphization remains unknown the discovery is an important find and could have a significant impact on whether ZrC would be a good choice of material given the reactor environment. It may also help to understand some of the bonding characteristics of the material and how they change at a given temperature. More work needs to be undertaken to better understand this process, it would be interesting to know if annealing the material after amorphization will lead to recovery or not.

Unfortunately, the grids used during experimentation would often tear leading to different areas of the sample being observed and making it difficult to maintain exact focus conditions. If a stronger grid could be sourced re conducting the experiments would lead to clearer to read images. Due to time constraints this was not possible in this work.

6 Conclusions

This report set out to investigate how radiation damage affects materials. A solid background understanding was established in the literature review to gain understanding into the various defects, their production and mobility, as well as effects on a materials behaviour. Part of this review highlighted potential new materials for use in reactor design and identified any shortfalls in the literature. A section dedicated to SiC was written up in detail as ZrC is seen as a potential replacement for this material. By summarising the various characteristics of the two materials a comparison can be drawn. Accompanying this was an overview of how TEMs work. This was necessary to ensure that the modification of the MIAMI-1 system did not negatively impact the TEM imaging capabilities.

The MIAMI 1 system was upgraded to allow for future researchers to perform valuable experiments in these undertakings. This involved the design, manufacture, and assembly of a large number of bespoke components. Whilst it was not possible in the time frame to perform a complete verification of the systems performance in relation to other systems the work of building the system was no small undertaking. The system is ready for use, and it is hoped that future researchers will be able to use it to further human knowledge of science.

Code was developed to simulate the differences between nanomaterials and their thin film counterparts. This code has already seen use in several scientific papers[73], [270]–[272], [274] and it will allow future users to perform more accurate pre-experiment calculations.

A set of experiments were conducted on ZrC micro and nanoparticles under He ion irradiation to fill a gap in the literature and provide valuable insight into the materials characteristics. A method of amorphising ZrC was discovered and an understanding of how He bubbles agglomerate and accumulate was achieved.

In all cases recommendations for future work was made.

7 References

- [1] IMechE (Institution of Mechanical Engineers), *Engineering the UK Electricity Gap*. 2016.
 - [2] BEIS, "Coal Generation in Great Britain - The pathway to a low-carbon future: consultation document," 2016.
https://www.gov.uk/government/uploads/system/uploads/attachment_data/file/577080/With_SIG_Unabated_coal_closure_consultation_FINAL__v6.1_.pdf.
 - [3] Nuclear AMRC, "UK new build plans," *Industry Intelligence*, 2015.
<http://namrc.co.uk/intelligence/uk-new-build-plans/> (accessed Oct. 09, 2017).
 - [4] G. E. N.-IV International-Forum, "A Technology Roadmap for Generation IV Nuclear Energy Systems," 2002.
 - [5] J. L. B. B.Mastel, "Voids in neutron irradiated," *J. Nucl. Mater.*, vol. 29, pp. 123–125, 1969, doi: 10.1002/pssa.2210050131.
 - [6] R. Garner, "How to Protect Astronauts from Space Radiation on Mars," *NASA.gov*, pp. 1–19, 2015, Accessed: Oct. 09, 2017. [Online]. Available:
<https://www.nasa.gov/feature/goddard/real-martians-how-to-protect-astronauts-from-space-radiation-on-mars>.
 - [7] L. de B.-A. der Physik and undefined 1925, "Researches on the quantum theory."
 - [8] C. Davisson and L. H. Germer, "Diffraction of electrons by a crystal of nickel," *Phys. Rev.*, vol. 30, no. 6, pp. 705–740, Dec. 1927, doi: 10.1103/PhysRev.30.705.
 - [9] M. Knoll, "Kathodenstrahl-Oszillograph Erzeugung und Sammlung des Elektronenstrahls," *Tech. Mess.*, vol. 1–12, no. JG, pp. 459–462, Dec. 1931, doi: 10.1524/teme.1931.112.jg.459.
 - [10] F. Krumeich, "Some Milestones in the History of Electron Microscopy."
-

<https://academic.oup.com/jmicro/article-lookup/doi/10.1093/jmicro/dfp012>
(accessed Dec. 04, 2017).

- [11] T. Mulvey, "The electron microscope: The British contribution," *J. Microsc.*, vol. 155, no. 3, pp. 327–338, Sep. 1989, doi: 10.1111/j.1365-2818.1989.tb02894.x.
 - [12] D. B. Williams and C. B. Carter, "Scattering and Diffraction," in *Transmission Electron Microscopy*, Boston, MA: Springer US, 2009, pp. 23–38.
 - [13] E. Rutherford, "The scattering of α and β particles by matter and the structure of the atom," *Philos. Mag. Ser. 6*, vol. 21, no. 125, pp. 669–688, May 1911, doi: 10.1080/14786440508637080.
 - [14] *JEOL TEM 2000FX Manual*. .
 - [15] J. A. Hinks, "A review of transmission electron microscopes with in situ ion irradiation," *Nucl. Instruments Methods Phys. Res. Sect. B Beam Interact. with Mater. Atoms*, vol. 267, no. 23–24, pp. 3652–3662, 2009, doi: 10.1016/j.nimb.2009.09.014.
 - [16] K. Hojou, S. Furuno, T. Soga, and K. Izui, "New in-situ parallel-detection electron energy-loss spectroscopy of SiC crystals irradiated with hydrogen ions," *J. Nucl. Mater.*, vol. 179–181, no. PART 1, pp. 411–414, 1991, doi: 10.1016/0022-3115(91)90112-K.
 - [17] R. F. Egerton, "An Introduction to EELS," in *Electron Energy-Loss Spectroscopy in the Electron Microscope*, Boston, MA: Springer US, 2011, pp. 1–28.
 - [18] J. Goldstein, *Scanning electron microscopy and x-ray microanalysis*. Kluwer Academic/Plenum Publishers, 2003.
 - [19] J. H. Pushker Kharecha, "Coal and gas are far more harmful than nuclear power," 2013. <https://climate.nasa.gov/news/903/coal-and-gas-are-far-more-harmful-than-nuclear-power/>.
-

- [20] World Nuclear Association, "Nuclear Reactors | Nuclear Power Plant | Nuclear Reactor Technology - World Nuclear Association," 2017. <http://www.world-nuclear.org/information-library/nuclear-fuel-cycle/nuclear-power-reactors/nuclear-power-reactors.aspx> (accessed Nov. 06, 2017).
 - [21] OECD Nuclear Energy Agency, "Technology Roadmap Update for Generation IV Nuclear Energy Systems," pp. 1–66, 2014, [Online]. Available: <https://www.gen-4.org/gif/upload/docs/application/pdf/2014-03/gif-tru2014.pdf>.
 - [22] G. Locatelli, M. Mancini, and N. Todeschini, "Generation IV nuclear reactors: Current status and future prospects," *Energy Policy*, vol. 61, pp. 1503–1520, 2013, doi: 10.1016/j.enpol.2013.06.101.
 - [23] M. K. Meyer, R. Fielding, and J. Gan, "Fuel development for gas-cooled fast reactors," *J. Nucl. Mater.*, vol. 371, no. 1–3, pp. 281–287, 2007, doi: 10.1016/j.jnucmat.2007.05.013.
 - [24] T. Obara, T. Koga, T. Miura, and H. Sekimoto, "Polonium evaporation and adhesion experiments for the development of polonium filter in lead-bismuth cooled reactors," *Prog. Nucl. Energy*, vol. 50, no. 2–6, pp. 556–559, 2008, doi: 10.1016/j.pnucene.2007.11.039.
 - [25] H. G. MacPherson, "The Molten Salt Reactor Adventure," *Nucl. Sci. Eng.*, vol. 90, no. 4, pp. 374–380, 1985, doi: 10.13182/NSE90-374.
 - [26] B. M. Elsheikh, "Safety assessment of molten salt reactors in comparison with light water reactors," *J. Radiat. Res. Appl. Sci.*, vol. 6, no. 2, pp. 63–70, 2013, doi: 10.1016/j.jrras.2013.10.008.
 - [27] S. J. Zinkle, K. A. Terrani, J. C. Gehin, L. J. Ott, and L. L. Snead, "Accident tolerant fuels for LWRs: A perspective," *J. Nucl. Mater.*, vol. 448, no. 1–3, pp. 374–379, 2014, doi: 10.1016/j.jnucmat.2013.12.005.
-

- [28] M. Ben-Belgacem, V. Richet, K. A. Terrani, Y. Katoh, and L. L. Snead, "Thermo-mechanical analysis of LWR SiC/SiC composite cladding," *J. Nucl. Mater.*, vol. 447, no. 1–3, pp. 125–142, 2014, doi: 10.1016/j.jnucmat.2014.01.006.
 - [29] K. A. Terrani, S. J. Zinkle, and L. L. Snead, "Advanced oxidation-resistant iron-based alloys for LWR fuel cladding," *J. Nucl. Mater.*, vol. 448, no. 1–3, pp. 420–435, 2014, doi: 10.1016/j.jnucmat.2013.06.041.
 - [30] C. Cawthorne and E. J. Fulton, "Voids in Irradiated Stainless Steel," *Nature*, vol. 216, pp. 575–576, 1967, doi: 10.1038/216575a0.
 - [31] Y. Hatamura, *The 2011 Fukushima nuclear power plant accident : how and why it happened*. 2015.
 - [32] Y. Katoh, K. A. Terrani, and L. L. Snead, *Systematic Technology Evaluation Program for SiC/SiC Composite-Based Accident-Tolerant LWR Fuel Cladding and Core Structures*, no. August. 2014.
 - [33] S. J. Zinkle and G. S. Was, "Materials challenges in nuclear energy," *Acta Mater.*, vol. 61, no. 3, pp. 735–758, 2013, doi: 10.1016/j.actamat.2012.11.004.
 - [34] A. Hasegawa, M. Fukuda, S. Nogami, and K. Yabuuchi, "Neutron irradiation effects on tungsten materials," *Fusion Eng. Des.*, vol. 89, no. 7–8, pp. 1568–1572, 2014, doi: 10.1016/j.fusengdes.2014.04.035.
 - [35] D. M. Duffy, "Fusion power: A challenge for materials science," *Philos. Trans. R. Soc. A Math. Phys. Eng. Sci.*, vol. 368, no. 1923, pp. 3315–3328, 2010, doi: 10.1098/rsta.2010.0060.
 - [36] R. Behrisch, G. Federici, A. Kukushkin, and D. Reiter, "Material erosion at the vessel walls of future fusion devices," *J. Nucl. Mater.*, vol. 313–316, no. SUPPL., pp. 388–392, 2003, doi: 10.1016/S0022-3115(02)01580-5.
 - [37] J. D. Sethian *et al.*, "An overview of the development of the first wall and other
-

- principal components of a laser fusion power plant,” *J. Nucl. Mater.*, vol. 347, pp. 161–177, 2005, [Online]. Available: <https://doi.org/10.1016/j.jnucmat.2005.08.019>.
- [38] M. J. Baldwin and R. P. Doerner, “Helium induced nanoscopic morphology on tungsten under fusion relevant plasma conditions,” *Nucl. Fusion*, vol. 48, no. 3, pp. 0–5, 2008, doi: 10.1088/0029-5515/48/3/035001.
- [39] R. Gauntt *et al.*, “Fukushima Daiichi Accident Study (Status as of April 2012),” *Sandia Natl. Lab. Report, SAND2012-6173, Albuquerque, NM*, no. August, 2012.
- [40] C. Kittel, *Introduction to Solid State Physics*. 2010.
- [41] W. Schilling, “Radiation Induced Damage in Metals,” *J. Nucl. Mater.*, vol. 72, pp. 1–4, 1978.
- [42] R. Raj, “Fundamental Research in Structural Ceramics for Service Near 2000°C,” *J. Am. Ceram. Soc.*, vol. 76, no. 9, pp. 2147–2174, 1993, doi: 10.1111/j.1151-2916.1993.tb07750.x.
- [43] OECD, “Primary Radiation Damage in Materials,” *OCDE / Nucl. Sci.*, p. NEA/NSC/DOC(2015)9, 2015.
- [44] J. F. Ziegler, J. P. Biersack, and M. D. Ziegler, “SRIM-The Stopping and Range of Ions in Matter,” *Energy*, vol. I, p. 8.2, 2008, doi: 10.1016/j.nimb.2004.01.208.4.
- [45] G. P. Cherepanov, “Point Defects in Solids,” Springer, Dordrecht, 1997, pp. 124–153.
- [46] S. S. Huang, X. Q. Pan, K. Sato, Q. Xu, and T. Yoshiie, “Early stage irradiation effects in F82H model alloys,” *J. Nucl. Mater.*, vol. 449, no. 1–3, pp. 248–251, 2014, doi: 10.1016/j.jnucmat.2013.07.072.
- [47] B. N. Singh and J. H. Evans, “Significant differences in defect accumulation behaviour between fcc and bcc crystals under cascade damage conditions,” *J. Nucl. Mater.*, vol. 226, no. 3, pp. 277–285, 1995, doi: 10.1016/0022-3115(95)00121-2.
-

- [48] A. P. Druzhkov, V. L. Arbuzov, and D. A. Perminov, "The effect of neutron irradiation dose on vacancy defect accumulation and annealing in pure nickel," *J. Nucl. Mater.*, vol. 421, no. 1–3, pp. 58–63, 2012, doi: 10.1016/j.jnucmat.2011.11.047.
 - [49] A. Fick, "Ueber Diffusion," *Ann. der Phys. und Chemie*, vol. 170, no. 1, pp. 59–86, Jan. 1855, doi: 10.1002/andp.18551700105.
 - [50] W. Schilling, "Self-interstitial atoms in metals," *J. Nucl. Mater.*, vol. 69–70, no. C, pp. 465–489, 1978, doi: 10.1016/0022-3115(78)90261-1.
 - [51] J. Frenkel, "Über die Wärmebewegung in festen und flüssigen Körpern," *Zeitschrift für Phys.*, vol. 35, no. 8–9, pp. 652–669, 1926, doi: 10.1007/BF01379812.
 - [52] G. S. Was, *Fundamentals of Radiation Materials Science*. 2007.
 - [53] R. S. Molla, "A study on Manufacturing of Deformed Bar (G 60-400W) at Elite Iron and Steel Industries," no. May, p. 123, 2018, doi: 10.13140/RG.2.2.24320.33289.
 - [54] F. Kroupa, "DISLOCATION DIPOLES AND DISLOCATION LOOPS," 1966.
 - [55] J. Silcox and P. B. Hirsch, "Direct observations of defects in quenched gold," *Philos. Mag.*, vol. 4, no. 37, pp. 72–89, 1959, doi: 10.1080/14786435908238228.
 - [56] M. Kiritani, "Story of stacking fault tetrahedra," *Mater. Chem. Phys.*, vol. 50, no. 2, pp. 133–138, 1997, doi: 10.1016/S0254-0584(97)80250-7.
 - [57] M. J. Makin and F. J. Minter, "Irradiation hardening in copper and nickel," *Acta Metall.*, vol. 8, no. 10, pp. 691–699, 1960, doi: 10.1016/0001-6160(60)90200-5.
 - [58] M. Kiritani, "Microstructure evolution during irradiation," *J. Nucl. Mater.*, vol. 216, no. C, pp. 220–264, 1994, doi: 10.1016/0022-3115(94)90014-0.
 - [59] E. Martínez, B. P. Uberuaga, and I. J. Beyerlein, "Interaction of small mobile stacking fault tetrahedra with free surfaces, dislocations, and interfaces in Cu and Cu-Nb,"
-

- Phys. Rev. B*, vol. 93, no. 5, pp. 1–10, 2016, doi: 10.1103/PhysRevB.93.054105.
- [60] J. Wei Wang, S. Narayanan, J. Yu Huang, Z. Zhang, T. Zhu, and S. X. Mao, “Atomic-scale dynamic process of deformation-induced stacking fault tetrahedra in gold nanocrystals,” *Nat. Commun.*, vol. 4, pp. 1–8, 2013, doi: 10.1038/ncomms3340.
- [61] S. Kojima, Y. Sano, T. Yoshiie, N. Yoshida, and M. Kiritani, “Conversion of stacking fault tetrahedra to voids in electron irradiated Fe-Cr-Ni,” *J. Nucl. Mater.*, vol. 141–143, no. PART 2, pp. 763–766, 1986, doi: 10.1016/0022-3115(86)90088-7.
- [62] “5.4.2 Dislocation Reactions Involving Partial Dislocations.” [http://www.tf.uni-kiel.de/matwis/amat/def_en/kap_5/backbone/r5_4_2.html#Thompson tetrahedron](http://www.tf.uni-kiel.de/matwis/amat/def_en/kap_5/backbone/r5_4_2.html#Thompson%20tetrahedron) (accessed Feb. 08, 2018).
- [63] M. Kiritani, “History, present status and future of the contribution of high-voltage electron microscopy to the study of radiation damage and defects in solids,” *Ultramicroscopy*, vol. 39, no. 1–4, pp. 135–159, 1991, doi: 10.1016/0304-3991(91)90193-A.
- [64] P. R. Okamoto, S. D. Harkness, and J. J. Laidler, “ANS Transactions,” *Am. Nucl. Soc. Trans.*, vol. 16, p. 70, 1973.
- [65] P. R. Okamoto and L. E. Rehn, “Radiation-induced segregation in binary and ternary alloys,” *J. Nucl. Mater.*, vol. 83, no. 1, pp. 2–23, 1979, doi: 10.1016/0022-3115(79)90587-7.
- [66] L. K. Mansur and M. H. Yoo, “The effects of impurity trapping on irradiation-induced swelling and creep,” *J. Nucl. Mater.*, vol. 74, no. 2, pp. 228–241, 1978, doi: 10.1016/0022-3115(78)90362-8.
- [67] H. Wiedersich, “On the theory of void formation during irradiation,” *Radiat. Eff.*, vol. 12, no. 1–2, pp. 111–125, 1972, doi: 10.1080/00337577208231128.
- [68] M. K. Patel *et al.*, “Effect of helium irradiation on Ti₃AlC₂ at 500??C,” *Scr. Mater.*, vol.
-

- 77, pp. 1–4, 2014, doi: 10.1016/j.scriptamat.2013.12.010.
- [69] A. Debelle *et al.*, “Helium behaviour and vacancy defect distribution in helium implanted tungsten,” *J. Nucl. Mater.*, vol. 362, no. 2–3, pp. 181–188, 2007, doi: 10.1016/j.jnucmat.2007.01.021.
- [70] K. Suzuki, N. Shigenaku, T. Hashimoto, and E. Nishimura, “Development of a Dual-Ion Beam Accelerator Connected with a TEM for In-Situ Observation of Radiation-Induced Defects,” *Nucl. Instruments Methods Physics Res. B*, vol. 25, pp. 591–593, 1987.
- [71] M. K. Patel *et al.*, “Effect of helium irradiation on Ti₃AlC₂ at 500??C,” *Scr. Mater.*, vol. 77, pp. 1–4, 2014, doi: 10.1016/j.scriptamat.2013.12.010.
- [72] H. Iwakiri, K. Yasunaga, K. Morishita, and N. Yoshida, “Microstructure evolution in tungsten during low-energy helium ion irradiation,” *J. Nucl. Mater.*, vol. 283–287, no. PART II, pp. 1134–1138, 2000, doi: 10.1016/S0022-3115(00)00289-0.
- [73] E. Aradi *et al.*, “Enhanced Radiation Tolerance of Tungsten Nanoparticles to He Ion Irradiation,” *Nanomaterials*, vol. 8, no. 12, p. 1052, 2018, doi: 10.3390/nano8121052.
- [74] G. G. Bentle, “Gas Bubble Formation in Irradiated Plastics and Reactor Fuels,” *Nucl. Sci. Eng.*, vol. 7, no. 6, pp. 487–495, 1960, doi: 10.13182/nse60-a25755.
- [75] R. M. Cornell, “The growth of fission gas bubbles in irradiated uranium dioxide,” *Philos. Mag.*, vol. 19, no. 159, pp. 539–554, 1969, doi: 10.1080/14786436908216311.
- [76] K. Linga Murty, “Role and significance of source hardening in radiation embrittlement of iron and ferritic steels,” *J. Nucl. Mater.*, vol. 270, no. 1, pp. 115–128, 1999, doi: 10.1016/S0022-3115(98)00766-1.
- [77] W. J. S. Yang, D. S. Gelles, J. L. Straalsund, and R. Bajaj, “Post-irradiation ductility loss of Fe-Ni-base precipitation hardenable alloys,” *J. Nucl. Mater.*, vol. 132, no. 3, pp. 249–265, 1985, doi: 10.1016/0022-3115(85)90370-8.
-

- [78] R. S. Barnes, “Embrittlement of stainless steels and nickel-based alloys at high temperature induced by neutron radiation,” *Nature*, vol. 206, no. 4991, pp. 1307–1310, 1965, doi: 10.1038/2061307a0.
 - [79] A. M. Robinson *et al.*, “The effect of temperature on bubble lattice formation in copper under in situ He ion irradiation,” *Scr. Mater.*, vol. 131, pp. 108–111, 2017, doi: 10.1016/j.scriptamat.2016.12.031.
 - [80] O. El-Atwani, K. Hattar, J. a. Hinks, G. Greaves, S. S. Harilal, and a. Hassanein, “Helium bubble formation in ultrafine and nanocrystalline tungsten under different extreme conditions,” *J. Nucl. Mater.*, vol. 458, no. September 2014, pp. 216–223, 2015, doi: 10.1016/j.jnucmat.2014.12.095.
 - [81] S. E. Donnelly, “The density and pressure of helium in bubbles in implanted metals: A critical review,” *Radiat. Eff.*, vol. 90, no. 1–2, pp. 1–47, 1985, doi: 10.1080/00337578508222514.
 - [82] Q. Shen, G. Ran, J. Hinks, S. E. Donnelly, L. Wang, and N. Li, “In situ observation of microstructure evolution in 4H-SiC under 3.5 keV He+irradiation,” *J. Nucl. Mater.*, vol. 471, pp. 149–153, 2016, doi: 10.1016/j.jnucmat.2016.01.017.
 - [83] H. Ullmaier, “Review Paper the Influence of Helium on the Bulk Properties of Fusion Reactor,” *Nucl. Fusion*, vol. 24, no. 8, p. 1039, 1984, doi: 10.1088/0029-5515/24/8/009.
 - [84] “Fracture and Embrittlement,” in *Fundamentals of Radiation Materials Science*, Berlin, Heidelberg: Springer Berlin Heidelberg, 2007, pp. 643–709.
 - [85] K. Fukuya, “Current understanding of radiation-induced degradation in light water reactor structural materials,” *J. Nucl. Sci. Technol.*, vol. 50, no. 3, pp. 213–254, 2013, doi: 10.1080/00223131.2013.772448.
 - [86] J. Bertsch, R. Lindau, and A. Möslang, “In-situ and post-irradiation fatigue properties
-

- of the ferritic-martensitic steel Manet at $T = 250^{\circ}\text{C}$,” *J. Nucl. Mater.*, vol. 233–237, no. PART 1, pp. 276–279, 1996, doi: 10.1016/S0022-3115(96)00120-1.
- [87] Y. Katoh, L. L. Snead, T. Hinoki, S. Kondo, and A. Kohyama, “Irradiation creep of high purity CVD silicon carbide as estimated by the bend stress relaxation method,” *J. Nucl. Mater.*, vol. 367-370 A, no. SPEC. ISS., pp. 758–763, 2007, doi: 10.1016/j.jnucmat.2007.03.086.
- [88] J. R. Matthews and M. W. Finnis, “Irradiation Creep Models -An Overview,” *J. Nucl. Mater.*, vol. 159, pp. 257–285, 1988.
- [89] Y. Ashkenazy and R. S. Averback, “Irradiation Induced Grain Boundary Flow A New Creep Mechanism at the Nanoscale,” *Nano Lett.*, 2012, doi: 10.1021/nl301554k.
- [90] C. Xu and G. S. Was, “In situ proton irradiation creep of ferritic – martensitic steel T91,” *J. Nucl. Mater.*, vol. 441, no. 1–3, pp. 681–687, 2013, doi: 10.1016/j.jnucmat.2013.03.046.
- [91] P. Taylor, A. D. Brailsford, and R. Bullough, “Irradiation creep due to the growth of interstitial loops,” *Philos. Mag.*, vol. 27, no. 1, pp. 49–64, 1973, doi: 10.1080/14786437308228913.
- [92] P. Taylor, “A possible mechanism of irradiation creep and its reference to uranium,” *Philos. Mag.*, vol. 7, no. 80, pp. 1417–1420, 1962.
- [93] P. T. Heald and M. V. Speight, “Steady-state irradiation creep,” *Philos. Mag.*, vol. 29, no. 5, pp. 1075–1080, 1974, doi: 10.1080/14786437408226592.
- [94] R. Bullough and J. R. Willis, “The stress induced point defect dislocation interaction and its relevance to irradiation creep,” *Philos. Mag.*, vol. 35, no. May 2013, pp. 855–861, 1975.
- [95] L. K. Mansur, “Irradiation creep by climb-enabled glide of dislocations resulting from preferred absorption of point defects,” *Philos. Mag. A Phys. Condens. Matter, Struct.*
-

- Defects Mech. Prop.*, vol. 39, no. 4, pp. 497–506, 1979, doi: 10.1080/01418617908239286.
- [96] N. F. Mott, “CXVII. A theory of work-hardening of metal crystals,” *London, Edinburgh, Dublin Philos. Mag. J. Sci.*, vol. 43, no. 346, pp. 1151–1178, 1952, doi: 10.1080/14786441108521024.
- [97] D. J. Mazey, “Fundamental aspects of high-energy ion-beam simulation techniques and their relevance to fusion materials studies,” *J. Nucl. Mater.*, vol. 174, no. 2–3, pp. 196–209, 1990, doi: 10.1016/0022-3115(90)90234-E.
- [98] L. K. Mansur, “Irradiation Creep by Climb-Enabled Glide Driven by Transient Point Defect Processes,” *Mater. Sci. Forum*, vol. 97–99, pp. 489–498, 1992, doi: 10.4028/www.scientific.net/MSF.97-99.489.
- [99] M. Grossbeck, L. Mansur, and M. Tanaka, “Irradiation Creep in Austenitic Stainless Steels at 60 to 400°C with a Fusion Reactor Helium to dpa Ratio,” 1990, doi: 10.1520/STP49473S.
- [100] L. K. Mansur, W. A. Coghlan, and A. D. Brailsford, “Swelling with inhomogeneous point defect production—a cascade diffusion theory,” *J. Nucl. Mater.*, vol. 86, pp. 591–595, 1979, [Online]. Available: <http://www.sciencedirect.com/science/article/pii/0022311579905506>.
- [101] L. K. Mansur, A. D. Brailsford, and W. A. Coghlan, “A cascade diffusion theory of sink capture fluctuations during irradiation of a solid,” *Acta Metall.*, vol. 33, no. 8, pp. 1407–1423, 1985, doi: 10.1016/0001-6160(85)90042-2.
- [102] S. J. Zinkle, “Radiation-Induced Effects on Microstructure,” *Compr. Nucl. Mater.*, vol. 1, pp. 65–98, Jan. 2012, doi: 10.1016/B978-0-08-056033-5.00003-3.
- [103] J. W. Holmes, Y. H. Park, and J. W. Jones, “Tensile Creep and Creep-Recovery Behavior of a SiC-FiberSi₃N₄-Matrix Composite,” *J. Am. Ceram. Soc.*, vol. 76, no. 5, pp. 1281–
-

- 1293, May 1993, doi: 10.1111/j.1151-2916.1993.tb03753.x.
- [104] U. F. Kocks, “Laws for work-hardening and low-temperature Creep,” *J. Eng. Mater. Technol.*, vol. ASME(H)98P, no. January 1976, pp. 76–85, 1976.
- [105] “Salmonsens store illustrerede konversationsleksikon; en nordisk encyklopædi : Blangstrup, Johan Christian, 1857-1926, ed : Free Download, Borrow, and Streaming : Internet Archive.” <https://archive.org/details/salmonsensstore01unkngoog> (accessed Aug. 16, 2021).
- [106] S. J. Zinkle, H. Tanigawa, and B. D. Wirth, *Radiation and thermomechanical degradation effects in reactor structural alloys*. Elsevier Inc., 2019.
- [107] L. . Snead, S. J. Zinkle, J. . Hay, and M. . Osborne, “Amorphization of SiC under ion and neutron irradiation,” *Nucl. Instruments Methods Phys. Res. Sect. B Beam Interact. with Mater. Atoms*, vol. 141, no. 1–4, pp. 123–132, 1998, doi: 10.1016/S0168-583X(98)00085-8.
- [108] C. Fourdrin, T. Allard, I. Monnet, N. Menguy, M. Benedetti, and G. Calas, “Effect of Radiation-Induced Amorphization on Smectite Dissolution,” *Environ. Sci. Technol.*, vol. 44, no. 7, pp. 2509–2514, 2010, doi: 10.1021/es903300r.
- [109] B. J. Pawlak *et al.*, “Effect of amorphization and carbon co-doping on activation and diffusion of boron in silicon,” *Appl. Phys. Lett.*, vol. 89, no. 6, pp. 2004–2007, 2006, doi: 10.1063/1.2227863.
- [110] L. L. Snead and S. J. Zinkle, “Structural relaxation in amorphous silicon carbide,” *Nucl. Instruments Methods Phys. Res. B*, vol. 191, no. 1–4, pp. 497–503, 2002.
- [111] S. J. Zinkle and L. L. Snead, “Influence of irradiation spectrum and implanted ions on the amorphization of ceramics,” *Nucl. Instruments Methods Phys. Res. Sect. B Beam Interact. with Mater. Atoms*, vol. 116, no. 1–4, pp. 92–101, 1996, doi: 10.1016/0168-583X(96)00016-X.
-

- [112] Z. Zhu and P. Jung, "Irradiation induced dimensional changes in ceramics," *Nucl. Inst. Methods Phys. Res. B*, vol. 91, no. 1–4, pp. 269–273, 1994, doi: 10.1016/0168-583X(94)96229-4.
- [113] P. R. Okamoto, L. E. Rehn, J. Pearson, R. Bhadra, and M. Grimsditch, "Brillouin scattering and transmission electron microscopy studies of radiation-induced elastic softening, disordering and amorphization of intermetallic compounds," *J. Less Common Met.*, vol. 140, no. 10, pp. 231–244, Jun. 1988, doi: 10.1016/0022-5088(88)90384-0.
- [114] S. Chiba *et al.*, "Method to Reduce Long-lived Fission Products by Nuclear Transmutations with Fast Spectrum Reactors OPEN," doi: 10.1038/s41598-017-14319-7.
- [115] R. W. Harrison, "On the use of ion beams to emulate the neutron irradiation behaviour of tungsten," *Vacuum*, vol. 160, no. November 2018, pp. 355–370, 2019, doi: 10.1016/j.vacuum.2018.11.050.
- [116] N. Yao, *Handbook of Microscopy for Nanotechnology*, no. January 2005. 2005.
- [117] H. Wjetersich, "Section I . Metals : Kinematics and Metastable Phases KINETIC PROCESSES DURING ION BOMBARDMENT *," vol. 8, 1985.
- [118] N. Q. Lam and H. Wiedersich, "Section III Preferential sputtering and bombardment induced redistribution effects BOMBARDMENT-INDUCED SEGREGATION AND REDISTRIBUTION *," *Nucl. Instruments Methods Phys. Res.*, vol. 18, pp. 471–485, 1987.
- [119] H. W. Werner, "The depth dependence of the depth resolution in sputter profiling," *Surf. Interface Anal.*, vol. 4, no. 1, pp. 1–7, 1982, doi: 10.1002/sia.740040102.
- [120] Cui Fu-Zhai and Li Heng-De, "Recoil implantation and interface mixing: A computer simulation study," *Nucl. Inst. Methods Phys. Res. B*, vol. 7–8, no. PART 2, pp. 650–656,
-

- 1985, doi: 10.1016/0168-583X(85)90449-5.
- [121] U. Littmark and W. O. Hofer, "Recoil mixing in solids by energetic ion beams," *Nucl. Instruments Methods*, vol. 168, no. 1–3, pp. 329–342, 1980, doi: 10.1016/0029-554X(80)91274-4.
- [122] S. Matteson, B. M. Paine, M. G. Grimaldi, G. Mezey, and M.-A. Nicolet, "Ion Beam Mixing in Amorphous Silicon II. Theoretical Interpretation," *Nucl. Instruments Methods*, vol. 182–183, pp. 53–61, 1981, [Online]. Available: <https://www.sciencedirect.com/science/article/pii/0029554X81906704>.
- [123] R. S. Nelson, "The theory of recoil implantation," *Radiat. Eff.*, vol. 2, no. 1, pp. 47–50, 1969, doi: 10.1080/00337576908235579.
- [124] P. K. Haff and Z. E. Switkowski, "Ion-beam-induced atomic mixing," *J. Appl. Phys.*, vol. 48, no. 8, pp. 3383–3386, 1977, doi: 10.1063/1.324179.
- [125] S. Matteson, "Atomic mixing in ion impact: A collision cascade model," *Appl. Phys. Lett.*, vol. 39, no. 3, pp. 288–290, 1981, doi: 10.1063/1.92675.
- [126] R. Kelly and J. B. Sanders, "Recoil implantation from a thin source. I. Underlying theory and numerical results," *Surf. Sci.*, vol. 57, no. 1, pp. 143–156, 1976, doi: 10.1016/0039-6028(76)90174-6.
- [127] P. Sigmund and A. Gras-Marti, "Distortion of depth profiles during sputtering I. General description of collisional mixing," *Nucl. Instruments Methods*, vol. 168, no. 1–3, pp. 389–394, 1980.
- [128] P. Sigmund and A. Gras-Marti, "Theoretical aspects of atomic mixing by ion beams," *Nucl. Instruments Methods*, vol. 182–183, no. PART 1, pp. 25–41, 1981, doi: 10.1016/0029-554X(81)90668-6.
- [129] H. E. Roosendaal and J. B. Sanders, "Some properties of the relocation function in ion beam collisional mixing," *Nucl. Instruments Methods Phys. Res.*, vol. 218, no. 1–3, pp.
-

- 673–678, 1983, doi: 10.1016/0167-5087(83)91063-3.
- [130] J. B. Sanders, J. F. M. Westendorp, A. M. Vredenberg, and F. W. Saris, “Calculation of the shift of a thin marker layer in copper under ion bombardment,” *Nucl. Inst. Methods Phys. Res. B*, vol. 19–20, no. PART 2, pp. 659–661, 1987, doi: 10.1016/S0168-583X(87)80132-5.
- [131] C. Yang-Tse, G. W. Auner, M. H. Alkaisi, K. R. Padmanabhan, and M. M. Karmarkar, “Thermodynamic and ballistic aspects of ion mixing,” *Nucl. Inst. Methods Phys. Res. B*, vol. 59–60, no. PART 1, pp. 509–516, 1991, doi: 10.1016/0168-583X(91)95269-J.
- [132] H. Westendorp, Z. L. Wang, and F. W. Saris, “Ion beam mixing of CuAu and CuW systems,” *Nucl. Instruments Methods*, vol. 194, no. 1–3, pp. 453–456, 1982, doi: 10.1016/0029-554X(82)90563-8.
- [133] W. L. Johnson, Y. T. Cheng, M. Van Rossum, and M. A. Nicolet, “When is thermodynamics relevant to ion-induced atomic rearrangements in metals?,” *Nucl. Inst. Methods Phys. Res. B*, vol. 7–8, no. PART 2, pp. 657–665, 1985, doi: 10.1016/0168-583X(85)90450-1.
- [134] M. Van Rossum, Y. T. Cheng, M. A. Nicolet, and W. L. Johnson, “Correlation between cohesive energy and mixing rate in ion mixing of metallic bilayers,” *Appl. Phys. Lett.*, vol. 46, no. 6, pp. 610–612, 1985, doi: 10.1063/1.95557.
- [135] D. B. Williams and C. B. Carter, “The Transmission Electron Microscope,” in *Transmission Electron Microscopy*, Boston, MA: Springer US, 2009, pp. 3–22.
- [136] T. Muroga, R. Sakamoto, M. Fukui, and N. Yoshida, “In situ study of microstructural evolution in molybdenum during irradiation with low energy hydrogen ions,” *J. Nucl.*, vol. 198, pp. 1013–1017, 1992, [Online]. Available: <http://www.sciencedirect.com/science/article/pii/S0022311506801868>.
- [137] K. Suzuki, E. Nishimura, and T. Hashimoto, “Development of a dual ion beam system
-

- with single accelerator for materials studies,” *Nucl. Instruments Methods Phys. Res. A*, vol. 249, no. 2–3, pp. 491–495, 1986, [Online]. Available: [https://doi.org/10.1016/0168-9002\(86\)90707-2](https://doi.org/10.1016/0168-9002(86)90707-2).
- [138] S. Ishino, H. Kawanishi, K. Fukuya, and T. Muroga, “In situ studies of the effects of ion beams on materials using the electron microscope ion beam interface,” *IEEE Trans. Nucl. Sci.*, vol. 30, no. 2, pp. 1255–1258, 1983, doi: 10.1109/TNS.1983.4332503.
- [139] T. Takeyama, S. Ohnuki, and H. Takahashi, “Study of Cavity Formation in 316 Stainless Steels by Means of HVEM Ion-Accelerator Dual Irradiation,” *J. Nucl. Mater.*, vol. 133–134, pp. 571–574, 1985.
- [140] N. Ishikawa and K. Furuya, “Dual ion beam irradiation system interfaced with a transmission electron microscope and the observation of defect evolution in Ni during irradiation,” *Ultramicroscopy*, vol. 56, no. 1–3, pp. 211–215, 1994, doi: 10.1016/0304-3991(94)90160-0.
- [141] A. Taylor, C. W. Allen, and E. A. Ryan, “The HVEM-Tandem Accelerator Facility at Argonne National Laboratory,” *Nucl. Inst. Methods Phys. Res. B*, vol. 24–25, no. PART 1, pp. 598–602, 1987, doi: 10.1016/0168-583X(87)90718-X.
- [142] Y. Serruys, M. O. Ruault, P. Trocellier, S. Henry, O. Kaïtasov, and P. Trouslard, “Multiple ion beam irradiation and implantation: JANNUS project,” *Nucl. Instruments Methods Phys. Res. Sect. B Beam Interact. with Mater. Atoms*, vol. 240, no. 1–2, pp. 124–127, 2005, doi: 10.1016/j.nimb.2005.06.100.
- [143] L. P. Guo *et al.*, “Establishment of in situ TEM-implanter/accelerator interface facility at Wuhan University,” *Nucl. Instruments Methods Phys. Res. Sect. A Accel. Spectrometers, Detect. Assoc. Equip.*, vol. 586, no. 2, pp. 143–147, 2008, doi: 10.1016/j.nima.2007.11.029.
- [144] W. A. Jesser, “Dynamic HVEM Observations of Metals and Alloys During In-Situ Helium Ion Irradiations,” *IEEE Trans. Nucl. Sci.*, vol. 30, no. 2, pp. 1259–1262, 1983.
-

- [145] W. A. Jesser, "Light Ion Accelerator High Voltage Electron Microscope Facility for CTR Radiation Damage Studies," *IEEE Trans. Nucl. Sci.*, vol. 26, no. 1, pp. 1252–1256, 1979.
- [146] M. O. Ruault, M. Lerme, B. Jouffrey, and J. Chaumont, "Adaptation of an ion implanter on a 100 kV electron microscope for in situ irradiation experiments," *J. Phys. E.*, vol. 11, no. 11, pp. 1125–1128, 1978, doi: 10.1088/0022-3735/11/11/013.
- [147] J. A. Hinks, J. A. van den Berg, and S. E. Donnelly, "MIAMI: Microscope and ion accelerator for materials investigations," *J. Vac. Sci. Technol. A Vacuum, Surfaces, Film.*, vol. 29, no. 2, p. 021003, 2011, doi: 10.1116/1.3543707.
- [148] "MIAMI-1 - University of Huddersfield." <https://research.hud.ac.uk/institutes-centres/emma/miamifacilities/miami-1/> (accessed Apr. 04, 2018).
- [149] K. Furuya, K. Mitsuishi, M. Song, and T. Saito, "In-situ, analytical, high-voltage and high-resolution transmission electron microscopy of Xe ion implantation into Al," *J. Electron Microsc. (Tokyo)*, vol. 48, no. 5, pp. 511–518, 1999, doi: <http://dx.doi.org/10.1093/oxfordjournals.jmicro.a023709>.
- [150] W. A. Jesser, J. A. Horton, and L. L. Scribner, "Adaptation of an Ion Accelerator to a High Voltage Electron Microscope," *Radiat. Eff.*, vol. 29, no. 2, pp. 79–82, 1976, doi: 10.1080/00337577608233489.
- [151] C. W. Allen, L. L. Funk, and E. A. Ryan, "New instrumentation in Agronne's HVEM-Tandem facility: expanded capability for in situ ion beam studies," *Mater. Res. Soc. Symp. Proc.*, vol. 396, p. 641, 1996, doi: 10.1557/PROC-396-641.
- [152] M. O. Ruault, F. Fortuna, H. Bernas, J. Chaumont, O. Kaïtasov, and V. A. Borodin, "In situ transmission electron microscopy ion irradiation studies at Orsay," *J. Mater. Res.*, vol. 20, no. 7, pp. 1758–1768, 2005, doi: 10.1557/JMR.2005.0219.
- [153] M. O. Ruault, J. Chaumont, and H. Bernas, "Transmission electron microscopy study of ion implantation induced Si amorphization," *Nucl. Instruments Methods*, vol. 209–
-

- 210, no. 1, pp. 351–356, 1983, [Online]. Available: [https://doi.org/10.1016/0167-5087\(83\)90822-0](https://doi.org/10.1016/0167-5087(83)90822-0).
- [154] M. I. Idris, H. Konishi, M. Imai, K. Yoshida, and T. Yano, “Neutron Irradiation Swelling of SiC and SiCf/SiC for Advanced Nuclear Applications,” *Energy Procedia*, vol. 71, pp. 328–336, 2015, doi: 10.1016/j.egypro.2014.11.886.
- [155] L. L. Snead, T. Nozawa, Y. Katoh, T. S. Byun, S. Kondo, and D. A. Petti, “Handbook of SiC properties for fuel performance modeling,” *J. Nucl. Mater.*, vol. 371, no. 1–3, pp. 329–377, 2007, doi: 10.1016/j.jnucmat.2007.05.016.
- [156] J. J. Powers and B. D. Wirth, “A review of TRISO fuel performance models,” *J. Nucl. Mater.*, vol. 405, no. 1, pp. 74–82, 2010, doi: 10.1016/j.jnucmat.2010.07.030.
- [157] L. L. Snead, R. H. Jones, A. Kohyama, and P. Fenici, “Status of silicon carbide composites for fusion,” *J. Nucl. Mater.*, vol. 233–237, no. PART 1, pp. 26–36, 1996, doi: 10.1016/S0022-3115(96)00318-2.
- [158] R. B. Matthews, “Irradiation damage in reaction-bonded silicon carbide,” *J. Nucl. Mater.*, vol. 51, no. 2, pp. 203–208, 1974, doi: 10.1016/0022-3115(74)90003-8.
- [159] G. W. Hollenberg *et al.*, “The effect of irradiation on the stability and properties of monolithic silicon carbide and SiCf/SiC composites up to 25 dpa,” *J. Nucl. Mater.*, vol. 219, pp. 70–86, 1995, doi: 10.1016/0022-3115(94)00391-2.
- [160] L. L. Snead, Y. Katoh, and S. Kondo, “Effects of fast neutron irradiation on zirconium carbide,” *J. Nucl. Mater.*, vol. 399, no. 2–3, pp. 200–207, 2010, doi: 10.1016/j.jnucmat.2010.01.020.
- [161] J. Gan, Y. Yang, C. Dickson, and T. Allen, “Proton irradiation study of GFR candidate ceramics,” *J. Nucl. Mater.*, vol. 389, no. 2, pp. 317–325, 2009, doi: 10.1016/j.jnucmat.2009.02.021.
- [162] S. Agarwal, P. Trocellier, Y. Serruys, S. Vaubailon, and S. Miro, “Helium mobility in
-

- advanced nuclear ceramics,” *Nucl. Instruments Methods Phys. Res. Sect. B Beam Interact. with Mater. Atoms*, vol. 327, no. 1, pp. 117–120, 2014, doi: 10.1016/j.nimb.2013.09.039.
- [163] C. J. Ulmer, A. T. Motta, and M. A. Kirk, “In situ ion irradiation of zirconium carbide,” *J. Nucl. Mater.*, vol. 466, pp. 606–614, 2015, doi: 10.1016/j.jnucmat.2015.08.009.
- [164] Y. Katoh, G. Vasudevamurthy, T. Nozawa, and L. L. Snead, “Properties of zirconium carbide for nuclear fuel applications,” *J. Nucl. Mater.*, vol. 441, no. 1–3, pp. 718–742, 2013, doi: 10.1016/j.jnucmat.2013.05.037.
- [165] “Dissertation Tesfaye Ayalew.”
<https://www.iue.tuwien.ac.at/phd/ayalew/node20.html>.
- [166] H. O. Pierson, *Handbook of refractory carbides and nitrides : properties, characteristics, processing, and applications*. 1996.
- [167] G. Griffith, “U.S. Department of Energy Accident Resistant SiC Clad Nuclear Fuel Development,” p. 14, 2011.
- [168] R. W. Olesinski and G. J. Abbaschian, “The C-Si (Carbon-Silicon) system,” *Bull. Alloy Phase Diagrams*, vol. 5, no. 5, pp. 486–489, 1984, doi: 10.1007/BF02872902.
- [169] J. Dong and A.-B. Chen, “Fundamental Properties of SiC: Crystal Structure, Bonding Energy, Band Structure, and Lattice Vibrations,” pp. 63–87, 2004, doi: 10.1007/978-3-662-09877-6_2.
- [170] P. Kisly, “The chemical bond strength and the hardness of high melting point compounds,” *Sci. hard Mater.*, 1984.
- [171] M. A. Pickering, R. L. Taylor, J. T. Keeley, and G. A. Graves, “Chemically vapor deposited silicon carbide (SiC) for optical applications,” *Nucl. Inst. Methods Phys. Res. A*, vol. 291, no. 1–2, pp. 95–100, 1990, doi: 10.1016/0168-9002(90)90040-D.
-

- [172] D. M. Liu and B. W. Lin, "Thermal conductivity in hot-pressed silicon carbide," *Ceram. Int.*, vol. 22, no. 5, pp. 407–414, 1996, doi: 10.1016/0272-8842(95)00125-5.
- [173] L. S. Sigl, "Thermal conductivity of liquid phase sintered silicon carbide," *J. Eur. Ceram. Soc.*, vol. 23, no. 7, pp. 1115–1122, Jun. 2003, doi: 10.1016/S0955-2219(02)00271-6.
- [174] R. G. Munro, "Material properties of a sintered α -SiC," *J. Phys. Chem. Ref. Data*, vol. 26, no. 5, pp. 1195–1203, 1997, doi: 10.1063/1.556000.
- [175] W. D. KINGERY, "Thermal Conductivity: XII, Temperature Dependence of Conductivity for Single-Phase Ceramics," *J. Am. Ceram. Soc.*, vol. 38, no. 7, pp. 251–255, Jul. 1955, doi: 10.1111/j.1151-2916.1955.tb14940.x.
- [176] A. K. Collins, M. A. Pickering, and R. L. Taylor, "Grain size dependence of the thermal conductivity of polycrystalline chemical vapor deposited β -SiC at low temperatures," *J. Appl. Phys.*, vol. 68, no. 12, pp. 6510–6512, 1990, doi: 10.1063/1.346852.
- [177] K. K. Kelley, "The Specific Heats at Low Temperatures of Crystalline Boric Oxide, Boron Carbide and Silicon Carbide," *J. Am. Chem. Soc.*, vol. 63, no. 4, pp. 1137–1139, 1941, doi: 10.1021/ja01849a072.
- [178] B. E. Walker, C. T. Ewing, and R. R. Miller, "Specific Heat of Some High Temperature Materials," *J. Chem. Eng. Data*, vol. 7, no. 4, pp. 595–597, 1962, doi: 10.1021/je60015a049.
- [179] J. M. Grow and R. A. Levy, "Micromechanical characterization of chemically vapor deposited ceramic films," *J. Mater. Res.*, vol. 9, no. 8, pp. 2072–2078, Aug. 1994, doi: 10.1557/JMR.1994.2072.
- [180] L. L. Snead, D. Steiner, and S. J. Zinkle, "Measurement of the effect of radiation damage to ceramic composite interfacial strength," *J. Nucl. Mater.*, vol. 191–194, pp. 566–570, 1992, doi: 10.1016/S0022-3115(09)80109-8.
- [181] G. Singh, T. Koyanagi, C. Petrie, K. Terrani, and Y. Katoh, "Evaluating the irradiation
-

- effects on the elastic properties of miniature monolithic SiC tubular specimens,” *J. Nucl. Mater.*, vol. 499, pp. 107–110, 2018, doi: 10.1016/j.jnucmat.2017.10.060.
- [182] B. O. Yavuz and R. E. Tressler, “High temperature mechanical behavior of a chemically vapor deposited beta silicon carbide,” *Ceram. Int.*, vol. 18, no. 1, pp. 19–26, 1992, doi: 10.1016/0272-8842(92)90057-K.
- [183] A. G. EVANS and E. A. CHARLES, “Fracture Toughness Determinations by Indentation,” *J. Am. Ceram. Soc.*, vol. 59, no. 7–8, pp. 371–372, Jul. 1976, doi: 10.1111/j.1151-2916.1976.tb10991.x.
- [184] Y. M. Chiang, R. P. Messner, C. D. Terwilliger, and D. R. Behrendt, “Reaction-formed silicon carbide,” *Mater. Sci. Eng. A*, vol. 144, no. 1–2, pp. 63–74, 1991, doi: 10.1016/0921-5093(91)90210-E.
- [185] J. D. Stempien, D. M. Carpenter, G. Kohse, and M. S. Kazimi, “Characteristics of Composite Silicon Carbide Fuel Cladding After Irradiation Under Simulated PWR Conditions Nuclear Systems,” *Nucl. Technol.*, vol. 183, no. 1, pp. 13–29, 2013, doi: 10.13182/NT12-86.
- [186] D. Kim, H. G. Lee, J. Y. Park, and W. J. Kim, “Fabrication and measurement of hoop strength of SiC triplex tube for nuclear fuel cladding applications,” *J. Nucl. Mater.*, vol. 458, pp. 29–36, 2015, doi: 10.1016/j.jnucmat.2014.11.117.
- [187] T. Narushima, T. Goto, and T. Hirai, “High-Temperature Passive Oxidation of Chemically Vapor Deposited Silicon Carbide,” *J. Am. Ceram. Soc.*, vol. 72, no. 8, pp. 1386–1390, Aug. 1989, doi: 10.1111/j.1151-2916.1989.tb07658.x.
- [188] M. J. H. Balat, “Determination of the Active-to-Passive Transition in the Oxidation of Silicon Carbide in Standard and Microwave-Excited Air,” *J. Eur. Ceram. Soc.*, vol. 16, no. 1, pp. 55–62, 1996, doi: 10.1016/0955-2219(95)00104-2.
- [189] B. Schneider, A. Guette, R. Naslain, M. Cataldi, and A. Costecalde, “A theoretical and
-

- experimental approach to the active-to-passive transition in the oxidation of silicon carbide: Experiments at high temperatures and low total pressures," *J. Mater. Sci.*, vol. 33, no. 2, pp. 535–547, 1998, doi: 10.1023/A:1004313022769.
- [190] Y. Song' and F. W. Smith, "Effects of low-pressure oxidation on the surface composition of single crystal silicon carbide," *J. Am. Ceram. Soc.*, vol. 88, no. 7, pp. 1864–1869, 2005, doi: 10.1111/j.1551-2916.2005.00357.x.
- [191] K. A. Terrani, Y. Yang, Y. J. Kim, R. Rebak, H. M. Meyer, and T. J. Gerczak, "Hydrothermal corrosion of SiC in LWR coolant environments in the absence of irradiation," *J. Nucl. Mater.*, vol. 465, pp. 488–498, 2015, doi: 10.1016/j.jnucmat.2015.06.019.
- [192] R. Förthmann and E. Gyarmati, "Investigations on the transport behaviour of strontium in coated particles at high temperatures," *J. Nucl. Mater.*, vol. 58, no. 2, pp. 189–195, Nov. 1975, doi: 10.1016/0022-3115(75)90105-1.
- [193] A. W. Mehner, W. Heit, K. Röllig, H. Ragoss, and H. Müller, "Spherical fuel elements for advanced HTR manufacture and qualification by irradiation testing," *J. Nucl. Mater.*, vol. 171, no. 1, pp. 9–18, 1990, doi: 10.1016/0022-3115(90)90341-J.
- [194] Y. Katoh *et al.*, "Continuous SiC fiber, CVI SiC matrix composites for nuclear applications: Properties and irradiation effects," *J. Nucl. Mater.*, vol. 448, no. 1–3, pp. 448–476, 2014, doi: 10.1016/j.jnucmat.2013.06.040.
- [195] R. J. Price, "Effects of fast-neutron irradiation on pyrolytic silicon carbide," *J. Nucl. Mater.*, vol. 33, no. 1, pp. 17–22, 1969, doi: 10.1016/0022-3115(69)90003-8.
- [196] R. J. Price, "Neutron irradiation-induced voids in β -silicon carbide," *J. Nucl. Mater.*, vol. 48, no. 1, pp. 47–57, 1973, doi: 10.1016/0022-3115(73)90077-9.
- [197] M. I. Idris, H. Konishi, M. Imai, K. Yoshida, and T. Yano, "Neutron Irradiation Swelling of SiC and SiCf/SiC for Advanced Nuclear Applications," *Energy Procedia*, vol. 71, pp.
-

- 328–336, 2015, doi: 10.1016/j.egypro.2014.11.886.
- [198] W. Jiang, W. J. Weber, S. Thevuthasan, and V. Shutthanandan, “Accumulation and recovery of disorder on silicon and carbon sublattices in ion-irradiated 6H-SiC,” *J. Nucl. Mater.*, vol. 289, no. 1–2, pp. 96–101, 2001, doi: 10.1016/S0022-3115(00)00687-5.
- [199] J. C. Nappé *et al.*, “Microstructural changes induced by low energy heavy ion irradiation in titanium silicon carbide,” *J. Eur. Ceram. Soc.*, vol. 31, no. 8, pp. 1503–1511, 2011, doi: 10.1016/j.jeurceramsoc.2011.01.002.
- [200] M. I. Idris, S. Yamazaki, K. Yoshida, and T. Yano, “Defects annihilation behavior of neutron-irradiated SiC ceramics densified by liquid-phase-assisted method after post-irradiation annealing,” *Nucl. Mater. Energy*, vol. 9, pp. 199–206, 2016, doi: 10.1016/j.nme.2016.05.014.
- [201] S. Kondo, T. Koyanagi, and T. Hinoki, “Irradiation creep of 3C-SiC and microstructural understanding of the underlying mechanisms,” *J. Nucl. Mater.*, vol. 448, no. 1–3, pp. 487–496, 2014, doi: 10.1016/j.jnucmat.2013.09.004.
- [202] Y. Katoh, L. L. Snead, I. Szlufarska, and W. J. Weber, “Radiation effects in SiC for nuclear structural applications,” *Curr. Opin. Solid State Mater. Sci.*, vol. 16, no. 3, pp. 143–152, 2012, doi: 10.1016/j.cossms.2012.03.005.
- [203] D. J. Senor *et al.*, “Defect structure and evolution in silicon carbide irradiated to 1 dpa-SiC at 1100 °C,” *J. Nucl. Mater.*, vol. 317, no. 2–3, pp. 145–159, 2003, doi: 10.1016/S0022-3115(03)00077-1.
- [204] M. Liu *et al.*, “Investigation of the damage behavior in CVD SiC irradiated with 70 keV He ions by NEXAFS, Raman and TEM,” *J. Eur. Ceram. Soc.*, vol. 37, no. 4, pp. 1253–1259, 2017, doi: 10.1016/j.jeurceramsoc.2016.11.046.
- [205] J. J. Powers and B. D. Wirth, “A review of TRISO fuel performance models,” *Journal of*
-

- Nuclear Materials*, vol. 405, no. 1. pp. 74–82, 2010, doi: 10.1016/j.jnucmat.2010.07.030.
- [206] S. Saito, T. Tanaka, and Y. Sudo, “Design of high temperature Engineering Test Reactor (HTTR).” 1994, Accessed: Oct. 16, 2019. [Online]. Available: https://inis.iaea.org/search/search.aspx?orig_q=RN:27002401.
- [207] K. Sawa and S. Ueta, “Research and development on HTGR fuel in the HTTR project,” *Nucl. Eng. Des.*, vol. 233, no. 1–3, pp. 163–172, 2004, doi: 10.1016/j.nucengdes.2004.08.006.
- [208] Y. Xu and K. Zuo, “Overview of the 10 MW high temperature gas cooled reactor - Test module project,” *Nucl. Eng. Des.*, vol. 218, no. 1–3, pp. 13–23, 2002, doi: 10.1016/S0029-5493(02)00181-4.
- [209] N. Baghdasaryan and T. Kozlowski, “Review of Progress in Coated Fuel Particle Performance Analysis,” *Nuclear Science and Engineering*, vol. 194, no. 3. Taylor and Francis Inc., pp. 169–180, Mar. 03, 2020, doi: 10.1080/00295639.2019.1686882.
- [210] K. Minato, T. Ogawa, K. Fukuda, H. Sekino, I. Kitagawa, and N. Mita, “Fission product release from ZrC-coated fuel particles during post-irradiation heating at 1800 and 2000°C,” *J. Nucl. Mater.*, vol. 249, no. 2–3, pp. 142–149, 1997, doi: 10.1016/S0022-3115(97)00223-7.
- [211] E. G. Acheson, “Carborundum: Its history, manufacture and uses,” *J. Franklin Inst.*, vol. 136, no. 3, pp. 194–203, 1893, doi: 10.1016/0016-0032(93)90369-6.
- [212] J. S. Goela, L. E. Burns, and R. L. Taylor, “Transparent chemical vapor deposited β -SiC,” *Appl. Phys. Lett.*, vol. 64, no. 2, pp. 131–133, 1994, doi: 10.1063/1.111541.
- [213] “Chemical Vapor Deposition - an overview | ScienceDirect Topics.” <https://www.sciencedirect.com/topics/materials-science/chemical-vapor-deposition> (accessed Oct. 21, 2019).
-

- [214] S. Yajima, J. Hayashi, J. Omori, and K. Okamura, "Development of a Silicon carbide fibre with high tensile strength," *Nature*, vol. 261, no. 5562, pp. 683–685, 1976, doi: 10.1038/261683a0.
- [215] J. N. Ness and T. F. Page, "Microstructural evolution in reaction-bonded silicon carbide," *J. Mater. Sci.*, vol. 21, no. 4, pp. 1377–1397, 1986, doi: 10.1007/BF00553278.
- [216] K. Yueh and K. A. Terrani, "Silicon carbide composite for light water reactor fuel assembly applications," *J. Nucl. Mater.*, vol. 448, no. 1–3, pp. 380–388, 2014, doi: 10.1016/j.jnucmat.2013.12.004.
- [217] Z. Liu *et al.*, "The development of cladding materials for the accident tolerant fuel system from the Materials Genome Initiative," *Scr. Mater.*, vol. 141, no. December, pp. 99–106, 2017, doi: 10.1016/j.scriptamat.2017.07.030.
- [218] C. H. CARTER, R. F. DAVIS, and J. BENTLEY, "Kinetics and Mechanisms of High-Temperature Creep in Silicon Carbide: II, Chemically Vapor Deposited," *J. Am. Ceram. Soc.*, vol. 67, no. 11, pp. 732–740, 1984, doi: 10.1111/j.1151-2916.1984.tb19510.x.
- [219] S. Zhu, M. Mizuno, Y. Nagano, J. Cao, Y. Kagawa, and H. Kaya, "Creep and Fatigue Behavior in an Enhanced SiC / SiC Composite at," *System*, vol. 77, pp. 2269–2277, 1998.
- [220] D. Henderson, L. El-Guebaly, P. Wilson, A. Abdou, and A. Team, "Activation, decay heat, and waste disposal analyses for the ARIES-AT power plant," *Fusion Technol.*, vol. 39, no. 2, pp. 444–448, 2001.
- [221] E. A. Mogahed, L. El-Guebaly, A. Abdou, P. Wilson, D. Henderson, and A. Team, "Loss of coolant accident and loss of flow accident analysis of the ARIES-AT design," *Fusion Technol.*, vol. 39, no. 2, pp. 462–466, 2001.
- [222] R. Naslain, "Design, preparation and properties of non-oxide CMCs for application in
-

- engines and nuclear reactors: An overview,” *Compos. Sci. Technol.*, vol. 64, no. 2, pp. 155–170, 2004, doi: 10.1016/S0266-3538(03)00230-6.
- [223] S. Pellegrino, L. Thomé, A. DeBelle, S. Miro, and P. Trocellier, “Radiation effects in carbides: TiC and ZrC versus SiC,” *Nucl. Instruments Methods Phys. Res. Sect. B Beam Interact. with Mater. Atoms*, vol. 327, no. 1, pp. 103–107, 2014, doi: 10.1016/j.nimb.2013.11.046.
- [224] C. W. Watson, “Nuclear Rockets: High-Performance Propulsion for Mars,” 1994.
- [225] J. M. Taub, “A Review of Fuel Element Development for Nuclear Rocket Engine,” no. June, pp. 1–48, 1975, doi: LA-5931.
- [226] E. K. Storms, *The refractory carbides*. Academic Press, 1967.
- [227] H. F. Jackson and W. E. Lee, *Properties and characteristics of zrc*, vol. 2. Elsevier Inc., 2012.
- [228] M. B. Chadwick *et al.*, “ENDF/B-VII.1 nuclear data for science and technology: Cross sections, covariances, fission product yields and decay data,” *Nucl. Data Sheets*, vol. 112, no. 12, pp. 2887–2996, 2011, doi: 10.1016/j.nds.2011.11.002.
- [229] E. K. Storms and P. Wagner, “Thermal conductivity of substoichiometric ZrC and NbC,” *High Temp. Sci.*, v. 5, no. 6, pp. 454–462, Dec. 1973, Accessed: Jun. 05, 2019. [Online]. Available: <https://www.osti.gov/biblio/4344444>.
- [230] R. V. SARA, “The System Zirconium—Carbon,” *J. Am. Ceram. Soc.*, vol. 48, no. 5, pp. 243–247, 1965, doi: 10.1111/j.1151-2916.1965.tb14729.x.
- [231] A. Arya and E. A. Carter, “Structure, bonding, and adhesion at the ZrC(1 0 0)/Fe(1 1 0) interface from first principles,” *Surf. Sci.*, vol. 560, no. 1–3, pp. 103–120, 2004, doi: 10.1016/j.susc.2004.04.022.
- [232] J. Li, D. Liao, S. Yip, R. Najafabadi, and L. Ecker, “Force-based many-body interatomic
-

- potential for ZrC,” *J. Appl. Phys.*, vol. 93, no. 11, pp. 9072–9085, 2003, doi: 10.1063/1.1567819.
- [233] W. S. Williams, “The thermal conductivity of metallic ceramics,” *JOM*, vol. 50, no. 6, pp. 62–66, Jun. 1998, doi: 10.1007/s11837-998-0131-y.
- [234] L. N. GROSSMAN, “High-Temperature Thermophysical Properties of Zirconium Carbide,” *J. Am. Ceram. Soc.*, vol. 48, no. 5, pp. 236–242, 1965, doi: 10.1111/j.1151-2916.1965.tb14728.x.
- [235] J. Kim and Y. J. Suh, “Temperature- and pressure-dependent elastic properties, thermal expansion ratios, and minimum thermal conductivities of ZrC, ZrN, and Zr(C_{0.5}N_{0.5}),” *Ceram. Int.*, vol. 43, no. 15, pp. 12968–12974, 2017, doi: 10.1016/j.ceramint.2017.06.195.
- [236] C. R. Houska, “Thermal expansion and atomic vibration amplitudes for TiC, TiN, ZrC, ZrN, and pure tungsten,” *J. Phys. Chem. Solids*, vol. 25, no. 4, pp. 359–366, 1964, doi: 10.1016/0022-3697(64)90001-0.
- [237] R. O. Elliott and C. P. Kempter, “Thermal expansion of some transition metal carbides,” *J. Phys. Chem.*, vol. 62, no. 5, pp. 630–631, 1958, doi: 10.1021/j150563a030.
- [238] R. Chang and L. J. Graham, “Low-temperature elastic properties of ZrC and TiC,” *J. Appl. Phys.*, vol. 37, no. 10, pp. 3778–3783, 1966, doi: 10.1063/1.1707923.
- [239] D. W. LEE and J. S. HAGGERTY, “Plasticity and Creep in Single Crystals of Zirconium Carbide,” *J. Am. Ceram. Soc.*, vol. 52, no. 12, pp. 641–647, 1969, doi: 10.1111/j.1151-2916.1969.tb16067.x.
- [240] S. Shimada, “Interfacial reaction on oxidation of carbides with formation of carbon,” *Solid State Ionics*, vol. 141–142, pp. 99–104, 2001, doi: 10.1016/S0167-2738(01)00727-5.
-

- [241] S. Shimada, M. Nishisako, M. Inagaki, and K. Yamamoto, "Formation and Microstructure of Carbon-Containing Oxide Scales by Oxidation of Single Crystals of Zirconium Carbide," *Journal of the American Ceramic Society*, vol. 78, no. 1, pp. 41–48, 1995, doi: 10.1111/j.1151-2916.1995.tb08358.x.
- [242] S. Shimada, M. Inagaki, and M. Suzuki, "Microstructural observation of the ZrC/ZrO₂ interface formed by oxidation of ZrC," *J. Mater. Res.*, vol. 11, no. 10, pp. 2594–2597, 1996, doi: 10.1557/JMR.1996.0326.
- [243] L. Tan, T. R. Allen, and P. Demkowicz, "High temperature interfacial reactions of TiC, ZrC, TiN, and ZrN with palladium," *Solid State Ionics*, vol. 181, no. 25–26, pp. 1156–1163, 2010, doi: 10.1016/j.ssi.2010.06.054.
- [244] W. A. Stark, "Cesium solubility, diffusion and permeation in zirconium carbide," *J. Nucl. Mater.*, vol. 73, no. 2, pp. 169–179, 1978, doi: 10.1016/0022-3115(78)90557-3.
- [245] K. Fukuda, K. Ikawa, and K. Iwamoto, "Fission product diffusion in ZrC coated fuel particles," *J. Nucl. Mater.*, vol. 87, no. 2–3, pp. 367–374, 1979, doi: 10.1016/0022-3115(79)90574-9.
- [246] A. Auskern, "Rare gas diffusion in nonstoichiometric zirconium carbide," *J. Nucl. Mater.*, vol. 22, no. 3, pp. 257–268, 1967, doi: 10.1016/0022-3115(67)90043-8.
- [247] K. Minato *et al.*, "Fission product release from ZrC-coated fuel particles during postirradiation heating at 1600°C," *J. Nucl. Mater.*, vol. 224, no. 1, pp. 85–92, 1995, doi: 10.1016/0022-3115(95)00032-1.
- [248] T. Ogawa and K. Ikawa, "Diffusion of metal fission products in ZrC_{1.0}," *J. Nucl. Mater.*, vol. 105, no. 2–3, pp. 331–334, 1982, doi: 10.1016/0022-3115(82)90391-9.
- [249] P. Patriarca and W. O. Harms, "FUELS AND MATERIALS DEVELOPMENT PROGRAM. Quarterly Progress Report for Period Ending September 30, 1968.," Oak Ridge, TN (United States), Feb. 1969. doi: 10.2172/4804320.
-

- [250] G. W. Keilholtz, R. E. Moore, and M. F. Osborne, "Fast-Neutron Effects on the Carbides of Titanium, Zirconium, Tantalum, Niobium, and Tungsten," *Nucl. Appl.*, vol. 4, no. 5, pp. 330–336, 2017, doi: 10.13182/nt68-a26398.
- [251] Y. Huang, B. R. Maier, and T. R. Allen, "Irradiation-induced effects of proton irradiation on zirconium carbides with different stoichiometries," *Nucl. Eng. Des.*, vol. 277, pp. 55–63, 2014, doi: 10.1016/j.nucengdes.2014.06.001.
- [252] Y. Yang, C. A. Dickerson, H. Swoboda, B. Miller, and T. R. Allen, "Microstructure and mechanical properties of proton irradiated zirconium carbide," *J. Nucl. Mater.*, vol. 378, no. 3, pp. 341–348, 2008, doi: 10.1016/j.jnucmat.2008.06.042.
- [253] Y. Yang, W. Y. Lo, C. Dickerson, and T. R. Allen, "Stoichiometry effect on the irradiation response in the microstructure of zirconium carbides," *J. Nucl. Mater.*, vol. 454, no. 1–3, pp. 130–135, 2014, doi: 10.1016/j.jnucmat.2014.07.071.
- [254] J. Gan, M. Meyer, R. Birtcher, and T. Allen, "Microstructure Evolution in ZrC Irradiated with Kr ions," *J. ASTM Int.*, vol. 3, no. 4, p. 12376, Feb. 2006, doi: 10.1520/JAI12376.
- [255] D. Gosset, M. Dollé, D. Simeone, G. Baldinozzi, and L. Thomé, "Structural evolution of zirconium carbide under ion irradiation," *J. Nucl. Mater.*, vol. 373, no. 1–3, pp. 123–129, 2008, doi: 10.1016/j.jnucmat.2007.05.034.
- [256] D. Gosset, M. Dollé, D. Simeone, G. Baldinozzi, and L. Thomé, "Structural behaviour of nearly stoichiometric ZrC under ion irradiation," *Nucl. Instruments Methods Phys. Res. Sect. B Beam Interact. with Mater. Atoms*, vol. 266, no. 12–13, pp. 2801–2805, 2008, doi: 10.1016/j.nimb.2008.03.121.
- [257] S. Pellegrino, L. Thomé, A. Debelle, S. Miro, and P. Trocellier, "Damage production in carbide single crystals irradiated with MeV heavy ions," *Nucl. Instruments Methods Phys. Res. Sect. B Beam Interact. with Mater. Atoms*, vol. 307, pp. 294–298, 2013, doi: 10.1016/j.nimb.2012.11.091.
-

- [258] M. L. Taubin, S. V. Fateev, M. V. Ivanov, and P. V. Shutov, "Change of the physical properties of zirconium carbide in a short exposure to a neutron current," *Sov. At. Energy*, vol. 71, no. 1, pp. 74–76, 1991, [Online]. Available: <https://link.springer.com/article/10.1007%2FBF01129994>.
- [259] A. D. Mazzoni and M. S. Conconi, "Synthesis of Group IVB Metals Oxidecarbides by Carbo-reduction Reactions," *Mater. Res.*, vol. 5, no. 4, pp. 459–466, 2005, doi: 10.1590/s1516-14392002000400011.
- [260] G. Vasudevamurthy, T. W. Knight, E. Roberts, and T. M. Adams, "Laboratory production of zirconium carbide compacts for use in inert matrix fuels," *J. Nucl. Mater.*, vol. 374, no. 1–2, pp. 241–247, 2008, doi: 10.1016/j.jnucmat.2007.08.016.
- [261] M. D. Sacks, C. A. Wang, Z. Yang, and A. Jain, "Carbothermal reduction synthesis of nanocrystalline zirconium carbide and hafnium carbide powders using solution-derived precursors," *J. Mater. Sci.*, vol. 39, no. 19, pp. 6057–6066, 2004, doi: 10.1023/B:JMSC.0000041702.76858.a7.
- [262] Y. Wang, Q. Liu, J. Liu, L. Zhang, and L. Cheng, "Deposition mechanism for chemical vapor deposition of zirconium carbide coatings," *J. Am. Ceram. Soc.*, vol. 91, no. 4, pp. 1249–1252, 2008, doi: 10.1111/j.1551-2916.2007.02253.x.
- [263] O. El-Atwani *et al.*, "In-situ TEM observation of the response of ultrafine- and nanocrystalline-grained tungsten to extreme irradiation environments," *Sci. Rep.*, vol. 4, no. 1, p. 4716, 2015, doi: 10.1038/srep04716.
- [264] X. M. Bai and B. P. Uberuaga, "The influence of grain boundaries on radiation-induced point defect production in materials: A review of atomistic studies," *Jom*, vol. 65, no. 3, pp. 360–373, 2013, doi: 10.1007/s11837-012-0544-5.
- [265] X. M. Bai, a. F. Voter, R. G. Hoagland, M. Nastasi, and B. P. Uberuaga, "Efficient Annealing of Radiation Damage Near Grain Boundaries via Interstitial Emission," *Science (80-.)*, vol. 327, no. 5973, pp. 1631–1634, 2010, doi:
-

10.1126/science.1183723.

- [266] E. M. Bringa *et al.*, “Are nanoporous materials radiation resistant?,” *Nano Lett.*, vol. 12, no. 7, pp. 3351–3355, 2012, doi: 10.1021/nl201383u.
- [267] J. Li, H. Wang, and X. Zhang, “A Review on the Radiation Response of Nanoporous Metallic Materials,” *Jom*, vol. 70, no. 11, pp. 2753–2764, 2018, doi: 10.1007/s11837-018-3111-x.
- [268] G. Ackland, “Controlling radiation damage,” *Science (80-.)*, vol. 327, no. 5973, pp. 1587–1588, 2010, doi: 10.1126/science.1188088.
- [269] S. a. Thibeault, J. H. Kang, G. Sauti, C. Park, C. C. Fay, and G. C. King, “Nanomaterials for radiation shielding,” *MRS Bull.*, vol. 40, no. 10, pp. 836–841, 2015, doi: 10.1557/mrs.2015.225.
- [270] E. Aradi *et al.*, “Radiation damage suppression in AISI-316 steel nanoparticles: Implications for the design of future nuclear materials,” *ACS Appl. Nano Mater.*, vol. 3, no. 10, pp. 9652–9662, Oct. 2020, doi: 10.1021/acsanm.0c01611.
- [271] E. Aradi, J. Lewis-Fell, G. Greaves, S. E. Donnelly, and J. A. Hinks, “In Situ TEM Investigations of the Microstructural Changes and Radiation Tolerance in SiC Nanowhiskers Irradiated with He Ions at High Temperatures,” *SSRN Electron. J.*, Sep. 2020, doi: 10.2139/ssrn.3674678.
- [272] E. Aradi *et al.*, “Direct Comparison of Tungsten Nanoparticles and Foils under Helium Irradiation at High Temperatures Studied via In-Situ Transmission Electron Microscopy,” *Microsc. Microanal.*, vol. 25, no. S2, pp. 1576–1577, Aug. 2019, doi: 10.1017/s1431927619008614.
- [273] B. Tyburska-Püschel *et al.*, “Size distribution of black spot defects and their contribution to swelling in irradiated SiC,” *J. Nucl. Mater.*, vol. 476, pp. 132–139, 2016, doi: 10.1016/j.jnucmat.2016.04.044.
-

- [274] E. Aradi, J. Lewis-Fell, G. Greaves, S. E. Donnelly, and J. A. Hinks, "Low-temperature investigations of ion-induced amorphisation in silicon carbide nanowhiskers under helium irradiation," *Appl. Surf. Sci.*, no. September, p. 143969, 2019, doi: 10.1016/j.apsusc.2019.143969.
- [275] E. M. Bringa *et al.*, "Are nanoporous materials radiation resistant?," *Nano Lett.*, vol. 12, no. 7, pp. 3351–3355, 2012, doi: 10.1021/nl201383u.
- [276] A. Moitra *et al.*, "Melting tungsten nanoparticles: A molecular dynamics study," *J. Phys. D: Appl. Phys.*, vol. 41, no. 18, 2008, doi: 10.1088/0022-3727/41/18/185406.
- [277] J.-M. Teulon *et al.*, "On the Operational Aspects of Measuring Nanoparticle Sizes," *Nanomaterials*, vol. 9, no. 1, p. 18, 2018, doi: 10.3390/nano9010018.
- [278] N. Shalkevich, W. Escher, T. Bürgi, B. Michel, L. Si-Ahmed, and D. Poulikakos, "On the thermal conductivity of gold nanoparticle colloids," *Langmuir*, vol. 26, no. 2, pp. 663–670, 2010, doi: 10.1021/la9022757.
- [279] E. Aradi, J. Lewis-Fell, G. Greaves, S. E. Donnelly, and J. A. Hinks, "Low-temperature investigations of ion-induced amorphisation in silicon carbide nanowhiskers under helium irradiation," *Appl. Surf. Sci.*, no. September, p. 143969, 2019, doi: 10.1016/j.apsusc.2019.143969.
- [280] A. V. Krasheninnikov and K. Nordlund, "Ion and electron irradiation-induced effects in nanostructured materials," *J. Appl. Phys.*, vol. 107, no. 7, 2010, doi: 10.1063/1.3318261.
- [281] F. Seitz, "On the disordering of solids by action of fast massive particles," *Discuss. Faraday Soc.*, vol. 5, pp. 271–282, 1949, doi: 10.1039/DF9490500271.
- [282] E. W. Etherington, J. I. Bramman, R. S. Nelson, and M. J. Norgett, "A UKAEA evaluation of displacement damage models for iron," *Nucl. Eng. Des.*, vol. 33, no. 1, pp. 82–90, 1975, doi: 10.1016/0029-5493(75)90039-4.
-

- [283] P. Sigmund, "On the number of atoms displaced by implanted ions or energetic recoil atoms," *Appl. Phys. Lett.*, vol. 14, no. 3, pp. 114–117, 1969, doi: 10.1063/1.1652730.
- [284] W. S. Snyder and J. Neufeld, "Disordering of solids by neutron radiation," *Phys. Rev.*, vol. 97, no. 6, pp. 1636–1646, 1955, doi: 10.1103/PhysRev.97.1636.
- [285] M. J. Norgett, M. T. Robinson, and I. M. Torrens, "A proposed method of calculating displacement dose rates," *Nucl. Eng. Des.*, vol. 33, no. 1, pp. 50–54, 1975, doi: 10.1016/0029-5493(75)90035-7.
- [286] R. E. Stoller, M. B. Toloczko, G. S. Was, a. G. Certain, S. Dwaraknath, and F. a. Garner, "On the use of SRIM for computing radiation damage exposure," *Nucl. Instruments Methods Phys. Res. Sect. B Beam Interact. with Mater. Atoms*, vol. 310, pp. 75–80, 2013, doi: 10.1016/j.nimb.2013.05.008.
- [287] W. J. Weber and Y. Zhang, "Predicting damage production in monoatomic and multi-elemental targets using stopping and range of ions in matter code: Challenges and recommendations," *Curr. Opin. Solid State Mater. Sci.*, no. May, pp. 0–1, 2019, doi: 10.1016/j.cossms.2019.06.001.
- [288] O. Camara, M. A. Tunes, G. Greaves, A. H. Mir, S. Donnelly, and J. A. Hinks, "Understanding amorphization mechanisms using ion irradiation in situ a TEM and 3D damage reconstruction," *Ultramicroscopy*, vol. 207, p. 112838, Dec. 2019, doi: 10.1016/j.ultramic.2019.112838.
- [289] A. Claverie, A. Roumili, N. Gessinn, and J. Beauvillain, "Kinetics of silicon amorphization by N⁺ implantation: Dose rate and substrate temperature effects," *Mater. Sci. Eng. B*, vol. 4, no. 1–4, pp. 205–209, 1989, doi: 10.1016/0921-5107(89)90243-2.
- [290] M. Nelkon, *Physics and Radio*. Edward Arnold LTD, 1944.
- [291] B. N. Singh, "Effect of grain size on void formation during high-energy electron
-

irradiation of austenitic stainless steel," *Philos. Mag.*, vol. 29, no. 1, p. 25, 1974, doi: 10.1080/14786437408213551.

- [292] M. R. Gilbert, S. L. Dudarev, S. Zheng, and L. W. Packer, "Transmutation , gas production , and helium embrittlement in materials under neutron irradiation," no. 12, p. 2012, 2012.
-


```
os.chdir(Srim_out_path) #Changes directory to output folder
```

```
#Bellow creates various text files to write data to
```

```
first_open_new = open('All_Colisions_in_sphere.txt', 'w')
```

```
first_open_new.write('Recoil, Atom Num, Atom Energy(eV), X (A), Y (A), Z (A), Vac, Repl \n')
```

```
first_open_new.close()
```

```
first_open_new = open('All_Colisions_in_sphere_rounded_to_nearest_10.txt', 'w')
```

```
#first_open_new.write('Recoil, Atom Num, Atom Energy(eV), X (A), Y (A), Z (A), Vac, Repl \n')
```

```
first_open_new.close()
```

```
ff1 = open('Sphere_RANGE_3D.txt', 'w')
```

```
ff1.write('lon, Depth X, Lateral Y, Lateral Z\n')
```

```
ff1.close
```

```
ff1 = open('Sphere_RANGE_3D_rounded.txt', 'w')
```

```
#ff1.write('lon, Depth X, Lateral Y, Lateral Z\n')
```

```
ff1.close
```

```
first_open_new = open('All_Vacancies_in_Sphere.txt', 'w')

first_open_new.write('Recoil, Atom Num, Atom Energy(eV), X (A), Y (A), Z (A), Vac, Repl \n')

first_open_new.close()


first_open_new = open('All_Vacancies_in_Sphere_rounded.txt', 'w')

#first_open_new.write('Recoil, Atom Num, Atom Energy(eV), X (A), Y (A), Z (A), Vac, Repl \n')

first_open_new.close()


first_open_new = open('All_Replacements_in_sphere.txt', 'w')

first_open_new.write('Recoil, Atom Num, Atom Energy(eV), X (A), Y (A), Z (A), Vac, Repl \n')

first_open_new.close()


first_open_new = open('All_Replacements_in_sphere_rounded.txt', 'w')

#first_open_new.write('Recoil, Atom Num, Atom Energy(eV), X (A), Y (A), Z (A), Vac, Repl \n')

first_open_new.close()


first_open_new = open('Minimum_Distance_to_Surface.txt', 'w')

#first_open_new.write('Recoil, Atom Num, Atom Energy(eV), Distance, Vac, Repl \n')

first_open_new.close()


first_open_new = open('Minimum_Distance_to_Surface_rounded.txt', 'w')
```

```
first_open_new.write('Recoil, Atom Num, Atom Energy(eV), Distance, Vac, Repl \n')

first_open_new.close()


first_open_new = open('Backscat1.txt', 'w')

first_open_new.write('Recoil, Atom Num, Atom Energy(eV), Distance, Vac, Repl \n')

first_open_new.close()


os.chdir(Path) # Changes directory to SRIM.exe location


# Below changes TRIM auto text file to allow for no user input

Trim_auto_new = open('TRIMAUTO', 'w')

Trim_auto_new.write('1\n\n TRIMAUTO allows the running of TRIM in batch mode (without any keyboard
inputs).\nThis feature is controlled by the number in line #1 (above).\n 0 = Normal TRIM - New Calculation
based on TRIM.IN made by setup program.\n 1 = Auto TRIM - TRIM based on TRIM.IN. No inputs required.
Terminates after all ions.\n 2 = RESUME - Resume old TRIM calculation based on files: SRIM Restore\*.SAV.\n
\n Line #2 of this file is the Directory of Resumed data, e.g. A:/TRIM2/\n If empty, the default is the
SRIM/SRIM Restore directory.\n\nSee the file TRIMAUTO.TXT for more details.')

Trim_auto_new.close()


os.chdir(Srim_out_path) # Changes back to output folder

ele_num = '0' #Defines ele_num as string

rad = input('What is the radius of the sphere in Angstroms? \n') #Asks user for Radius of sphere

NI = float(10)#input('How many iterations would you like to run?\n') #Defines number of iterations now set to
10 but may change back to user input in the future
```

```
print 'This program can split compounds into elements (Up to 4 elements)'

Q = raw_input('Are you analysing a compound?\nY/N\n') #Asks if compound is being analysed

if Q == 'Y' or Q == 'y':

    ele_num = raw_input('How many elements are there in the compound? \n') #Asks for number of
elements

#Below creates files depending on number of elements in compound

if ele_num == '2':

    first_open_new = open("All_Colisions_Element1_in_sphere.txt", "w")

    first_open_new.write('Recoil, Atom Num, Atom Energy(eV), X (A), Y (A), Z (A), Vac, Repl \n')

    first_open_new.close()

    first_open_new = open("All_Colisions_Element1_in_sphere_rounded.txt", "w")

    first_open_new.write('Recoil, Atom Num, Atom Energy(eV), X (A), Y (A), Z (A), Vac, Repl \n')

    first_open_new.close()

    first_open_new = open("All_Colisions_Element2_in_sphere.txt", "w")

    first_open_new.write('Recoil, Atom Num, Atom Energy(eV), X (A), Y (A), Z (A), Vac, Repl \n')

    first_open_new.close()
```

```
first_open_new = open("All_Colisions_Element2_in_sphere_rounded.txt", "w")

first_open_new.write('Recoil, Atom Num, Atom Energy(eV), X (A), Y (A), Z (A), Vac, Repl \n')

first_open_new.close()


f4 = open("All_Colisions_Element1_in_sphere.txt", "a")

round_ele1 = open("All_Colisions_Element1_in_sphere_rounded.txt", "a")

f5 = open("All_Colisions_Element2_in_sphere.txt", "a")

round_ele2 = open("All_Colisions_Element2_in_sphere_rounded.txt", "a")


Atom_number = raw_input('What is the first atom number would you like to single out from your
compound? \n Note that number 6 would be 06. Only input 2 numbers. \n') #Defines atom numbers to split

anum1 = Atom_number[0]

anum2 = Atom_number[1]


Atom_number2 = raw_input('What is the second atom number would you like to single out from your
compound? \n Note that number 6 would be 06. Only input 2 numbers. \n')

anum21 = Atom_number2[0]

anum22 = Atom_number2[1]


if ele_num == '3':

    first_open_new = open("All_Colisions_Element1_in_sphere.txt", "w")
```

```
first_open_new.write('Recoil, Atom Num, Atom Energy(eV), X (A), Y (A), Z (A), Vac, Repl \n')

first_open_new.close()
```

```
first_open_new = open("All_Colisions_Element1_in_sphere_rounded.txt", "w")

first_open_new.write('Recoil, Atom Num, Atom Energy(eV), X (A), Y (A), Z (A), Vac, Repl \n')

first_open_new.close()
```

```
first_open_new = open("All_Colisions_Element2_in_sphere.txt", "w")

first_open_new.write('Recoil, Atom Num, Atom Energy(eV), X (A), Y (A), Z (A), Vac, Repl \n')

first_open_new.close()
```

```
first_open_new = open("All_Colisions_Element2_in_sphere_rounded.txt", "w")

first_open_new.write('Recoil, Atom Num, Atom Energy(eV), X (A), Y (A), Z (A), Vac, Repl \n')

first_open_new.close()
```

```
first_open_new = open("All_Colisions_Element3_in_sphere.txt", "w")

first_open_new.write('Recoil, Atom Num, Atom Energy(eV), X (A), Y (A), Z (A), Vac, Repl \n')

first_open_new.close()
```

```
first_open_new = open("All_Colisions_Element3_in_sphere_rounded.txt", "w")

first_open_new.write('Recoil, Atom Num, Atom Energy(eV), X (A), Y (A), Z (A), Vac, Repl \n')
```

```
first_open_new.close()
```

```
f4 = open("All_Colisions_Element1_in_sphere.txt", "a")
```

```
round_ele1 = open("All_Colisions_Element1_in_sphere_rounded.txt", "a")
```

```
f5 = open("All_Colisions_Element2_in_sphere.txt", "a")
```

```
round_ele2 = open("All_Colisions_Element2_in_sphere_rounded.txt", "a")
```

```
f6 = open("All_Colisions_Element3_in_sphere.txt", "a")
```

```
round_ele3 = open("All_Colisions_Element3_in_sphere_rounded.txt", "a")
```

```
Atom_number = raw_input('What is the first atom number would you like to single out from your compound? \n Note that number 6 would be 06. Only input 2 numbers. \n')
```

```
anum1 = Atom_number[0]
```

```
anum2 = Atom_number[1]
```

```
Atom_number2 = raw_input('What is the second atom number would you like to single out from your compound? \n Note that number 6 would be 06. Only input 2 numbers. \n')
```

```
anum21 = Atom_number2[0]
```

```
anum22 = Atom_number2[1]
```

```
Atom_number3 = raw_input('What is the third atom number would you like to single out from your compound? \n Note that number 6 would be 06. Only input 2 numbers. \n')
```

```
anum31 = Atom_number3[0]
```



```
anum32 = Atom_number3[1]

if ele_num == '4':

    first_open_new = open("All_Colisions_Element1_in_sphere.txt", "w")

    first_open_new.write('Recoil, Atom Num, Atom Energy(eV), X (A), Y (A), Z (A), Vac, Repl \n')

    first_open_new.close()

    first_open_new = open("All_Colisions_Element2_in_sphere.txt", "w")

    first_open_new.write('Recoil, Atom Num, Atom Energy(eV), X (A), Y (A), Z (A), Vac, Repl \n')

    first_open_new.close()

    first_open_new = open("All_Colisions_Element3_in_sphere.txt", "w")

    first_open_new.write('Recoil, Atom Num, Atom Energy(eV), X (A), Y (A), Z (A), Vac, Repl \n')

    first_open_new.close()

    first_open_new = open("All_Colisions_Element4_in_sphere.txt", "w")

    first_open_new.write('Recoil, Atom Num, Atom Energy(eV), X (A), Y (A), Z (A), Vac, Repl \n')

    first_open_new.close()

    f4 = open("All_Colisions_Element1_in_sphere.txt", "a")

    round_ele1 = open("All_Colisions_Element1_in_sphere_rounded.txt", "a")
```

```
f5 = open("All_Colisions_Element2_in_sphere.txt", "a")
```

```
round_ele2 = open("All_Colisions_Element2_in_sphere_rounded.txt", "a")
```

```
f6 = open("All_Colisions_Element3_in_sphere.txt", "a")
```

```
round_ele3 = open("All_Colisions_Element3_in_sphere_rounded.txt", "a")
```

```
f7 = open("All_Colisions_Element4_in_sphere.txt", "a")
```

```
round_ele4 = open("All_Colisions_Element4_in_sphere_rounded.txt", "a")
```

```
Atom_number = raw_input('What is the first atom number would you like to single out from your  
compound? \n Note that number 6 would be 06. Only input 2 numbers. \n')
```

```
anum1 = Atom_number[0]
```

```
anum2 = Atom_number[1]
```

```
Atom_number2 = raw_input('What is the second atom number would you like to single out from your  
compound? \n Note that number 6 would be 06. Only input 2 numbers. \n')
```

```
anum21 = Atom_number2[0]
```

```
anum22 = Atom_number2[1]
```

```
Atom_number3 = raw_input('What is the third atom number would you like to single out from your  
compound? \n Note that number 6 would be 06. Only input 2 numbers. \n')
```

```
anum31 = Atom_number3[0]
```

```
anum32 = Atom_number3[1]
```

```
Atom_number4 = raw_input('What is the third atom number would you like to single out from your compound? \n Note that number 6 would be 06. Only input 2 numbers. \n')
```

```
anum41 = Atom_number4[0]
```

```
anum42 = Atom_number4[1]
```

```
#Below defines variables
```

```
rad = float(rad) #converts rad to float
```

```
rad_neg = float(rad * -1)
```

```
z_mod = float(0)
```

```
y_mod = float(0)
```

```
NIhalf = float(NI/2)
```

```
calczrad = float(0)
```

```
calczradneg = float(0)
```

```
ymodsqr = float(0)
```

```
gg2 = 0
```

```
yzmod = float(0)
```

```
radsqr = float(rad*rad)
```

```
while y_mod >= rad_neg: #Code loops as long a y mod doesn't become less than rad negative
```

```
if yzmod < rad: #Makes sure that SRIM only runs when variables in sphere. Cuts down run time.
```

```
os.chdir(Path) #Changes to SRIM.exe path

os.system('TRIM.exe') #Runs TRIM

Trim = open('TRIM.IN', 'r') #Reads TRIM.IN file

Trimlist = Trim.readlines()

Trim.close()

Trim_new = open('TRIM.IN', 'w') #Writes over TRIM.IN

Linecount = 1

os.chdir(Srim_out_path) #Changes directory to output

f = open('COLLISON.txt', 'r') #Reads Collision file

linelist = f.readlines()

f.close

ff = open('RANGE_3D.txt', 'r') #Reads Range file

Rangelist = ff.readlines()

ff.close
```

```
fff = open('BACKSCAT.txt', 'r') #Reads Backscat file
```

```
Backscatlist = fff.readlines()
```

```
fff.close
```

```
#Below opens created files to append data to
```

```
f1 = open("All_Colisions_in_sphere.txt", "a")
```

```
f8 = open('All_Vacancies_in_Sphere.txt', 'a')
```

```
f9 = open('All_Replacements_in_sphere.txt', 'a')
```

```
min_dist = open('Minimum_Distance_to_Surface.txt', 'a')
```

```
ff2 = open('Sphere_RANGE_3D.txt', 'a')
```

```
round_all = open('All_Colisions_in_sphere_rounded_to_nearest_10.txt', 'a')
```

```
round_rep = open('All_Replacements_in_sphere_rounded.txt', 'a')
```

```
round_vac = open('All_Vacancies_in_Sphere_rounded.txt', 'a')
```

```
round_range = open('Sphere_RANGE_3D_rounded.txt', 'a')
```

```
round_min = open('Minimum_Distance_to_Surface_rounded.txt', 'a')
```

```
backscatf = open('Backscat1.txt', 'a')
```

```
for line in Backscatlist: #Loops over each line in Backscatter file
```

```
    if len(line) > 64 and "B" in line[0]: #Checks for backscattered ion
```

```
        backscatf.write(line) #Writes to appended file
```

```

#Below edits Trim.IN file

for line in Trimlist:

    if Linecount != 5:

        Trim_new.write(line)

    else:

        Seedcount = int(''.join(line[57:59]))

        Seedcount = (Seedcount + 1)

        if Seedcount < 10:

            Seedcount = str(Seedcount)

            Trim_new.write('          2          ' + Seedcount + '
0\n')

        else:

            if Seedcount < 100:

                Seedcount = str(Seedcount)

                Trim_new.write('          2          ' +
Seedcount + '  0\n')

            else:

                Seedcount = str(Seedcount)

                Trim_new.write('          2          ' +
Seedcount + '  0\n')

```

```
Linecount = (Linecount + 1)
```

```
Trim_new.close()
```

```
#Below Calculating Damage
```

```
if y_mod >= rad_neg: #Code loops as long a y mod doesn't become less than rad negative
```

```
for line in linelist: #Loops over each line in collision file
```

```
    if len(line) > 64 and chr(0x000db) in line[0]: #Checks for data
```

```
        Xa = float(''.join(line[25:29])) #Pulls X data
```

```
        Ya = float(''.join(line[36:40])) #Pulls y data
```

```
        Za = float(''.join(line[47:51])) #Pulls z data
```

```
        Zpm = line[46] #checks for negative
```

```
        Ypm = line[35] #checks for negative
```

```
        Xpm = line[24] #checks for negative
```

```
        Xf = float(''.join(line[31:34])) #Pulls power
```

```
        Yf = float(''.join(line[42:45])) #Pulls power
```

```
        Zf = float(''.join(line[53:56])) #Pulls power
```

```
        Xfn1 = float(Xa*10**Xf) #Creates true value
```

```
        Yfn1 = float(Ya*10**Yf) #Creates true value
```

```
        Zfn1 = float(Za*10**Zf) #Creates true value
```

```

if Zpm == '-': #Checks negative and converts true value to negative
if it exists

    Zfn1 = float(Zfn1*-1)

if Ypm == '-': #Checks negative and converts true value to negative
if it exists

    Yfn1 = float(Yfn1*-1)

if Xpm == '-': #Checks negative and converts true value to negative
if it exists

    Xfn2 = float(Xfn2*-1)

gg = int(''.join(line[1:7])) #Pulls Ion number

ion_num = (''.join(line[9:12])) #Despite its name pulls the atom
number

Energy = float(''.join(line[13:19])) #Pulls Energy data

Energyf = float(''.join(line[21:24])) # Pulls energy power

Energy_s = float(Energy*10**Energyf) #Creates true energy

Vac = int(line[58]) #Checks for vacancy 0-1

Repl = int(''.join(line[61:64])) #checks for replacement 0-1

Zfn2 = float(Zfn1 + z_mod) #Shifts Z by z_mod

Yfn2 = float(Yfn1 + y_mod) #Shifts Y by y_mod

Y_round = round(Yfn2, 0) #Rounds Z and Y

Z_round = round(Zfn2, 0) #Rounds Z and Y

Zfn1sqr = float(Zfn2*Zfn2) #Squares Z

```



```

yfn1sqr = float(Yfn2*Yfn2)
#####
#####

Yfn_neg = float(Yfn2 * -1) #Creates a Y and Z negative

Zfn2_neg = float(Zfn2 * -1) #Creates a Y and Z negative

if Zfn2 < rad and Zfn2 > rad_neg and Yfn2 < rad and Yfn2 >
rad_neg: #Checks Z value is less than rad, avoids math domain errors

r1sqr = float(radsqr - Zfn1sqr) #Created to work out x
shift

r1sqr2 = float(radsqr - yfn1sqr) #for x shift
#####

xy_mod_c = float(math.sqrt(r1sqr)) #Created to work out
x shift

xy_mod_c2 =
float(math.sqrt(r1sqr2))#####
#####

xy_mod = float(rad - xy_mod_c) #Created to work out x
shift

xy_mod2 = float(rad -
xy_mod_c2)#####
#####

if xy_mod > xy_mod2:

Xfn2 = float(Xfn1 + xy_mod) #shifts X

else:

Xfn2 = float(Xfn1 + xy_mod2)

Xfn3 = float(Xfn2 - rad) #Can't remeber why I did this

```

	<code>Xfn1sqr = float(Xfn3 * Xfn3) #Creates X squared</code>
	<code>X_round = round(Xfn2, 0) #Rounds X value</code>
calculated radius at z value	<code>r1 = float(math.sqrt(r1sqr)) #creates r1 which is</code>
	<code>calc_dia = float(r1*2) #converts r1 to diameter</code>
distance	<code>X_min_dist = float(calc_dia - Xfn1) #Checks minimum</code>
distance	<code>X_min_dist = float(X_min_dist / 2) #Checks minimum</code>
minimum distance	<code>if Yfn2 > 0: #Checks if y is positive or negative to work out</code>
	<code>Y_min_dist = float(r1 - Yfn2)</code>
	<code>else:</code>
	<code>Y_min_dist = float(r1 + Yfn_neg)</code>
minimum distance	<code>if Zfn2 > 0: #Checks if z is positive or negative to work out</code>
	<code>Z_min_dist = float(r1 - Zfn2)</code>
	<code>else:</code>
	<code>Z_min_dist = float(r1 + Zfn2_neg)</code>
distance	<code>X_min_round = round(X_min_dist) #Rounds minimum</code>
distance	<code>Y_min_round = round(Y_min_dist) #Rounds minimum</code>

```

distance
Z_min_round = round(Z_min_dist) #Rounds minimum

Yfn1sqr = float(Yfn2 * Yfn2) #Does Y square

rad_checksqr = float(Xfn1sqr+Yfn1sqr+Zfn1sqr) #Creates
square value for checking if damage in sphere

rad_check = float(math.sqrt(rad_checksqr)) #Square
roots above

if rad_check < rad: #This checks it's within sphere. If it is
then it writes various data below

    if X_min_dist < Y_min_dist and X_min_dist <
Z_min_dist:

        if gg==1 or gg==(gg2+1):

            ma = str(gg)

            mb = str(ion_num)

            mc = str(Energy_s)

            md = str(X_min_dist)

            me = str(X_min_round)

            mg = str(Vac)

            mh = str(Repl)

            min_dist.write(ma + ' , ' + mb +
', ' + mc + ' , ' + md + ' , ' + mg + ' , ' + mh + '\n')

            round_min.write(ma + ' , ' +
mb + ' , ' + mc + ' , ' + me + ' , ' + mg + ' , ' + mh + '\n')

```

```

if Z_min_dist < X_min_dist and Z_min_dist <
Y_min_dist:

    if gg==1 or gg==(gg2+1):

        ma = str(gg)

        mb = str(ion_num)

        mc = str(Energy_s)

        md = str(Z_min_dist)

        me = str(Z_min_round)

        mg = str(Vac)

        mh = str(Repl)

        min_dist.write(ma + ' , ' + mb +
' , ' + mc + ' , ' + md + ' , ' + mg + ' , ' + mh + '\n')

        round_min.write(ma + ' , ' +
mb + ' , ' + mc + ' , ' + me + ' , ' + mg + ' , ' + mh + '\n')

if Y_min_dist < X_min_dist and Y_min_dist <
Z_min_dist:

    if gg==1 or gg==(gg2+1):

        ma = str(gg)

        mb = str(ion_num)

        mc = str(Energy_s)

        md = str(Y_min_dist)

        me = str(Y_min_round)

        mg = str(Vac)

```

```

mh = str(Repl)

min_dist.write(ma + ' ', ' + mb +
', ' + mc + ' ', ' + md + ' ', ' + mg + ' ', ' + mh + '\n')

round_min.write(ma + ' ', ' +
mb + ' ', ' + mc + ' ', ' + me + ' ', ' + mg + ' ', ' + mh + '\n')

if gg==1 or gg==(gg2+1):

    a = str(gg)

    b = str(ion_num)

    d = str(Xfn2)

    e = str(Yfn2)

    f = str(Zfn2)

    c = str(Energy_s)

    g = str(Vac)

    h = str(Repl)

    i = str(X_round)

    j = str(Y_round)

    k = str(Z_round)

f1.write(a + ' ', ' + b + ' ', ' + c + ' ', ' + d + ' ',
' + e + ' ', ' + f + ' ', ' + g + ' ', ' + h + '\n')

round_all.write(a + ' ', ' + b + ' ', ' + c + ' ', '
+ i + ' ', ' + j + ' ', ' + k + ' ', ' + g + ' ', ' + h + '\n')

if g == '1':

```

```

f8.write(a + ' , ' + b + ' , ' + c + ' ,
'+ d + ' , ' + e + ' , ' + f + ' , ' + g + ' , ' + h + '\n')

round_vac.write(a + ' , ' + b + ' ,
'+ c + ' , ' + i + ' , ' + j + ' , ' + k + ' , ' + g + ' , ' + h + '\n')

if h == '1':

f9.write(a + ' , ' + b + ' , ' + c + ' ,
'+ d + ' , ' + e + ' , ' + f + ' , ' + g + ' , ' + h + '\n')

round_rep.write(a + ' , ' + b + ' ,
'+ c + ' , ' + i + ' , ' + j + ' , ' + k + ' , ' + g + ' , ' + h + '\n')

if ele_num == '2':

if anum1 in line[10] and anum2

in line[11]:

f4.write(a + ' , ' + b +
' , ' + c + ' , ' + d + ' , ' + e + ' , ' + f + ' , ' + g + ' , ' + h + '\n')

round_ele1.write(a +
' , ' + b + ' , ' + c + ' , ' + i + ' , ' + j + ' , ' + k + ' , ' + g + ' , ' + h + '\n')

if anum21 in line[10] and
anum22 in line[11]:

f5.write(a + ' , ' + b +
' , ' + c + ' , ' + d + ' , ' + e + ' , ' + f + ' , ' + g + ' , ' + h + '\n')

round_ele2.write(a +
' , ' + b + ' , ' + c + ' , ' + i + ' , ' + j + ' , ' + k + ' , ' + g + ' , ' + h + '\n')

if ele_num == '3':

if anum1 in line[10] and anum2

in line[11]:

```

' , ' + c + ' , ' + d + ' , ' + e + ' , ' + f + ' , ' + g + ' , ' + h + '\n')	f4.write(a + ' , ' + b +
' , ' + b + ' , ' + c + ' , ' + i + ' , ' + j + ' , ' + k + ' , ' + g + ' , ' + h + '\n')	round_ele1.write(a +
anum22 in line[11]:	if anum21 in line[10] and
' , ' + c + ' , ' + d + ' , ' + e + ' , ' + f + ' , ' + g + ' , ' + h + '\n')	f5.write(a + ' , ' + b +
' , ' + b + ' , ' + c + ' , ' + i + ' , ' + j + ' , ' + k + ' , ' + g + ' , ' + h + '\n')	round_ele2.write(a +
anum32 in line[11]:	if anum31 in line[10] and
' , ' + c + ' , ' + d + ' , ' + e + ' , ' + f + ' , ' + g + ' , ' + h + '\n')	f6.write(a + ' , ' + b +
' , ' + b + ' , ' + c + ' , ' + i + ' , ' + j + ' , ' + k + ' , ' + g + ' , ' + h + '\n')	round_ele3.write(a +
	if ele_num == '4':
in line[11]:	if anum1 in line[10] and anum2
' , ' + c + ' , ' + d + ' , ' + e + ' , ' + f + ' , ' + g + ' , ' + h + '\n')	f4.write(a + ' , ' + b +
' , ' + b + ' , ' + c + ' , ' + i + ' , ' + j + ' , ' + k + ' , ' + g + ' , ' + h + '\n')	round_ele1.write(a +
anum22 in line[11]:	if anum21 in line[10] and
' , ' + c + ' , ' + d + ' , ' + e + ' , ' + f + ' , ' + g + ' , ' + h + '\n')	f5.write(a + ' , ' + b +

```

round_ele2.write(a +
', ' + b + ', ' + c + ', ' + i + ', ' + j + ', ' + k + ', ' + g + ', ' + h + '\n')

if anum31 in line[10] and
anum32 in line[11]:

    f6.write(a + ', ' + b +
', ' + c + ', ' + d + ', ' + e + ', ' + f + ', ' + g + ', ' + h + '\n')

    round_ele3.write(a +
', ' + b + ', ' + c + ', ' + i + ', ' + j + ', ' + k + ', ' + g + ', ' + h + '\n')

    if anum41 in line[10] and
    anum42 in line[11]:

        f7.write(a + ', ' + b +
', ' + c + ', ' + d + ', ' + e + ', ' + f + ', ' + g + ', ' + h + '\n')

        round_ele4.write(a +
', ' + b + ', ' + c + ', ' + i + ', ' + j + ', ' + k + ', ' + g + ', ' + h + '\n')

        gg2 = gg

for line in Rangelist: #This does the same as above but does it for implantation

    if len(line) > 20 and '0' in line[0]:

        Xa = float(''.join(line[9:16]))

        Ya = float(''.join(line[21:28]))

        Za = float(''.join(line[33:40]))

        Zpm = line[33]

        Ypm = line[21]
```



```
Xpm = line[9]

Xf = float(''.join(line[17:20]))

Yf = float(''.join(line[29:32]))

Zf = float(''.join(line[41:44]))

Xfn1 = float(Xa*10**Xf)

Yfn1 = float(Ya*10**Yf)

Zfn1 = float(Za*10**Zf)

if Zpm == '-':

    Zfn1 = float(Zfn1*-1)

if Ypm == '-':

    Yfn1 = float(Yfn1*-1)

if Xpm == '-':

    Xfn2 = float(Xfn2*-1)

gg = int(''.join(line[0:7]))

Zfn2 = float(Zfn1 + z_mod)

Yfn2 = float(Yfn1 + y_mod)

Y_round = round(Yfn2, 0)

Z_round = round(Zfn2, 0)

Zfn1sqr = float(Zfn2*Zfn2)

Yfn1sqr = float(Yfn2*Yfn2)

#####
#####
```

```

Yfn_neg = float(Yfn2 * -1) #Creates a Y and Z negative

Zfn2_neg = float(Zfn2 * -1) #Creates a Y and Z negative

if Zfn2 < rad and Zfn2 > rad_neg and Yfn2 < rad and Yfn2 >
rad_neg: #Checks Z value is less than rad, avoids math domain errors

    r1sqr = float(radsqr - Zfn1sqr) #Created to work out x
shift

    r1sqr2 = float(radsqr - Yfn1sqr) #for x shift
#####

    xy_mod_c = float(math.sqrt(r1sqr)) #Created to work out
x shift

    xy_mod_c2 =
float(math.sqrt(r1sqr2))#####
#####

    xy_mod = float(rad - xy_mod_c) #Created to work out x
shift

    xy_mod2 = float(rad -
xy_mod_c2)#####
#####

    if xy_mod > xy_mod2:

        Xfn2 = float(Xfn1 + xy_mod) #shifts X

    else:

        Xfn2 = float(Xfn1 + xy_mod2)

    # Yfn_neg = float(Yfn2 * -1)

    # Zfn2_neg = float(Zfn2 * -1)

    # if Zfn2 < rad and Zfn2 > rad_neg:

```

```
# r1sqr = float(radsqr - Zfn1sqr)

# xy_mod_c = float(math.sqrt(r1sqr))

# xy_mod = float(rad - xy_mod_c)

# #xy_mod = float(xy_mod + y_mod)

# Xfn2 = float(Xfn1 + xy_mod)

Xfn3 = float(Xfn2 - rad)

Xfn1sqr = float(Xfn3 * Xfn3)

X_round = round(Xfn2, 0)

r1 = float(math.sqrt(r1sqr))

calc_dia = float(r1*2)

X_min_dist = float(calc_dia - Xfn1)

X_min_dist = float(X_min_dist / 2)

if Yfn2 > 0:

    Y_min_dist = float(r1 - Yfn2)

else:

    Y_min_dist = float(r1 + Yfn_neg)

if Zfn2 > 0:

    Z_min_dist = float(r1 - Zfn2)

else:

    Z_min_dist = float(r1 + Zfn2_neg)

X_min_round = round(X_min_dist)
```

```
Y_min_round = round(Y_min_dist)

Z_min_round = round(Z_min_dist)

rad_checksqr = float(Xfn1sqr+Yfn1sqr+Zfn1sqr)

rad_check = float(math.sqrt(rad_checksqr))

if rad_check < rad:

    a = str(gg)

    d = str(Xfn2)

    e = str(Yfn2)

    f = str(Zfn2)

    i = str(X_round)

    j = str(Y_round)

    k = str(Z_round)

    ff2.write(a + ' , ' + d + ' , ' + e + ' , ' + f + '\n')

    round_range.write(a + ' , ' + i + ' , ' + j + ' , ' + k +
'\n')

#closes files and reset some variables

gg2 = 0

ff2.close()

f1.close()

f8.close()

f9.close()
```

```
min_dist.close()
```

```
round_all.close()
```

```
round_vac.close()
```

```
round_rep.close()
```

```
round_range.close()
```

```
round_min.close()
```

```
backscatf.close()
```

```
radfe = float(rad/50) #This is how much the values will shift. 1/6 of the radius
```

```
if y_mod >= rad or y_mod <= rad_neg: #Checks y-mod if it's in sphere range z mod shift is calculated.  
If not it becomes rad to avoid math domain error
```

```
    calczrad = rad
```

```
    calczradneg = rad_neg
```

```
else:
```

```
    calczradsqr = float(radsqr-ymodsqr)
```

```
    calczrad = float(math.sqrt(calczradsqr))
```

```
if z_mod < calczrad and z_mod >= 0: #Checks whether to make z-mod positive or negative
```

```
    z_mod = float(z_mod + radfe)
```

```
if z_mod < 0:
```

```
z_mod = (z_mod - radfe)

if z_mod >= calczrad:

    z_mod = (0 - radfe)


calczradneg = float(calczrad * -1) #Creates negative for z check


if z_mod <= calczradneg: #When Z leaves check value it resets and a y shift occurs.

    z_mod = 0

    if y_mod < rad and y_mod >= 0:

        y_mod = float(y_mod + radfe)

    if y_mod < 0:

        y_mod = (y_mod - radfe)

    if y_mod >= rad:

        y_mod = (0 - radfe)


ymodsqr = float(y_mod*y_mod)

zmodsqr = float(z_mod*z_mod)

yzmodsqr = float(ymodsqr+zmodsqr)

yzmod = float(math.sqrt(yzmodsqr))
```

```
BS = 0
```

```
with open("Backscat1.txt", "r") as BSfile:
```

```
    for line in BSfile:
```

```
        BS += 1
```

```
print "\nAmount Backscatter is"
```

```
print (BS)
```

```
print "\nIt is safe to assume that half of these ions Backscattered have the potential to have created damage\n"
```

```
print "The total number of ions is 5592"
```

```
if ele_num == '2':
```

```
    f4.close()
```

```
    f5.close()
```

```
    round_ele1.close()
```

```
    round_ele2.close()
```

```
if ele_num == '3':
```

```
    f4.close()
```

```
    f5.close()
```

```
    f6.close()
```

```
    round_ele1.close()
```

```
round_ele2.close()
```

```
round_ele3.close()
```

```
if ele_num == '4':
```

```
    f4.close()
```

```
    f5.close()
```

```
    f6.close()
```

```
    f7.close()
```

```
    round_ele1.close()
```

```
    round_ele2.close()
```

```
    round_ele3.close()
```

```
    round_ele4.close()
```

```
#Plotting data as graphs
```

```
xro = []
```

```
yro = []
```

```
zro = []
```

```
xin = []
```

```
yin = []
```

```
zin = []
```



```
xr = []

yr = []

zr = []

xv = []

yv = []

zv = []

mind = []

with open('Minimum_Distance_to_Surface.txt' , 'r') as csvfile:

    plots = csv.reader(csvfile, delimiter=',')

    for row in plots:

        mind.append(int(float(row[2])))

bins = [0,
(rad/100*5),(rad/100*10),(rad/100*15),(rad/100*20),(rad/100*25),(rad/100*30),(rad/100*35),(rad/100*40),(
rad/100*45), (rad/100*50), (rad/100*55), (rad/100*60), (rad/100*65), (rad/100*70), (rad/100*75),
(rad/100*80), (rad/100*85), (rad/100*90), (rad/100*95), rad]

plt.hist(mind, bins, histtype='bar', rwidth= 0.8)

plt.xlabel('Distance')

plt.ylabel('Damage')
```

```
plt.title('Minimum Distance to Surface Histogram')

plt.legend()

plt.show()

with open('All_Colisions_in_sphere_rounded_to_nearest_10.txt' , 'r') as csvfile:

    plots = csv.reader(csvfile, delimiter=',')

    for row in plots:

        xro.append(int(float(row[3])))

        yro.append(int(float(row[4])))

        zro.append(int(float(row[5])))

fig = plt.figure()

# ax = fig.add_subplot(111, projection='3d')

# ax.plot_surface(xro, yro, zro)

# plt.xlabel('x')

# plt.ylabel('y')

# plt.zlabel('z')

# plt.title('3D Surface plot')

# plt.show()

plt.hist2d(xro, yro, (100, 100), cmap=plt.cm.jet)
```

```
plt.colorbar()

plt.xlabel('x')

plt.ylabel('y')

plt.title('XY All collision Density')

#plt.legend()

plt.show()

plt.hist2d(xro, zro, (100, 100), cmap=plt.cm.jet)

plt.colorbar()

plt.xlabel('x')

plt.ylabel('z')

plt.title('XZ All collision Density')

#plt.legend()

plt.show()

plt.hist2d(zro, yro, (100, 100), cmap=plt.cm.jet)

plt.colorbar()

plt.xlabel('z')
```

```
plt.ylabel('y')

plt.title('zy All collision Density')

#plt.legend()

plt.show()

with open('Sphere_RANGE_3D_rounded.txt' , 'r') as csvfile:

    plots = csv.reader(csvfile, delimiter=',')

    for row in plots:

        xin.append(int(float(row[1])))

        yin.append(int(float(row[2])))

        zin.append(int(float(row[3])))

plt.hist2d(xin, yin, (100, 100), cmap=plt.cm.jet)

plt.colorbar()

plt.xlabel('x')

plt.ylabel('y')

plt.title('XY Implantation')

#plt.legend()

plt.show()
```

```
plt.hist2d(xin, zin, (100, 100), cmap=plt.cm.jet)
```

```
plt.colorbar()
```

```
plt.xlabel('x')
```

```
plt.ylabel('z')
```

```
plt.title('XZ Implantation')
```

```
#plt.legend()
```

```
plt.show()
```

```
plt.hist2d(zin, yin, (100, 100), cmap=plt.cm.jet)
```

```
plt.colorbar()
```

```
plt.xlabel('z')
```

```
plt.ylabel('y')
```

```
plt.title('zy Implantation')
```

```
#plt.legend()
```

```
plt.show()
```

```
with open('All_Replacements_in_sphere_rounded.txt', 'r') as csvfile:
```

```
    plots = csv.reader(csvfile, delimiter=',')
```

```
        for row in plots:

            xr.append(int(float(row[3])))

            yr.append(int(float(row[4])))

            zr.append(int(float(row[5])))

plt.hist2d(xr, yr, (100, 100), cmap=plt.cm.jet)

plt.colorbar()

plt.xlabel('x')

plt.ylabel('y')

plt.title('XY Replacement Density')

#plt.legend()

plt.show()

plt.hist2d(xr, zr, (100, 100), cmap=plt.cm.jet)

plt.colorbar()

plt.xlabel('x')

plt.ylabel('z')

plt.title('XZ Replacement Density')
```

```
#plt.legend()

plt.show()

plt.hist2d(zr, yr, (100, 100), cmap=plt.cm.jet)

plt.colorbar()

plt.xlabel('z')

plt.ylabel('y')

plt.title('zy Replacement Density')

#plt.legend()

plt.show()

with open('All_Vacancies_in_Sphere_rounded.txt' , 'r') as csvfile:

    plots = csv.reader(csvfile, delimiter=',')

    for row in plots:

        xv.append(int(float(row[3])))

        yv.append(int(float(row[4])))

        zv.append(int(float(row[5])))

plt.hist2d(xv, yv, (100, 100), cmap=plt.cm.jet)
```

```
plt.colorbar()
```

```
plt.xlabel('x')
```

```
plt.ylabel('y')
```

```
plt.title('XY Vacancy Density')
```

```
#plt.legend()
```

```
plt.show()
```

```
plt.hist2d(xv, zv, (100, 100), cmap=plt.cm.jet)
```

```
plt.colorbar()
```

```
plt.xlabel('x')
```

```
plt.ylabel('z')
```

```
plt.title('XZ Vacancy Density')
```

```
#plt.legend()
```

```
plt.show()
```

```
plt.hist2d(zv, yv, (100, 100), cmap=plt.cm.jet)
```

```
plt.colorbar()
```

```
plt.xlabel('z')
```



```
plt.ylabel('y')
```

```
plt.title('zy Vacancy Density')
```

```
#plt.legend()
```

```
plt.show()
```

8.2 SICMod Guide

The following is a simple user guide on how to run the SICMod code and some of the results obtained.

The first step is to run the TRIM setup window and enter the values for the material and ions as normal. Detailed calculations should be selected in the damage drop down menu and the number of ions should be set to ~10 to allow for quick run time. It is also advantageous although not necessary to select no graphics in the basic plots. This will cut down the run time of the code. The width of the layer needs to be set to or greater than the diameter of the particle being analysed. It is also necessary that all the output disk files are checked. This is because SICMod reads the data from these files. Figure 101 shows an example of a correctly prepared setup window for calculating 20keV Kr transported to SiC.

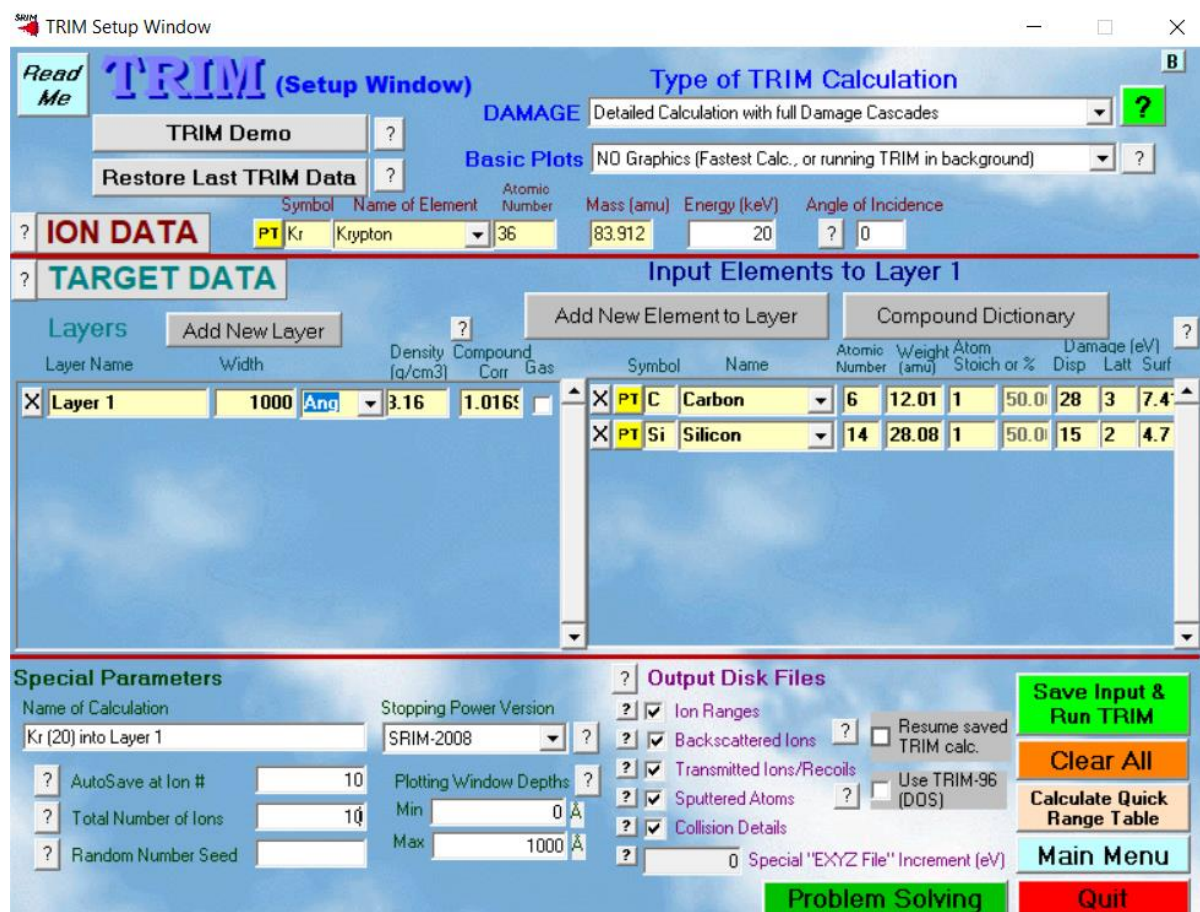


Figure 101 TRIM Setup GUI

Once the setup is complete it is necessary to run TRIM once and when closing the software ensure that the setup is saved for later use.

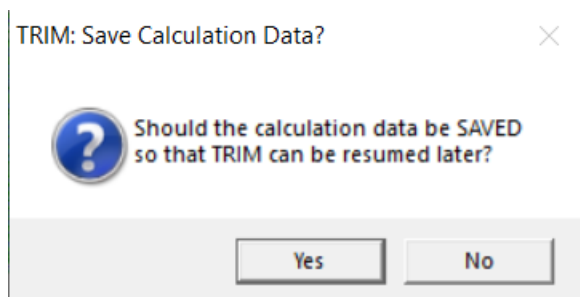


Figure 102 TRIM Confirmation

SICMod is now ready to be run. Open the executable file and you will be greeted with the GUI as seen in Figure 103. At this point select whether you are analysing a sphere or a cylinder. Also select the number of elements in the material and the radius of the particle. Once the fields have been filled click the run SRIM button.

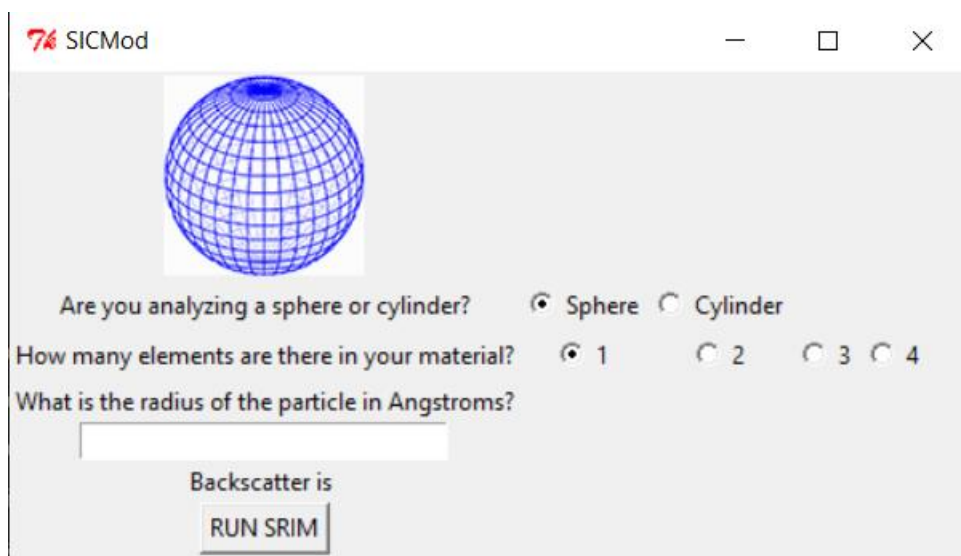


Figure 103 SICMod GUI

At this point TRIM should run and close itself continuously. Dependant upon your CPU core speed this may take a while. Once the program has finished running you will be presented with a minimum distance to surface histogram of each ion that has been implanted into the sphere.

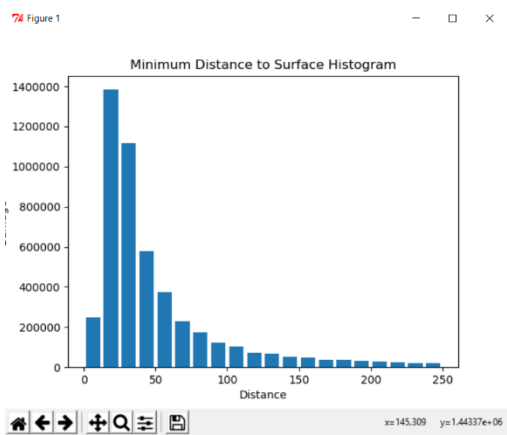


Figure 104 Minimum Distance Surface Diagram for Implanted Ions

After this closing the histogram will cause the remaining heatmaps to display. Two examples are provided below in Figure 105.

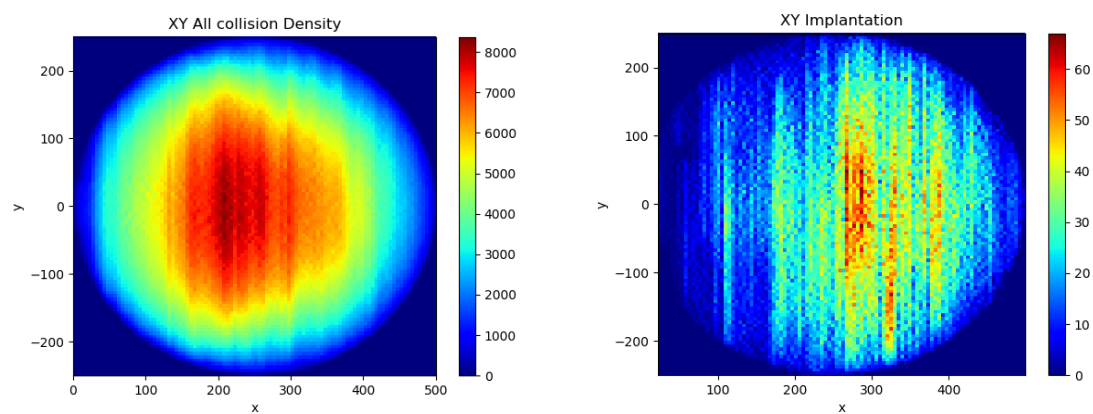


Figure 105 Examples of SICMod Heatmaps

8.3 Figures

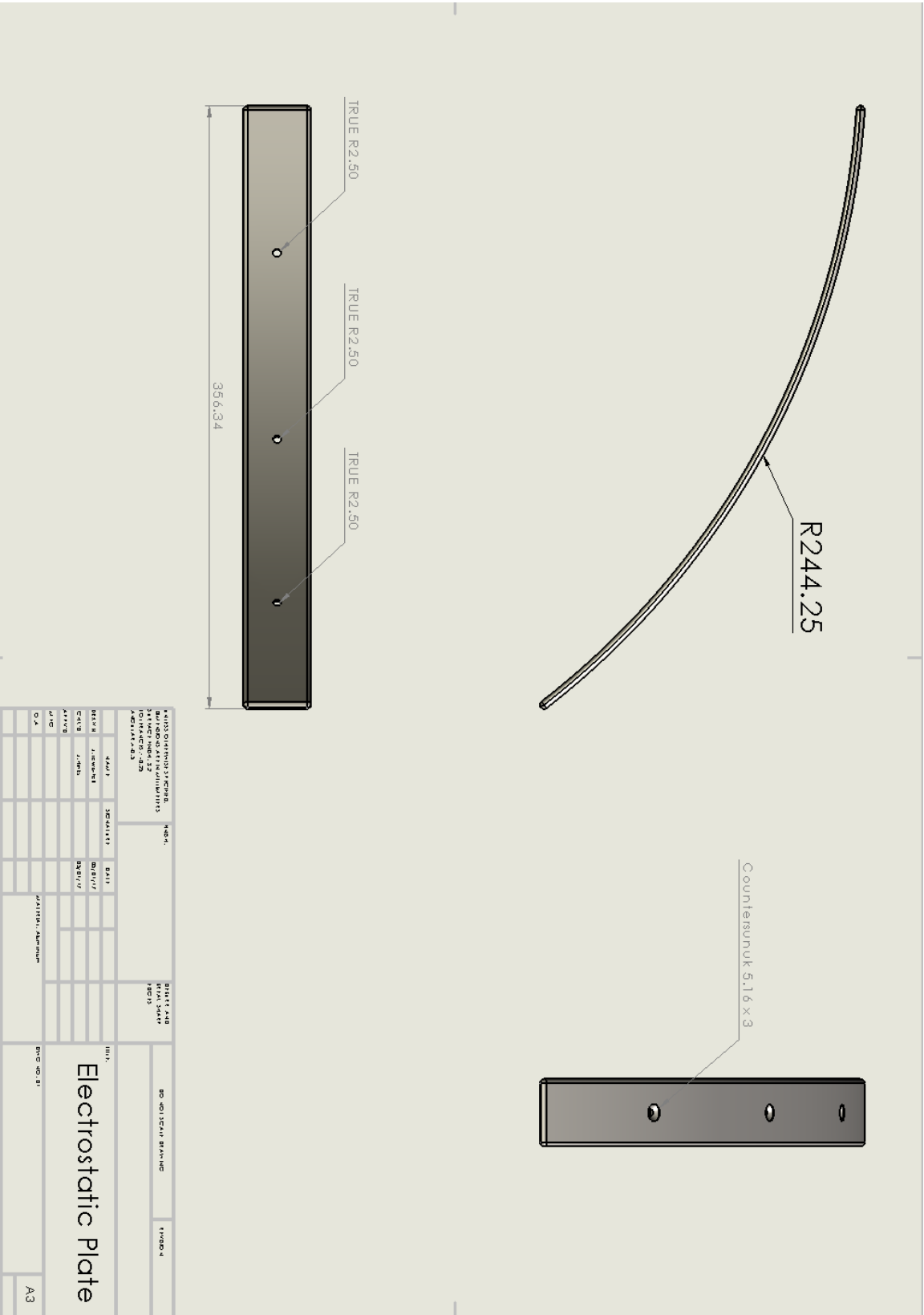


Figure 106 Electrostatic Plate

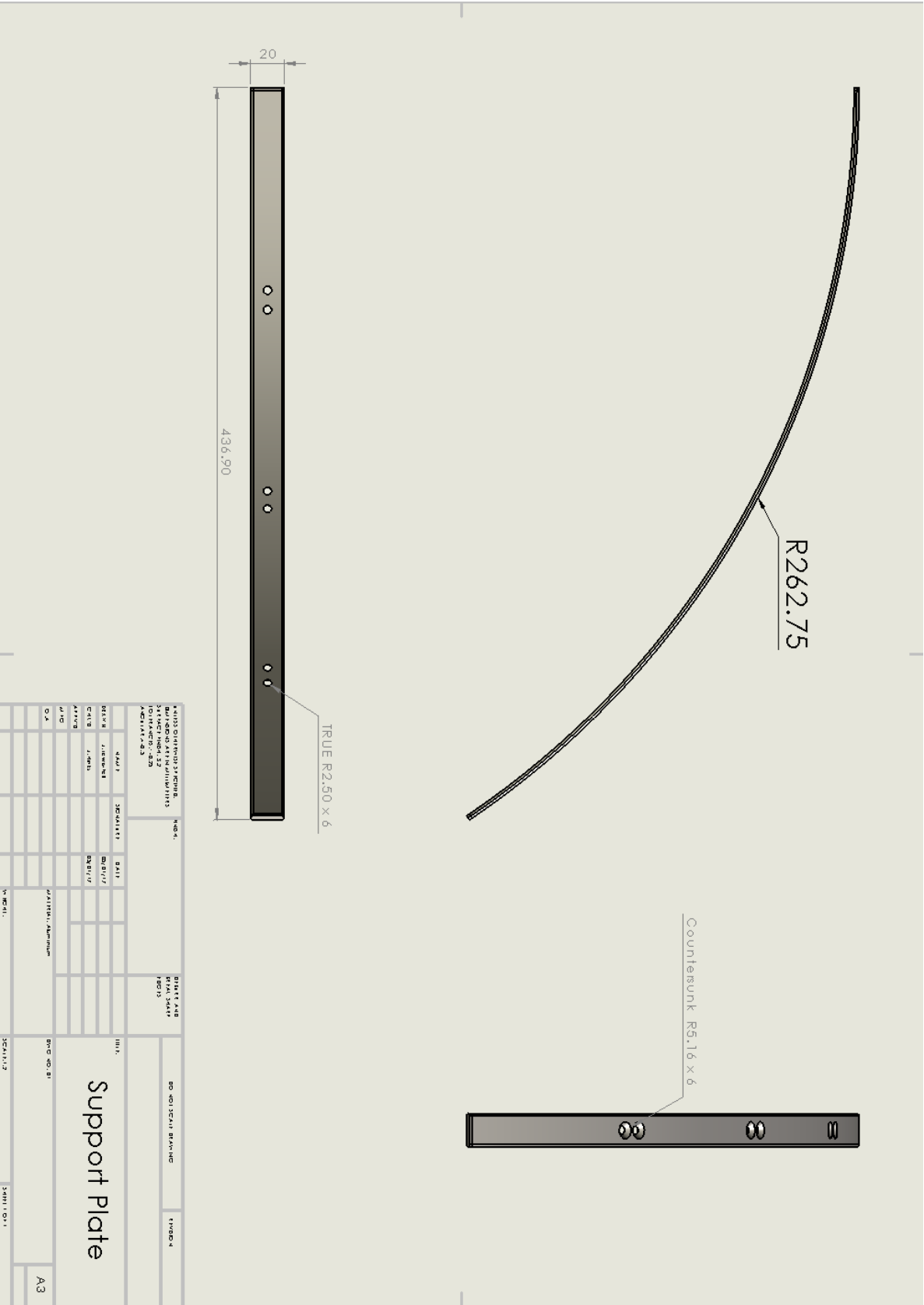


Figure 107 Support Strip

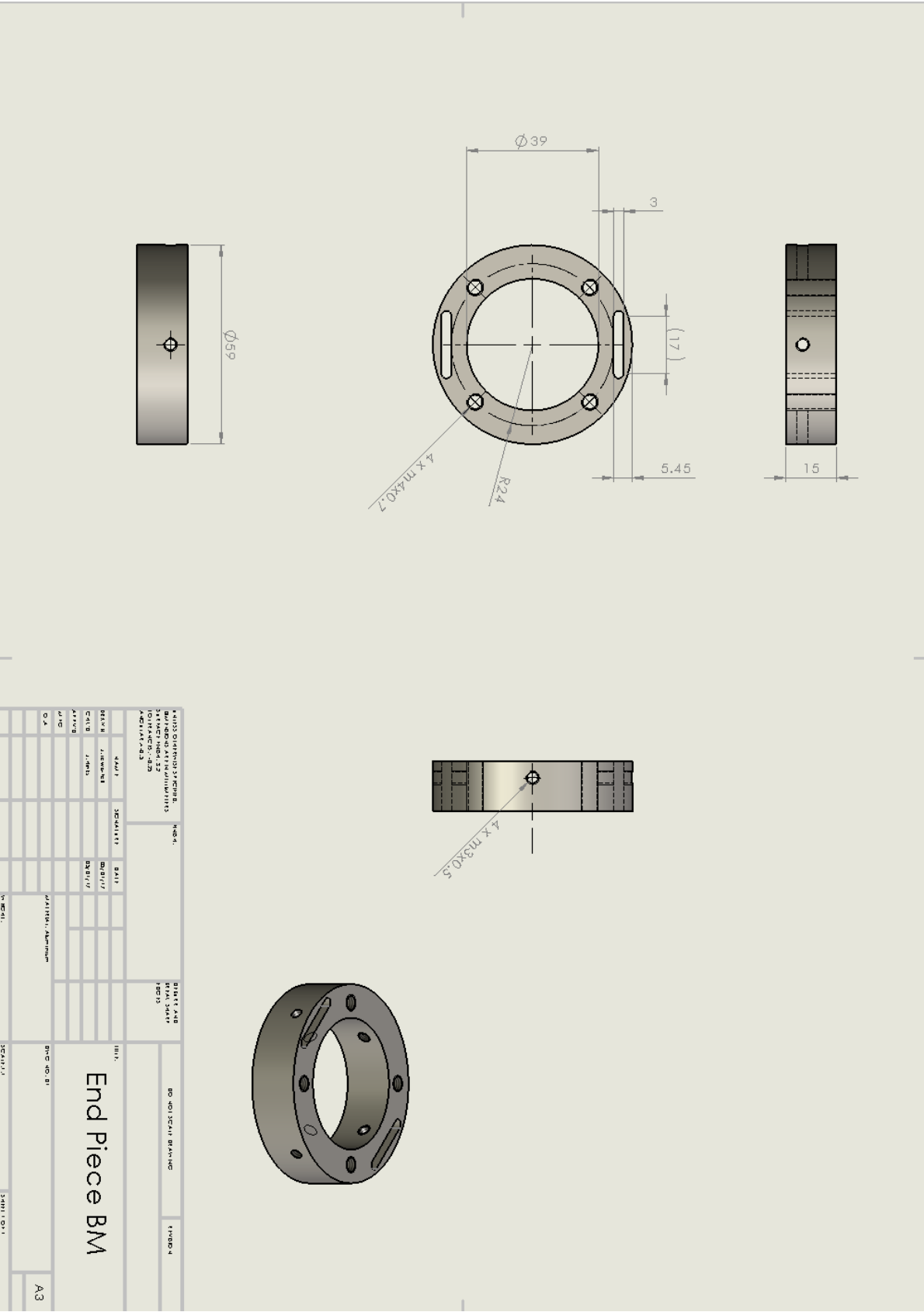


Figure 108 End Piece Electrostatic Deflector

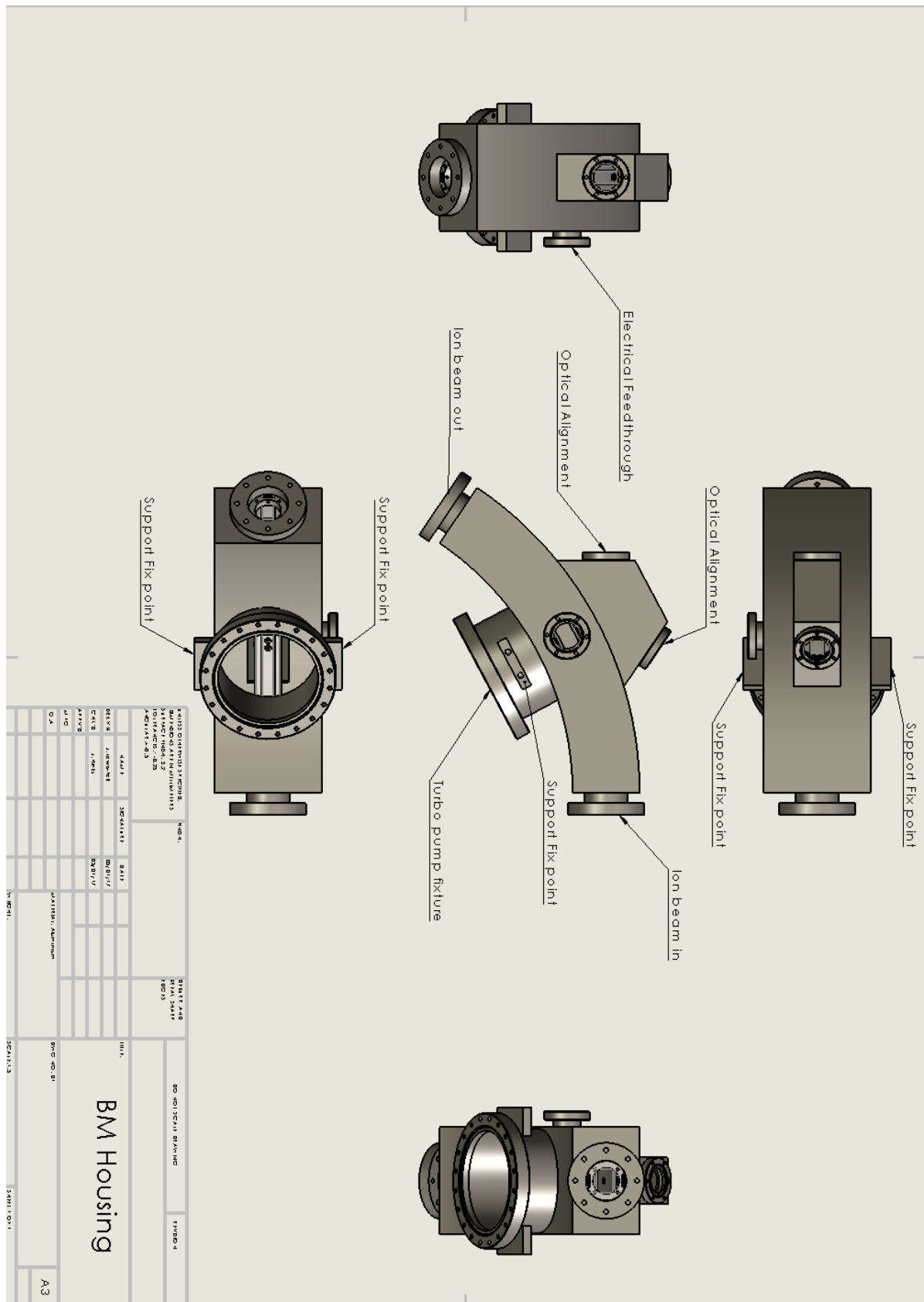


Figure 109 Electrostatic Deflector Housing

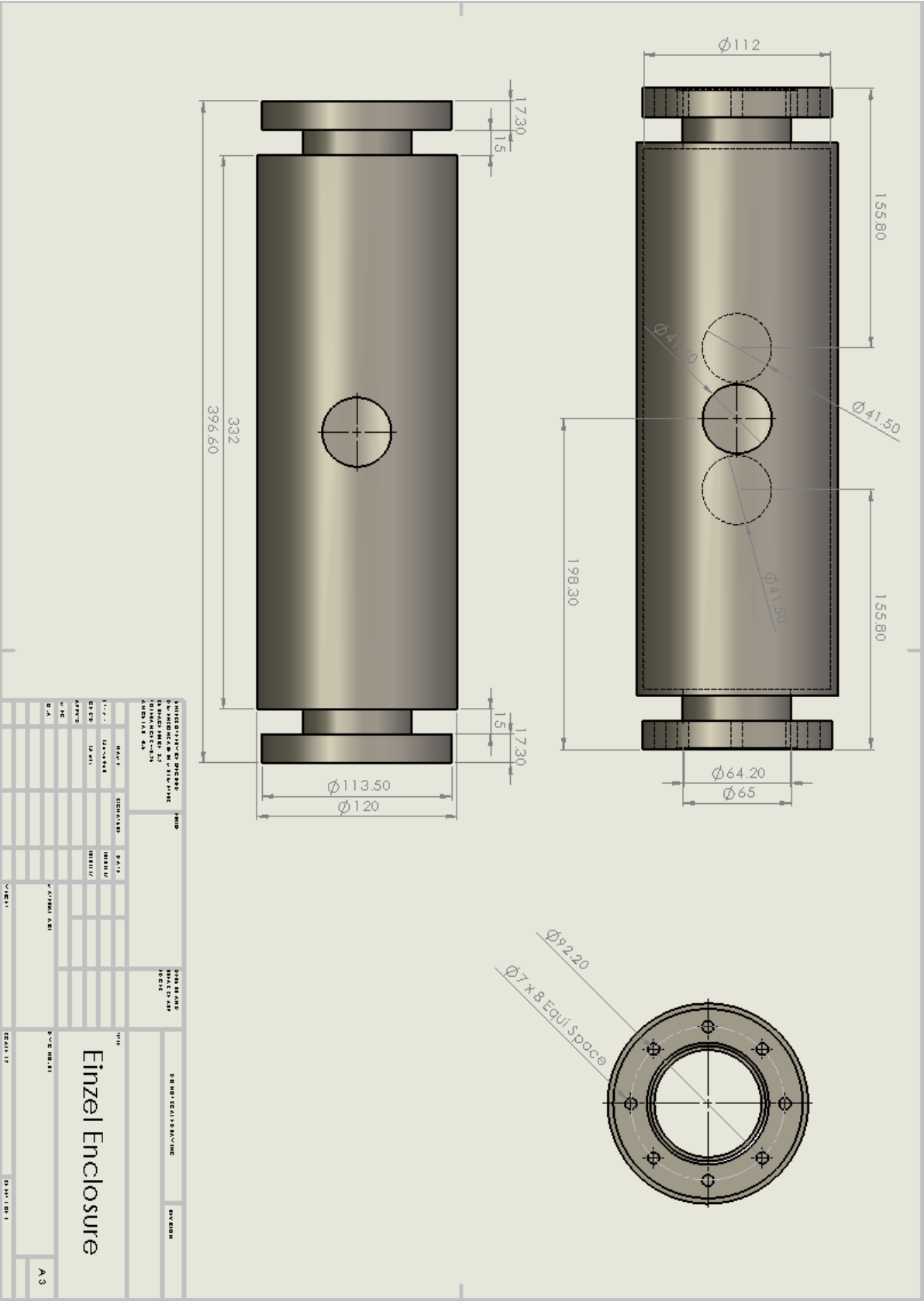


Figure 110 Einzel Enclosure

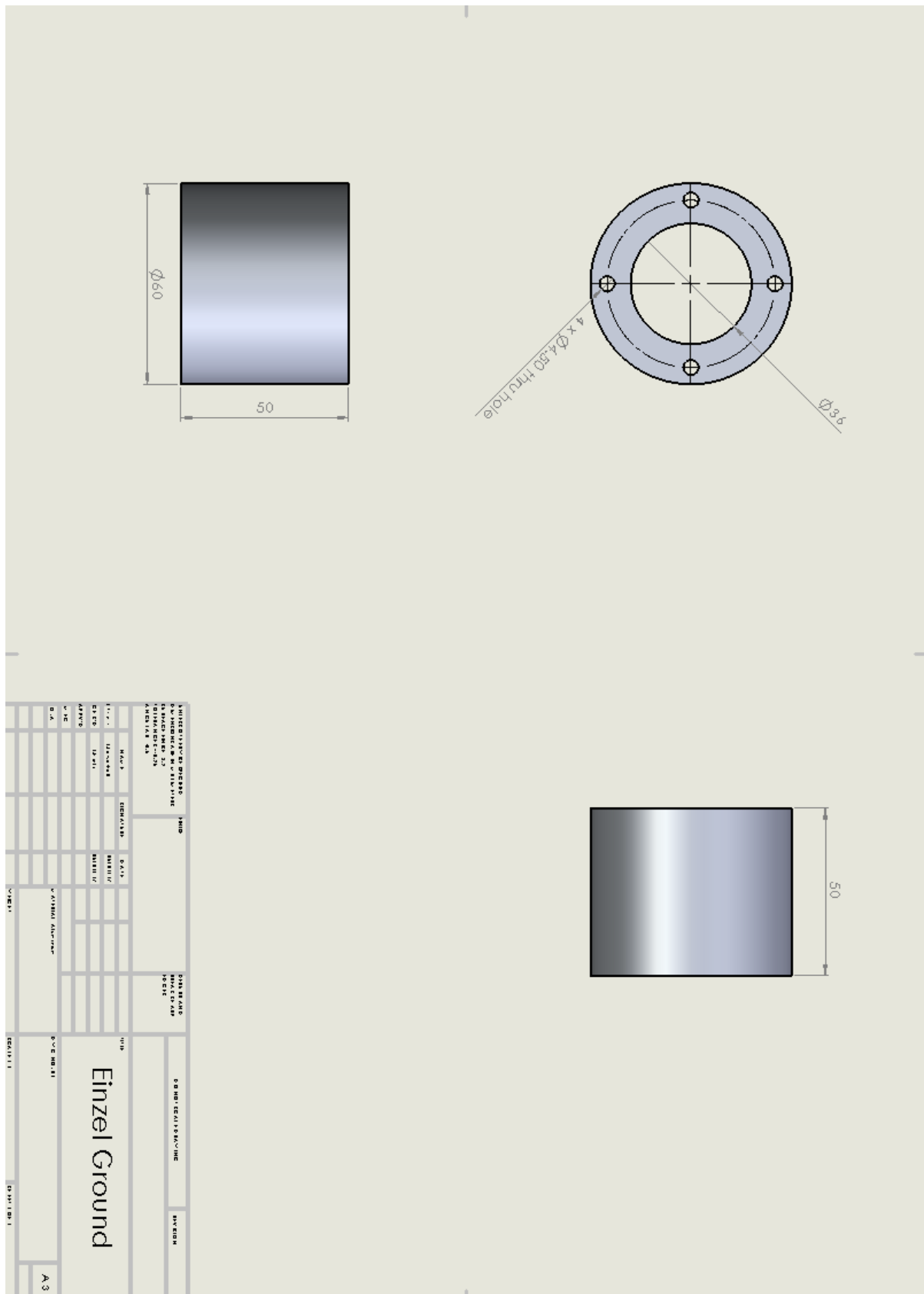


Figure 111 Einzel Ground Tube

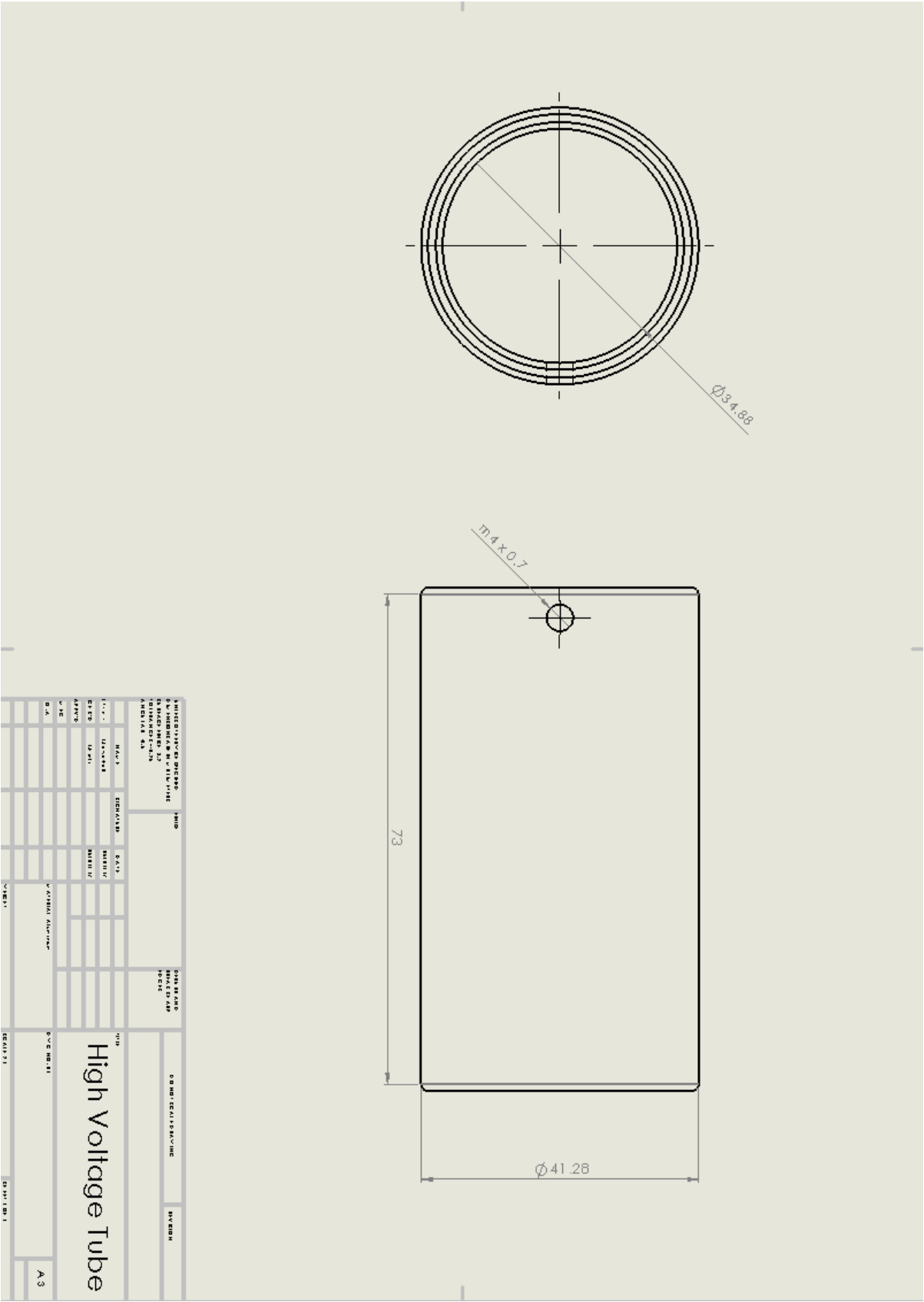


Figure 112 High Voltage Tube

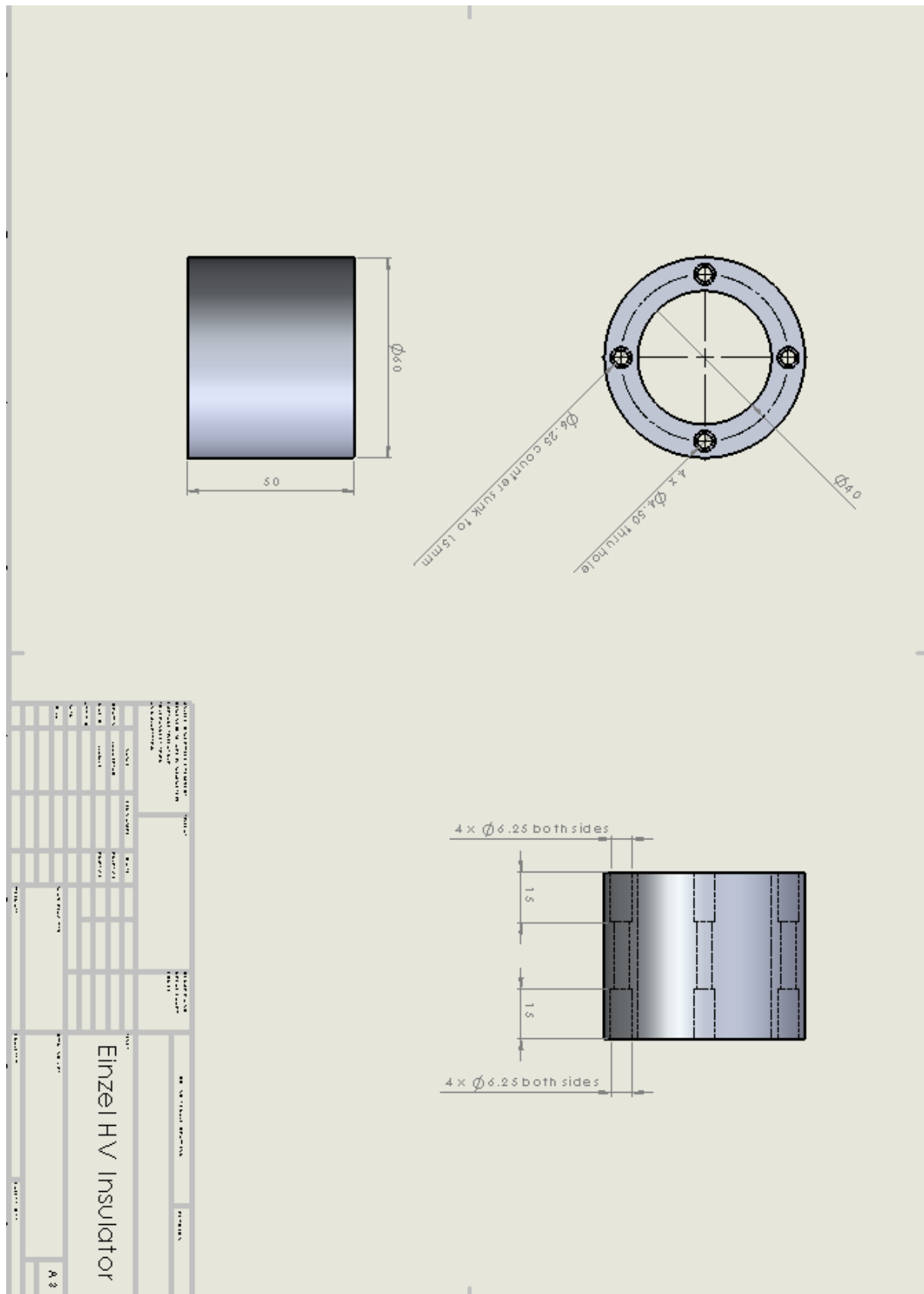


Figure 113 High Voltage Isolator

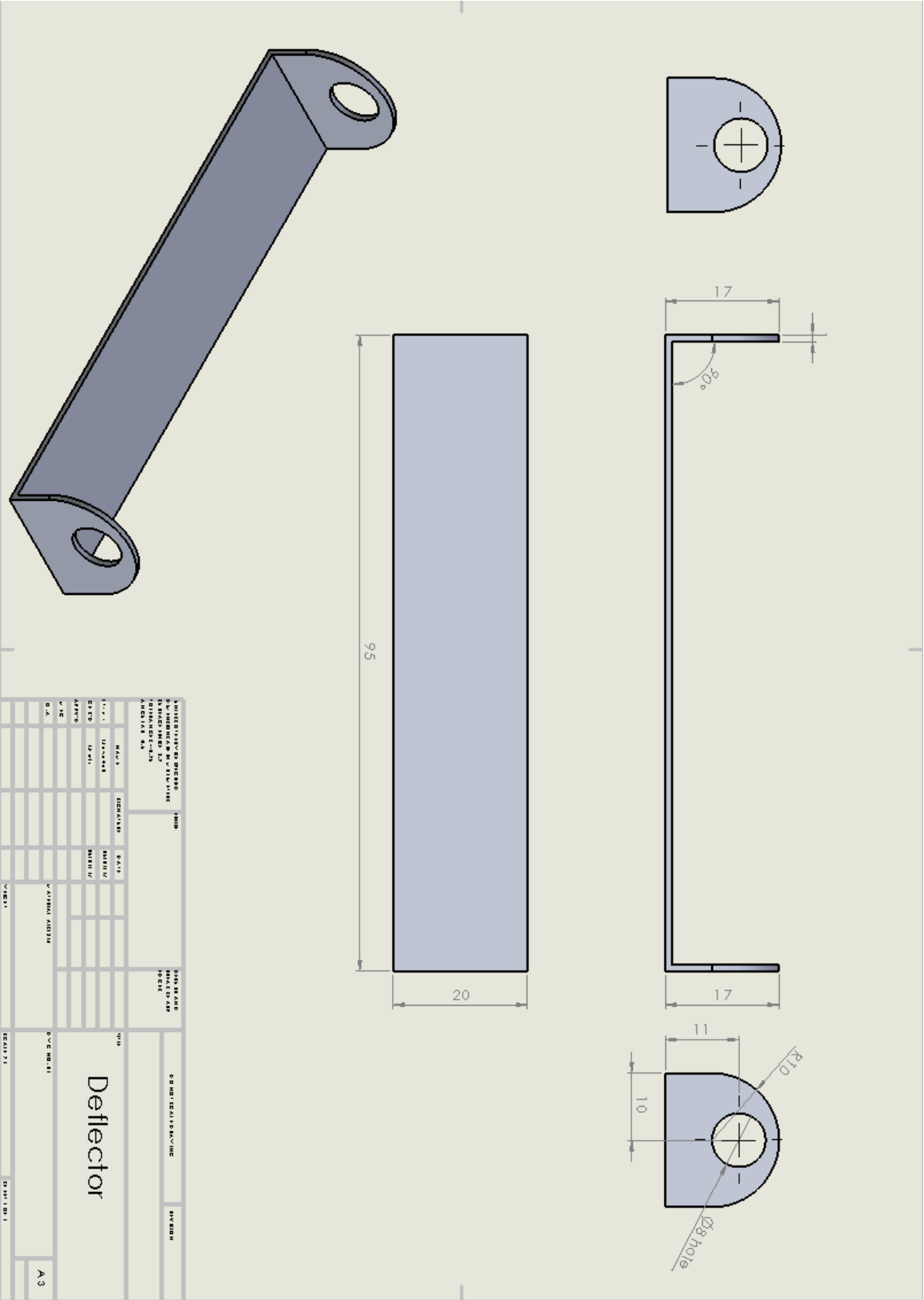


Figure 114 Deflector Plate

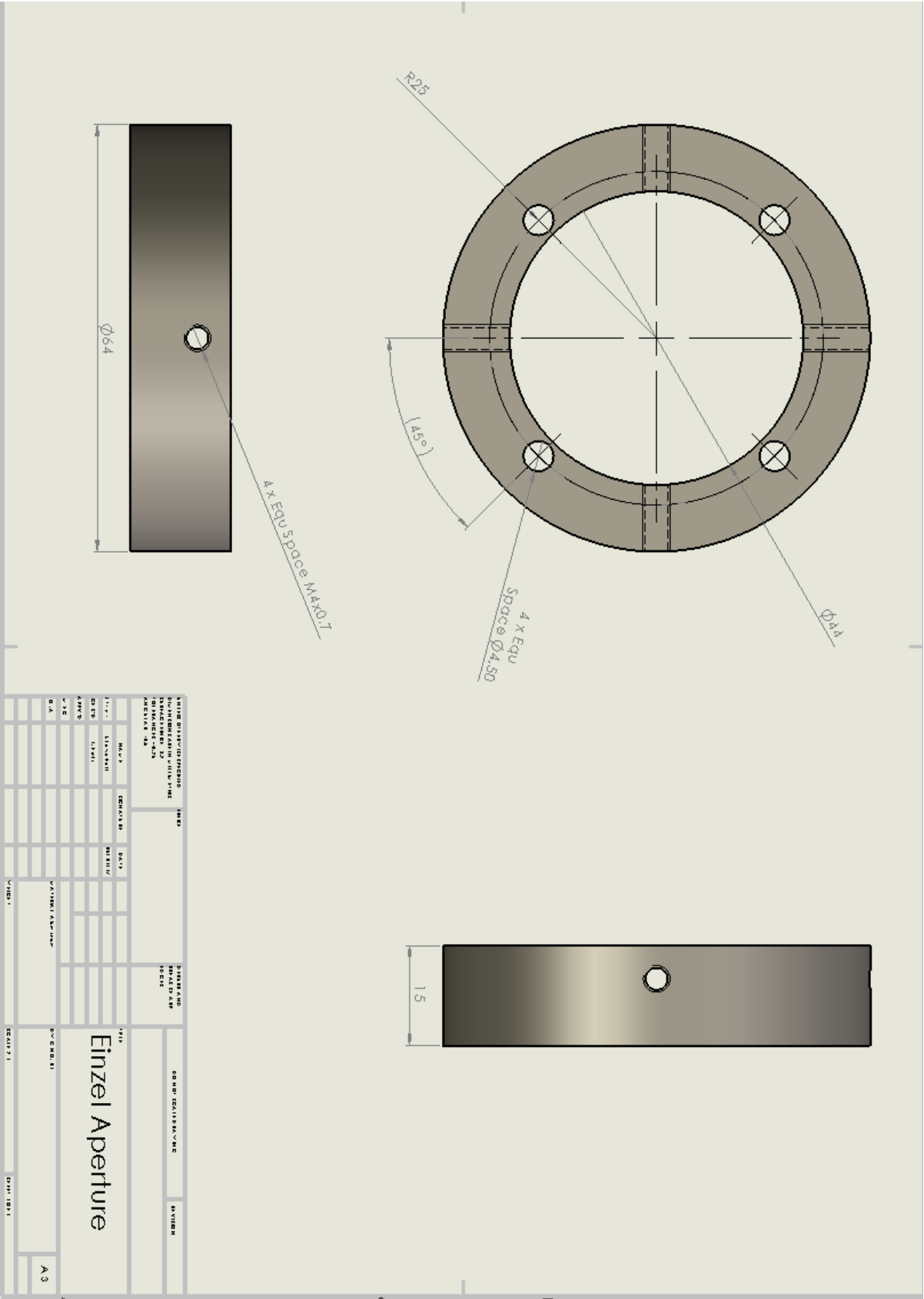


Figure 115 End Piece

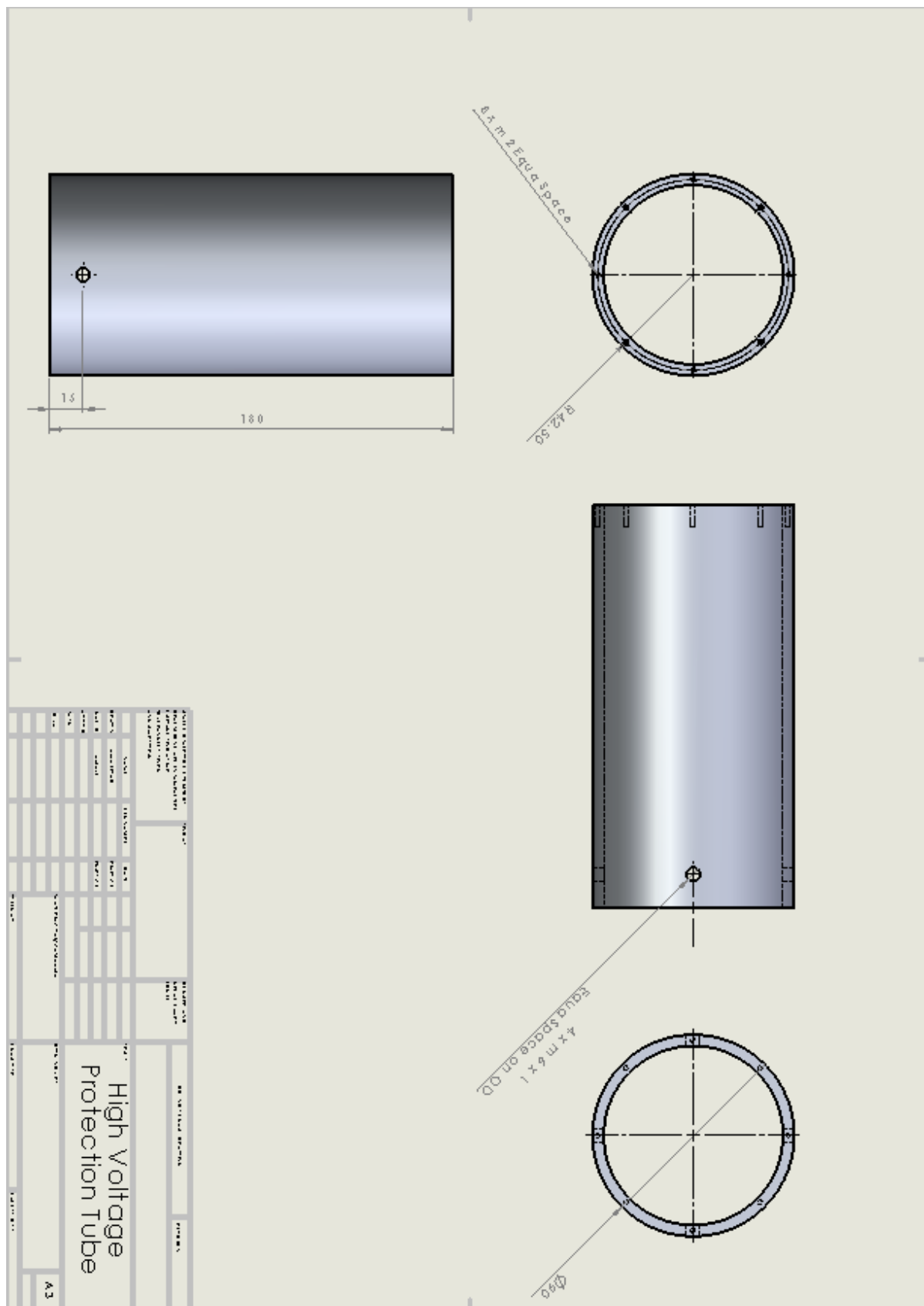


Figure 117 High Voltage Tube

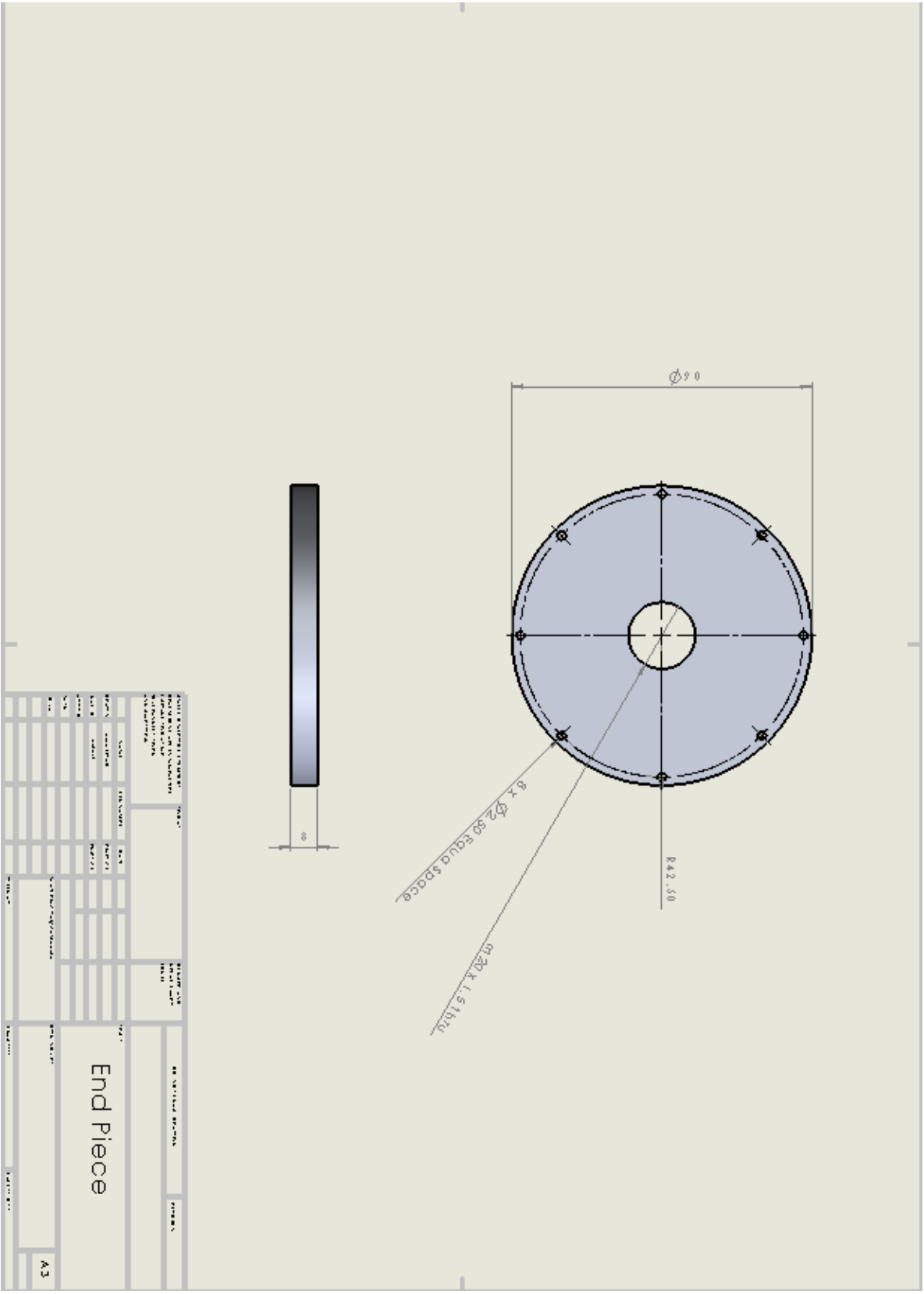


Figure 118 End Piece

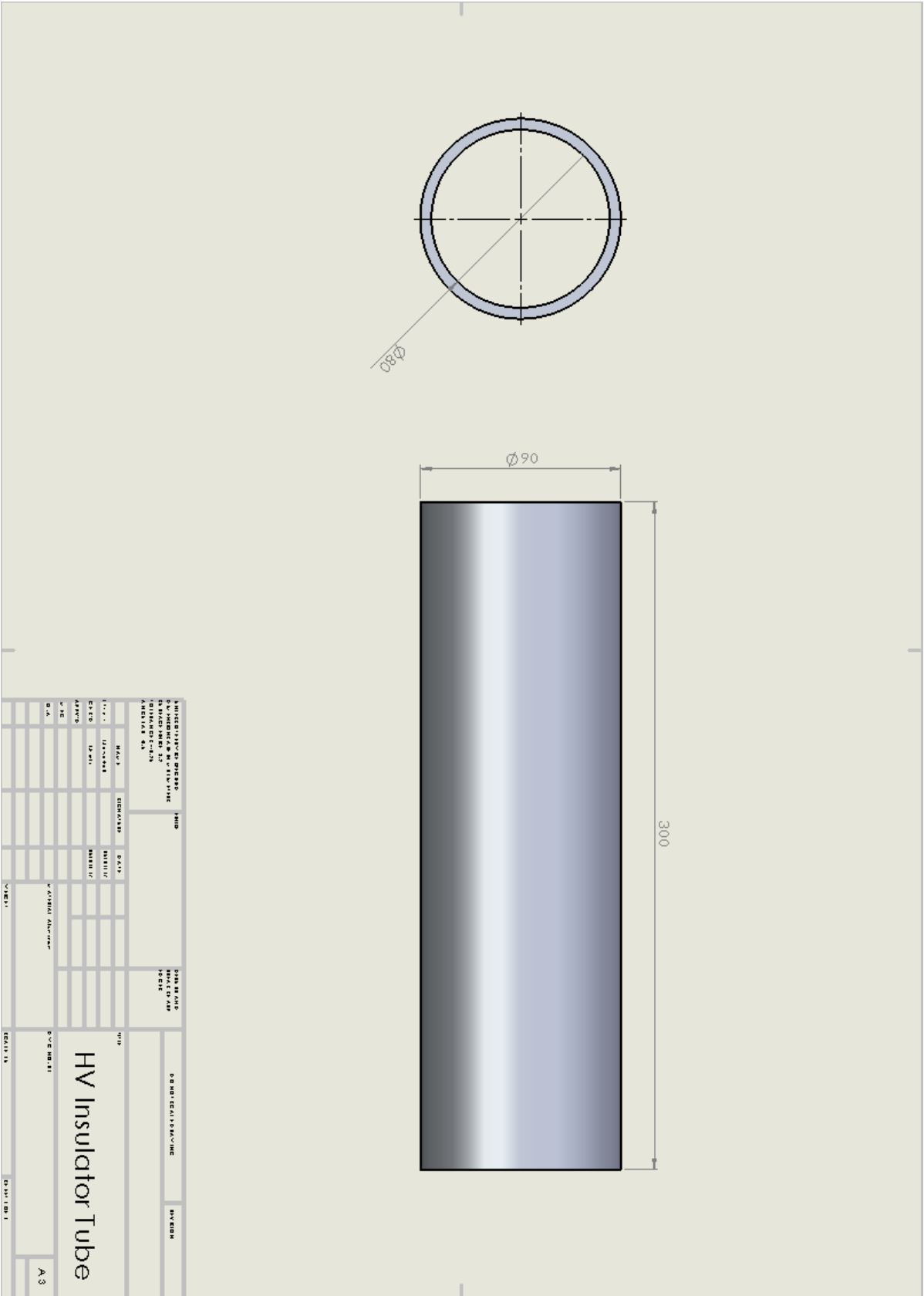


Figure 119 High Voltage Tube V2

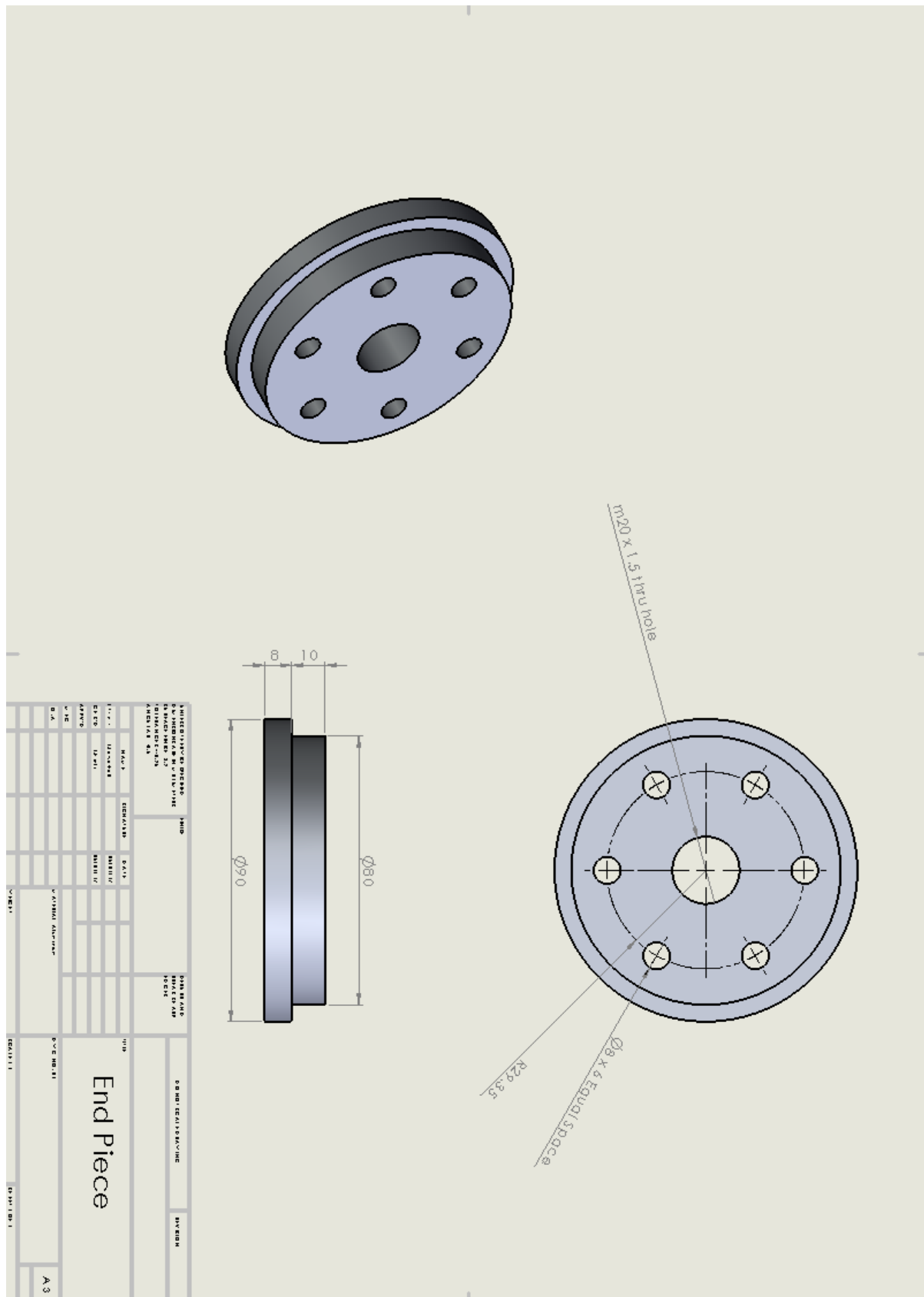


Figure 120 End Piece V2

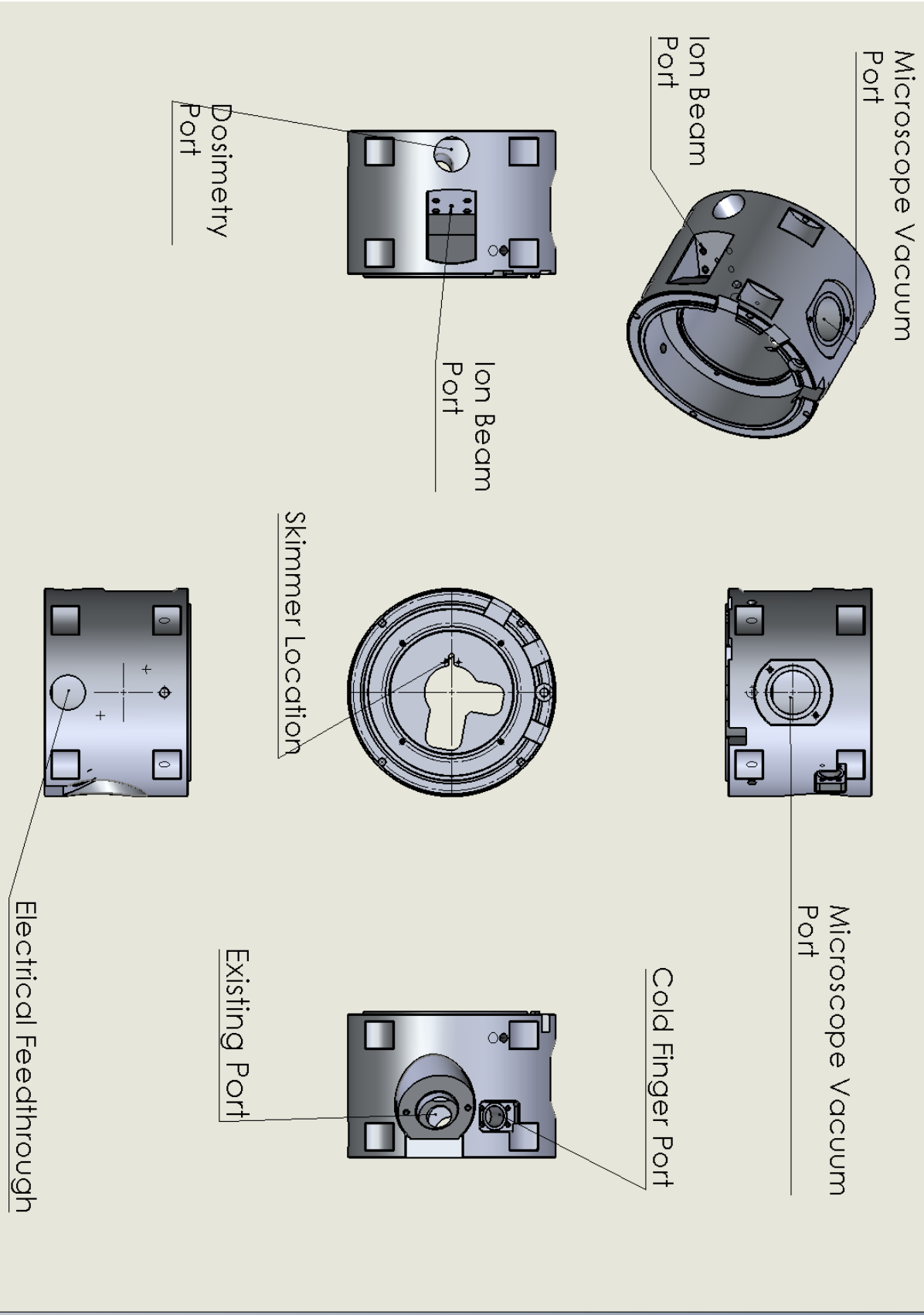


Figure 121 CML key locations

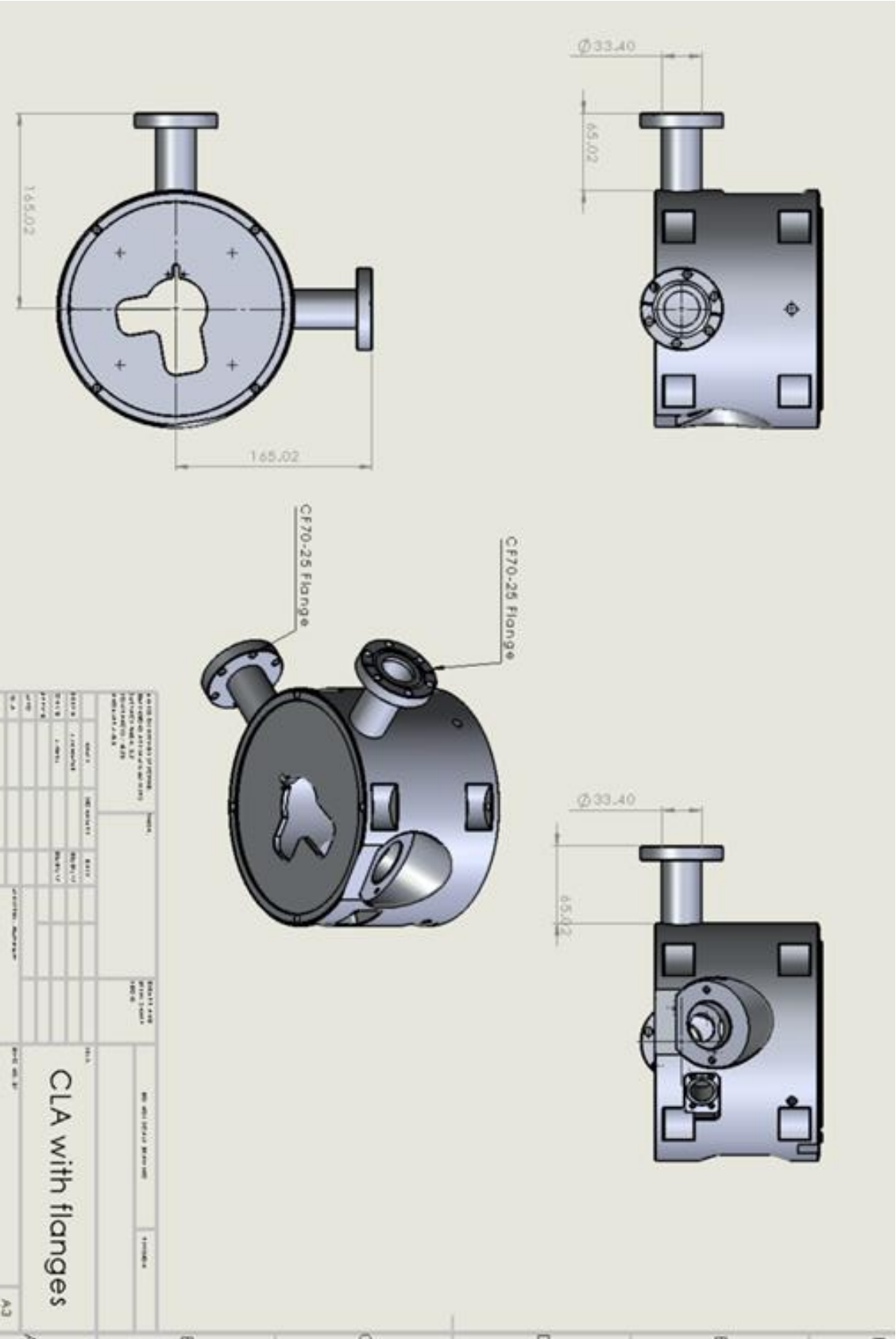


Figure 122 CML with flanges

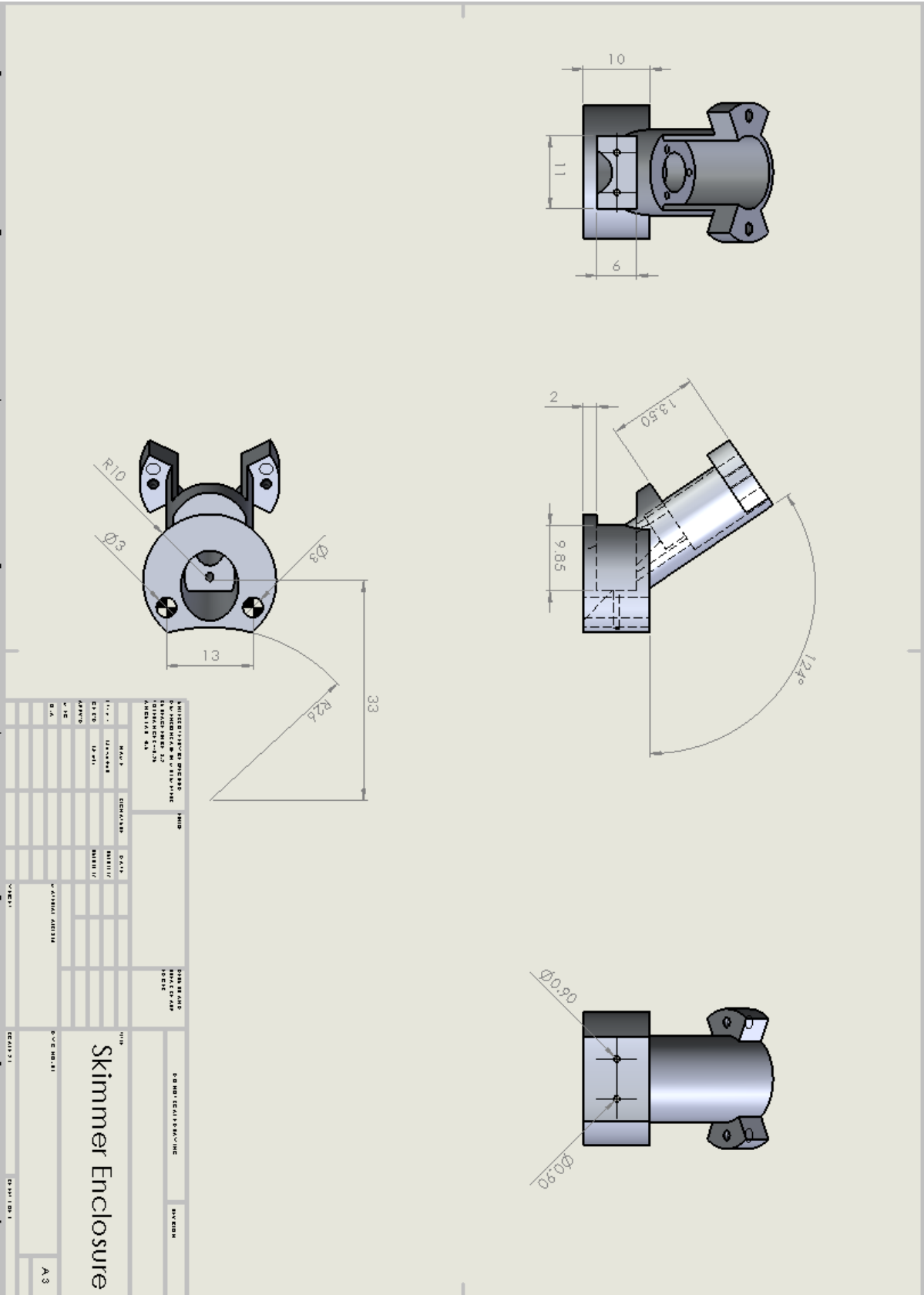


Figure 123 Skimmer Enclosure 1

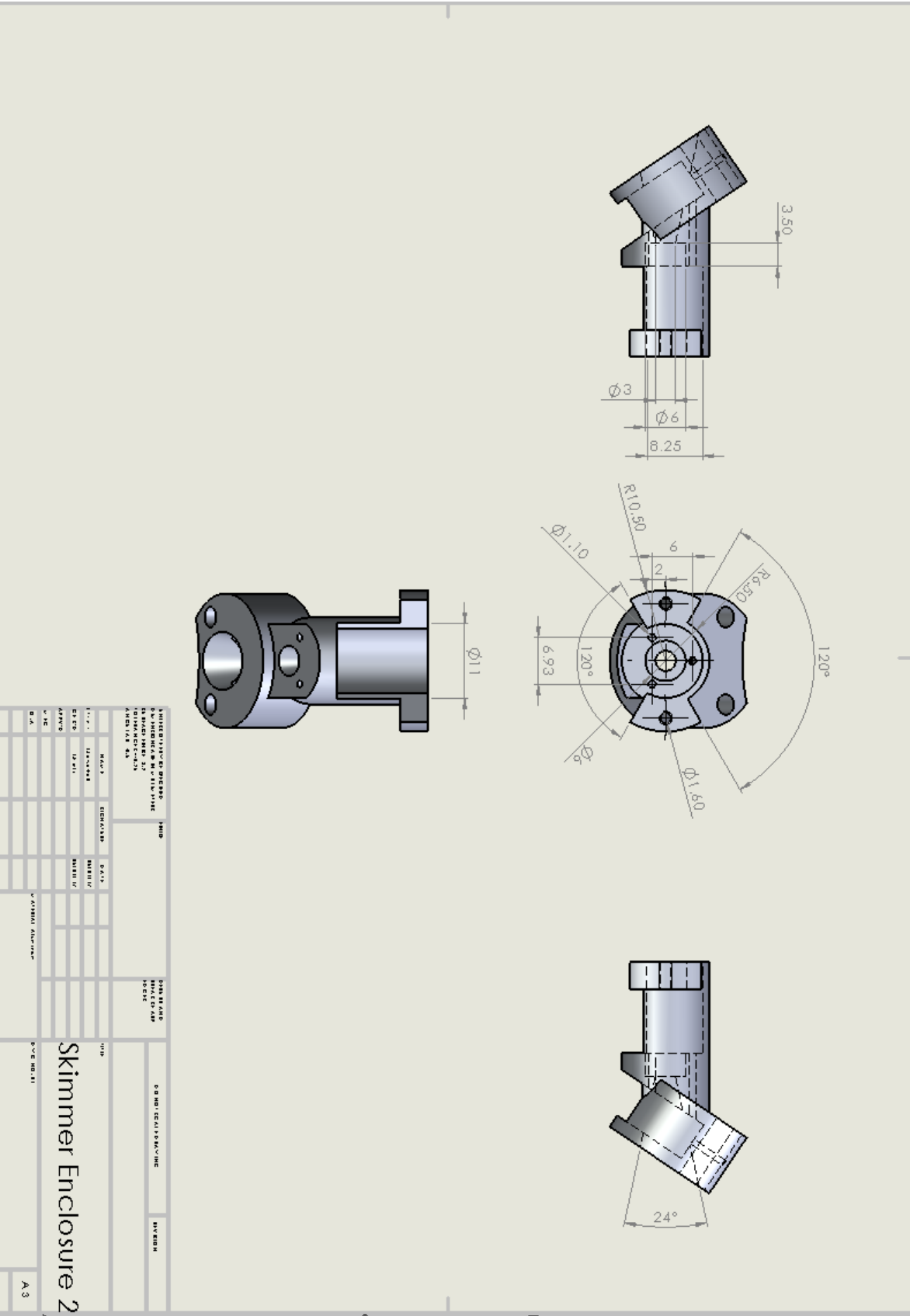


Figure 124 Skimmer Enclosure 2

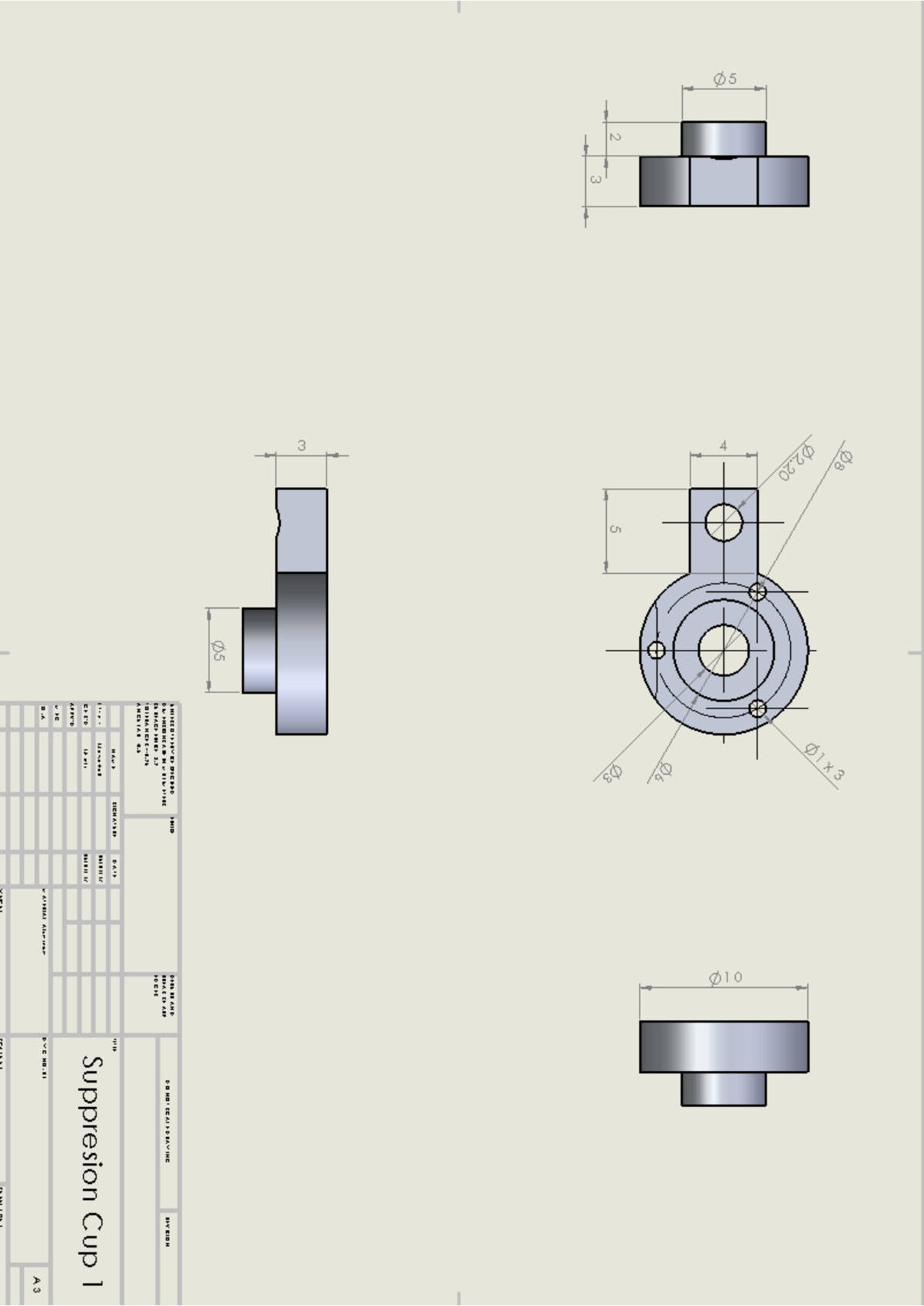


Figure 125 1st Suppression Cup

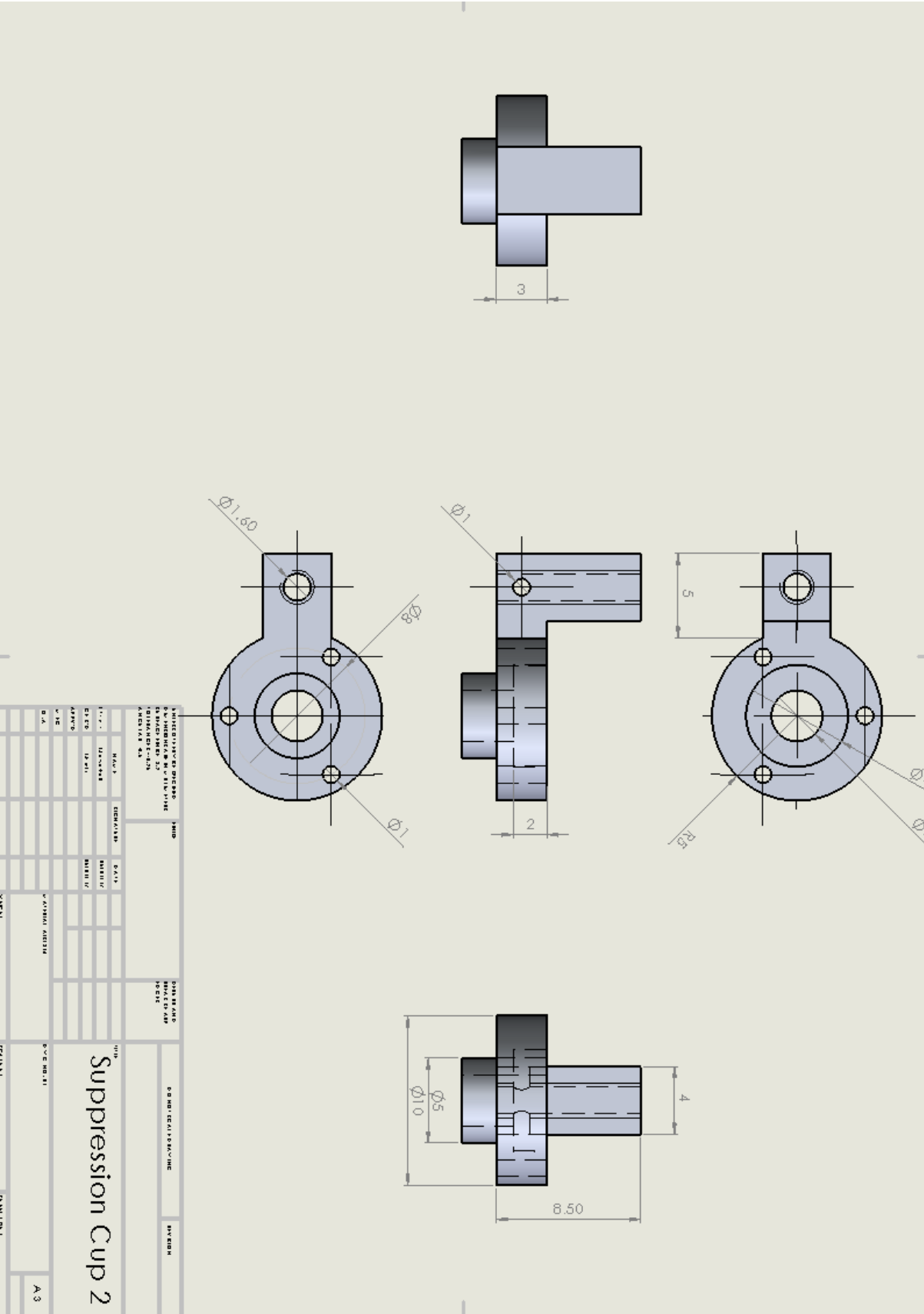
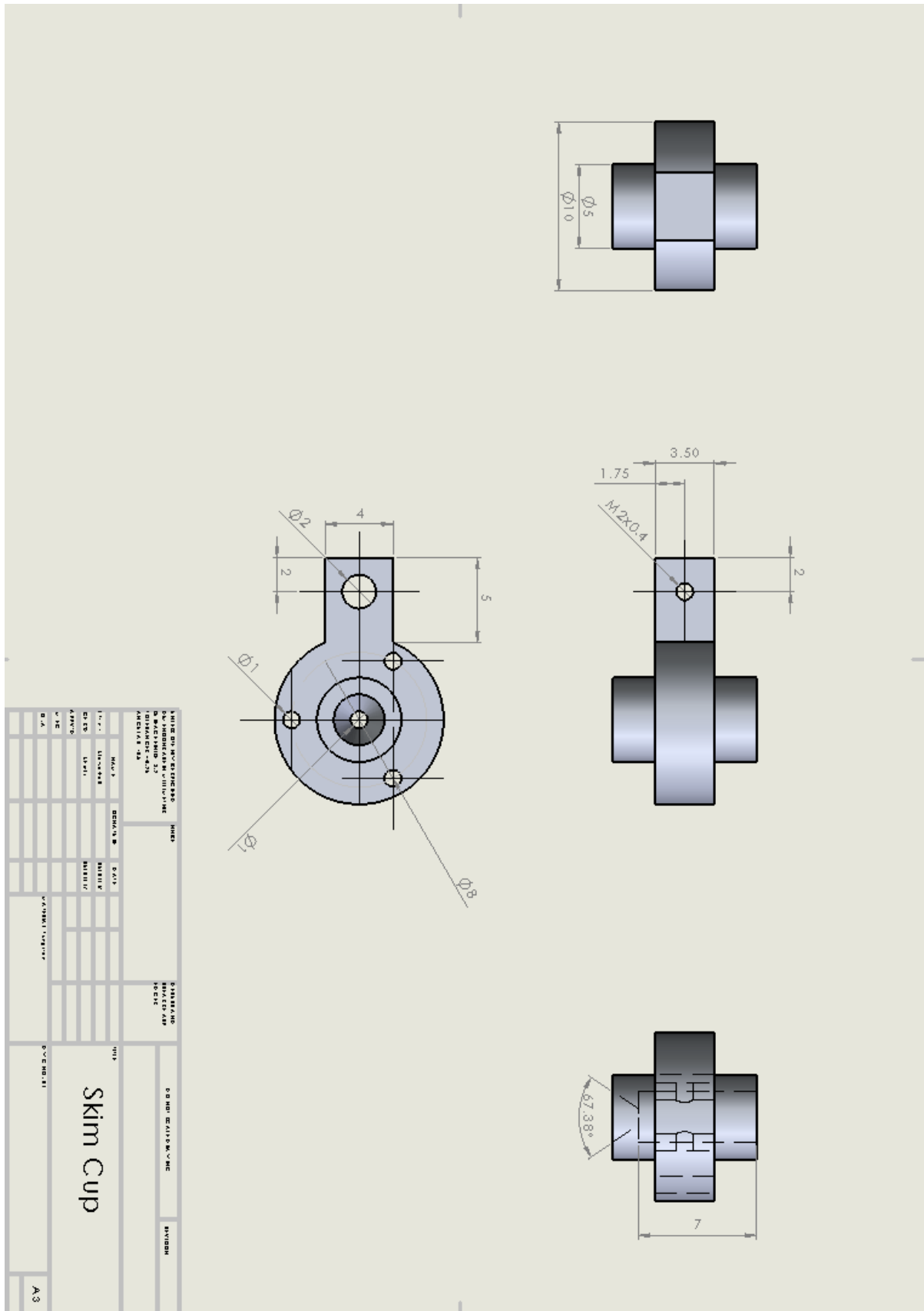


Figure 126 Suppression Cup 2



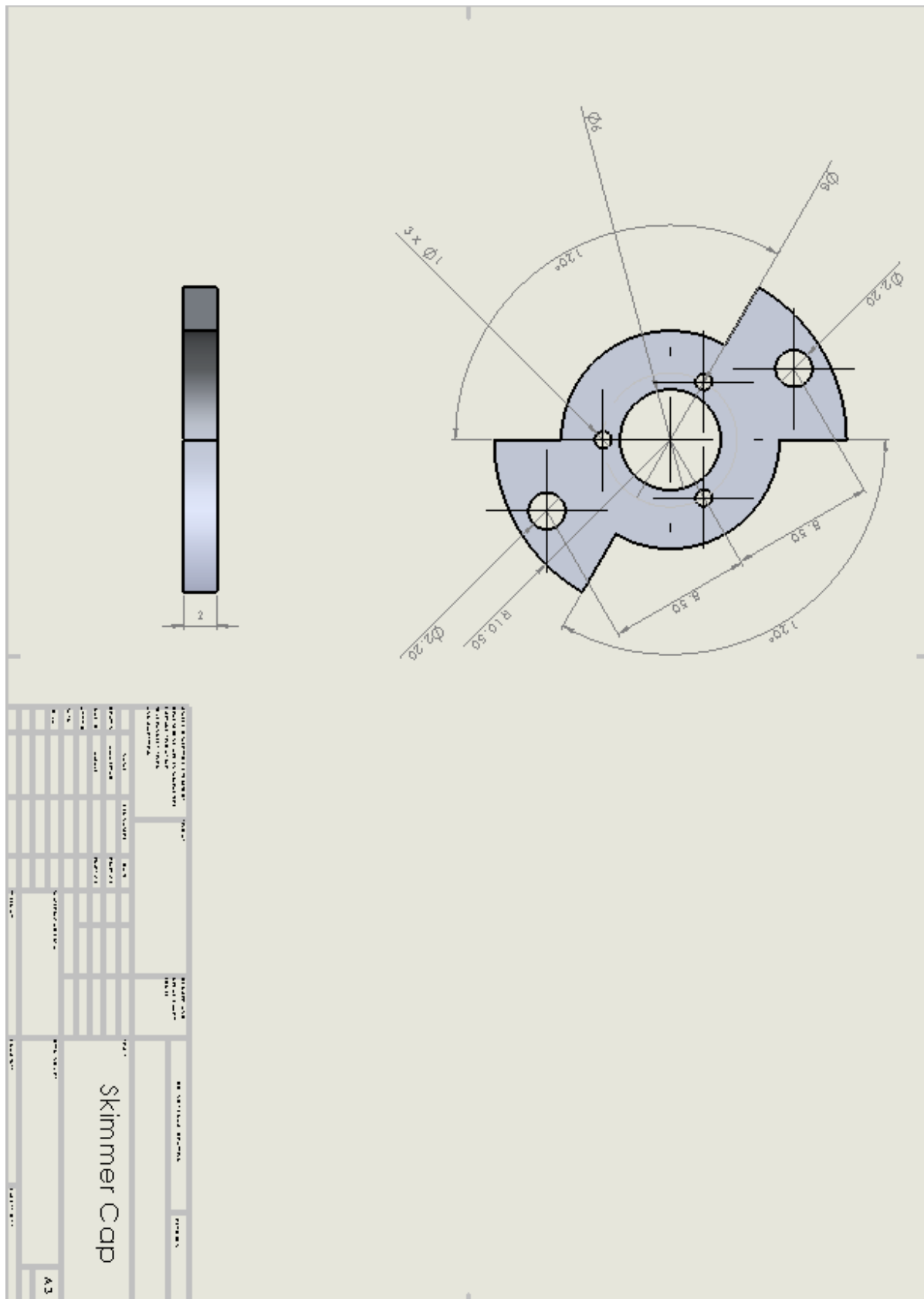


Figure 128 Skimmer Cap

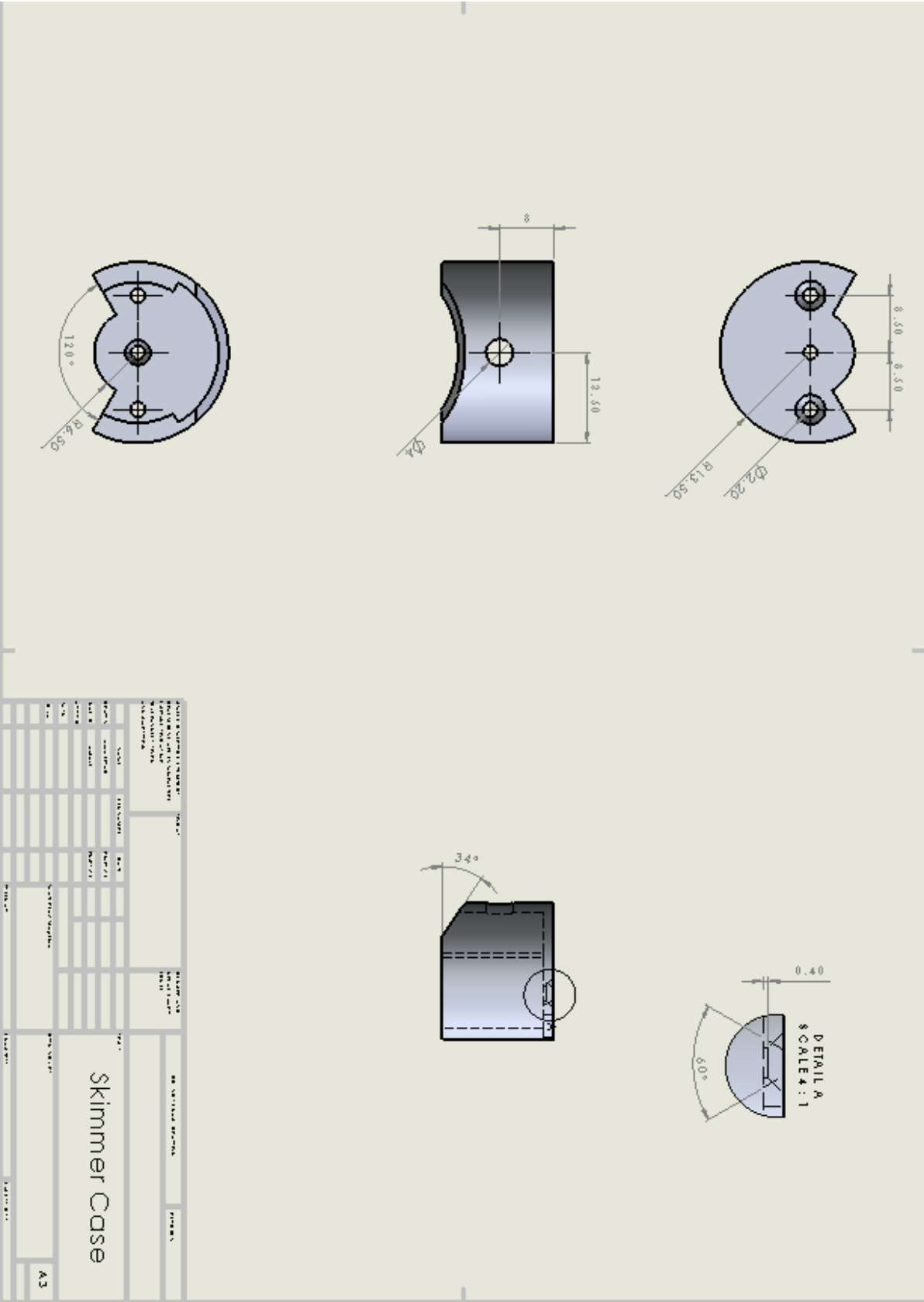


Figure 129 Skimmer Case

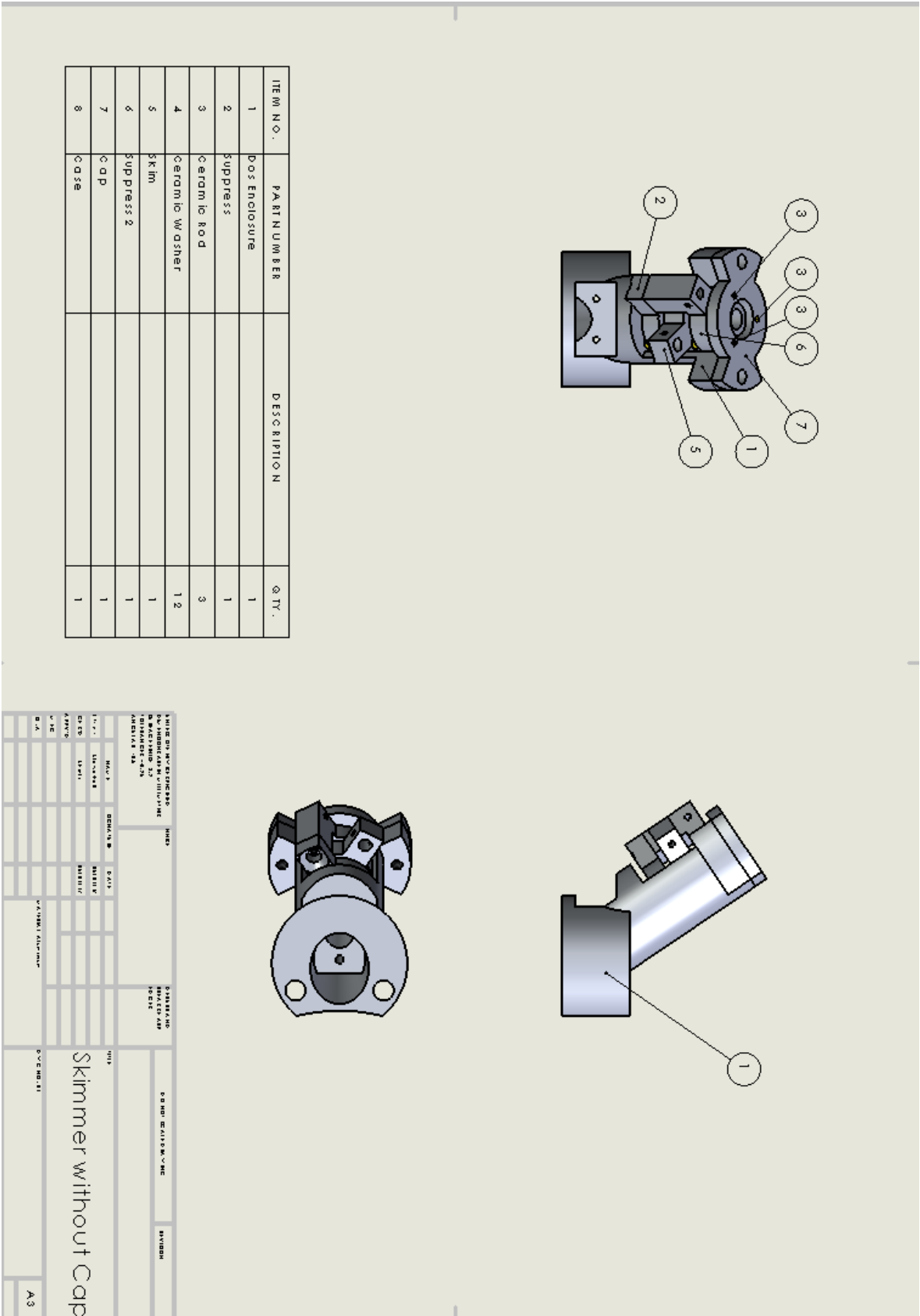


Figure 130 Skimmer Assembly without Cap

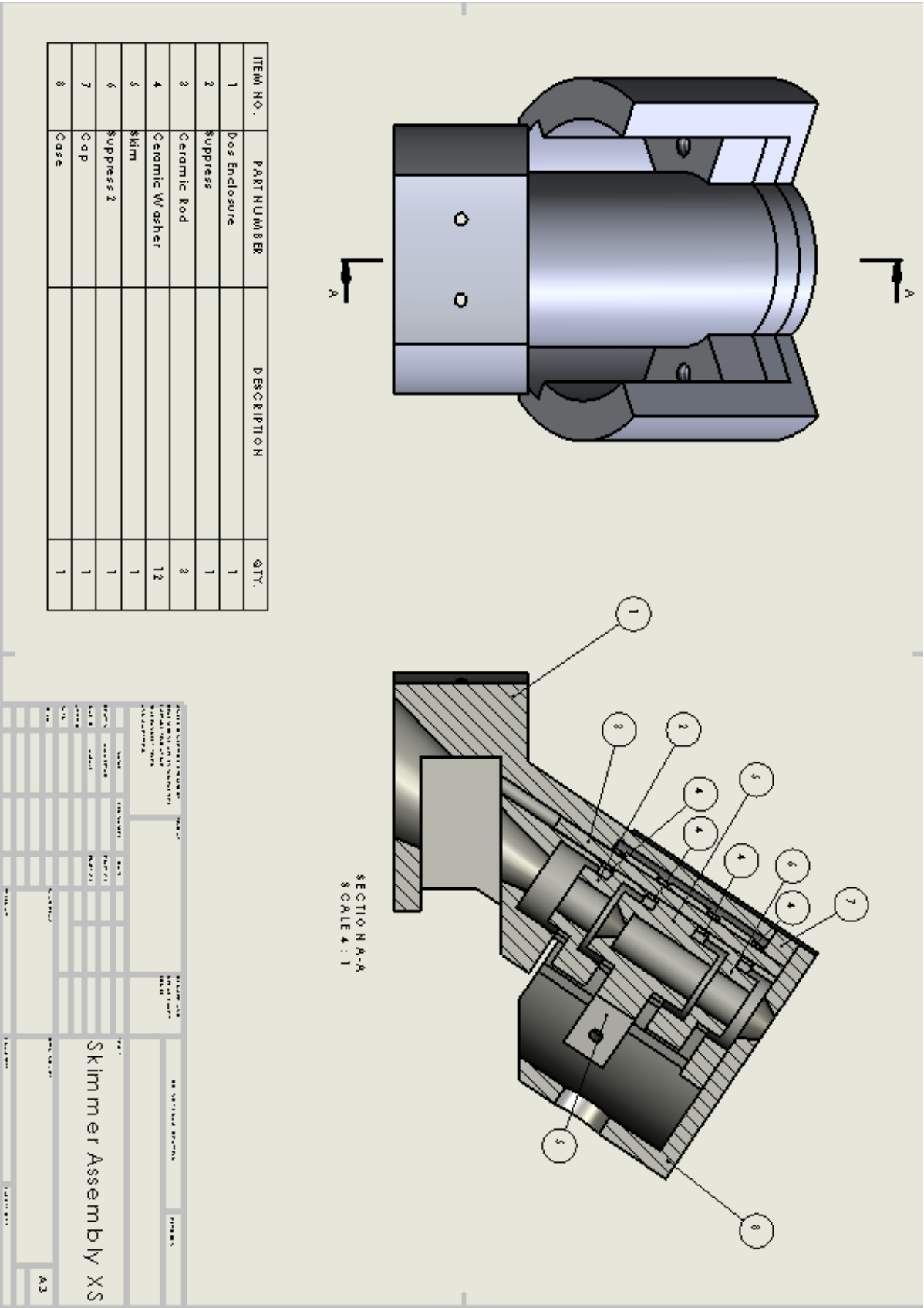


Figure 131 Skimmer assembly cross-section

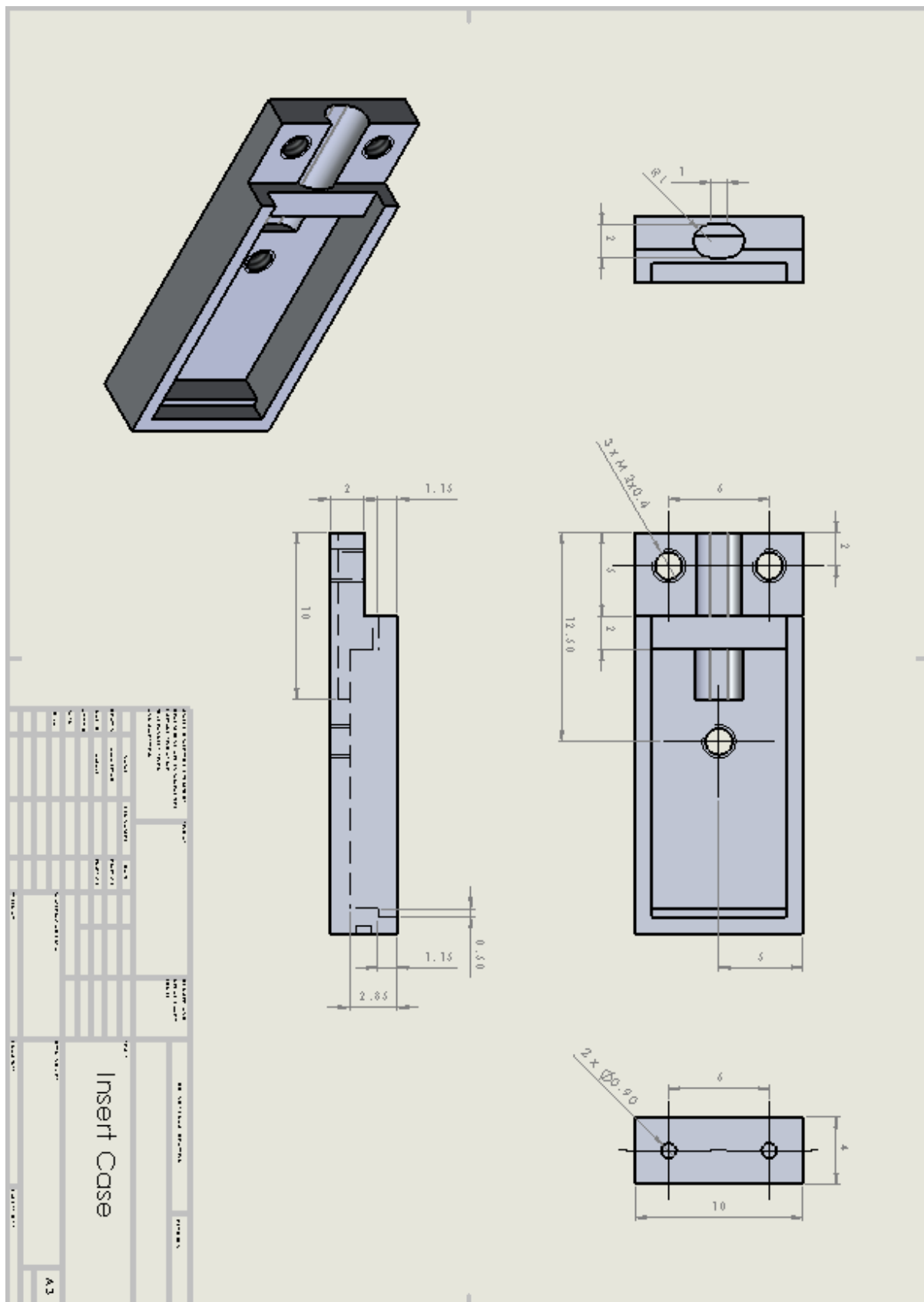


Figure 132 Dosimetry Insert Case

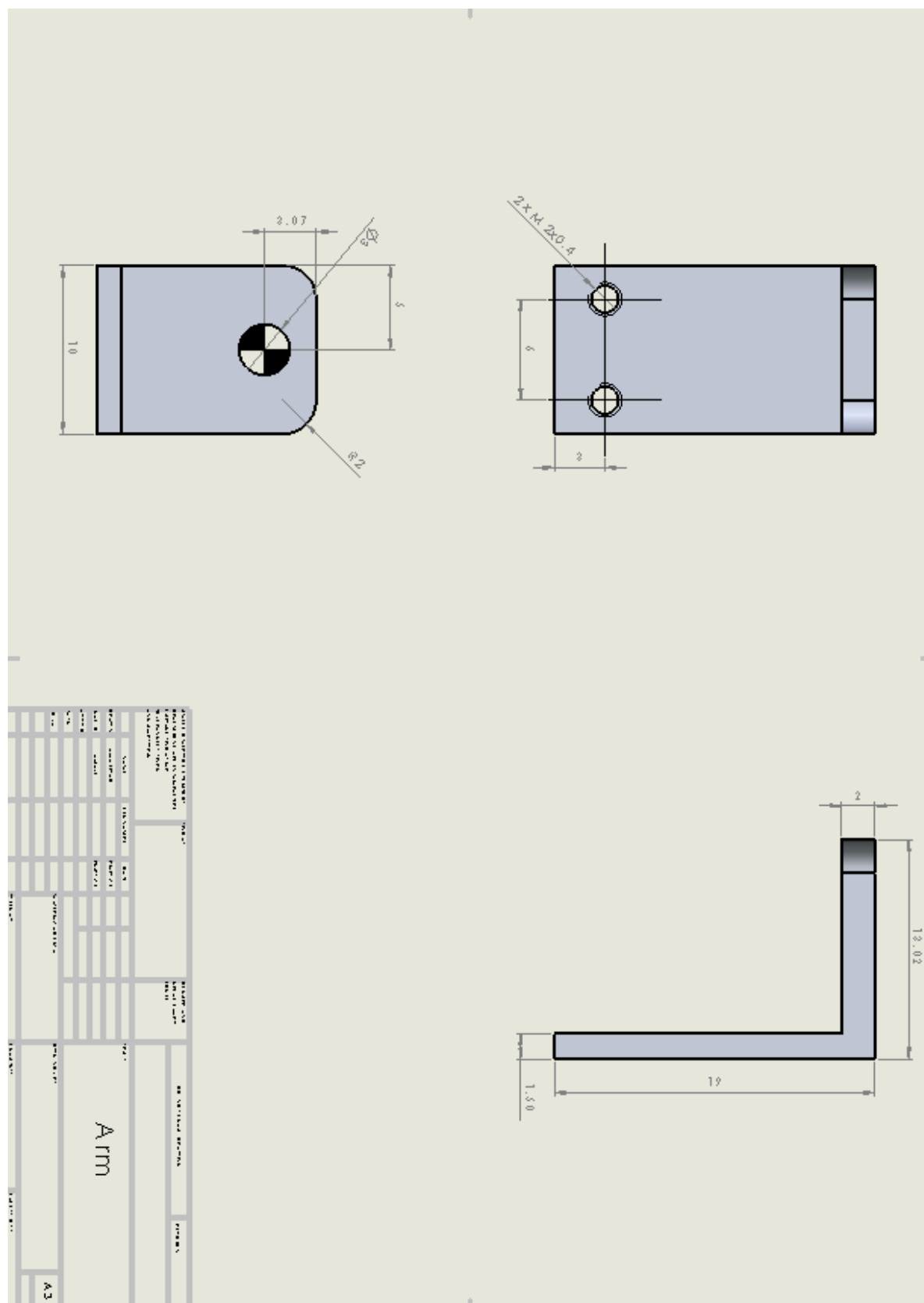


Figure 133 Dosimetry Arm

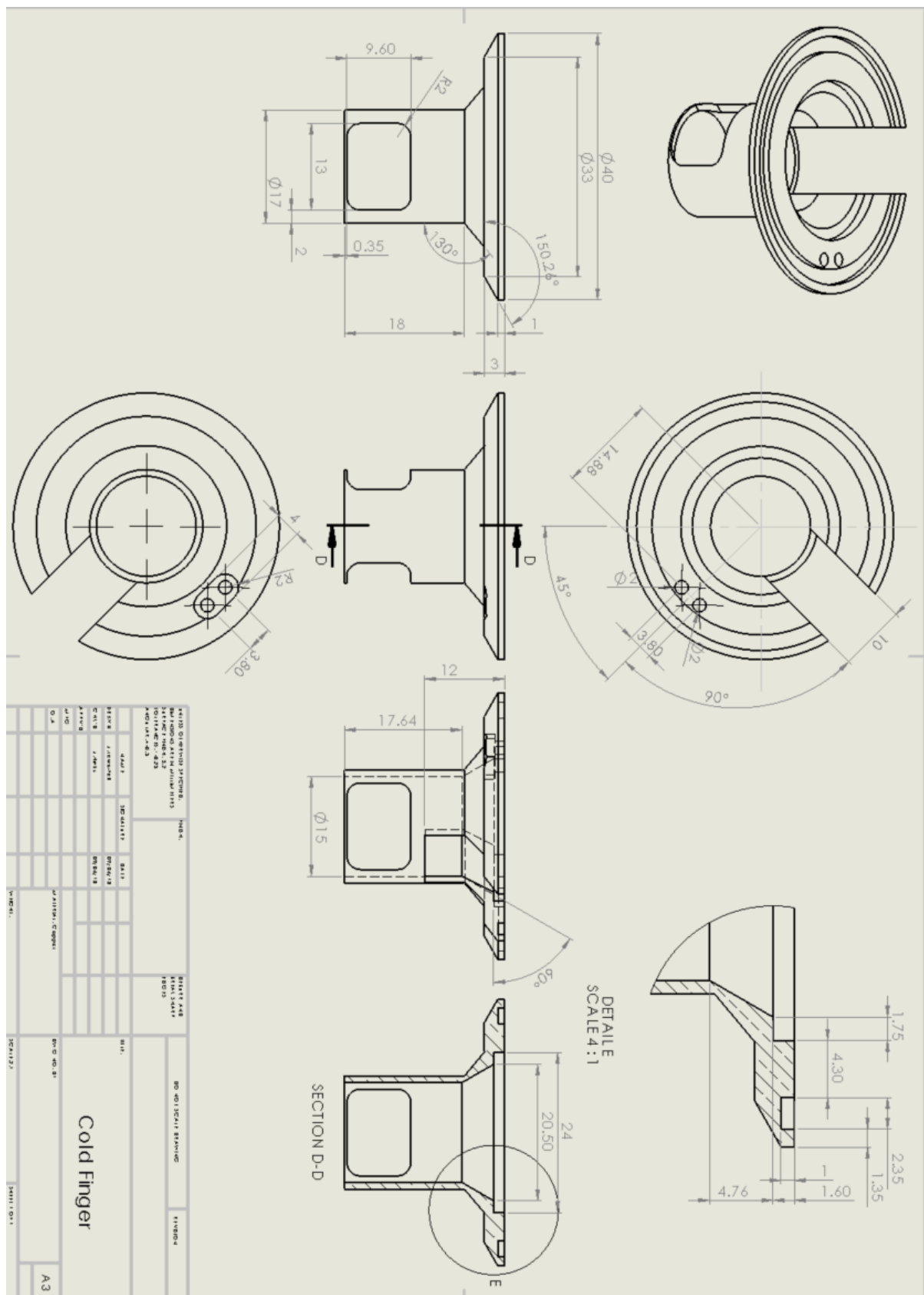


Figure 134 Modified Cold Finger